

Nur, Havva Hasret (2026) *Search for New Physics with an angular analysis and measurement of the shape of the $B^0 \to D^{*-}\mu^+\nu\mu$ differential decay rate.* PhD thesis.

https://theses.gla.ac.uk/86317/

Copyright and moral rights for this work are retained by the author

A copy can be downloaded for personal non-commercial research or study, without prior permission or charge

This work cannot be reproduced or quoted extensively from without first obtaining permission from the author

The content must not be changed in any way or sold commercially in any format or medium without the formal permission of the author

When referring to this work, full bibliographic details including the author, title, awarding institution and date of the thesis must be given

Enlighten: Theses
https://theses.gla.ac.uk/
research-enlighten@glasgow.ac.uk

Search for New Physics with an angular analysis and measurement of the shape of the $B^0 \to D^{*-}\mu^+\nu_\mu$ decay rate

Havva Hasret Nur

Supervised by Dr Lucia Grillo



University of Glasgow

Department of Physics and Astronomy

Submitted in fulfillment of the requirements
for the degree of Doctor of Philosophy

Abstract

New Physics Wilson coefficients and hadronic form factor parameters are measured with an analysis of the differential decay rate of $B^0 \to D^{*-}\mu^+\nu_\mu$ in q^2 and helicity angles. The data sample used corresponds to an integrated luminosity of 3 fb^{-1} collected by the LHCb experiment in proton-proton collisions at centre of mass energies 7 TeV and 8 TeV. The reconstructed final states are formed combining D^{*-} mesons with μ^+ candidates, where the D^{*-} is reconstructed via the $D^{*-} \to \overline{D}^0\pi^-$ and $\overline{D}^0 \to K^+\pi^-$ decay. Three different hadronic form factors parametrisations are used, and the measured parameters are compatible with existing determination while achieving higher precisions. The New Physics search is performed assuming different scenarios for the structure of the potential new interactions. The measured New Physics Wilson coefficient values are compatible with zero, in agreement with the Standard Model prediction.

To address theoretical tensions associated with hadronic dynamics, a high-precision measurement of the differential decay rate shape of $B^0 \to D^{*-}\mu^+\nu_\mu$, $d\Gamma/dw$, as a function of the hadronic recoil parameter w is presented, utilising a data sample corresponding to an integrated luminosity of 5.4 fb^{-1} collected by the LHCb experiment in proton-proton collisions at a centre of mass energy of 13 TeV. The reconstructed signal spectrum is efficiency-corrected and unfolded into discrete w bins. This measurement is expected to have comparable or better precision than the current experimental world average.

Finally, in preparation for the extreme radiation and occupancy environment of the High-Luminosity LHC era, simulation developments for the LHCb Mighty Tracker upgrade are presented. This includes the modelling of electronic signal digitisation for the silicon pixel sensors, alongside the implementation of a computationally optimised, stand-alone fast-track reconstruction algorithm designed to early studies for different track models.

Acknowledgements

I can confidently say that I am not the same person I was four years ago. This PhD has been a unique journey, full of challenges, discoveries, frustrations, friendships, and experiences that have shaped me both as a physicist and as a person. It would not have been possible without the support, guidance and patience of many people, to whom I owe a great deal of gratitude.

My greatest thanks go to my supervisor, Lucia Grillo, who has always been there for me, whatever happened along the way. I feel incredibly fortunate to have had the opportunity to work with her, to witness her brilliance first-hand, and to benefit from her deep knowledge of the field. She has taught me an enormous amount, both about physics and about how to approach research, and her guidance and support have accompanied me throughout every stage of this PhD. Without her, this thesis would quite simply not have been possible. I would also like to express my sincere thanks to my second supervisor, Mark Whitehead, who has always been generous with his time and support whenever I needed it.

I am also particularly grateful to Manuel Schiller, not least for teaching me how to write *decent code*, but also for his invaluable help in turning the Mighty Tracker simulation from an idea into a substantial technical project and in helping me develop it further.

I would like to thank all members of the Glasgow LHCb group for creating such a welcoming and supportive environment. I am particularly grateful to Niall McHugh, who was kind enough to share his University of Glasgow thesis template, within which these very words are now being written. I wish the very best to my fellow PhD students, Dylan and Will, for the remainder of their own journeys. I would also like to mention Aleksandrina Docheva, my academic sister, and Theo Maurin and Adam Anderson, my academic brothers—*les gars*—whose friendship has made this experience considerably more enjoyable.

I am very grateful to the members of the working groups within the LHCb collaboration with whom I worked during my physics analyses. The many discussions, questions, suggestions and occasional difficult problems shared along the way contributed enormously to the work presented in this thesis. In particular, I would like to thank Biljana Mitreska, Greg Ciezarek, Tobias Knospe and Marcello Rotondo for their help, insight and immensely useful discussions.

I would also like to thank my examiners, Mirco Dorigo and Mark Owen, for their thorough reading of this thesis, for an interesting and valuable discussion during my defence, and for their constructive comments and suggestions, which ultimately helped to improve this work.

Outside of physics, I owe an immeasurable amount to my family. To my mother, father and sister: thank you for raising me, supporting me throughout every stage of my life and education, and, perhaps most impressively, never seeming to grow tired of listening to me ramble about my work.

Last, but certainly not least, I want to thank my partner, my equal and my better half, Cihan Pazarbasi. Thank you for everything. For being the light to my darkness, the peace to my chaos, and the music to my cacophony. I would not be complete without you.

I dedicate this thesis to my favourite fictional character, Naruto, who helped shape my unyielding attitude towards life, and to my favourite non-fictional person, Hermann Hesse, who taught me so much about myself that I did not even know was there.

Declaration

The research results presented in this thesis are the product of my own work. Appropriate references are provided when results of third parties are mentioned. The research presented here was not submitted for another degree in any other department or university.

Havva Hasret Nur

Contents

Abstract i

Acknowledgements ii

Declaration iv

List of Tables x

List of Figures xvi

1 Introduction 1

2 Semileptonic B decays 4

2.1 The Standard Model of Particle Physics 4

2.1.1 Elementary particles 5

2.1.2 The Standard Model formalism 5

2.1.2.1 Quantum Electrodynamics (QED) 6

2.1.2.2 Quantum Chromodynamics (QCD) 6

2.1.3 Electroweak interactions 7

2.1.3.1 The Higgs mechanism 9

2.2 Flavour Physics 11

2.3 The SM as an effective field theory and New Physics scenarios 15

2.4 Theoretical formalism of $B^0 \to D^{*-}\ell^+\nu_\ell$ 19

2.4.1 $B \to D^* l\nu$ form factors 26

2.4.1.1 BGL parametrisation 27

2.4.1.2 BLPR form factor parametrisation 30

2.4.1.3 CLN parametrisation 34

2.4.2 $B \to D^{**} l\nu$ form factors 35

2.5 Anomalies in measurements of $B \to D^* \ell \nu$ decays . . . 37
2.5.1 NP searches using $B \to D^* \ell \nu$ . . . 40
2.5.2 Current state of art of hadronic form factors . . . 43
2.6 Summary . . . 51

3 The LHCb experiment and Upgrade II **52**
3.1 The LHC . . . 53
3.2 The LHCb detector in Run 1 and Run 2 . . . 56
3.2.1 The Vertex Locator (VELO) . . . 57
3.2.2 Tracking Stations . . . 58
3.2.2.1 TT . . . 59
3.2.2.2 T-stations . . . 60
3.2.3 RICH . . . 61
3.2.4 Calorimeters . . . 62
3.2.5 Muon system . . . 63
3.2.6 Particle identification . . . 65
3.2.7 The Trigger System . . . 65
3.2.7.1 Hardware (L0) Trigger . . . 67
3.2.7.2 High Level Trigger (HLT): HLT1 and HLT2 . . . 68
3.3 HL-LHC and Upgrade II . . . 72
3.3.1 Motivation and physics case . . . 72
3.3.2 Challenges and detector upgrades for HL-LHC . . . 72
3.4 Mighty Tracker . . . 75
3.4.1 Mighty Tracker Simulation . . . 78
3.4.2 Digitisation of MightyPix . . . 79
3.4.3 A Fast-Tracking Model in MightyPix (MP) . . . 82
3.4.3.1 An example case study . . . 84
3.4.3.2 Summary and Outlook . . . 91

4 New physics search in $B^0 \to D^{*-} \mu^+ \nu_\mu$ **92**
4.1 An Overview . . . 92
4.2 Neutrino reconstruction . . . 99
4.2.1 Approximate B rest frame . . . 100
4.2.2 Full quadratic equation . . . 101

4.3 Reweighting for different form factor parametrisations and/or New Physics . . . 103
4.4 Sensitivity to New Physics scenarios . . . 107
4.4.1 Vector operator . . . 108
4.4.2 Tensor operator . . . 110
4.4.3 Scalar operator . . . 113
4.5 Fit model . . . 115
4.5.1 Blinded fit results and sensitivity . . . 120
4.5.1.1 Results for SM fit using BGL . . . 121
4.5.1.2 Truncation order estimation for the BGL parametrisation . . . 121
4.5.1.3 Results for SM fit using CLN . . . 125
4.5.1.4 Results for SM fit using BLPR . . . 128
4.5.1.5 Results for NP fit with V_{qRlL} contribution . . . 132
4.5.1.6 Results for NP fit with S_{qLlL} contribution . . . 136
4.5.1.7 Results for NP fit with T_{qLlL} contribution . . . 138
4.5.1.8 Results for NP fit with scalar, vector and tensor contribution (Reel parts only) . . . 140
4.5.1.9 Results for NP fit with scalar, vector and tensor contribution (Reel and Imaginary parts) . . . 142
4.6 Toy studies . . . 145
4.6.1 Toy fit results . . . 146
4.6.1.1 CLN toy studies . . . 146
4.6.1.2 BGL toy studies . . . 147
4.6.1.3 BLPR toy studies . . . 148
4.6.1.4 BLPR SM toy studies . . . 148
4.6.1.5 BLPR NP toy studies . . . 149
4.6.1.6 Toys with multiple WCs . . . 153
4.6.2 Summary on the pseudo-experiment studies . . . 156
4.7 Systematic uncertainties . . . 157
4.8 Unblinded results and conclusion . . . 160

5 Differential decay rate shape measurement of $B^0 \to D^{*-}\mu^+\nu_\mu$ 169
5.1 Motivation and analysis overview . . . 169
5.2 Datasets and Simulation . . . 171

5.2.1 Simulation . . . 172
5.3 Candidate selection . . . 173
5.3.1 Trigger . . . 173
5.3.2 Centralised offline selection: Stripping . . . 175
5.3.3 Reconstruction and offline selection . . . 175
5.3.4 Gaussian Process Regression to reconstruct neutrinos . . . 179
5.3.4.1 Gaussian process . . . 179
5.3.4.2 Implementation on $B^0 \to D^{*-}\mu^+\nu_\mu$ decay . . . 181
5.4 Trigger and PID emulation for tracker-only MC samples . . . 188
5.4.0.1 L0 Trigger emulation . . . 188
5.4.1 HLT1 emulation . . . 190
5.4.2 PID emulation . . . 191
5.5 Fitter . . . 193
5.5.1 Simulation derived templates . . . 194
5.5.1.1 Signal . . . 194
5.5.1.2 Feed down from $B^0 \to D^*\tau\nu$ . . . 194
5.5.1.3 Feed down from $B \to D^{**}\mu\nu$ . . . 195
5.5.1.4 Feed down from $B^0 \to D^{**}\tau\nu$ . . . 196
5.5.1.5 Feed down from B_s^0 decays . . . 197
5.5.1.6 Higher D^{**} states . . . 197
5.5.1.7 Double charm backgrounds . . . 198
5.5.2 Data derived templates . . . 198
5.5.2.1 Combinatorial background . . . 198
5.5.2.2 Muon MisID . . . 198
5.5.3 Fit model structure and parameters . . . 199
5.5.4 Fit results . . . 205
5.6 Corrections to simulation . . . 206
5.6.1 Initial reweighting procedure . . . 208
5.6.1.1 Tracking efficiency correction . . . 208
5.6.1.2 B occupancy and kinematics corrections . . . 209
5.6.2 Final reweighting procedure . . . 210
5.7 Efficiency correction . . . 216
5.8 Unfolded decay rate spectrum . . . 217
5.9 Systematic uncertainties . . . 220
5.9.1 Simulation sample size . . . 221

5.9.2 Data and simulation differences . . . 221
5.9.3 Higher charm states background modelling . . . 222
5.9.4 Choice of form factor parametrisation . . . 223
5.9.5 Unfolding . . . 224
5.9.6 Electromagnetic interactions . . . 225
5.10 Conclusion . . . 225

6 Conclusion **228**

Appendices **231**
A Single Wilson coefficient toys . . . 231
A.1 S_{qLlL} toys . . . 231
A.1.1 Generation fixed to 0.0 . . . 231
B Toy studies with multiple Wilson coefficients . . . 232
B.1 Generation fixed to 0.0 . . . 232
B.2 Generation fixed to 0.0 . . . 233
B.3 Scanning different WC values . . . 234
B.4 Using asymmetric uncertainties in RooFit minimization . . . 241
B.5 Fit behaviour for starting values of 0.0 for the Wilson coefficients 242
B.5.1 Reparameterization of S_{qLlL}Im . . . 244
B.5.2 Constraining S_{qLlL}Im, T_{qLlL}Re and T_{qLlL}Im . . . 246
B.6 Further correlations between Wilson coefficients . . . 247
B.6.1 Linear reparametrisation using Principal Component Analysis . . . 248
B.7 Choice of positive real on different WCs in nominal configuration 249
B.7.1 Choosing vector to be real and positive . . . 249
B.7.2 Choosing right handed scalar to be real and positive 250
B.8 Toys with true distributions . . . 251
B.8.1 Generation values of WCs fixed to 0.0: . . . 252
B.8.2 Finer binning in toys with true distributions . . . 252
C Toy study with different binning for the fit variables . . . 256
D Hadronic form factors measured in Run 1 analysis and theory predictions . . . 258
E GPFlow studies . . . 260
F m^2_{miss}fit templates in Run 2 . . . 264

F.1 $B \to D^{**}\tau\nu$ . . . 264
F.2 MisID . . . 266
F.3 D^{**} grouped templates . . . 268
G m^2_{miss}fit results . . . 270
H Initial reweighting . . . 272
I Final reweighting . . . 272
J Alternative m^2_{miss} fit for systematics studies . . . 272

Bibliography **274**

List of Tables

2.1 The fundamental forces described the SM and their force carrier particles bosons are listed with their strength, spins, and mass. 5
2.2 The SM fermions are categorised according to their generation families and their corresponding electric charge and mass given. 6
2.3 Current status of the independent experimental measurements of LFU ratios and angular observables. The first and second errors are statistical and systematic, respectively. 39
2.4 Summary of theoretical predictions and experimental data for R_D, R_{D^*}, $F_L^{D^*}$ used in the fit of [1]. 41
2.5 The fit results of the single NP operator scenarios assuming real WCs. The WCs are given at the μ_b scale (explained in text). The allowed ranges of WC from the B_c lifetime and the current LHC bounds are also shown (*very loose* represents very weak bounds). Fitted WCs and predictions of $P_{D\tau}$,$P_{D^*\tau}$ and $R(J/\psi)$ are in the range of $\Delta\chi^2 = \chi^2 - \chi^2_{\text{best}} \leq 1$. 41

3.1 L0 trigger E_T/p_T and SPD thresholds for 2015, 2016, and 2017. . . . 68
3.2 Bit-packing allocation and hierarchy for the `MPChannelID` within the Mighty Tracker geometry. 81
3.3 Mean (μ) values of the track fit parameters for the $x-z$ and $y-z$ planes. 84

4.1 Trigger selection. 97
4.2 Selection for the `Hlt2CharmHadD02HH_D02KPi` trigger line. 98
4.3 Stripping selection. 98
4.4 `IsMuon` algorithm hit requirements in the muon stations based on the momentum of the particle track. 99

4.5 Offline selection. 99
4.6 NP operator basis and coupling conventions as given in HAMMER. The lower index of λ denotes the helicity of the neutrino and the lower index of χ is the helicity of the b quark. The Wilson coefficients considered in this analysis are marked with (*). 105
4.7 BLPR form factor parameters with central values obtained from [2]. Parameters that are not floated in the fit in this analysis are noted with † in the table (The explanation is given in 4.5.1.4). 117
4.8 CLN form factor parameters with central values from [3]. 117
4.9 BGL form factor parameters with central values as given in HAMMER. Parameters that are not floated in the fit in this analysis are noted with † in the table (The explanation is given in 4.5.1.1). 118
4.10 BLR form factor parameters with central values as given in HAMMER. 118
4.11 BLR FF parameters results from the $R(D^0)$ vs $R(D^*)$ analysis. These values are used for applying a Gaussian constraint to the fit parameters for the D^{**} background contributions. 118
4.12 Fit components summary and their corresponding parameters. The shape of the fit templates can be taken directly from simulation (MC), simulation and additional weights from HAMMER or from data which is stated in the second column. The third column lists the associated fit parameters to each of the components where N_i corresponds to the measured yield, WCs are the Wilson coefficients and FFs are the form factor parameters. 119
4.13 NP operator basis and coupling conventions as given in HAMMER. 120
4.14 Summary of the BIC values for several fitting models that use the combination of fitting parameters as stated in the order of fitting in the table. There is a separate d parameter that we fit for the muonic and tauonic template. 122
4.15 Values of the parameters and statistical uncertainty determined by the fit to Run 1 data using the SM scenario with the BGL form factor parametrisation. 123
4.16 Correlation coefficients of the form factor parameters determined by the fit to Run 1 data in the SM scenario with the BGL form factor parametrisation. 124

4.17 Values of the parameters and statistical uncertainty determined by the fit to Run 1 data using the SM scenario with the CLN form factor parametrisation. 126
4.18 Correlation coefficients of the form factor parameters determined by the fit to Run 1 data in the SM scenario with the CLN form factor parametrisation. 127
4.19 Values of the parameters and statistical uncertainty determined by the fit to Run 1 data using the SM scenario with the BLPR form factor parametrisation. 130
4.20 Correlation coefficients of the form factor parameters determined by the fit in the SM scenario with the BLPR form factor parametrisation. 131
4.21 Values of the parameters determined by the fit to Run 1 data using the NP scenario including V_{qRlL} with the BLPR form factor parametrisation. 135
4.22 Correlation coefficients of the form factor parameters determined by the fit in the NP scenario including V_{qRlL} with the BLPR form factor parametrization. 136
4.23 Values of the parameters determined by the fit using the NP scenario including S_{qLlL} with the BLPR form factor parametrisation. 137
4.24 Correlation coefficients of the form factor parameters determined by the fit in the NP scenario including S_{qLlL} with the BLPR form factor parametrisation. 138
4.25 Values of the parameters and statistical uncertainty determined by the fit to Run 1 data using the NP scenario including T_{qLlL} with the BLPR form factor parametrisation. 139
4.26 Correlation coefficients of the form factor parameters determined by the fit in the NP scenario including T_{qLlL} with the BLPR form factor parametrisation. 140
4.27 Values of the parameters and statistical uncertainty determined by the fit to Run 1 data using the NP scenario including real parts only of the Wilson coefficients using the BLPR form factor parameterization. 141
4.28 Correlation coefficients of the form factor parameters determined by the fit in the NP scenario with the real parts only of the Wilson coefficients using the BLPR form factor parameterization. 142

4.29 Values of the parameters determined by the fit to Run 1 data using the multi-parameter NP scenario with the BLPR form factor parametrisation. . . . 144
4.30 Correlation coefficients of the parameters determined by the fit in the multi-parameter NP scenario with the BLPR form factor parametrization. . . . 145
4.31 WCs generation and fitting interval in the BLPR NP toys. . . . 150
4.32 Wilson coefficients used in this parametrization shown here along with their generation and starting values and fitting intervals. . . . 155
4.33 Systematic uncertainties affecting the measurement of hadronic form-factor parameters. The total systematic uncertainties are obtained assuming no correlations among the contributions. For comparison, the statistical uncertainties are also reported. . . . 158
4.34 Systematic uncertainties affecting the measurement of the NP Wilson coefficients. The total systematic uncertainties are obtained assuming no correlations among the contributions. . . . 159
4.35 Standard Model fit results. On the left measured values are reported alongside the statistical and systematic uncertainties. On the right the statistical correlation matrix is shown. . . . 165
4.36 NP Wilson coefficient fit results for the five NP scenarios considered. 166
4.37 Statistical correlations among the Wilson coefficients for the different NP scenarios. . . . 167

5.1 Simulated decay modes, cocktail notes (mixture of several states of the particle) and sample sizes used in this analysis are given. . . . 172
5.2 `Hlt2XcMuXForTauB2XcMu` selection variables and the cuts. . . . 174
5.3 Stripping selection. . . . 175
5.4 Offline selection. The slow-pion (π_s) requirements are applied during tuple production. . . . 176
5.5 Input variables for the isolation MVA. . . . 178
5.6 Variables used to train XGboost for L0 Hadron emulation where E_T measured by the tracker. HCAL region indicates whether the hits are in the inner or outer region of HCAL. . . . 189
5.7 Global Events cuts applied before the HLT1 reconstructions 191

5.8 The binning scheme used for efficiency histograms produced by PIDCalib2. 192
5.9 Binning in w for 1D fit to m^2_{miss} 194
5.10 Description of groups of D^{**}components and corresponding yield parameter in the fit 200
5.11 Fit components summary and their corresponding parameters. The third column lists the associated fit parameters to each of the components where N_i corresponds to the measured yield. Nuisance parameters are used for reparametrisation of the $N_{D^*\mu}$ and $N_{D_s^{**}}$ and they are gaussian constrained (see text for more details). 203
5.12 List of variables used in the data/MC corrections. The meaning of the variables is explained at the beginning of section 4.1. 208
5.13 Stages of sequential reweighting with each of them representing a 3D histogram with the given binning. 212
5.14 Observed yields $N^{\text{obs}}_{D^*\mu}$, unfolded yields $N^{\text{unf}}_{D^*\mu}$ and unfolded yields corrected with the global efficiencies $N^{\text{unf+corr}}_{D^*\mu}$ for each w bin, all the yields are normalized to the total numbers over the whole w range. Uncertainties are only statistical. 220
5.15 The signal yields extracted with final data/MC weights and nominal procedure along with the relative systematic uncertainty. 222
5.16 Unfolded signal yield using different iterations and the relative systematic uncertainty from unfolding regularization. 225
5.17 Statistical uncertainties on the unfolded and efficiency corrected signal yields binned in w from different measurements, normalized to the total yield. 226

6.1 Different WC generation values considered in the toys. Each row (labelled with different letter) represents the fixed generation value for the Wilson coefficient in the toys. 235
6.2 Wilson coefficients used in this parametrization shown here along with their generation and starting values and fitting intervals. 249
6.3 Wilson coefficients used in this parametrization shown here along with their generation and starting values and fitting intervals. 250
6.4 Fit results for Bin 1 270
6.5 Correlation matrix for the first w bin. 270

List of Figures

2.1 Fundamental particles of the Standard Model. 4

2.2 Measurement of the angles and sides of the unitarity triangle as of summer 2025. They are measured via decays that feature the CKM elements in their definition, see Eq. 2.44 and the text for details. . . . 15

2.3 SM Feynman diagram for the $b \to c\bar{u}d$ transition mediated by W exchange. 15

2.4 Local four-fermion interaction obtained after integrating out the W boson. 16

2.5 $B \to D^*\ell\nu$ transition showing a tree-level diagram in the SM, proceeding via a mediating W boson. 19

2.6 Schematic view of the $B \to D^*\ell\nu$ decay featuring the three angles in the process. θ_l is the angle between the direction of the lepton and the B meson, θ_d is the angle between the D meson from the D^* decay and χ is the angle between the D^* and W plane. 20

2.7 Graphical summary of measurements of ratios $R(D)$ and $R(D^*)$ for Belle, BaBar and LHCb as of spring 2025 [3]. The black and blue points show the SM prediction. The average of the experimental results from LHCb, Belle-Belle II and BaBar is shown as a red ellipse. 38

2.8 Unfolded normalised differential decay rate of $B_s \to D_s^*\mu\nu$ with the fit superimposed for the CLN parametrisation (green), and BGL (orange). The band in the fit results includes both the statistical and systematic uncertainty on the data yields. Image taken from Ref. [4]. 46

2.9 Comparison of the fitted partial decay rates with 1σ uncertainties in the BGL and CLN parametrizations to the unfolded experimental data (shown as points with error bars). Note that the BGL (hatched) band almost completely overlaps the CLN (solid) band. Image taken from Ref. [5]. 46
2.10 One-dimensional projections of the normalised differential decay rates for $B \to D^* \ell \bar{\nu}_\ell$. The panels display, from left to right, the kinematic recoil w, the lepton helicity angle $\cos\theta_\ell$, the hadron helicity angle $\cos\theta_V$ (equivalent to the $\cos\theta_D$ notation used in this work), and the azimuthal angle χ. The unfolded data points are shown in black. The coloured bands represent the fit results and their associated uncertainties for different BGL parametrisation configurations: a lower-order BGL_{121} fit (blue), a higher-order BGL_{332} fit (red), and a BGL_{332} fit incorporating LQCD constraints (green). Image taken from Ref. [6]. . 47
2.11 The points show LQCD results in Ref. [7] for each SM form factor for both $B \to D^*$ (filled points) and $B_s \to D_s^*$ (empty points) as a function of the recoil parameter, w. The legend gives the mapping between symbol colour and shape and the set of gluon field configurations used, as given by the lattice spacing, and the heavy quark mass in lattice units. The blue curve with error band is the result of correlator fit in the continuum limit and with the physical b quark mass for the decays. 48
2.12 The points show LQCD results in Ref. [7] for each tensor form factor for both $B \to D^*$ (filled points) and $B_s \to D_s^*$ (empty points) as a function of the recoil parameter, w. The legend gives the mapping between symbol colour and shape and the set of gluon field configurations used, as given by the lattice spacing, and the heavy quark mass in lattice units. The blue curve with error band is the result of correlator fit in the continuum limit and with the physical b quark mass for the decays. Image taken from Ref. [7]. 49

2.13 The lattice-only normalised differential decay rates for $B^0 \to D^{*-}\ell^+\nu_\ell$, with respect to the angular variables defined in Fig. 2.6, are shown as the red bands. We also include binned untagged data for e/μ from Belle. Note the clear difference in shape, particularly for the differential rate with respect to w. The tauonic differential decay rates are shown in green. Image taken from Ref. [7]. 50
2.14 The normalised differential decay rate for $B_s \to D_s^*\ell\nu$ with respect to w is shown as the blue band. The binned data from LHCb is also shown. Here, they note that a similar difference in shape between SM theory and experiment to that seen for Belle data in Fig. 2.13. The semi-tauonic mode is plotted as the green band. Image taken from Ref. [7]. 50

3.1 An schematic drawing [8] of the accelerator complex, where stages of accelerators are used to accelerate protons before feeding into the LHC. 53
3.2 A side view of the Run 1-2 LHCb detector, containing layers of sub-detectors covering a region close to the proton beams, with the proton collisions occurring on the left [9]. 56
3.3 The top shows the layout of the modules along the proton beam, with the proton-proton collision region shown in blue. The bottom shows two modules from opposite halves when the VELO is closed (left) and opened (right); for each module, only either the R (red) or Φ (blue) layer of silicon strip sensor is shown. Reproduced from [10]. 57
3.4 Sketch [11] of the different tracking detectors and types of tracks within LHCb. 59
3.5 Layout of the TT, the four layers are shown. Image taken from Ref. [12]. 59
3.6 Layout of the first IT station. Only the first layer is shown. In light blue are the sensors. Image taken from Ref. [12]. 60
3.7 (a) Module cross section. (b) Arrangement of OT straw-tube modules in layers and stations. Image taken from Ref. [13]. 61
3.8 The optical system of (a) RICH1 and (b) RICH2. Image taken from Ref. [14]. 62

3.9 Lateral segmentation of the SPD/PS and ECAL (left) and the HCAL (right). One quarter of the detector front face is shown. In the left figure the cell dimensions are given for the ECAL. Image taken from Ref. [9]. 63
3.10 Side view of the muon system [9]. 64
3.11 The typical signals left by different particle species on different sub-detector components. A straight line corresponds to a track and a bunch of scattered lines corresponds to a particle shower. The differences between the particles species are used for their identification. [15]. 65
3.12 Overview of the LHCb trigger system during Run 1 [11]. 66
3.13 Overview of the LHCb trigger system during Run 2 [11]. 67
3.14 Sketch of the HLT1 track and vertex reconstruction sequence [11]. . . 69
3.15 Sketch of the HLT2 track and vertex reconstruction sequence [11]. . . 71
3.16 View of LHCb detector in Upgrade II [16]. 74
3.17 View of Mighty Tracker for Upgrade II [16]. The region near the beam pipe is covered with HV-CMOS sensors (in the colours of pink and light blue). The outer region use scintillating fibre technology. . . 76
3.18 View of the components and dimensions of a SciFi module. This example corresponds to one of the most external modules in a station where the scintillating fibre arrays (fibre mats) cover the full area. For modules sharing detection area with the MT MAPS detector, the scintillating fibre mats are shorter and the ESR foil mirrors are placed closer to the extremities of the module [16]. 77
3.19 Optical scan of a six-layer array of densely packed 250 µm diameter scintillating fibres [16]. 77
3.20 The overall design and dimensions of the one Silicon panel -Mighty Pixel (MP)- (28 modules) [16]. 78
3.21 Mighty tracker module layout, with the grey rectangles representing MAPS chips. The underlying kapton tapes can be seen in the gaps between the MAPS chips. The other side of the module has an offset arrangement of the chip to provide full coverage of the plane. The service hybrids are also visible with red and blue rectangles representing the readout components [16]. 78
3.22 A diagram of the digitization chain of algorithms. 80

3.23 An illustrative sketch to show how polynomial function can be used for different track models using LHCb coordinate system where z is the direction of beam line, y is in the magnetic field direction and x is the bending plane with dz the distance of z to the the centre of the T station. 82
3.24 Correlations between χ^2_X, χ^2 distribution in the $x-z$ plane and χ^2_Y, χ^2 distribution in the $y-z$ plane; χ^2 probability distribution in the $x-z$ plane and in the $y-z$plane. 85
3.25 The residual distributions $(x_{reco} - x_{true})$ of tracks in the $x-z$ plane (left) and $y-z$ plane (right), fitted with Gaussian function reporting μ (mean) and σ (standard deviation). 85
3.26 The correlation between the residual distributions in the x-z plane and in the y-z plane. 86
3.27 The correlation between track fit parameters in $x-z$ plane showing relation between different orders of contribution. 87
3.28 The correlation between track fit parameters in $y-z$ plane showing relation between different orders of contribution. 88
3.29 The correlation between same order terms of $x-z$ plane and $y-z$ plane. 89

4.1 $m(D^*)-m(D^0)$ distribution for the signal candidates of $D^{*+}\mu^-$ (blue) and the wrong sign $D^0\pi^+\mu^+$ candidates (red). A cut is placed in the offline selection at $m(D^*) - m(D^0) < 147$ and > 144 MeV. 95
4.2 Resolution of θ_l (top left), θ_d (top right), χ (bottom left) and q^2 (bottom right) for two types of neutrino reconstruction. The quadratic equation approach (red) and B rest frame approximation (blue) are compared. The quadratic approach yields a better resolution in the θ_l and χ. 102
4.3 Resolution of θ_l (top left), θ_d (top right), χ (bottom left) and q^2 (bottom right) for the two cases when the events with $r = 0.0$ are accepted (red) and discarded (blue). 103
4.4 Plots of distribution of the fitting variables for values in the range [-1.0, 1.0] for the real part of the right handed vector operator. 109
4.5 Plots of distribution of the fitting variables for values in the range [-1.0, 1.0] for the imaginary part of the right handed vector operator. 110

4.6 Plots of distribution of the fitting variables for values in the range [-1.0, 1.0] for the real part of the left handed tensor operator. 111
4.7 Plots of distribution of the fitting variables for values in the range [-1.0, 1.0] for the imaginary part of the left handed tensor operator. . 112
4.8 Plots of distribution of the fitting variables for values in the range [-1.0, 1.0] for the real part of the left handed scalar operator. 114
4.9 Plots of distribution of the fitting variables for values in the range [-1.0, 1.0] for the imaginary part of the left handed scalar operator. . 115
4.10 Fit projections of the fitting variables for the SM fit with BGL form factor parametrisation. The signal ($B^0 \to D^*\mu\nu$) is shown in purple and rest of the backgrounds in different colours. The black points represent the data. 125
4.11 Fit projections for the SM fit with the CLN form factor parametrisation. The signal ($B^0 \to D^*\mu\nu$) is shown in purple and rest of the backgrounds in different colours. The black points represent the data. The rest of the fit configurations show similar fit quality. 127
4.12 Template shapes for the five fitting variables overlayed for different values of the ΔV_{20} parameter. It can be seen that there is no change in the template under this parameter. 128
4.13 Template shapes for the five fitting variables overlayed for different values of the $\Delta\chi_3(1)'$ parameter. It can be seen that there is no change in the template under this parameter. 129
4.14 Fit projections for the SM fit with the BLPR form factor parametrisation. The signal ($B^0 \to D^*\mu\nu$) is shown in purple and rest of the backgrounds in different colours. The black points represent the data. The rest of the fit configurations show similar fit quality. 132
4.15 Correlation matrix for the New Physics V_{qRl} toy fit. 133
4.16 Template shapes for the five fitting variables overlayed for different values of the $\Delta\chi_2(1)$ parameter. The range of values determined in a way that it will cover all the possible fitted values seen in toys. It can be seen that there is only some slight variation in the template for $cos\theta_l$, $cos\theta_d$ and q^2. 134
4.17 Summary plots of the mean values and standard deviations of the pull distributions within the CLN fit configuration. 147

4.18 Summary plots of the mean values and standard deviations of the pull distributions within the BGL fit configuration. 148
4.19 Summary plots of the mean values and standard deviations of the pull distributions within the BLPR fit configuration. 149
4.20 Summary plot of the mean values and standard deviations of the pull distributions in single WC-V_{qRlL} scenario. The respective WC and the form factor parameters from the signal are shown. 150
4.21 Likelihood scans of V_{qRlL}. Fitted values: V_{qRlL}Re = 0.01482, V_{qRlL}Im = 0.01108; generated values : V_{qRlL}Re = 0.01953, V_{qRlL}Im=0.007845 151
4.22 Summary plot of the mean values and standard deviations of the pull distributions in single WC-S_{qLlL} scenario. The respective WC and the form factor parameters from the signal are shown. 152
4.23 Likelihood scans of S_{qLlL}. Fitted values: S_{qLlL}Re = -0.08892, S_{qLlL}Im = 0.004298; generated values : S_{qLlL}Re = 0.004271, S_{qLlL}Im=0.02892. 152
4.24 Summary plot of the mean values and standard deviations of the pull distributions in single WC-T_{qLlL} scenario. The respective WC and the form factor parameters from the signal and the backgrounds are shown. 153
4.25 Likelihood scans of T_{qLlL}. Fitted values: T_{qLlL}Re = -0.04603, T_{qLlL}Im = 0.51; generated values : T_{qLlL}Re = -0.09512, T_{qLlL}Im=-0.5028. . . . 153
4.26 Pull distributions in the real-only WC scenario. 154
4.27 Summary plot of the mean values and standard deviations of the pull distributions of the Wilson coefficients from Tab. 4.32. 155
4.28 Likelihood scans of WCs when they generated and fitted as in Tab. 4.32 and the fitted values: V_{qRlL}Re = 0.094, V_{qRlL}Im = 0.099, T_{qLlL}Re = 0.102 C_pRe = -0.007 , C_pIm = -0.02. 156
4.29 Comparison of the results obtained in this form-factor measurement using CLN (blue), BGL (orange), and BLPR (green) parametrisations. The uncertainty bands are derived assuming that systematic uncertainties are uncorrelated. The BGL form-factor basis is used. The BGL form-factor parameters associated to $\mathcal{F}_2$ are fixed in this measurement and therefore the uncertainty band is not available. . . 161

4.30 Comparison of the results obtained in this form-factor measurement using the BGL parametrisation (orange) to lattice QCD calculations from HPQCD (blue), Fermilab-MILC (red) and JLQCD (green). The uncertainty bands for this work are derived assuming that systematic uncertainties are uncorrelated. The results are compared in the BGL form-factor basis. The form-factor parameters associated to $\mathcal{F}_2$ in the BGL parametrisation are fixed (see Tab. 4.9) in this measurement therefore there is no uncertainty band. 162
4.31 Distribution of forward-backward asymmetry of the muon (A_{FB}), longitudinal polarisation of D^* (F_{L}) and polarisation of the muon ($\tilde{F}_{\mathrm{L}}$) estimated using the values of hadronic form-factors parameters measured in this analysis. The results for various form-factor parametrisations are compared with Belle results from Ref. [17] (red) and Ref. [18] (black points). The uncertainty bands for CLN, BGL and BLPR form-factor parametrisations from this work are derived assuming that systematic uncertainties are uncorrelated. 163
4.32 Normalised decay rate of $B^0 \to D^{*-}\mu^+\nu_\mu$ in w compared, with the total uncertainties. 164
4.33 The 1, 2 and 3σ confidence contours for S_{LL} and T_{LL} NP Wilson coefficients, obtained with a two-dimensional Feldman-Cousins scan for the real and imaginary part of each WC.S_{qLlL} and T_{qLlL} correspond to the results of the single WC scenario in Table 4.36. 166
4.34 Three 68% confidence contours for the S_{LL}, obtained assuming different values for the BLPR form factor parameter $\eta(1)$. The contours are obtained with a two-dimensional Feldman-Cousins scan for the real and imaginary part of the WC parameter. $\eta(1)$ is fixed to $\pm 1\sigma$ of the SM fit value for each alternative contour in blue and green respectively. The similarity of the contours shows that the NP parameters determination is uncorrelated to the hadronic form factors. 168
4.35 Comparison of NP Wilson coefficients measured when fitting one Wilson coefficient at a time (left) and determining multiple NP Wilson coefficients (right) to the results of the recent analysis reported in Ref. [19]. 168

5.1 Comparison of the shapes of the decay amplitude for the different calculations and experiments. Image taken from [20]. 170
5.2 D^0 impact parameter with respect to the best PV in right-sign and wrong-sign samples compared. 177
5.3 Distribution of the b-hadron momentum residuals ($\Delta = P_{b_{reco}} - P_{b_{true}}$). The label *This study* in the legend indicates the GPR application to the $\Lambda_b \to \Lambda_c \mu\nu$ decay channel, showing a narrower and more centred peak compared to the *random solution* and linear regression approaches. The respective improvements written on the plot as 41.59% and 21.88%. Image taken from LHCb-ANA-2024-058 (in preparation). 182
5.4 Correlation of training variables and target variable in 2016 signal MC sample with magnet up polarisation. 183
5.5 Correlations between prediction and the target variable in training (left) and test (right) samples (top-row). The distribution of true log-scaled B^0 momentum overlay with sGPR predictions (bottom-row). 185
5.6 Top comparison of B^0 momentum reconstruction using sGPR (Pred in red), random solution (Reco in green), and MC truth (True in blue). Bottom-left: Momentum residuals. Bottom-right: Fractional momentum residuals with statistical summary. 186
5.7 In top row, the w momentum distributions are compared between GPR prediction (red) and random solution (green) approximation compared with MC true (blue) distribution. In bottom row, w residual and resolutions are compared and the improvement in resolution with respect to the random approximation written on the residual plot. 187
5.8 The L0HadronTOS efficiency as a function of the reconstructed $P_T(D^0)$. The red line is emulation and the blue line is full simulation. 189
5.9 The L0GlobalTIS efficiency as a function of the reconstructed $P_T(B^0)$. The red line is emulation and the blue line is full simulation. 190
5.10 The HLT1TrackMVA TOS efficiency as a function of the reconstructed $P_T(D^0)$. The red line is emulation and the blue line is full simulation. 191
5.11 Kinematic distributions of $B \to D_1' \mu\nu$ sample overlayed with HAMMER and EvtGen corrections. 196

5.12 The $B \to D^{**}\tau\nu$ template shapes shown for the first w bin laid over signal template shape. Legend shows the number of events for both B meson charges from data taking years 2016/2017/2018 197
5.13 The misID template shapes shown in Bin 1 along with signal candidate. Legend shows the number of events for the different types of misID components from data taking years 2016/2017/2018 199
5.14 Combined D^{**} template shapes (black dashed-line) are shown together with its sub-components described as in Tab. 5.10 for the first w bin. 200
5.15 The template shapes used in 10 w bin fits shown. 204
5.16 The m^2_{miss} fit projection in the first w bin. 205
5.17 The fitted yields of signal component in each w bin 206
5.18 Fitted yields of background components in each w bin. 206
5.19 The comparison of correction variables for $B \to J/\psi K$ sample. 210
5.20 B^0 kinematic and occupancy variables comparison between data and simulation after final reweighting stage, where the black markers represent the data, while the blue markers represent the post-fit simulation cocktail. The lower panels display the data-to-model ratio. . . . 213
5.21 The comparison of kinematic and vertex variables of B^0 and D^0 between data and simulation after final reweighting stage across the whole w region, where the black markers represent the data, while the blue markers represent the post-fit simulation cocktail after final reweighting stage. The lower panels display the data-to-model ratio. . 214
5.22 The comparison of kinematic and vertex variables for the final-state decay products (K, π, μ) between data and simulation after final reweighting stage across the whole w region, where the black markers represent the data, while the blue markers represent the post-fit simulation cocktail after final reweighting stage. The lower panels display the data-to-model ratio. 215
5.23 Trigger variables comparison between data and simulation after final reweighting stage, where the black markers represent the data, while the blue markers represent the post-fit simulation cocktail. The lower panels display the data-to-model ratio. 216

5.24 Migration matrix $m_{i,j}$ showing the probability of reconstruction in w_{rec} bin i conditional on true-w bin j for selected simulated signal events. Each row, corresponding to a true-w bin, is normalised to unity. 218
5.25 The normalised unfolded signal yield distribution in w bins. 219
5.26 Normalised signal distribution in m^2_{miss} with two different form factor parametrisations. 224
5.27 Normalised decay rate of $B^0 \to D^{*-}\mu^+\nu_\mu$ in w compared, with the total uncertainties (except the Run 2 measurement). 227

A.1 Pull distributions of the Wilson coefficient. 231
A.2 Pull distributions of the Wilson coefficient. 231
A.3 Summary plot of the mean and sigma values of the pull distributions. The uncertainty on the data points is the error from the fit. 232
B.1 Pull distributions of the Wilson coefficient. 232
B.2 Summary plot of the mean and sigma values of the pull distributions. The uncertainty on the data points is the error from the fit. 233
B.3 Pull distributions of the Wilson coefficient. 233
B.4 Summary plot of the mean and sigma values of the pull distributions. The uncertainty on the data points is the error from the fit. 234
B.5 Summary plot of the mean values of the pull distributions when the Wilson coefficients are generated at a fixed point of 0.0 and fitted starting from 0.0 in the range [-1,1]. The uncertainty of the data points are the standard deviation of the pulls 235
B.6 Likelihood scans of WCs generated at 0.0 and float starting from 0.0 in the range of [-1,1]. 236
B.7 Correlation matrix for the toy with WCs generated at 0.0 and float around 0.0 in the range of [-1,1]. 237
B.8 Summary plot of the mean values of the pull distributions when vector part generated at 0.0 while other WCs generated at 0.1 and vector float around 0.0 while other Wilson coefficients at 0.1 in the range of [-1,1]. The uncertainty on the data points is the standard deviation of the pull distribution. 238

B.9 Summary plot of the mean values of the pull distributions. The uncertainty on the data points is the standard deviation of the pull distribution. . . . 238
B.10 Likelihood scans of WCs generated at 0.1 and float around 0.1 in the range of [-1,1]. . . . 239
B.11 Summary plot of the mean values of the pull distributions when WCs generated at 0.5 and float around 0.5 in the range of [-1,1]. The uncertainty on the data points is the standard deviation of the pull distribution. . . . 240
B.12 Likelihood scans of WCs generated at 0.5 and float with starting value of 0.5 in the range of [-1,1]. . . . 240
B.13 Summary plot of the mean values of the pull distributions when WCs generated at 0.1 and only real parts are floated in the fit. The uncertainty on the data points is the standard deviation of the pull distribution. . . . 241
B.14 Summary plot of the mean values of the pull distributions for the generation value of the WCs fixed at 0.0 and floated around 0.0 in the range of [-1,1]. The uncertainties used in the pull calculation is the MINOS uncertainty. . . . 242
B.15 Likelihood scans of WCs generated at 0.1 with starting value 0.0 in the range of [-1,1]. . . . 243
B.16 Final value distributions of WCs generated at 0.1 and float around 0.1 in the range of [-1,1]. . . . 243
B.17 Summary plot of the mean values of the pull distributions when WCs generated at 0.1 and float only real parts around 0.0 in the range of [-1,1]. The uncertainty on the data points is the standard deviation of the pull distribution. . . . 244
B.18 Final value distributions of WCs when S_{qLlL}Im is reparameterised. . 244
B.19 Correlation plots of final values of WCs without reparametrisation of S_{qLlL}Im. . . . 245
B.20 Correlation plots of final values of WCs when S_{qLlL}Im is reparameterised. . . . 245
B.21 Summary plot of the mean values of the pull distributions when S_{qLlL}Im is reparameterised to take positive values. The uncertainty on the data points is the standard deviation of the pull distribution. . 246

B.22 Summary plot of the mean values of the pull distributions when the S_{qLlL}Im, T_{qLlL}Re and T_{qLlL}Im are floating around 0.0 in the range of [0,1]. 246
B.23 Correlation plots of final distributions of the WCs when the S_{qLlL}Im, T_{qLlL}Re and T_{qLlL}Im are floating around 0.0 in the range of [0,1]. . . . 247
B.24 Correlation plots of final values (Config A) of S_{qLlL} and T_{qLlL}. 247
B.25 Correlation plots of the final distributions of the WCs when they are reparameterised using PCA. 248
B.26 Summary plot of the mean values of the pull distributions when the WCs are reparameterised using PCA. 249
B.27 Summary plot of the mean values of the pull distributions for the WCs generated and fitted as in Tab. 6.2. The uncertainty on the data points is the standard deviation of the pull distribution. 250
B.28 Summary plot of the mean values of the pull distributions for the WCs generated and fitted as in Tab. 6.3. The uncertainty on the data points is the standard deviation of the pull distribution. 251
B.29 Summary plot of the mean values of the pull distributions for the WCs generated and fitted as in Tab. 4.31 in true distributions. The uncertainty on the data points is the standard deviation of the pull distribution. 252
B.30 Summary plot of the mean values of the pull distributions in true distributions WCs generated at 0.0 and float around 0.0 in the range of [-1,1]. The uncertainty on the data points is the standard deviation of the pull distribution. 252
B.31 Summary plot of the mean values of the pull distributions in true distributions with more binning for the WCs generated and fitted as in Tab. 4.31 in true distributions. The uncertainty on the data points is the standard deviation of the pull distribution. 253
B.32 Summary plot of the mean values of the pull distributions in true distributions with finer binning when WCs generated at 0.0 and float around 0.0 in the range of [-1,1]. The uncertainty on the data points is the standard deviation of the pull distribution. 253

B.33 Summary plot of the mean values of the pull distributions when the Wilson coefficients are generated at a fixed point of 0.0 (first row), 0.1 (second row - left), 0.5 (second row - right) and fitted in the range [-1,1]. 254
B.34 Final value distributions of WCs generated at 0.1 but float around 0.0 in the range of [-1,1]. 255
B.35 Correlation plots of final values (Config D) of S_{qLlL} and T_{qLlL}. 256
C.1 Summary plot of mean and sigma values of the pull distributions on the components. The uncertainty on the data points is the uncertainty on the mean and the sigma parameters respectively of the Gaussian fit to the pull distributions. The colours of blue, orange, green and red respectively correspond to the 3 (nominal), 8, 10 and 20 binning. 257
C.2 Summary plot of mean and sigma values of the pull distributions on the components. The uncertainty on the data points is the uncertainty on the mean and the sigma parameters respectively of the Gaussian fit to the pull distributions. The blue, orange and green markers correspond to the 5 (nominal), 10 and 20 binning, respectively. 258
D.1 Comparison of the results obtained in this form-factor measurement using the CLN parametrisation (orange) to lattice QCD calculations from HPQCD (blue), Fermilab-MILC (red) and JLQCD (green). The uncertainty bands for this work are derived assuming that systematic uncertainties are uncorrelated. The results are compared in the BGL form-factor basis. 259
D.2 Comparison of the results obtained in this form-factor measurement using the BLPR parametrisation (orange) to lattice QCD calculations from HPQCD (blue), Fermilab-MILC (red) and JLQCD (green). The uncertainty bands for this work are derived assuming that systematic uncertainties are uncorrelated. The results are compared in the BGL form-factor basis. 260
E.1 Resolution improvements using GPR along with the distributions are shown here for the variables of interest in the signal simulation sample from 2016 with one magnet polarity. 261

E.2 Resolution improvements using GPR along with the distributions are shown here for the variables of interest in the signal simulation sample from 2017 with one magnet polarity. 262
E.3 Resolution improvements using GPR along with the distributions are shown here for the variables of interest in the signal simulation sample from 2018 with one magnet polarity. 263
F.1 The $B \to D^{**}\tau\nu$ template shapes shown for the w bins laid over signal template shape. Legend shows the number of events for both B meson charges from data taking years 2016/2017/2018 (left to right) 265
F.2 The MisID template shapes shown different w bins along with nominal data templates. Legend shows the number of events for the different types of MisID components from data taking years 2016/2017/2018 (left to right) 267
F.3 Combined D^{**} template shapes (black dashed-line) are shown together with its sub-components described as in Tab. 5.10 for the first w bin. 269
G.1 Fit projections in each w bin. 271
H.1 Mass plot for 2017-2018 (left-right) $B \to J/\psi K$ decays. 272
J.1 Fit projections in each w bin after final reweighting. 273

Chapter 1

Introduction

The differential decay rate of $B^0 \to D^{*-}\mu^+\nu_\mu$ as a function of the three decay angles and the squared momentum transferred to the lepton pair (q^2) is uniquely sensitive to the presence of New Physics (NP) interactions, while simultaneously remaining sensitive to the underlying hadronic dynamics.

Previous measurements of $B^0 \to D^{*-}\mu^+\nu_\mu$ decays by the Belle [6, 21, 22], Belle II [5], and BaBar [23, 24] collaborations have provided experimental determinations of the CKM matrix element $|V_{cb}|$ and the hadronic form factors using the Caprini–Lellouch–Neubert (CLN) [25] or Boyd–Grinstein–Lebed (BGL) [26] formalisms. More recently, model-independent extractions of the angular coefficients [18] have begun to characterise the angular structure of the decay without explicitly separating non-perturbative QCD formatting from potential NP impacts.

This thesis builds upon this experimental landscape by executing two distinct analytical strategies using data collected by the LHCb experiment, alongside simulation work for a future detector.

The first core contribution of this thesis is the first direct measurement of NP Wilson Coefficients (WCs) in the $B^0 \to D^{*-}\mu^+\nu_\mu$ decay channel, executed using a dataset corresponding to an integrated luminosity of 3 fb^{-1} collected by the LHCb experiment in proton-proton collisions at centre of mass energies 7 TeV and 8 TeV. This analysis uses a five-dimensional likelihood fit to the three decay angles, q^2, and the squared invariant mass missing from the visible system, $m^2_{\text{miss}} = (P_{B^0} - P_{D^{*-}} - P_{\mu^+})^2$. By describing the entire decay rate structure simultaneously, the fit fully exploits the multi-dimensional correlations across the kinematic phase space, maximising the sensitivity to NP contributions.

Under the Standard Model assumptions, this analysis provides determinations of the hadronic form factors using the CLN, BGL and Bernlochner–Ligeti–Papucci–

Robinson (BLPR) [17] formalisms, which provide vital insights into the compatibility between different parametrisations and the measured angular observables. Moving beyond the SM operator basis, the analysis extracts the NP Wilson coefficients simultaneously with the hadronic form factors parametrised via the BLPR framework. To define the strategy to be used for the measurements in data, an exhaustive exploration of the WC parameter space was performed using pseudo-data. Notably, this analysis presents the first direct measurement of NP WCs and hadronic form-factor parameters in $B^0 \to D^{*-}\mu^+\nu_\mu$ decays at the LHCb experiment. The measurement under the SM assumption has been shown at the Moriond EW conference in 2026 [27], while the NP results are presented at the ICHEP 2026 conference.

While integrated branching fractions and global fits are powerful tools, they remain inherently susceptible to underlying hadronic modelling assumptions. Precision tests of the SM rely on observables that can be both measured experimentally and computed theoretically with high accuracy. In semileptonic processes, the electroweak interaction is cleanly understood, meaning the dominant theoretical uncertainty arises from the strong-interaction dynamics encoded in the hadronic form factors. Though branching fraction ratios mitigate these effects, they are not completely immune; computing precise predictions or performing global fits still requires a rigid choice of form-factor parametrisation. This issue has become a critical focus with recent developments in Lattice QCD (LQCD). Modern, full-kinematic-range LQCD calculations exhibit notable shape tensions with existing experimental measurements. Furthermore, different theoretical formulations are not entirely unified, exhibiting internal variations alongside their mutual discrepancies with experimental data.

To address these tensions directly, the second part of this thesis presents a high-precision measurement of the differential decay rate shape, $d\Gamma/dw$, as a function of the hadronic recoil parameter w, utilising a sample corresponding to an integrated luminosity of 5.4 fb^{-1} collected by the LHCb experiment using proton-proton collisions at a centre of mass energy of 13 TeV. The reconstructed signal candidate spectrum is efficiency-corrected and detector-unfolded into w bins. Methodological advancements developed in this work yield a $\sim 20\%$ optimization in w resolution over traditional semileptonic reconstruction techniques.

Enhancing the capability to execute such high-precision measurements requires a dedicated focus on detector evolution, and the High-Luminosity LHC (HL-LHC) era will bring the unprecedented data to improve the precision of measurements, sensi-

tivity to rare processes and physics beyond the SM. The LHCb Upgrade II detector, foreseen for installation during Long Shutdown 4 (LS4), will operate from Run 5 onwards and therefore cover only the later part of the HL-LHC programme. It is designed to operate at a maximum instantaneous luminosity of 1.5×10^{34} cm^{-2}s^{-1}, 7.5 times the maximum instantaneous luminosity of the current LHCb detector (Run 3), with the aim of accumulating a sample corresponding to 300 fb^{-1}. In order to cope with the HL-LHC environment, major upgrades to the detector are foreseen, including the replacement of the current scintillating fibre tracker, with a dual technology silicon pixel and scintillating fibre detector, known as Mighty Tracker. The final component of this thesis summarises the simulation development for this new detector. Specifically, it details the framework used to model the electronic signal responses of the silicon pixel sensors, alongside the implementation of a computationally optimized, stand-alone track reconstruction algorithm.

Chapter 2

Semileptonic B decays

This chapter provides an overview of the theoretical formalism behind the measurements presented in Ch. 4 and Ch. 5. The Standard Model of particle physics is introduced, focussing on the physics of quarks and leptons, and an overview of the phenomenology of semileptonic b-hadron decays is presented.

2.1 The Standard Model of Particle Physics

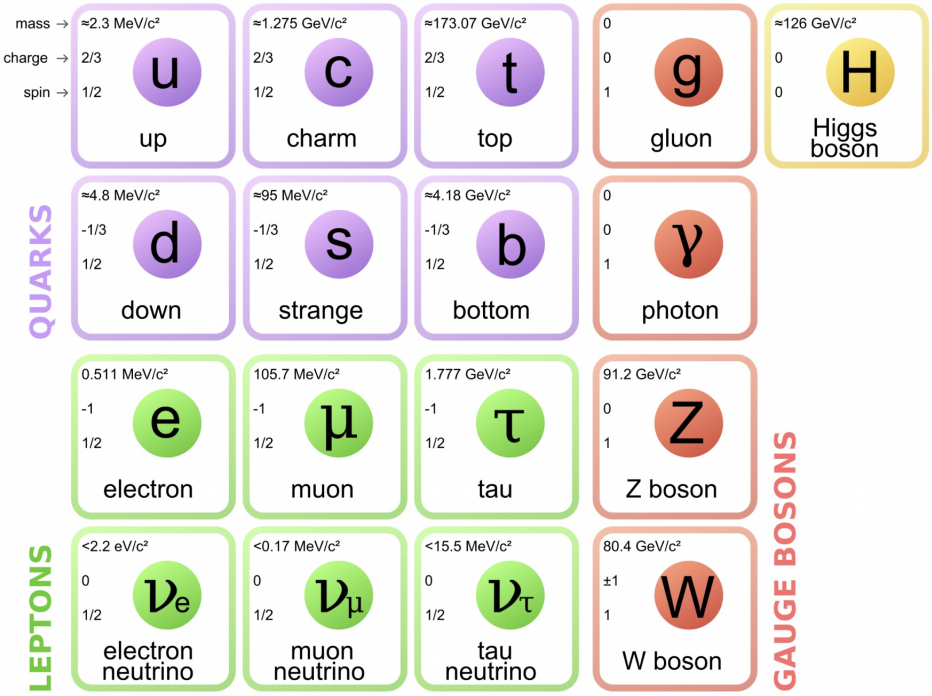


Figure 2.1: Fundamental particles of the Standard Model.

The Standard Model (SM) is a theoretical framework explaining the subatomic

particles and their interactions, presenting three families of fundamental particles, quarks and leptons, interacting through force carriers called bosons for the electromagnetic force, weak force and strong force, as it is summarised in Fig. 2.1. Despite its theoretical and experimental success, the SM is incomplete, for example, it cannot explain gravity, dark matter, neutrino masses.

2.1.1 Elementary particles

The SM states there are 17 fundamental particles which are responsible for all the matter surrounding us and describing all the forces between them. We can separate these particles into fermions and bosons according to their spins. Particles with integers spins are called bosons and they are the force carriers since the force is defined in the SM as the exchange of these particles. Bosons are listed in Tab. 2.1 according to their type of force resulted in their exchange. Fermions with half-integer spins can also be separated into quarks and leptons. Unlike leptons, quarks experience the strong interaction. Due to colour confinement, quarks (with the exception of the top quark) cannot exist as isolated particles and are instead confined within colour-singlet bound states known as hadrons (mesons and baryons). We can also re-group the fermions according to their generation families as 1st, 2nd and 3rd in order to visualise the hierarchy structure within SM while exploring the interactions between them (See Tab. 2.2).

Force	Strength	Boson	Spin	Mass(GeV)
Strong	1	Gluon g	1	0
Electromagnetism	10^-3	Photon γ	1	0
Weak	10^-8	W boson $W^{\pm}$	1	80.4
	10^-8	Z boson Z	1	91.2

Table 2.1: The fundamental forces described the SM and their force carrier particles bosons are listed with their strength, spins, and mass.

2.1.2 The Standard Model formalism

The SM is a Quantum Field Theory (QFT) where the excited states of quantum fields are considered as particles. It is a gauge theory based on the symmetry group $SU(3)_C \times SU(2)_L \times U(1)_Y$. Here, $SU(3)_C$ describes the strong interaction (Quantum Chromodynamics), while $SU(2)_L \times U(1)_Y$ together describe the unified electroweak

	Leptons			Quarks		
	Particle	Q	Mass(GeV)	Particle	Q	Mass(GeV)
1st generation	electron (e)	-1	0.0005	down (d)	-1/3	0.003
	neutrino (ν_e)	0	$< 10^{-9}$	up (u)	+2/3	0.005
2nd generation	muon (μ)	-1	0.106	strange (s)	-1/3	0.1
	neutrino (ν_μ)	0	$< 10^{-9}$	charm (c)	+2/3	1.3
3rd generation	tau (τ)	-1	1.78	bottom (b)	-1/3	4.5
	neutrino (ν_τ)	0	$< 10^{-9}$	top (t)	+2/3	174

Table 2.2: The SM fermions are categorised according to their generation families and their corresponding electric charge and mass given.

interaction. The electromagnetic interaction, described by $U(1)_{em}$, emerges only after electroweak symmetry breaking.

2.1.2.1 Quantum Electrodynamics (QED)

Quantum Electrodynamics (QED) is a gauge theory describing the electromagnetic interaction based on U(1) gauge symmetry group where the scalar field corresponds to the photon and the electric charged is the conserved quantity. The Lagrangian of the theory can be written for a free Dirac field (QFT description of fermions)

$$\mathcal{L} = \bar{\psi}(i\gamma^\mu \partial_\mu -)\psi \tag{2.1}$$

where γ^μ are the Dirac matrices and ψ is the field transforming under U(1) as $\psi \rightarrow \psi e^{-iw(x)}$. In order to keep Lagrangian invariant under U(1) transformation, the $A_\mu(x)$ vector field is introduced with the interaction term $-e\bar{\psi}\gamma^\mu A_\mu \psi$ and the field strength tensor as $F_{\mu\nu} = \partial_\mu A_\nu - \partial_\nu A_\mu$. Then, Lagrangian becomes

$$\mathcal{L} = -\frac{1}{4} F^a_{\mu\nu} F^{\mu\nu} + \bar{\psi}(i\gamma^\mu D_\mu - m)\psi \tag{2.2}$$

where D_μ is covariant derivative as $\partial_\mu + ieA_\mu$.

2.1.2.2 Quantum Chromodynamics (QCD)

Quantum Chromodynamics (QCD) is a theory describing the strong interactions under the symmetry group SU(3) where the scalar fields represent gluons and the conserved quantity is *colour* charge. There are 3 different colour charges: *red, green and blue*. Only particles with colour charge—quarks and gluons—experience the

strong interaction, which is why colour-neutral leptons are completely unaffected by it. Crucially, because gluons themselves carry colour charge, they constantly interact and couple with one another. This unique gluon self-interaction leads to a distance-dependent behaviour: At very close ranges, the strong force weakens, allowing quarks to behave almost independently (asymptotic freedom). However, as quarks are pulled apart, the force intensifies dramatically. This results in colour confinement [28], preventing quarks from existing in isolation and forcing them to permanently bind into colourless states, such as the proton.

According to QCD, a quark field transforms under SU(3) gauge group which is the group of 3×3 unitary matrices with unit determinant, where the group generator T^a defined with its commutator relation

$$[T^a, T^b] = i\epsilon^{abc}T^c \tag{2.3}$$

where ϵ^{abc} is the structure constant (representing the underlying Lie algebra of this gauge group)

This requires a SU(3) theory to have 8 new vector fields, A^a_μ, representing the colour states. A quark field has to transform as $q_i \to (e^{-iw^aT^a})^j_i q_j$ where i is the colour charge of quark; and quark-gluon interaction is described via this improved covariant derivative $D_\mu = \partial_\mu + igT^aA^a_\mu$. Hence, the theory stays invariant under SU(3) and Lagrangian becomes

$$L = -\frac{1}{4}F^a_{\mu\nu}F^{a\mu\nu} + \bar{q}^i(i\gamma^\mu D_\mu - m)^j_i q_j \tag{2.4}$$

with $F^a_{\mu\nu} = \partial_\mu A^a_\nu - g\varepsilon^{abc}A^b_\mu A^c_\nu$.

2.1.3 Electroweak interactions

The charged current weak interaction is invariant under local SU(2) transformations. Under this symmetry, a field transforms as $\psi(x) \to e^{igW^{\alpha(x).T}}\psi(x)$ where T is the generator of SU(2), a half of 2×2 Pauli spin matrices and therefore, ψ is now in a doublet state. When we consider also weak iso-spin space, the charged current weak interaction couples only to left-handed particles. Hence, the symmetry group becomes specifically $SU(2)_L$ and this requires 3 weak isospin fields, $W^k_\mu(k = 1, 2, 3)$, representing massless gauge bosons ; and the charged bosons can be written as linear

combination of the first two as

$$W_\mu^\pm = \frac{1}{\sqrt{2}}(W_\mu^1 \mp iW_\mu^2). \tag{2.5}$$

It might seem natural to identify W_μ^3 as neutral Z boson. However, this would impose that Z boson can only couple to left-handed fermions, which contradicts the experimental observations. To resolve this, we extend the $SU(2)_L$ symmetry by introducing an additional $U(1)_Y$ symmetry requiring a weak hypercharge Y and a new gauge field B_μ. The resulting interaction term in the Lagrangian is

$$g'\frac{Y}{2}\gamma^\mu B_\mu \psi \tag{2.6}$$

with coupling g' in a similar formalism to QED. The left handed fields can be written in a form of doublet as

$$\Psi_L^{quark} = \begin{pmatrix} u_L \\ d_L \end{pmatrix}, \begin{pmatrix} c_L \\ s_L \end{pmatrix}, \begin{pmatrix} t_L \\ b_L \end{pmatrix} \tag{2.7}$$

$$\Psi_L^{lepton} = \begin{pmatrix} \nu_{eL} \\ e_L \end{pmatrix}, \begin{pmatrix} \nu_{\mu L} \\ \mu_L \end{pmatrix}, \begin{pmatrix} \nu_{\tau L} \\ \tau_L \end{pmatrix} \tag{2.8}$$

and if we plug Ψ^e for electron and electron-neutrino coupling, the weak neutral current becomes

$$j_3^\mu = g_W \frac{1}{2}\bar{\nu_L}\gamma^\mu - g_W \frac{1}{2}\bar{e_L}\gamma^\mu e_L \tag{2.9}$$

where g_W is weak interaction coupling.

Since both the photon and Z boson are neutral, it is plausible to define their corresponding fields A_μ and Z_μ as the linear combination of W^3 relating to $SU(2)_L$ local gauge symmetry and B_μ relating to $U(1)_Y$.

$$A_\mu = +B_\mu \cos\theta_W + W_\mu^3 \sin\theta_W \tag{2.10}$$

$$Z_\mu = -B_\mu \sin\theta_W + W_\mu^3 \cos\theta_W \tag{2.11}$$

where θ_W is the weak mixing angle. The corresponding currents are

$$j^{\mu}_{em} = j^{\mu}_{Y} \cos\theta_W + j^{\mu}_{3} \sin\theta_W \tag{2.12}$$

$$j^{\mu}_{Z} = -j^{\mu}_{Y} \sin\theta_W + j^{\mu}_{3} \cos\theta_W. \tag{2.13}$$

We can write the following equation for electron and electron-neutrino interaction to make the connection between photon, W and Z making use of Eq. 2.12.

$$j^{\mu}_{em} = Q_e \bar{e_L} \gamma^{\mu} e_L + Q_e \bar{e_R} \gamma^{\mu} e_R = j^{\mu}_{Y} \cos\theta_W + j^{\mu}_{3} \sin\theta_W \tag{2.14}$$

with Q_e as electron electric charge, and the respective couplings are related by

$$e \;=\; g_W \sin\theta_W \;=\; g' \cos\theta_W. \tag{2.15}$$

2.1.3.1 The Higgs mechanism

In the previous section, the W and Z bosons correspond to the massless gauge fields in $SU(2)_L \times U(1)_Y$ but it is known that these bosons are massive. In the SM, particles acquire their masses through the interaction with the Higgs field. This is known as *Higgs mechanism*, which is driven by the spontaneous symmetry breaking of the electroweak sector, $SU(2)_L \times U(1)_Y \rightarrow U(1)_{\rm em}$. Through this mechanism, the $W^{\pm}$ and Z^0 gauge bosons acquire mass through their direct coupling to the non-zero vacuum expectation value of the scalar field, while quarks and leptons obtain their masses via Yukawa couplings to the same field.
Let us consider a new complex scalar field called, Higgs field (ϕ) governed by the self-interaction potential

$$V(\phi) = \mu^2 \phi^{\dagger}\phi + \lambda(\phi^{\dagger}\phi)^2 \tag{2.16}$$

where $\lambda > 0$ ensures that the potential is bounded from below. For $\mu^2 < 0$, the local symmetric state at $\phi = 0$ becomes unstable as the minimum of the potential shifts away from the origin. Consequently, the field acquires a non-zero vacuum expectation value, selecting a specific ground-state configuration from a continuum of degenerate minima, thereby spontaneously breaking the underlying symmetry.

The vacuum expectation value (VEV) minimizes the potential, breaking the

continuous symmetry, and is parametrised in the unitary gauge as

$$\langle\phi\rangle = \frac{1}{\sqrt{2}}\begin{pmatrix}0\\ \nu\end{pmatrix}, \quad \text{with} \quad \nu = \sqrt{-\frac{\mu^2}{\lambda}}. \tag{2.17}$$

The kinetic term of the Higgs field in the SM Lagrangian is given by

$$\mathcal{L}_{\text{Higgs}} = (D_\mu\phi)^\dagger(D^\mu\phi) \tag{2.18}$$

where the electroweak covariant derivative for the $SU(2)_L \times U(1)_Y$ gauge group is defined as

$$D_\mu = \partial_\mu - ig_W T^a W_\mu^a - ig'\frac{Y}{2}B_\mu. \tag{2.19}$$

Here, g_W and g' are the $SU(2)_L$ and $U(1)_Y$ coupling constants, respectively, and $T^a = \sigma^a/2$ (where σ^a denote the Pauli matrices) represent the weak isospin generators. Assigning the Higgs doublet its standard hypercharge $Y = 1$, we evaluate the action of the covariant derivative on the constant vacuum configuration $\langle\phi\rangle$. Since $\partial_\mu\langle\phi\rangle = 0$, substituting Eq. (2.17) into Eq. (2.19) yields

$$D_\mu\langle\phi\rangle = -\frac{i}{2\sqrt{2}}\begin{pmatrix}g_W(W_\mu^1 - iW_\mu^2)\\ -g_W W_\mu^3 + g'B_\mu\end{pmatrix}\nu. \tag{2.20}$$

Plugging this result into the mass sector of the scalar Lagrangian, $\mathcal{L}_{\text{mass}} = (D_\mu\langle\phi\rangle)^\dagger(D^\mu\langle\phi\rangle)$, we obtain the bilinear terms for the gauge fields

$$\mathcal{L}_{\text{mass}} = \frac{1}{8}\nu^2 g_W^2\left[(W_\mu^1)^2 + (W_\mu^2)^2\right] + \frac{1}{8}\nu^2\left(g_W W_\mu^3 - g'B_\mu\right)^2. \tag{2.21}$$

To extract the physical mass eigenstates, we transform the algebraic gauge fields into the physical vector boson fields by defining the charged $W_\mu^\pm$ bosons and diagonalizing the neutral sector mixing:

$$W_\mu^\pm = \frac{1}{\sqrt{2}}(W_\mu^1 \mp iW_\mu^2) \tag{2.22}$$

$$Z_\mu = \frac{g_W W_\mu^3 - g'B_\mu}{\sqrt{g_W^2 + g'^2}} \tag{2.23}$$

$$A_\mu = \frac{g'W_\mu^3 + g_W B_\mu}{\sqrt{g_W^2 + g'^2}}. \tag{2.24}$$

Substituting these field definitions back into Eq. (2.21) casts the mass Lagrangian into the form expressed as

$$\mathcal{L}_{\text{mass}} = m_W^2 W_\mu^+ W^{\mu-} + \frac{1}{2} m_Z^2 Z_\mu Z^\mu + \frac{1}{2} m_A^2 A_\mu A^\mu \tag{2.25}$$

By direct comparison, the masses of the electroweak gauge bosons are fundamentally generated by their coupling to the scalar vacuum

$$m_W = \frac{1}{2} g_W \nu, \qquad m_Z = \frac{\nu}{2}\sqrt{g_W^2 + g'^2}, \qquad m_A = 0. \tag{2.26}$$

The appearance of a strictly vanishing mass eigenvalue ($m_A = 0$) for the photon field A_μ demonstrates that the $U(1)_{\text{em}}$ gauge symmetry of electromagnetism remains unbroken.

To incorporate fermion masses into the Standard Model without violating local gauge invariance, we introduce the Yukawa interaction. Focusing first on the lepton sector for a single generation, the Lagrangian term is written as

$$\mathcal{L}_{\text{Yukawa}} = -Y_e \bar{L}_L \phi e_R + \text{h.c.} \tag{2.27}$$

where Y_e is the dimensionless Yukawa coupling, L_L is the left-handed lepton doublet defined in Eq. 2.8, e_R is the right-handed charged lepton singlet, and ϕ is the Higgs doublet. Following the same spontaneous symmetry breaking procedure used for the gauge bosons, the Higgs field acquires a vacuum expectation value, $\langle\phi\rangle = (0, \nu/\sqrt{2})^T$. Substituting this into Eq. 2.27 generates the physical mass term for the lepton

$$m_e = \frac{Y_e \nu}{\sqrt{2}}. \tag{2.28}$$

2.2 Flavour Physics

The complete Standard Model Lagrangian formulated thus far can be summarised as

$$\mathcal{L}_{\text{SM}} = -\frac{1}{4} F_{\mu\nu} F^{\mu\nu} + i\bar{\psi} \not{D} \psi + (D_\mu \phi)^\dagger (D^\mu \phi) - V(\phi) + \mathcal{L}_{\text{Yukawa}}. \tag{2.29}$$

It is crucial to emphasize that this entire Lagrangian strictly respects the $SU(2)_L \times U(1)_Y$ gauge symmetry. The symmetry is not explicitly broken by the Yukawa interactions, but rather spontaneously broken by the Higgs potential $V(\phi)$.

To structure the flavour sector of the SM, we expand the Yukawa Lagrangian to include all three generations of quarks and leptons (as listed in Tab. 2.2):

$$\mathcal{L}_{\text{Yukawa}} = -Y_d^{ij}\bar{Q}_L^i\phi d_R^j - Y_u^{ij}\bar{Q}_L^i\tilde{\phi}u_R^j - Y_e^{ij}\bar{L}_L^i\phi e_R^j + \text{h.c.} \tag{2.30}$$

where $i, j = 1, 2, 3$ are generation indices, Q_L and L_L represent the left-handed quark and lepton doublets, respectively, while u_R, d_R, e_R are the right-handed singlets. The matrices Y_u, Y_d, Y_e are complex 3×3 Yukawa matrices in flavour space, and $\tilde{\phi} = i\sigma_2\phi^*$ is the charge-conjugated Higgs doublet necessary to give mass to the up-type quarks.

Upon spontaneous symmetry breaking, we replace ϕ with its VEV, generalizing the mass generation mechanism from Eq. 2.28 into 3×3 mass matrices

$$M_d = \frac{\nu}{\sqrt{2}}Y_d, \quad M_u = \frac{\nu}{\sqrt{2}}Y_u, \quad M_e = \frac{\nu}{\sqrt{2}}Y_e. \tag{2.31}$$

Generally, these 3×3 Yukawa matrices are non-diagonal and complex, meaning the weak interaction flavour eigenstates do not coincide with the physical mass eigenstates. To transition to the physical basis, we must diagonalize these mass matrices using bi-unitary transformations on the left- and right-handed fields:

$$u_L \to U_L^u u_L^{\text{mass}}, \quad u_R \to U_R^u u_R^{\text{mass}}, \quad d_L \to U_L^d d_L^{\text{mass}}, \quad d_R \to U_R^d d_R^{\text{mass}}. \tag{2.32}$$

By choosing the appropriate unitary matrices $U_{L,R}^{u,d}$, we obtain the diagonalized mass matrices containing the physical quark masses

$$U_L^{u\dagger} M_u U_R^u = \text{diag}(m_u, m_c, m_t) \tag{2.33}$$

$$U_L^{d\dagger} M_d U_R^d = \text{diag}(m_d, m_s, m_b). \tag{2.34}$$

(Note: The lepton sector is trivially diagonalized through a single rotation matrix since, in the Standard Model, neutrinos are strictly massless and no analogous misalignment occurs).

While the neutral currents (photon and Z boson couplings) remain diagonal in this new basis—avoiding flavour-changing neutral currents at tree level—the charged current weak interactions are altered. Expressing the $W^\pm$ interaction in terms of the mass eigenstates yields

$$\mathcal{L}_{W^\pm} \propto \bar{u}_L^{\text{mass}}\gamma^\mu \left(U_L^{u\dagger}U_L^d\right) d_L^{\text{mass}} W_\mu^+ + \text{h.c.} \tag{2.35}$$

The residual 3×3 unitary matrix appearing in this vertex, defined as $V_{\rm CKM} = U_L^{u\dagger}U_L^d$, is the Cabibbo–Kobayashi–Maskawa (CKM) matrix. It geometrically quantifies the relative misalignment between the up-type and down-type quark mass bases, dictating the probability of flavour-changing transitions under the weak interaction.

$$V_{CKM} = U_L^{u\dagger}U_L^d = \begin{pmatrix} V_{ud} & V_{us} & V_{ub} \\ V_{cd} & V_{cs} & V_{cb} \\ V_{td} & V_{ts} & V_{tb} \end{pmatrix} \tag{2.36}$$

$$= \begin{pmatrix} c_{12}c_{13} & s_{12}c_{13} & s_{13}e^{-i\delta} \\ -s_{12}c_{23} - c_{12}s_{23}s_{13}e^{i\delta} & c_{12}c_{23} - s_{12}s_{23}s_{13}e^{i\delta} & s_{23}c_{13} \\ s_{12}s_{23} - c_{12}c_{23}s_{13}e^{i\delta} & -c_{12}s_{23} - s_{12}c_{23}s_{13}e^{i\delta} & c_{23}c_{13} \end{pmatrix} \tag{2.37}$$

where $c_{ij} = \cos\theta_{ij}$ and $s_{ij} = \sin\theta_{ij}$ $(i, j = 1,2,3)$ noting that θ_{12} is the Cabibbo angle, which dictates the mixing between the first and second generations of quarks as $\approx 13°$. Each element of the CKM matrix can be measured experimentally. The magnitudes of the off-diagonal elements show a distinct hierarchical pattern: $|V_{us}|$ and $|V_{cd}|$ have a value of approximately 0.22, while $|V_{cb}|$ and $|V_{ts}|$ are of the order of 0.04, and $|V_{ub}|$ and $|V_{td}|$ are of the order of 0.004 [29]. A suitable way to show this hierarchy is the Wolfenstein parametrisation which is an expansion of the CKM matrix elements in powers of the $\lambda = V_{us} \approx 0.22$ for which CKM matrix takes the form

$$V = \begin{pmatrix} 1 - \frac{\lambda^2}{2} & \lambda & A\lambda^3(\rho - i\eta) \\ -\lambda & 1 - \frac{\lambda^2}{2} & A\lambda^2 \\ A\lambda^3(1 - \rho - i\eta) - A\lambda^2 1 & & \end{pmatrix} + \mathcal{O}(\lambda^4) \tag{2.38}$$

where A, ρ, η are free parameters of order 1. If necessity of including higher orders arises, the CKM matrix takes the form

$$\begin{pmatrix} 1 - \frac{\lambda^2}{2} - \frac{\lambda^4}{8} & \lambda + \mathcal{O}(\lambda^7) & A\lambda^3(\rho - i\eta) \\ -\lambda + \frac{1}{2}A^2\lambda^5[1 - 2(\rho + i\eta)] & 1 - \frac{\lambda^2}{2} - \frac{\lambda^4}{8}(1 + 4A^2) & A\lambda^2 + \mathcal{O}(\lambda^8) \\ A\lambda^3(1 - \bar{\rho} - i\bar{\eta}) & -A\lambda^2 + \frac{1}{2}A\lambda^4[1 - 2(\rho + i\eta)] & 1 - \frac{1}{2}A^2\lambda^4 \end{pmatrix} \tag{2.39}$$

where

$$\bar{\rho} = \rho(1 - \frac{\lambda}{2}) + \mathcal{O}(\lambda^4) \tag{2.40}$$

$$\bar{\eta} = \eta(1 - \frac{\lambda}{2}) + \mathcal{O}(\lambda^4) \tag{2.41}$$

The CKM matrix elements describe the probability of the transition from one quark flavour to another one and the probability must be preserved as the time evolution in QM is unitary. Hence, the elements of the CKM matrix must satisfy this unitary condition

$$\sum_{k=1,2,3} V_{ki}^* V_{kj} = \delta_{ij}. \tag{2.42}$$

The unitarity of the CKM matrix implies several orthogonality relations between its columns and rows, which can be represented as triangles in the complex plane. The most commonly studied *Unitarity Triangle* arises from the relation

$$V_{ud}V_{ub}^* + V_{cd}V_{cb}^* + V_{td}V_{tb}^* = 0. \tag{2.43}$$

To obtain the conventional normalized triangle, this relation is divided by $V_{cd}V_{cb}^*$. This normalisation scales the base of the triangle to unit length and aligns it with the real axis. This Eq. 2.43 represents the unitarity triangle in the complex plane with the angles expressed as following,

$$\alpha = arg\Big(-\frac{-V_{td}V_{tb}^*}{V_{ud}V_{ub}^*}\Big), \quad \beta = arg\Big(-\frac{-V_{cd}V_{cb}^*}{V_{td}V_{tb}^*}\Big), \quad \gamma = arg\Big(-\frac{-V_{ud}V_{ub}^*}{V_{cd}V_{cb}^*}\Big). \tag{2.44}$$

The angles and the sides of the unitary triangle are shown in Fig. 2.2 and they can be measured experimentally. The position of three vertices of the triangle in Fig. 2.2 are (0,0), 0,1 and ($\bar{\rho}$, $\bar{\eta}$) as given in Eq. 2.40. The V_{td} and V_{ts} matrix elements can be measured through the oscillation frequencies of B^0 and B_s mesons (Δm_d and Δm_s); and V_{ub} and V_{cb} can be obtained through the semileptonic b-hadron decays. The matrix elements, V_{cd} and V_{cs} can be measured with semileptonic charm and kaon decays respectively. V_{ud} can be obtained via nuclear beta decays and V_{tb} can be studied in single top production (Refer to [30] for the latest measurements).

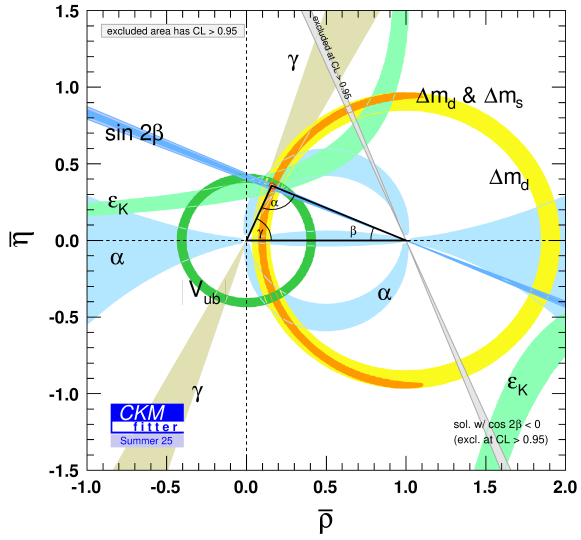


Figure 2.2: Measurement of the angles and sides of the unitarity triangle as of summer 2025. They are measured via decays that feature the CKM elements in their definition, see Eq. 2.44 and the text for details.

2.3 The SM as an effective field theory and New Physics scenarios

Heavy-flavour weak decays provide a natural framework to illustrate the Effective Field Theory (EFT) approach. As a paradigmatic example, we consider the charged-current transition $b \to c\bar{u}d$, which at the fundamental level in the SM is mediated by the exchange of a W boson at tree level.

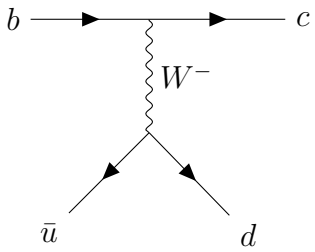


Figure 2.3: SM Feynman diagram for the $b \to c\bar{u}d$ transition mediated by W exchange.

At energies well below the electroweak scale, $E \ll m_W$, the heavy W boson cannot be resolved as a propagating degree of freedom. Its effects can therefore be incorporated

by integrating it out, replacing the tree-level W-exchange diagram with a local four-fermion interaction as depicted in Fig. 2.4.

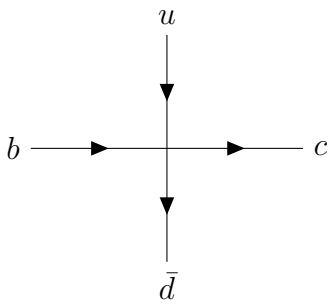


Figure 2.4: Local four-fermion interaction obtained after integrating out the W boson.

This procedure leads to the effective weak Hamiltonian

$$\mathcal{H}_{\text{eff}} = \frac{G_F}{\sqrt{2}} V_{cb} V_{ud}^* \, (\bar{c}\gamma_\mu(1-\gamma_5)b) \left(\bar{d}\gamma^\mu(1-\gamma_5)u\right), \tag{2.45}$$

which corresponds to the leading-order Fermi theory of weak interactions. Including QCD corrections modifies this simple picture. Gluon exchanges between quark lines mix the colour flow of the two currents. While the 4-point Fermi operator is a simple product of two colour-singlet currents, QCD loop corrections allow gluons to connect quarks belonging to different currents. This generates operators with different colour contractions, leading to non-trivial colour structures beyond the original singlet–singlet form. During this evolution, operators mix under QCD renormalization, which necessitates introducing a complete operator basis containing both colour-singlet and colour-octet structures. As a result, the four-quark operator basis must be enlarged to include both colour-singlet and colour-octet operators,

$$O_1 = (\bar{c}_\alpha\gamma_\mu(1-\gamma_5)b_\alpha)(\bar{d}_\beta\gamma^\mu(1-\gamma_5)u_\beta), \qquad O_2 = (\bar{c}_\alpha\gamma_\mu(1-\gamma_5)b_\beta)(\bar{d}_\beta\gamma^\mu(1-\gamma_5)u_\alpha), \tag{2.46}$$

where α, β denote colour indices. The effective Hamiltonian then takes the form

$$\mathcal{H}_{\text{eff}} = \frac{G_F}{\sqrt{2}} V_{cb} V_{ud}^* \left[C_1(\mu)\, O_1(\mu) + C_2(\mu)\, O_2(\mu)\right]. \tag{2.47}$$

The short-distance physics associated with scales of order m_W is encoded in the Wilson coefficients $C_i(\mu)$, while the long-distance hadronic effects are contained in the matrix elements of the operators $O_i(\mu)$. Large logarithmic corrections are sys-

tematically re-summed by means of renormalisation group equations, allowing the Wilson coefficients to be evolved from the electroweak scale down to the characteristic scale of the decay process. This separation of scales is a defining feature of the EFT framework: Short-distance dynamics is factorised into perturbatively calculable Wilson coefficients, while long-distance physics is described by local operators whose matrix elements must be evaluated using non-perturbative methods. The same logic can be extended beyond the SM. Assuming that possible New Physics (NP) degrees of freedom appear at a scale $\Lambda \gg m_W$, their low-energy effects can be parametrised by higher-dimensional operators constructed from SM fields and suppressed by inverse powers of Λ. The effective Lagrangian can then be written as

$$\mathcal{L} = \mathcal{L}_{\text{SM}} + \frac{1}{\Lambda^2} \sum_i g_i O_i^{\text{NP}}, \tag{2.48}$$

where O_i^{NP} are dimension-six operators and g_i are dimensionless couplings encoding the underlying NP dynamics. In this framework, the effective Hamiltonian for heavy-flavour decays can be expressed as

$$\mathcal{H}_{\text{eff}} = \frac{4G_F}{\sqrt{2}} \sum_i V_{\text{CKM}}^i \left(C_i^{\text{SM}} + C_i^{\text{NP}} \right) O_i, \tag{2.49}$$

where the Wilson coefficients C_i^{NP} vanish in the SM.

The EFT approach therefore provides a framework to analyse deviations from SM predictions, allowing all possible NP scenarios to be systematically explored through their low-energy imprints. For $b \to c\ell\nu$ transitions, the relevant CKM element is V_{cb}. In the SM, the only non-zero contribution comes from the left-handed vector operator, conventionally normalised such that $C_{V_{LL}}^{\text{SM}} = 1$. Dropping the NP superscript for brevity, the Effective Hamiltonian including both SM and NP contributions is therefore written as

$$\begin{aligned}\mathcal{H}_{\text{eff}} &= \frac{4G_F}{\sqrt{2}} V_{cb} \sum_i C_i O_i \\ &= \frac{4G_F}{\sqrt{2}} V_{cb} [(1 + C_{V_{LL}}) O_{C_{V_{LL}}} + C_{V_{RL}} O_{C_{V_{RL}}} \\ &+ C_{V_{LR}} O_{C_{V_{LR}}} + C_{V_{RR}} O_{C_{V_{RR}}} + C_{S_{LL}} O_{C_{S_{LL}}} \\ &+ C_{S_{RL}} O_{C_{S_{RL}}} + C_{S_{LR}} O_{C_{S_{LR}}} + C_{S_{RR}} O_{C_{S_{RR}}} \\ &+ C_{T_{LL}} O_{C_{T_{LL}}} + C_{T_{RR}} O_{C_{T_{RR}}} + C_{T_{RL}} O_{C_{T_{RL}}} + C_{T_{LR}} O_{C_{T_{LR}}}] + h.c., \end{aligned} \tag{2.50}$$

where G_F is the Fermi constant and V_{cb} is the CKM matrix element for $b \to c$ transitions. $C_{I_{q\ell}}$ are the WCs representing Vector (V), Scalar (S) and Tensor (T) interactions couplings with subscripts of chirality of quark (c,b) and lepton (l) currents respectively and the corresponding operators have the following definitions [31]

$$\begin{aligned} O_{C_{V_{LL}}} &= \bar{c}_L \gamma^\mu b_L \bar{l_L} \gamma_\mu \nu_L \\ O_{C_{V_{RL}}} &= \bar{c}_R \gamma^\mu b_R \bar{l_L} \gamma_\mu \nu_L \\ O_{C_{V_{LR}}} &= \bar{c}_L \gamma^\mu b_L \bar{l_R} \gamma_\mu \nu_R \\ O_{C_{V_{RR}}} &= \bar{c}_R \gamma^\mu b_R \bar{l_R} \gamma_\mu \nu_R \\ O_{C_{S_{LL}}} &= \bar{c}_L b_L \bar{l_L} \nu_L \\ O_{C_{S_{RL}}} &= \bar{c}_R b_R \bar{l_L} \nu_L \\ O_{C_{S_{LR}}} &= \bar{c}_L b_L \bar{l_R} \nu_R \\ O_{C_{S_{RR}}} &= \bar{c}_R b_R \bar{l_R} \nu_R \\ O_{C_{T_{LL}}} &= \bar{c}_L \sigma^{\mu\nu} b_L \bar{l_L} \sigma^{\mu\nu} \nu_L \\ O_{C_{T_{LR}}} &= \bar{c}_L \sigma^{\mu\nu} b_L \bar{l_R} \sigma^{\mu\nu} \nu_R \\ O_{C_{T_{RL}}} &= \bar{c}_R \sigma^{\mu\nu} b_R \bar{l_L} \sigma^{\mu\nu} \nu_L \\ O_{C_{T_{RR}}} &= \bar{c}_R \sigma^{\mu\nu} b_R \bar{l_R} \sigma^{\mu\nu} \nu_R. \end{aligned} \tag{2.51}$$

Here, $\bar{c}, b$ represent quarks, l for lepton, and ν for neutrino; and the lower indices of them represent their chirality. This is the complete basis for the four-Fermi operators, including right handed neutrinos. A NP contribution can be added with the corresponding non-zero Wilson coefficient(s). The size of the NP contribution can be estimated by measuring the value of the Wilson coefficient for the corresponding operator(s).

2.4 Theoretical formalism of $B^0 \to D^{*-}\ell^+\nu_\ell$

In this section the theoretical formalism used to describe charged current semileptonic b decays is presented. In these decays a hadron decays into one or more hadrons, a charged lepton and its corresponding neutrino. An example Feynman diagram in the SM is shown on Fig. 2.5.

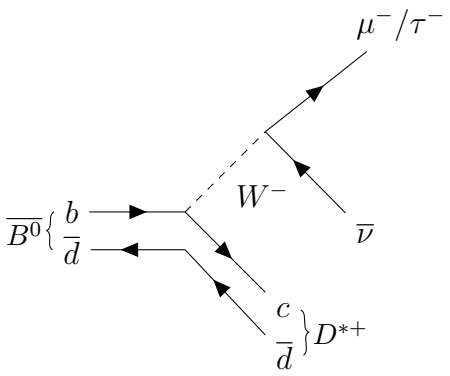


Figure 2.5: $B \to D^*\ell\nu$ transition showing a tree-level diagram in the SM, proceeding via a mediating W boson.

The kinematics of the process is characterized with several variables such as

$$q^2 = (p_B - p_{D^*})^2, \tag{2.52}$$

which stands for the momentum transfer onto the W that decays into a lepton and a neutrino (See Feynman diagram on Fig. 2.5). In addition, the decay is described by three helicity angles which are shown on Fig. 2.6, and are defined as

- θ_ℓ : angle between the direction of the lepton and the direction opposite the B meson in the virtual W rest frame.
- θ_D : angle between the direction of the D meson and the direction opposite the B meson in the D^* rest frame.
- χ : angle between the plane formed by the D^* decay and the plane formed by the W decay, defined in the B meson rest frame.

At the level of effective field theory the Hamiltonian for the $b \to c\ell\nu$ transition can be written as in Eq. 2.50, which includes the complete basis of the operators. Here, we assume that the right-handed neutrinos are absent, which leads to dropping the

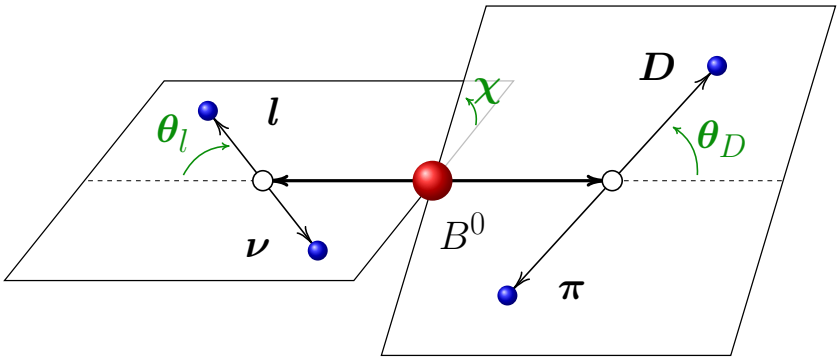


Figure 2.6: Schematic view of the $B \to D^* \ell \nu$ decay featuring the three angles in the process. θ_l is the angle between the direction of the lepton and the B meson, θ_d is the angle between the D meson from the D^* decay and χ is the angle between the D^* and W plane.

terms with Wilson coefficients of type $C_{L/R,R}$. In addition, the right handed tensor operator, with opposite quark and neutrino chirality, $(\bar{c}_L \sigma_{\mu\nu} b_R)(\bar{l}_R \sigma^{\mu\nu} \nu_L) = 0$ and vanishes from the Eq. 2.50 [32]. With these assumptions the effective Hamiltonian takes the form

$$\begin{aligned}\mathcal{H}_{eff} &= \frac{4G_F}{\sqrt{2}} V_{cb} \sum_i C_i O_i \\ &= \frac{4G_F}{\sqrt{2}} V_{cb} [(1 + C_{V_{LL}}) O_{C_{V_{LL}}} + C_{V_{RL}} O_{C_{V_{RL}}} \\ &+ C_{S_{LL}} O_{C_{S_{LL}}} + C_{S_{RL}} O_{C_{S_{RL}}} \\ &+ C_{T_{LL}} O_{C_{T_{LL}}}] + h.c., \end{aligned} \tag{2.53}$$

While the general EFT framework allows for New Physics to modify both the quark and leptonic currents (such as introducing right-handed neutrinos), this work adopts a standard simplified parametrisation. We assume the leptonic current remains SM-like, and all NP effects are cast onto the quark side of the operators. Under this assumption, a possible Lepton Flavour Universality violation manifests not as a change to the structure of the leptonic current, but as a lepton-mass dependence in the Wilson coefficients. The Effective Hamiltonian in Eq. 2.53 can be re-written in the hadronic current basis as formulated by Ref. [33]

$$\begin{aligned}\mathcal{H}_{\text{eff}} &= \frac{G_F}{\sqrt{2}} V_{cb}\, H^\mu L_\mu + \text{h.c.} \\ &= \frac{G_F}{\sqrt{2}} V_{cb}\Big[(1+g_V)\,\bar{c}\gamma^\mu b + (-1+g_A)\,\bar{c}\gamma^\mu\gamma_5 b + g_S\, i\partial^\mu(\bar{c}b) + g_P\, i\partial^\mu(\bar{c}\gamma_5 b) \\ &+ g_T\, i\partial_\nu(\bar{c}i\sigma^{\mu\nu}b) + g_{T_5}\, i\partial_\nu(\bar{c}i\sigma^{\mu\nu}\gamma_5 b)\Big]\,\bar{\ell}\gamma_\mu(1-\gamma_5)\nu_\ell + \text{h.c.} \end{aligned} \tag{2.54}$$

where g_V and g_A are dimensionless couplings modifying the vector and axial-vector channels; and g_S, g_P, g_T, g_{T_5} are dimension-full couplings, noting if NP couplings vanish the Hamiltonian becomes the SM current of $\bar{c}\gamma^\mu(1-\gamma_5)b$. The following relations for these NP couplings are satisfied

$$g_{V,A} = g_{V_R} \pm g_{V_L}, \quad g_{S,P} = g_{S_R} \pm g_{S_L}; \quad g_T = -g_{T_5} = g_{T_L}. \tag{2.55}$$

From the relations in 2.51, only left handed tensor operator can contribute to the effective Hamiltonian. The right handed tensor operator, with opposite quark and neutrino chirality, $O_{C_{T_{RL}}} = (\bar{c}_L\sigma_{\mu\nu}b_R)(\bar{l}_R\sigma^{\mu\nu}\nu_L) = 0$ and vanishes from the Hamiltonian [32].

The differential decay rate of $B \to D^*(D^* \to D\pi)\ell\nu$ in q^2, $D\pi$ invariant mass and decay angles decay can be expressed as

$$\frac{d^5\Gamma}{dq^2 dm_{D^*} d\cos\theta_{\text{D}} d\cos\theta_\ell d\chi} = \frac{1}{128(2\pi)^6 m_B^2}|q|\Big(1-\frac{m_l^2}{q^2}\Big)\frac{|\hat{p_D}|}{m_{D^*}}|\mathcal{M}(B\to D^*\ell\nu_\ell)|^2, \tag{2.56}$$

where m_l is the lepton mass, m_B is B meson mass, $\hat{p_D}$ is the three momentum of the D meson in the rest frame of D^* with the three angles given as in Fig. 2.6. To write the matrix element $\mathcal{M}(B \to D^*\ell\nu_\ell)$ explicitly, we decompose the non-vanishing hadronic matrix elements of the quark operators in Eq. 2.54 in terms of the Lorentz invariant hadronic form factors. Here, the scalar current is vanishing and the rest of the currents concerning the $B \to D^*$ transition are written in Eqs. 2.57 - 2.62.

Vector current

$$\langle D^*(k,\epsilon)|\bar{c}\gamma_\mu b|B(p)\rangle = \epsilon_{\mu\nu\rho\sigma}\epsilon^{\nu *}p^\rho k^\sigma \frac{2V(q^2)}{m_B + m_{D^*}}, \tag{2.57}$$

Axial-vector current

$$\begin{aligned}\langle D^*(k,\epsilon)|\bar{c}\gamma_\mu\gamma_5 b|B(p)\rangle = i\epsilon^*_\mu(m_B+m_{D^*})A_1(q^2) \\ - i(p+k)_\mu(\epsilon^*\cdot q)\frac{A_2(q^2)}{m_B+m_{D^*}} \\ - iq_\mu(\epsilon^*\cdot q)\frac{2m_{D^*}}{q^2}\big[A_3(q^2)-A_0(q^2)\big],\end{aligned} \tag{2.58}$$

where

$$A_3(q^2) = \frac{m_B+m_{D^*}}{2m_{D^*}}A_1(q^2) - \frac{m_B-m_{D^*}}{2m_{D^*}}A_2(q^2) \tag{2.59}$$

satisfying the condition $A_3(0) = A_0(0)$. The matrix element of the pseudo-scalar density is related to that of the axial current via the Ward identity [34].

Pseudo-scalar current

$$\begin{aligned}\langle D^*(k,\epsilon)|\big[\bar{c}\gamma_5 b\big](\mu)|B(p)\rangle &= \frac{1}{m_b(\mu)+m_c(\mu)}q_\nu\langle D^*(k,\epsilon)|\bar{c}\gamma^\nu\gamma_5 b(\mu)|B(p)\rangle \\ &= -i(\epsilon^*\cdot q)\frac{2m_{D^*}}{m_b(\mu)+m_c(\mu)}A_0(q^2).\end{aligned} \tag{2.60}$$

Tensor current

$$\langle D^*(k,\epsilon)|\big[\bar{c}\sigma_{\mu\nu}q^\nu b\big](\mu)|B(p)\rangle = i\epsilon_{\mu\nu\rho\sigma}\epsilon^{\nu*}p^\rho k^\sigma 2T_1(q^2,\mu). \tag{2.61}$$

Pseudo-tensor current

$$\begin{aligned}\langle D^*(k,\epsilon)|\big[\bar{c}\sigma_{\mu\nu}\gamma_5 q^\nu b\big](\mu)|B(p)\rangle = \big[(m_B^2-m_{D^*}^2)\epsilon^*_\mu - (\epsilon^*\cdot q)(p+k)_\mu\big]T_2(q^2,\mu) \\ + (\epsilon^*\cdot q)\left[q_\mu - \frac{q^2}{m_B^2-m_{D^*}^2}(p+k)_m u\right]T_3(q^2,\mu).\end{aligned} \tag{2.62}$$

where $A_i(q^2), T_i(q^2), V(q^2)$ are are non-perturbative functions that encode the QCD dynamics inside hadrons.

In order to proceed towards the helicity amplitudes the definitions of the polarisations are given. We chose the helicity axis to be along the D^* momentum while the polarisation vectors of $D^*(\epsilon)$ and the virtual vector boson $(\tilde{\epsilon})$ are defined as

$$\epsilon_{\pm} = \mp\frac{1}{\sqrt{2}}\begin{pmatrix}0\\1\\\pm i\\0\end{pmatrix}, \quad \epsilon_0 = \frac{1}{m_{D^*}}\begin{pmatrix}|\mathbf{q}|\\0\\0\\E_{D^*}\end{pmatrix}, \tag{2.63}$$

and

$$\tilde{\epsilon_{\pm}} = \mp\frac{1}{\sqrt{2}}\begin{pmatrix}0\\\pm 1\\-i\\0\end{pmatrix}, \quad \tilde{\epsilon_0} = \frac{1}{m_{D^*}}\begin{pmatrix}|\mathbf{q}|\\0\\0\\-q_0\end{pmatrix}, \quad \tilde{\epsilon_t} = \frac{1}{\sqrt{q^2}}\begin{pmatrix}q_0\\0\\0\\-|\mathbf{q}|\end{pmatrix}, \tag{2.64}$$

where in the B meson rest frame

$$q_0 = \frac{m_B^2 - m_{D^*}^2 + q^2}{2m_B}, \quad E_{D^*} = \frac{m_B^2 + m_{D^*}^2 - q^2}{2m_B}. \tag{2.65}$$

Using the definitions in Eqs. 2.63, 2.64, 2.65, we can write the helicity amplitudes for $B \to D^*\ell\nu$ decay as

$$H_{\pm,0} = \tilde{\epsilon_{\pm,0}^{\mu *}}\langle D^*(\epsilon_{\pm,0})|H_\mu|B\rangle, \tag{2.66}$$

$$H_t = \tilde{\epsilon_t^{\mu *}}\langle D^*(\epsilon_0)|H_\mu|B\rangle, \tag{2.67}$$

where H_μ stands for the hadronic part of the effective Hamiltonian. By using Eq. 2.54 and Eqs. 2.58 - 2.64, the expressions of the helicity amplitudes using the notation in Ref. [33] take the form

$$\begin{aligned} H_{\pm}(q^2) = i\Big(&\mp \Big[1 + g_V - g_T(m_B + m_{D^*})\frac{T_1(q^2)}{V(q^2)}\Big]\frac{\sqrt{\lambda(m_B^2, m_{D^*}^2)}}{m_B + m_{D^*}}V(q^2) \\ &- \Big[1 - g_A - g_{T_5}(m_B - m_{D^*})\frac{T_2(q^2)}{A_1(q^2)}\Big](m_B + m_{D^*})A_1(q^2)\Big) \end{aligned} \tag{2.68}$$

$$
\begin{aligned}
H_0(q^2) = & -\frac{i}{2m_{D^*}\sqrt{q^2}} \\
& \times \Bigg\{ \left[1 - g_A - g_{T_5}(m_B - m_{D^*})\frac{T_1(q^2)}{A_1(q^2)}\right](m_B + m_{D^*})(m_B^2 - m_{D^*}^2 - q^2)A_1(q^2) \\
& - \left[1 - g_A - g_{T_5}\left(\frac{(m_B + m_{D^*})T_2(q^2)}{A_1(q^2)} + \frac{q^2}{m_B - m_{D^*}}\frac{T_3(q^2)}{A_2(q^2)}\right)\right] \\
& \times \frac{\lambda(m_B^2, m_{D^*}^2, q^2)}{m_B + m_{D^*}} A_2(q^2) \Bigg\}
\end{aligned}
\tag{2.69}
$$

$$
H_t(q^2) = -i\Big[1 - g_A + g_P\frac{q^2}{m_b + m_c}\Big]\frac{\sqrt{\lambda(m_B^2, m_{D^*}^2), q^2)}}{\sqrt{q^2}} A_0(q^2) \tag{2.70}
$$

The full angular distribution is determined by the squared of matrix element [35]

$$
\begin{aligned}
|\mathcal{M}_{D^*}|^2 = N|g_{D^*D\pi}|^2|\hat{\mathbf{p}}_D|^2|B\tilde{W}_{D^*}|^2 \times \Big(& (|H_+|^2 + |H_-|^2)(1 + \cos^2\theta_\ell + \frac{\mathrm{m_l^2}}{\mathrm{q^2}}\sin^2\theta_\ell)\sin^2\theta_{\mathrm{D}}^2 \\
& + 2(|H_+|^2 - |H_-|^2)\cos\theta_\ell\sin^2\theta_{\mathrm{D}} \\
& + 4|H_0|^2(1 + \frac{m_l^2}{q^2})\sin^2\theta_{\mathrm{l}}\sin^2\theta_{\mathrm{D}} + 4|\mathrm{H_t}|^2\frac{\mathrm{m_l^2}}{\mathrm{q^2}}\cos^2\theta_{\mathrm{D}} \\
& - 2\beta_l^2(Re[H_+H_-^*]\cos 2\chi + \mathrm{Im[H_+H_0^* - H_-H_0^*]}\sin 2\chi)\sin^2\theta_\ell\sin^2\theta_{\mathrm{D}} \\
& - \beta_l^2(Re[H_+H_0^* + H_-H_0^* - \frac{m_l^2}{q^2}(H_+H_t^* + H_-H_t^*)]\cos\chi \\
& + Im[H_+H_0^* + H_-H_0^* - \frac{m_l^2}{q^2}(H_+H_t^* - H_-H_t^*)]\sin\chi)\sin\theta_\ell\sin 2\theta_{\mathrm{D}} \\
& + 8Re[H_0H_t^*]\frac{m_l^2}{q^2}\cos\theta_\ell\cos^2\theta_{\mathrm{D}}\Big)
\end{aligned}
\tag{2.71}
$$

The differential decay rate in Eq. 2.56 can be described with 12 terms of Eq. 2.71, each with different angular dependence, so-called *angular coefficients*. Thus, differential decay rate formula can be reformulated in terms of angular coefficients [36]

$$\begin{aligned}\frac{d^4\Gamma}{dq^2 d\cos\theta_D d\cos\theta_l d\chi} = \frac{9}{32\pi}\Big\{ & I_{1c}\cos^2\theta_D + I_{1s}\sin^2\theta_D \\ & + [I_{2c}\cos^2\theta_D + I_{2s}\sin^2\theta_D]\cos 2\theta_\ell \\ & + [I_{6c}\cos^2\theta_D + I_{6s}\sin^2\theta_D]\cos\theta_\ell \\ & + [I_3\cos 2\chi + I_9\sin 2\chi]\sin^2\theta_\ell\sin^2\theta_D \\ & + [I_4\cos\chi + I_8\sin\chi]\sin 2\theta_\ell\sin 2\theta_D \\ & + [I_5\cos\chi + I_7\sin\chi]\sin\theta_\ell\sin\theta_D\Big\}\end{aligned} \tag{2.72}$$

Explicit relations between angular coefficients and Helicity amplitudes given by

$$I_{1c} = 2N\left[|\tilde{H}_0^-|^2 + \frac{m_l^2}{q^2}|\tilde{H}_+^-|^2 + 2\frac{m_l^2}{q^2}|\tilde{H}_t^-|^2\right] \tag{2.73}$$

$$I_{1s} = \frac{N}{2}\left[3(|\tilde{H}_+^-|^2 + |\tilde{H}_-^-|^2) + \frac{m_l^2}{q^2}|\tilde{H}_+^+|^2 + 2\frac{m_l^2}{q^2}(|\tilde{H}_+^-|^2 + |\tilde{H}_-^-|^2)\right] \tag{2.74}$$

$$I_{2c} = 2N\left[-|\tilde{H}_0^-|^2 + \frac{m_l^2}{q^2}|\tilde{H}_0^+|^2\right] \tag{2.75}$$

$$I_{2s} = \frac{N}{2}\left[3(|\tilde{H}_+^-|^2 + |\tilde{H}_-^-|^2) - \frac{m_l^2}{q^2}(|\tilde{H}_+^+|^2 + |\tilde{H}_+^-|^2)\right] \tag{2.76}$$

$$I_3 = -2NRe\left(\tilde{H}_+^-\tilde{H}_-^{-*} - \frac{m_l^2}{q^2}\tilde{H}_+^+\tilde{H}_-^{+*}\right) = -2N\beta_l^2 Re\left(H_+H_-^* - 4H_{T,+}H_{T,-}^*\right) \tag{2.77}$$

$$\begin{aligned}I_4 &= NRe\left((\tilde{H}_+^-\tilde{H}_-^{-*})\tilde{H}_0^{-*} - \frac{m_l^2}{q^2}\tilde{H}_+^+\tilde{H}_-^{+*}\right) \\ &= N\beta_l^2 Re\left((H_+H_-^*)H_0^* - 4(H_{T,+}H_{T,-}^*)H_{T,0}^*\right)\end{aligned} \tag{2.78}$$

$$I_5 = 2NRe\left((\tilde{H}_+^-\tilde{H}_-^{-*})\tilde{H}_0^{-*} - \frac{m_l^2}{q^2}(\tilde{H}_-^+ + \tilde{H}_-^{+*})\tilde{H}_t^*\right) \tag{2.79}$$

$$I_{6c} = 8N\frac{m_l^2}{q^2}Re\left(\tilde{H}_0^+\tilde{H}_t^*\right) \tag{2.80}$$

$$I_{6s} = 2N\left(|\tilde{H}_+^-|^2 - |\tilde{H}_-^-|^2\right) \tag{2.81}$$

$$I_7 = 2NIm\left((\tilde{H}_+^- + \tilde{H}_-^-)\tilde{H}_0^{-*} - \frac{m_l^2}{q^2}(\tilde{H}_+^+ - \tilde{H}_-^+)\tilde{H}_t^*\right) \tag{2.82}$$

$$\begin{aligned} I_8 &= NIm\left((\tilde{H}_+^- - \tilde{H}_-^-)\tilde{H}_0^{-*} - \frac{m_l^2}{q^2}\tilde{H}_+^+\tilde{H}_-^{+*}\right) \\ &= N\beta_l^2 Im\left((H_+H_-^*)H_0^* - 4(H_{T,+}H_{T,-}^*)H_{T,0}^*\right) \end{aligned} \tag{2.83}$$

$$I_9 = -2NIm\left(\tilde{H}_+^-\tilde{H}_-^* - \frac{m_l^2}{q^2}\tilde{H}_+^+\tilde{H}_+^*\right) = -2N\beta_l^2 Im\left(H_+H_-^* - 4H_{T,+}H_{T,-}^*\right) \tag{2.84}$$

where $\tilde{H}_i$ terms represent the helicity amplitudes that absorbed NP couplings and

$$N \equiv N(q^2) = B(D^* \to D\pi)\frac{G_F^2|V_{cb}|^2}{48(2\pi)^3 m_B^3}q^2\sqrt{\lambda_{BD^*}(q^2)}(1 - \frac{m_l^2}{q^2})^2 \tag{2.85}$$

2.4.1 $B \to D^* l\nu$ form factors

The helicity amplitudes given in Eqs. 2.68, 2.69 and 2.70 describe the effects of strong interaction and can be parametrized in terms of functions of q^2 also known as form factors (FF). Several parametrisations have been proposed to model the form factors. They can be divided in the following categories:

1. The model by Boyd, Grinstein, and Lebed (BGL) [37] provides the most general, model-independent parametrisation. It is based on QCD dispersion relations and analyticity.

2. The form factors can be calculated order-by-order in $1/m_{c,b}$ and α_s using

Heavy Quark Effective Theory (HQET). This expansion, originally developed in the early 90s [38], was systematically improved by Bernlochner *et al.* [2] (the BLPR parametrisation) to incorporate higher-order corrections. The HQET framework naturally introduces symmetry relations between the different form factors, reducing the number of independent parameters.

3. The parametrisation derived by Caprini, Lellouch, and Neubert (CLN) [25] relies on heavy quark symmetry relations and fixed inputs from QCD sum rules to heavily constrain the free parameters. While recent theoretical developments have shown these constraints to be overly restrictive—leading to underestimated theoretical uncertainties—the CLN parametrisation has been widely used in past measurements and is therefore included for comparison.

According to the mathematical formalism, there are two conceptually distinct theoretical approaches to calculating form factor parameters:

1. **Analytical approaches (QCDSR and LCSR):** Methods such as QCD Sum Rules and Light-Cone Sum Rules rely on the Operator Product Expansion and the assumption of quark-hadron duality. They analytically bridge perturbative QCD with non-perturbative hadronic states using dispersion relations, making them highly effective at large hadronic recoil (low q^2).

2. **Numerical approaches (LQCD):** Lattice QCD is a first-principles numerical technique that discretises spacetime into a finite grid to directly evaluate QCD path integrals. While it avoids the theoretical approximations of sum rules, it suffers from discretisation artefacts when simulating highly energetic outgoing hadrons. Consequently, LQCD calculations are typically restricted to the low-recoil (high q^2) region. Parametrisations like BGL are commonly used to extrapolate these precise LQCD data points across the full kinematic range.

The next section gives an overview of the relevant parameters of the CLN, BGL and BLPR form factor parametrisations for $B \to D^* \ell \nu$ and the BLR parametrization for $B \to D^{**} \ell \nu$.

2.4.1.1 BGL parametrisation

The BGL parametrization was proposed in [37] and further developed in [39] and [40]. For all the further formulas the notation from [40] and [41] is adopted. The

amplitudes governing the $B \to D^* \ell\nu$ decays in Eq. 2.71 can be expressed in terms of the form factors F_1, g and F_2 and f as follows

$$H_\pm(w) = f(w) \mp m_B m_{D^*} \sqrt{w^2 - 1} g(w) \tag{2.86}$$

$$H_0(w) = \frac{F_1(w)}{\sqrt{q^2}} \tag{2.87}$$

$$H_t(w) = m_B \left(\frac{rw^2 - 1}{1 + r^2 - 2rw} F_2(w)\right). \tag{2.88}$$

where $r = \frac{m_{D^*}}{m_B}$ and the parameter w is the scalar product of the four-velocities of the B and D^* meson

$$w(q^2) = v_B \cdot v_{D^*} = \frac{m_B^2 + m_{D^*}^2 - q^2}{2 m_{D^*} m_B}. \tag{2.89}$$

A new variable z is introduced such that

$$\frac{1 + z}{1 - z} = \sqrt{\frac{(m_B + m_{D^*})^2 - q^2}{4 m_B m_{D^*}}} \tag{2.90}$$

which converges rapidly over the entire physical region of $|z| << 1$. Unitarity of the underlying QCD correlators then translates into a normalisation condition on a contour integral over the unit circle, which in turn implies bounds on the coefficients of the z-expansion. In this way, the BGL parametrisation provides a model-independent and systematically improvable description of the form factors consistent with analyticity and unitarity. The resulting functions are analytic and bounded within $|z| << 1$, enabling the use of complex analysis techniques. Hence, the form factors written in terms of z satisfy the inequality

$$\frac{1}{2\pi i} \int_C \frac{dz}{z} |\phi_i(z) F_i(z)|^2 \leq 1, \tag{2.91}$$

where the integral is over the contour C defined by the unit circle $|z| = 1$ and $\phi_i(z)$ is a weight function (also called an outer function) which depends on z and the meson masses.

The Taylor expansion of the form factors is of the form

$$F_i(z) = \frac{1}{P_i(z)\phi_i(z)} \sum_{n=0}^{\infty} a_n z^n. \tag{2.92}$$

where $P_i(z)$ are Blaschke functors (exact forms given in [41]) ensuring the analyticity of $F_i(z)$. The exact form and the derivation of $F_i(z)$ is explained in detail in [42]. One can choose to truncate the series from Eq. 2.92 at a specific value N for which we get an approximation of $F_i^N(z)$ as

$$F_i^N(z) = \frac{1}{P_i(z)\phi(z)} \sum_{n=0}^{N} a_n z^n. \tag{2.93}$$

The maximum error by truncating the series after N terms is

$$max|F_i(z) - F_i^N(z)| = \frac{1}{|P_i(z)\phi_i(z)|} \sum_{n=N+1}^{\infty} |a_n| z^n \tag{2.94}$$

$$\leq \frac{1}{|P_i(z)\phi_i(z)|} \sqrt{\sum_{n=N+1}^{\infty} |a_n|^2} \sqrt{\sum_{n=N+1}^{\infty} z^{2n}} \tag{2.95}$$

$$< \frac{1}{|P_i(z_{max})\phi_i(z_{max})|} \frac{{z_{max}}^{N+1}}{\sqrt{1 - z_{max}^2}} \tag{2.96}$$

For N as small as 2 this error is of the order of a few % as reported in [40]. After truncating the series in Eq. 2.93 at $N = 2$ as in [40], the general notation for the form factors can be transferred into the four series expressed as following

$$f(z) = \frac{1}{P_{1^+}(z)\phi_f(z)} \sum_{n=0}^{N} b_n z^n \tag{2.97}$$

$$F_1(z) = \frac{1}{P_{1^+}(z)\phi_{F_1}(z)} \sum_{n=0}^{N} c_n z^n \tag{2.98}$$

$$g(z) = \frac{1}{P_{1^-}(z)\phi_g(z)} \sum_{n=0}^{N} a_n z^n \tag{2.99}$$

$$F_2(z) = \frac{1}{P_{0^-}(z)\phi_{F_2}(z)} \sum_{n=0}^{N} d_n z^n. \tag{2.100}$$

noting that F_2 is the helicity suppressed term which causes the rate to be proportional to the mass of the lepton. Due to the mass dependence the sensitivity for this parameter increases in decays to τ leptons.

2.4.1.2 BLPR form factor parametrisation

A quark is considered as a heavy quark if its mass, m_Q is much larger than QCD scale, $m_Q >> \Lambda_{QCD}$. According to this definition, the quarks in the SM; u, d and s are light quarks, whereas c, b and t are heavy quarks. It is easy to describe the heavy quarks system since the effective coupling constant $\alpha_s(m_Q)$ is small and the strong interactions are perturbative. However, the systems containing one heavy quark and one light quark is complicated to described because the heavy quark is surrounded by the cloud of strongly interacting light (anti)quarks and gluons. This cloud is referred as *brown muck* [38] to indicate the difficulty to solve those systems. On the other hand, the fact that Compton wavelength is much smaller than hadron size, $1/m_Q \sim \Lambda_Q << R_{Had}$, leads to some simplifications since the exchange of gluons between light and heavy quark will not be distinguishable in such small scale. Therefore, the light degrees of freedom are blind to flavour(mass) and spin orientation of the heavy quark. The B^0 and D^* mesons belong to a heavy quark spin symmetry doublet of a pseudo-scalar and a vector meson. There can be two states formed each with angular momentum $J_{V,P} = \frac{1}{2} \pm \frac{1}{2}$ whose mass can be written as

$$m_{P,V} = m_Q + \bar{\Lambda} - \frac{\lambda_1}{1m_Q} \mp \frac{(2J_{V,P}+1)\lambda_2}{2m_Q} + ... \tag{2.101}$$

where m_Q is the heavy quark mass parameter of HQET, $\bar{\Lambda} = O(\Lambda(QCD))$ is the brown muck kinetic energy for $m_Q \to \infty$ and $\lambda_{1,2} = O(\Lambda^2_{QCD})$. The matrix element for the $B \to D^*$ transition can be written in the form [38]

$$\frac{\langle D^{(*)}|\bar{c}\ \Gamma\ b|\bar{B}\rangle}{\sqrt{m_{D^{(*)}} m_B}} = -\xi(w) Tr[\bar{H_{v'}}^{(c)} \Gamma H_v^{(b)}] + \epsilon_c Tr[\bar{H}^{(c,1)}_{v',v}] + \epsilon_b Tr[\bar{H}^{(c)}_{v'} \Gamma H^{(b,1)}_{v,v'}] \tag{2.102}$$

where $\epsilon_{c,b} = \bar{\Lambda}/(2m_{c,b})$, Γ is a Dirac matrix, $H^{(c,b)}$ are HQET representations of the heavy-quark doublet, $\xi(w)$ is the Isgur-Wise function, $v = \frac{p_B}{m_B}$ and $v' = \frac{p_{D^*}}{m_{D^*}}$. In Eq. 2.102 the leading order Isgur-Wise function can be considered via $\xi(w) \to \xi(w) + 2(\epsilon_c + \epsilon_b)\chi_1(w)$, where w has the definition from Eq. 2.89. The function χ_1 satisfies $\chi_1(1) = 0$ [43] and the Isgur-Wise function satisfies $\xi(1) = 1$.
In a more general picture, the matrix elements of $\langle D^{(*)}|O_\Gamma|\bar{B}\rangle$ can be written , where a full operator basis is

$$O_S = \bar{c}b, \quad O_P = \bar{c}\gamma^5 b, \quad O_V = \bar{c}\gamma^\mu b, \quad O_A = \bar{c}\gamma^\mu\gamma^5 b, \quad O_T = \bar{c}\sigma^{\mu\nu} b. \tag{2.103}$$

At $O(\alpha_s)$, these operators can be expanded by matching QCD onto HQET [44] as following,

$$\bar{c}b \to \bar{c}^{'}_{\nu}(1+\hat{\alpha_s}C_S)b_\nu, \tag{2.104}$$

$$\bar{c}\gamma^5 b \to \bar{c}^{'}_{\nu}(1+\hat{\alpha_s}C_P)\gamma^5 b_\nu, \tag{2.105}$$

$$\bar{c}\gamma^\mu b \to \bar{c}^{'}_{\nu}[(1+\hat{\alpha_s}C_{V_1})\gamma^\mu + \hat{\alpha_s}C_{V_2}v^\mu + \hat{\alpha_s}C_{V_3}v^{\mu^{'}}]b_\nu, \tag{2.106}$$

$$\bar{c}\gamma^\mu\gamma^5 b \to \bar{c}^{'}_{\nu}[(1+\hat{\alpha_s}C_{A_1})\gamma^\mu + \hat{\alpha_s}C_{A_2}v^\mu + \hat{\alpha_s}C_{A_3}v^{\mu^{'}}]\gamma^5 b_\nu v, \tag{2.107}$$

$$\begin{aligned}\bar{c}\sigma^{\mu\nu}b \to \bar{c}^{'}_{\nu}[&(1+\hat{\alpha_s}C_{T_1})\sigma^{\mu\nu} + \hat{\alpha_s}C_{T_2}i(v^\mu\gamma^\nu - v^\nu\gamma^\mu) \\ &+ \hat{\alpha_s}C_{T_3}i(v^{\mu^{'}}\gamma^\nu - v^{\nu^{'}}\gamma^\mu) + C_{T_4}(v^{\mu^{'}}v^\nu - v^{\nu^{'}}v^\mu)]b_\nu\end{aligned} \tag{2.108}$$

where the C_{Γ_i} are the functions of w, $z = m_c/m_b$ and $\hat{\alpha}_s = \alpha_s/\pi$.
The definitions of the matrix elements are

$$\langle D^*|\bar{c}b|B\rangle = 0, \tag{2.109}$$

$$\langle D^*|\bar{c}\gamma^5 b|B\rangle = -\sqrt{m_B m_{D^*}}h_P(\epsilon^*\ v), \tag{2.110}$$

$$\langle D^*|\bar{c}\gamma^\mu b|B\rangle = i\sqrt{m_B m_{D^*}}h_V\epsilon^{\mu\nu\alpha\beta}\epsilon^*_\nu v'_\alpha v_\beta, \tag{2.111}$$

$$\langle D^*|\bar{c}\gamma^\mu\gamma^5 b|B\rangle = \sqrt{m_B m_{D^*}}[h_{A_1}(w+1)\epsilon^{*\mu} - h_{A_2}(\epsilon^*\cdot v)v^\mu - h_{A_3}(\epsilon^*\cdot v)v^{'\mu}], \tag{2.112}$$

$$\langle D^*|\bar{c}\sigma^{\mu\nu}\gamma^5 b|B\rangle = -\sqrt{m_B m_{D^*}}\epsilon^{\mu\nu\alpha\beta}[h_{T_1}\epsilon^*_\alpha(v+v')_\beta + h_{T_2}\epsilon^*_\alpha(v-v')_\beta + h_{T_3}(\epsilon^*\cdot v)v_{\alpha v'_\beta}] \tag{2.113}$$

where h_i are form-factor functions equal to the sub-leading Isgur-Wise functions as defined in [45], $\hat{h_i}(w) = h_i(w)/\xi(w)$ which are explicitly defined as

$$\hat{h_V} = 1 + \hat{\alpha_s} C_{V_1} + \epsilon_c(\hat{L}_2 - \hat{L}_5) + \epsilon_b(\hat{L_1} - \hat{L_4}), \tag{2.114}$$

$$\hat{h_{A_1}} = 1 + \hat{\alpha_s} C_{A_1} + \epsilon_c(\hat{L}_2 - \hat{L}_5\frac{w-1}{w+1}) + \epsilon_b(\hat{L_1} - \hat{L_4}\frac{w-1}{w+1}), \tag{2.115}$$

$$\hat{h_{A_2}} = \hat{\alpha_s} C_{A_2} + \epsilon_c(\hat{L}_3 + \hat{L}_6), \tag{2.116}$$

$$\hat{h_{A_3}} = 1 + \hat{\alpha_s}(C_{A_1} + C_{A_3}) + \epsilon_c(\hat{L}_2 - \hat{L}_3 + \hat{L}_6 - \hat{L}_5) + \epsilon_b(\hat{L_1} - \hat{L_4}), \tag{2.117}$$

$$\hat{h_P} = 1 + \hat{\alpha_s} C_P + \epsilon_c[\hat{L}_2 + \hat{L}_3(w-1) + \hat{L}_5 - \hat{L}_6(w+1)] + \epsilon_b(\hat{L_1} - \hat{L_4}), \tag{2.118}$$

$$\hat{h_{T_1}} = 1 + \hat{\alpha_s}[C_{T_1} + \frac{w-1}{2}(C_{T_2} - C_{T_3})] + \epsilon_c\hat{L_2} + \epsilon_b\hat{L_1}, \tag{2.119}$$

$$\hat{h_{T_2}} = \hat{\alpha_s}\frac{w+1}{2}(C_{T_2} - C_{T_3}) + \epsilon_c\hat{L_5} + \epsilon_b\hat{L_4}, \tag{2.120}$$

$$\hat{h_{T_3}} = \hat{\alpha_s} C_{T_2} + \epsilon_c(\hat{L_6} - \hat{L_3}) \tag{2.121}$$

where w dependent $\hat{L}_i$ functions are defined as

$$\hat{L_1} = -4(w-1)\hat{\chi_2} + 12\hat{\chi_3}, \hat{L_2} = -4\hat{\chi_3}, \hat{L_3} = 4\hat{\chi_2}, \tag{2.122}$$

$$\hat{L_4} = 2\eta - 1, \hat{L_5} = -1, \hat{L_6} = -2(1+\eta)/(w+1) \tag{2.123}$$

Integrating Eq. 2.56 over the angular variables gives the differential decay rates in the recoil parameter w. These one-dimensional distributions are introduced here to express the recoil spectra in terms of the HQET form factors used in the BLPR parametrisation. They are angular-integrated projections of the decay distributions, rather than replacements for the full angular description introduced earlier, and can be written as

$$\frac{d\Gamma(B \to Dl\nu)}{dw} = \frac{G_F^2|V_{cb}|^2 m_B^5}{48\pi^3}(w^2-1)^{3/2} r_D^3 (1+r_D)^2 G(w), \tag{2.124}$$

$$\begin{aligned}\frac{d\Gamma(B \to D^* l\nu)}{dw} = &\frac{G_F^2|V_{cb}|^2 m_B^5}{48\pi^3}(w^2-1)^{1/2}(w+1)^2 r_{D^*}^3 (1-r_{D^*})^2 \\ &\times \Big[1 + \frac{4w}{w+1}\frac{1-2wr_{D^*}+r_{D^*}^2}{(1-r_{D^*})^2}F(w)^2\Big],\end{aligned} \tag{2.125}$$

where $r_{D^*} = \frac{m_{D^*}}{m_B}$ and $G(w), F(w)^2, R_1(w), R_2(w)$ are explicitly written as

$$G(w) = h_+ - \frac{1-r_D}{1+r_D} h_- \tag{2.126}$$

$$F(w)^2 = h_{A_1}^2 2(1-2(wr_{D^*})+r_{D^*}^2)(1+R_1^2\frac{w-1}{w+1}) + [1-r_{D^*}+(w-1)(1-R_2)]^2$$
$$\times [(1-r_{D^*})^2 + \frac{4w}{w+1}(1-2wr_{D^*})]^{-1}, \tag{2.127}$$

$$R_1(w) = \frac{h_V}{h_{A_1}}, \tag{2.128}$$

$$R_2(w) = \frac{h_{A_3} + r_{D^*} h_{A_2}}{h_{A_1}}. \tag{2.129}$$

Here h_+ and h_- are the form factors that describe $B \to Dl\nu$ decay [45]. In the heavy quark limit $R_{1,2}(w) = 1$ and $F(w) = G(w) = \xi(w)$. $G(w)$ can be further parametrized with $\rho^2 = -\frac{G'(w)}{G(w_0)}$ and

$$\frac{G(w)}{G(w_0)} \approx 1 - 8a^2\rho_*^2 z_* + (V_{21}\rho_*^2 - V_{20}) z_*^2. \tag{2.130}$$

$$z_*(w) = \frac{\sqrt{w+1}-\sqrt{2}a}{\sqrt{w+1}+\sqrt{2}a} \quad a = \sqrt{\frac{1+r_D}{2\sqrt{r_D}}} \quad \rho_*^2 = -\frac{G'(w_0)}{G(w_0)} \tag{2.131}$$

Here, $w_0 = 2a^2 - 1 \approx 1.28$ is defined such that $z_*(w_0) = 0$ while $V_{21} = 57$, $V_{20} = 7.5$ are numerical evaluation from [25]. The sub-leading Isgur-Wise functions can be approximated up to the terms $O(\epsilon_{c,b}(w-1))$

$$\hat{\chi_2}(w) \approx \hat{\chi}_2(1) + \hat{\chi_2}'(1)(w-1), \tag{2.132}$$

$$\hat{\chi_3}(w) \approx \hat{\chi}_3'(1)(w-1), \tag{2.133}$$

$$\eta(w) \approx \eta(1) + \eta'(1)(w-1). \tag{2.134}$$

From here the leading Isgur-Wise function $\xi(w)$ can be extracted from the parametrisation introduced in Eq. 2.130. The full derivation is given in [45] and here we refer to the final relation

$$\frac{\xi(w)}{\xi(w_0)} \approx 1 - 8a^2\bar{\rho}_*^2 z_* + z_*^2\Bigg(V_{21}\bar{\rho}_*^2 - V_{20} + (\epsilon_b - \epsilon_c)\left[2\Theta\eta'(1)\frac{1-r_D}{1+r_D}\right] + (\epsilon_b + \epsilon_c)\left[\Theta[12\hat{\chi}_3'(1) - 4\hat{\chi}_2(1)] - 16[(a^2-1)\Theta - 16a^2]\hat{\chi}_2'(1)\right] + \frac{\alpha_s}{\pi}\left[\Theta\left(C_{V_1}'(w_0) + \frac{C_{V_3}(w_0) + r_D C_{V_2}(w_0)}{1+r_D}\right) + 2a^2(\Theta - 32a^2)\frac{C_{V_3}'}{1+r_D}\right] - 64a^6\frac{C_{V_3}''(w_0) + r_D C_{V_2}''(w_0)}{1+r_D} - 32a^4 C_{V_1}''(w_0)\Bigg), \tag{2.135}$$

where $\Theta = 64a^4\bar{\rho}_*^2 - 16a^2 - V_{21}$, $\bar{\rho}_*^2 = \frac{\xi'(w_0)}{\xi(w_0)}$ and C_i are the functions of w, m_c/m_b and α_s/π. The exact expressions for C_i are also given in [38] and [45]. This expression for $\xi(w)$, combined with the HQET expansions in Eq. 2.114, allows us to parametrise all $B \to D^{(*)}$ form factors in six parameters: $\bar{\rho}_*^2$, $\hat{\chi}_2(1)$, $\hat{\chi}_2'(1)$, $\hat{\chi}_3'(1)$, $\eta(1)$ and $\eta'(1)$.

2.4.1.3 CLN parametrisation

The CLN parametrisation is built on top of the HQET framework improved with perturbative corrections from QCD sum rules. The QCD sum rules introduce gauge invariant operators with their operator product expansion beyond perturbation theory. The sum rules give an approximation for the subleading Isgur-Wise functions [44] $\eta(w)$ and $\chi(w)$. According to them $\eta(w)$ is a constant function and the contributions of χ_2 and χ_3 are small. These assumptions are used to decrease the number of relevant parameters and predict values for R_1 and R_2 using Eq. 2.128 and Eq. 2.129. Having the helicity amplitudes defined as Eqs. 2.68, 2.69, 2.70 we can see that they are function of the form factors A_0, A_1, A_2 and V, which are functions of q^2 [46] [33]. In the HQET framework it is more useful to work in terms of the four-momentum transfer so the form factors are usually expressed as a function of the parameter w, defined in Eq. 2.89. All four form factors may be expressed in terms of a single function and it is therefore conventional to write them in terms of the $h_{A_1}(w)$ as given below [25]

$$A_1(w) = \frac{w+1}{2} r_{D^*} h_{A_1}(w), \quad A_0(w) = \frac{R_0(w)}{r_{D^*}} h_{A_1}(w), \tag{2.136}$$

$$A_2(w) = \frac{R_2(w)}{r_{D^*}} h_{A_1}(w), \quad V(w) = \frac{R_1(w)}{r_{D^*}} h_{A_1}(w), \tag{2.137}$$

where

$$r_{D^*} = \frac{2\sqrt{m_B m_{D^*}}}{m_B + m_{D^*}}, \tag{2.138}$$

$$h_{A_1}(w) = h_{A_1}(1)[1 - 8\rho^2_{D^*} z(w) + (53\rho^2_{D^*} - 15)z^2(w) - (231\rho^2_{D^*} - 91)z^3(w)], \tag{2.139}$$

$$R_1(w) = R_1(1) - 0.12(w-1) + 0.05(w-1)^2, \tag{2.140}$$

$$R_2(w) = R_2(1) + 0.11(w-1) + 0.06(w-1)^2, \tag{2.141}$$

$$R_0(w) = R_0(1) - 0.11(w-1) + 0.01(w-1)^2, \tag{2.142}$$

$$z(w) = \frac{\sqrt{w+1} - \sqrt{2}}{\sqrt{w+1} + \sqrt{2}}. \tag{2.143}$$

This parametrization is called Caprini-Lellouch-Neubert (CLN) [25] and the values for the form factors can be extracted from various measurements of the $B \to D^* \ell\nu$ distributions. The parameters of interest are the values R_i at $w = 1$ and the slope of the Isgur-Wise function ρ_{D^*}. Three of these parameters can be measured using $B \to D^* \ell\nu$ decays. The most recent averages [47] give the values

$$\begin{aligned} \rho^2_{D^*} &= 1.122 \pm 0.024, \\ R_1(1) &= 1.270 \pm 0.026, \\ R_2(1) &= 0.852 \pm 0.018. \end{aligned} \tag{2.144}$$

The R_0 parameter features in the expression 2.70. This is the helicity suppressed term which causes the rate to be proportional to the mass of the lepton. Due to the mass dependence the sensitivity for this parameter increases in decays to τ leptons. An estimation of R_0 can be made using sum rules [46] with the relation

$$\frac{R_2(1)(1-r) + r[R_0(1)(1+r) - 2]}{(1-r)^2} = 0.97, \tag{2.145}$$

where $r = \frac{m_{D^*}}{m_B}$. Using the value for $R_2(1)$ from the current world average the value for R_0 yields to 1.15 with an estimate of 10% uncertainty according to Ref. [46].

2.4.2 $B \to D^{**} l\nu$ form factors

The D^{**} states that are of interest in this thesis, identified in $B \to (D^{**} \to D^{*+}\pi^-)\mu\nu$ decays are: $D^{**} = D_1(D_1(2420)), D_2^*(D_2^*(2460)), D_1'(D_1(2430)^0)$. In the

analysis of $B \to D^* \mu\nu$ transitions, semileptonic decays involving higher resonances, $B \to D^{**}\mu\nu$, constitute a dominant source of background. These D^{**} states frequently decay to the signal-like D^* final state accompanied by one or more additional pions (e.g., $D^{**} \to D^*\pi$). If these accompanying soft pions are not reconstructed in the detector, the event mimics the $B \to D^*\mu\nu$ signal topology.

The first form factor parametrisation for these decays was introduced by Leibovich et al. (LLSW) [48]. A more recent model has been proposed by Bernlocher et al. (BLR) [45]. The D^{**} states in the quark model correspond to combining the heavy quark and light quark spins with $L = 1$ orbital angular momentum with the total light quark angular momentum $J_q = 3/2(D_2^*$ and $D_1)$ or $J_q = 1/2(D_1')$. Therefore three different form factor models can be considered. The matrix elements for the vector ($V^\mu = \bar{c}\gamma_\mu b$) and for the axial vector ($A^\mu = \bar{c}\gamma_\mu\gamma_5 b$) currents can be written for the two different doublets (states 3/2 and 1/2).

In the heavy quark symmetry $m_{c,b} \gg \Lambda_{QCD}$ the form factors above can be described by a universal Isgur-Wise function: $\tau(w)$ for the 3/2 states and $\zeta(w)$ for the 1/2 states. The full expressions for the form factors are given in Appendix A of [45]. The leading order Isgur-Wise function can be written in the form

$$\tau(w) = \tau(1)[1 + (w-1)\tau'(1) + ...], \tag{2.146}$$

In the BLR paper [45] there are three approximations introduced for calculating the form factor parameters, so called approximation A, B and C. These approximations provide a controlled truncation of the heavy-quark and recoil expansion of the form factors, allowing the dominant symmetry structure to be retained while limiting the number of independent non-perturbative parameters entering the decay amplitudes.

Here the normalisation of the Isgur-Wise functions is taken from experimental constraints from the B-factories (Belle and BaBar) when the fit values were determined. As seen from BLR paper the Approximation C constrains the decay rate stronger than the LLSW parametrisation. The overall derivation of the helicity amplitudes and the best fit values for the parameters of each approximation is given in [45].

2.5 Anomalies in measurements of $B \to D^*\ell\nu$ decays

Precision tests of the SM rely on observables that can be both measured experimentally and computed theoretically with high accuracy. One of the most powerful probes comes from semileptonic decays of heavy mesons, such as $B^0 \to D^{*-}\ell^+\nu_\ell$. In these processes, the electroweak interaction is cleanly described by the SM, and the dominant theoretical uncertainty arises from the strong-interaction dynamics encoded in hadronic form factors (FFs). Hadronic form factors parametrise the non-perturbative QCD effects in matrix elements of quark currents between hadronic states, which is discussed in section 2.4.1.

One of the key features of the SM is Lepton Flavour Universality (LFU), which states that the electroweak gauge bosons couple to all three generations of leptons with identical strength. Any observed differences in the decay rates or angular distributions among the different lepton flavours arise purely from their different masses, which dictate the available kinematic phase space and helicity structure of the decays. LFU can be tested by measuring the ratio of branching fractions for decays involving different lepton flavours. This observable is defined as

$$\mathcal{R}(H_c) = \frac{\mathcal{B}(H_b \to H_c\ell_1\nu_{\ell_1})}{\mathcal{B}(H_b \to H_c\ell_2\nu_{\ell_2})}, \tag{2.147}$$

where H_b is a hadron containing a b quark, H_c is a hadron containing a c quark, and ℓ_1, ℓ_2 denote two different lepton generations.

So far at LHCb and B-factories (Belle and BaBar), several ratios of branching fractions have been measured as

$$\mathcal{R}(D^{(*)}) = \frac{\mathcal{B}(B \to D^{(*)}\tau\nu)}{\mathcal{B}(B \to D^{(*)}\ell\nu)} \tag{2.148}$$

where D refers to D^0, D^* or D^+. The LHCb collaboration can measure $R(D^*)$ with two decay modes for τ: $\tau \to \mu\nu\nu$ (muonic) and $\tau \to 3\pi\nu$ (hadronic). With the muonic mode, the most recent results from LHCb can be summarised as $R(D^0) = 0.441 \pm 0.060 \pm 0.066$, $R(D^*) = 0.281 \pm 0.018 \pm 0.024$ [49] with the correlation -0.49/-0.43 (stat./syst.), $R(D^+) = 0.249 \pm 0.043 \pm 0.047$ and $R(D^{+*}) = 0.402 \pm 0.081 \pm 0.085$ [50] with the correlation -0.48/-0.39 (stat./syst.); and with hadronic mode, $R(D^*) = 0.267 \pm 0.012 \pm 0.019$ [51] stating the tension with the SM prediction of

$R(D^*) = 0.254 \pm 0.005$ and $R(D^0) = 0.298 \pm 0.004$ [52].

The combined experimental measurements of $R(D)$ and $R(D^*)$ show a deviation of approximately 3.8σ from the SM expectation. These include results from BaBar [53], Belle [54] and Belle II [55]. A graphical summary of the combined measurements can be found in Fig. 2.7. The origin of this discrepancy remains unresolved: while it could indicate New Physics (NP) beyond the SM, other possible explanations include statistical fluctuations, underestimated experimental or theoretical uncertainties, and biases in the measurements or predictions. NP therefore remains a possible interpretation, motivating further observables that can test its contributions. In this context, an angular analysis of the decay $B^0 \to D^{*-}\ell^+\nu_\ell$ has been widely advocated as a particularly sensitive probe of NP contributions [56].

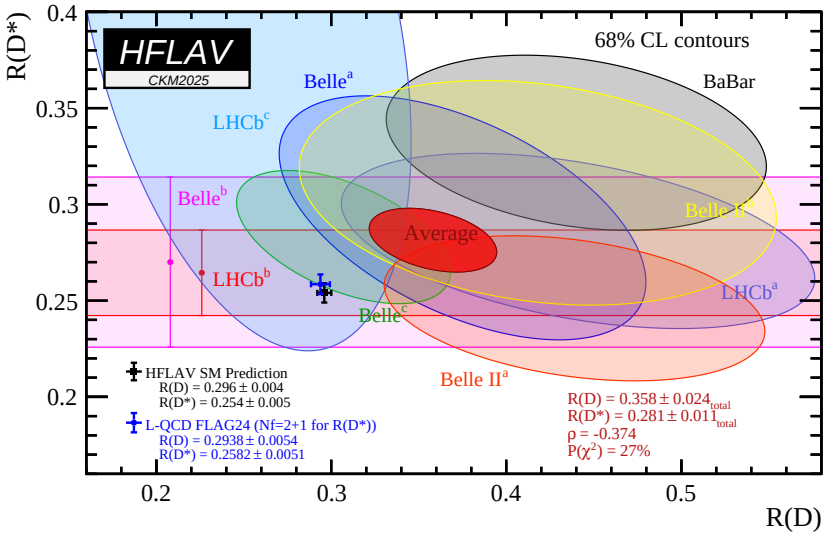


Figure 2.7: Graphical summary of measurements of ratios $R(D)$ and $R(D^*)$ for Belle, BaBar and LHCb as of spring 2025 [3]. The black and blue points show the SM prediction. The average of the experimental results from LHCb, Belle-Belle II and BaBar is shown as a red ellipse.

There are other observables beside LFU test ratios which are sensitive to flavour anomalies i.e. angular coefficients (reported from Belle [6]) in Eq. 2.72, lepton polarisation asymmetry $P_\tau^{D^{(*)}}$, longitudinal helicity fraction $F_L^{D^*}$ of D^* meson, forward backward asymmetry $A_{D^{(*)}}^{FB}$, which are defined in Eq. 2.149. The set of measurements

of observables to test the SM is provided in Tab. 2.3.

$$P_\tau^{D^{(*)}}(q^2) = \frac{\frac{d\Gamma^{D^{(*)}}_{\lambda_\tau=+1/2}}{dq^2} - \frac{d\Gamma^{D^{(*)}}_{\lambda_\tau=-1/2}}{dq^2}}{\frac{d\Gamma^{D^{(*)}}_{\lambda_\tau=+1/2}}{dq^2} + \frac{d\Gamma^{D^{(*)}}_{\lambda_\tau=-1/2}}{dq^2}}, \tag{2.149}$$

$$F_L^{D^*}(q^2) = \frac{\frac{d\Gamma^{D^*}_{\lambda_{D^*}=0}}{dq^2}}{\frac{d\Gamma^{D^*}}{dq^2}}, \tag{2.150}$$

$$A_{FB}^{D^{(*)}}(q^2) = \frac{\int_0^1 d\cos\theta_\tau \frac{d^2\Gamma^{D^{(*)}}}{dq^2 d\cos\theta_\tau} - \int_{-1}^0 d\cos\theta_\tau \frac{d^2\Gamma^{D^{(*)}}}{dq^2 d\cos\theta_\tau}}{\frac{d\Gamma^{D^{(*)}}}{dq^2}}. \tag{2.151}$$

where $\lambda_\tau = \pm\ 1/2$ is the lepton helicity, $\lambda_{D^*} = 0$ denotes the longitudinal polarization of the D^*; and θ_ℓ is the angle between the lepton momentum and the $D^{(*)}$ direction in the lepton rest frame, q^2 is the momentum transfer to the boson.

Table 2.3: Current status of the independent experimental measurements of LFU ratios and angular observables. The first and second errors are statistical and systematic, respectively.

	R_D	R_{D^*}	Corr.	$P_\tau(D^*)$
BaBar [57, 58]	0.440(58)(42)	0.332(24)(18)	-0.27	-
Belle [59]	0.375(64)(26)	0.293(38)(15)	-0.49	-
Belle [60]	-	0.302(30)(11)	-	-
Belle [61]	-	$0.270(35)(^{+0.028}_{-0.025})$	0.33	$-0.38(51)(^{+0.21}_{-0.16})$
LHCb [62–64]	-	0.257(12)(18)	-	-
Belle [65]	0.307(37)(16)	0.283(18)(14)	-0.54	-
LHCb [66, 67]	0.281(18)(24)	0.441(60)(66)	-0.43	-
Belle II [68]	-	$0.262(^{-0.041}_{-0.039})(^{+0.035}_{-0.032})$	-	-
LHCb [69]	0.249(43)(47)	0.402(81)(85)	-0.39	-
	$R_{J/\psi}$	$F_L^{D^*}$	R_{Λ_c}	
LHCb [70]	0.71(17)(18)	-	-	
LHCb [71]	0.51(12)(08)	-	-	
Belle [72, 73]	-	0.60(8)(4)	-	
LHCb [74]	-	-	0.242(26)(40)(59)	
LHCb [75]	-	0.43(6)(3)	-	
CMS [76]	0.49(11)(24)	-	-	

2.5.1 NP searches using $B \to D^* \ell\nu$

A large amount of current theoretical research is devoted to studying the NP scenarios in $b \to c\ell\nu$ transitions and predicting values for possible NP Wilson coefficients. The theoretical calculations provide the parameter space for different NP models for $b \to c\ell\nu$ transitions. Many of them involve angular observables that are related to corresponding NP effective couplings [33], [77], [46], [78], [79]. Among the most popular virtual particles in the NP scenarios is the existence of a new vector boson such as the W' that is similar to the SM W boson but has couplings with a different strength with different leptons and quarks [80], [81]. Extensions of the SM with a charged scalar particle (charged Higgs) [82] have also been considered. The constraints of the charged Higgs with the experimental measurements are discussed in [83] however the charged scalar particle idea has been disfavoured since the constraints on the lifetime of B_c meson rule-out, model independently, the explanations of enhancement in $R(D^*)$ based on scalar operators.

Recently, considerable attention has been devoted to global analyses of the LFU anomalies in $b \to c\tau\nu$ transitions. In particular, Ref. [1] performs a comprehensive global fit to the latest measurements of $R(D)$, $R(D^*)$, and $F_{D^*}^L$ from Belle, Belle II, LHCb, and BaBar as of Spring 2024 (The current averaged values of the experimental measurements are written in the last row of Tab. 2.4). In their analysis, these three observables are included in a χ^2 fit to determine the preferred regions of the new physics (NP) parameter space, defined by $\Delta\chi^2 = \chi^2 - \chi^2_{\text{best}} \leq 1$ and, the goodness-of-fit for each NP scenario is expressed by the *Pull* value defined as following

$$\text{Pull (single WC)} = \sqrt{\chi^2_{\text{SM}} - \chi^2_{\text{NP-best}}}(\sigma) \tag{2.152}$$

where the baseline SM minimum, χ^2_{SM}, is tabulated in Ref. [84] (see Tab. 2.4). Expressed in units of standard deviations (σ), the Pull value quantifies the significance by which a given NP hypothesis improves the description of the experimental data compared to the Standard Model. A threshold of Pull > 4 denotes an excellent fit; statistically, this indicates that the introduction of specific NP Wilson coefficients reduces the global χ^2 sufficiently to shift the theoretical predictions directly into the 1σ experimental confidence intervals of the $R(D^{(*)})$ world averages. Consequently, this metric provides a rigorous, objective criterion, allowing competing NP scenarios to be quantitatively ranked and compared according to their phenomenological vi-

ability. After identifying the relevant NP WCs, additional constraints are imposed, notably from the B_c lifetime and LHC searches, to assess the viability of each scenario. For solutions that remain consistent with these bounds, the authors further evaluate NP predictions for other observables such as $P_{D\tau}$, $P_{D^*\tau}$ and $R(J/\psi)$. The fitted values of NP WCs, their pulls, and the angular observable predictions for the corresponding NP WC along with the constraints used can be found in See Tab. 2.5.

Reference	R_D	R_{D^*}	$F_L^{D^*}$
Iguro, Watanabe [84]	0.290(3)	0.248(1)	0.464(3)
Data	0.342(26)	0.287(12)	0.49(5)

Table 2.4: Summary of theoretical predictions and experimental data for R_D, R_{D^*}, $F_L^{D^*}$ used in the fit of [1].

	Pull	Fitted C_x	$B_c \to \tau\nu$	LHC
SM	- [23.1]	-	-	-
$C_{V_{LL}}$	4.8 [0.3]	+0.079(16)	very loose	[-0.32, 0.32]
$C_{V_{RL}}$	2.6 [16.3]	-0.070(26)	very loose	[-0.33, 0.33]
$C_{S_{RL}}$	3.1 [13.6]	+0.165(48)	[-0.94, 1.4]	[-0.55, 0.55]
$C_{S_{LL}}$	3.9 [8.0]	+0.182(42)	[-1.4, 0.94]	[-0.55, 0.55]
$C_{T_{LL}}$	4.1 [6.4]	-0.033(7)	-	[-0.17, 0.17]
	Predictions $\Delta\chi^2 \leq 1$	$P_{D\tau}$	$-P_{D^*\tau}$	$R(J/\psi)$
SM		0.331 ± 0.004	0.497 ± 0.007	0.258 ± 0.004
$C_{V_{LL}}$		[0.331, 0.331]	[0.497, 0.497]	[0.291, 0.309]
$C_{V_{RL}}$		[0.331, 0.331]	[0.495, 0.496]	[0.280, 0.307
$C_{S_{RL}}$		[0.435, 0.508]	[0.516, 0.531]	[0.254, 0.256]
$C_{S_{LL}}$		[0.454, 0.516]	[0.458, 0.473]	[0.261, 0.263]
$C_{T_{LL}}$		[0.350, 0.361]	[0.457, 0.473]	[0.290, 0.311]

Table 2.5: The fit results of the single NP operator scenarios assuming real WCs. The WCs are given at the μ_b scale (explained in text). The allowed ranges of WC from the B_c lifetime and the current LHC bounds are also shown (*very loose* represents very weak bounds). Fitted WCs and predictions of $P_{D\tau}$,$P_{D^*\tau}$ and $R(J/\psi)$ are in the range of $\Delta\chi^2 = \chi^2 - \chi^2_{\text{best}} \leq 1$.

Tab. 2.5 presents the fit results for single New Physics operator scenarios under the assumption of strictly real Wilson coefficients, thereby restricting the parameter space to CP-conserving New Physics. These Wilson coefficients are evaluated at the renormalisation scale $\mu_b \simeq m_b \approx 4.18$ GeV. Choosing this scale corresponds to the characteristic energy of the b-quark decay and ensures consistency with the running

b and c quark masses, $m_b(\mu_b)$ and $m_c(\mu_b)$, which are required to evaluate the scalar contributions without introducing large logarithmic corrections.

The paper considers all NP WCs in Eq. 2.53 that are contributing $b \to c\ell\nu$ interaction, namely, $C_{V_{LL}}, C_{V_{RL}}, C_{S_{LL}}, C_{S_{RL}}, C_{T_{LL}}$. All considered new-physics (NP) scenarios provide a substantially better fit to the data than the Standard Model. Compared to earlier analyses performed before the latest LHCb updates [62–64], an important change is that the $C_{S_{RL}}$ scenario is now compatible with the data at the 95% confidence level. However, this solution cannot be realized within the usual type-II two-Higgs-doublet model (2HDM), since it requires a negative $C_{S_{RL}}$, which is incompatible with the model's structure. Even in a more general 2HDM framework, generating a sufficiently large $C_{S_{RL}}$ contribution is strongly constrained by ΔM_{B_s} (mass difference of heavy and light B_s eigenstates) [85] and LHC search limits [86]. On the other hand, the real $C_{S_{LL}}$ scenario remains disfavoured at the 2σ level because its interference with the SM contribution has opposite signs in $R(D)$ and $R(D^*)$, preventing a simultaneous explanation of both anomalies — a situation unchanged by the new LHCb and Belle II measurements. The $C_{V_{LL}}$ scenario continues to provide an excellent fit, while $C_{V_{RL}}$ leads to a smaller improvement. The tensor $C_{T_{LL}}$ solution predicts distinctive effects in other observables, offering a way to discriminate among NP hypotheses; in particular, it implies a negative shift in $F_L^{D^*}$, which is in some tension with current measurements [73, 87].

It also has been seen that when imaginary parts of $C_{V_{RL}}, C_{S_{LL}}, C_{T_{LL}}$ along with real parts included the fit improves further and the best-fit points are

$$C_{V_{RL}} \simeq +0.01 \pm i0.41 \quad C_{S_{LL}} \simeq -0.79 \pm i0.86 \quad C_{T_{LL}} \simeq +0.02 \pm i0.13 \tag{2.153}$$

Another set of hypothetical particles are the lepto-quarks (LQs) [88], [36], [89], [90]. There are 3 categories of LQ which can explain $R(D^{(*)})$ tension which are U_1^μ (a SU(2)$_L$-singlet vector), S_1 (a SU(2)$_L$-singlet scalar), and R_2 (a SU(2)$_L$-doublet scalar) [31].

$$U_1^\mu : C_{V_{LL}}, C_{S_{RL}}, \quad S_1 : C_{V_{LL}}, C_{S_{LL}} = -4C_{T_{LL}}, \quad R_2 : C_{V_{RL}}, C_{S_{LL}} = 4C_{T_{LL}} \tag{2.154}$$

at the LQ scale $\Lambda_{LQ} = M_{LQ} = 2$ TeV since $M_{LQ} > 1.5$ TeV is constrained from LQ pair production searches [91], [92], [93]. It has been seen that these three general

LQ scenarios are equivalently favoured by the current data; and the best-fit points that the U_1^μ, S_1, and R_2 LQ scenarios prefer, are purely real, purely imaginary, and complex scalar NP contributions, respectively. The detailed results can be found in Table 5 of Ref. [1].

While the most prominent experimental hints of LFU violation manifest as tensions in the semitauonic observables $\mathcal{R}(D^{(*)})$, high-precision studies of the muonic mode, $B \to D^*\mu\nu$, are indispensable to this landscape for two primary reasons. First, the muonic channel serves as the critical denominator in the $\mathcal{R}(D^*)$ ratio. The precision of SM predictions for $\mathcal{R}(D^*)$ is currently limited by the uncertainty in the hadronic form factors. Because muons are reconstructed with excellent resolution at LHCb, high-statistics angular analyses of $B \to D^*\mu\nu$ provide the most stringent constraints on these form factor parameters, effectively reducing the theoretical uncertainty in the semitauonic predictions. Second, New Physics models that couple preferentially to the third generation (such as LQs or Z' bosons) can still allow for non-standard couplings to the second generation. Therefore, rather than merely acting as an SM-like baseline, the $B \to D^*\mu\nu$ transition is an active testing ground. By leveraging the vast experimental statistics available for muons, one can perform an angular analysis to place constraints on NP Wilson coefficients.

2.5.2 Current state of art of hadronic form factors

QCD is the renormalizable gauge theory describing quark and gluon interactions as introduced in section 2.1.2.2. While it is perturbative at high energies due to asymptotic freedom, it becomes strongly coupled at hadronic scales (Λ_{QCD} ~200 MeV). In this regime, the coupling constant is large, thus, perturbation theory breaks down; also quarks and gluons are confined inside hadrons. As a result, hadronic transition matrix elements cannot be computed using perturbative methods. Understanding semileptonic decays therefore requires fully non-perturbative techniques. One of the most powerful non-perturbative tools is Lattice QCD (LQCD). LQCD reformulates QCD on a discrete, finite four-dimensional Euclidean spacetime lattice where spacetime is replaced by a grid with spacing a and quark fields live on lattice sites while gluon fields live on links between sites. Therefore, path integrals which are originally divergent and cannot be computed analytically in QCD are evaluated numerically using Monte Carlo methods. By simulating QCD directly from first principles, LQCD allows controlled calculations of hadronic observables with systematically

improvable uncertainties. Results are extrapolated to the continuum limit ($a \to 0$), infinite volume, and physical quark masses. Modern simulations include dynamical up, down, strange, and charm quarks, and in some approaches such as HISQ [94] can access bottom physics with controlled extrapolations. Form factors are obtained from appropriate correlation functions:

1. Two-point correlators determine meson masses and overlap factors:

$$C_2(t) = \langle 0|O_H(t)O_H^\dagger(0)|0\rangle \tag{2.155}$$

2. Three-point correlators give matrix elements of the weak current:

$$C_3(t,T) = \langle 0|O_{D^*}(T)J^\mu(t)O_B^\dagger(0)|0\rangle \tag{2.156}$$

By fitting these correlators and forming suitable ratios, the desired hadronic matrix elements are extracted. These matrix elements are then decomposed into Lorentz-invariant form factors as functions of q^2 or equivalently w (recoil parameter) as mentioned in section 2.4.1.

The differential decay rate in w gives direct sensitivity to the hadronic form factors and it can be written for $B^0 \to D^{*-}\ell^+\nu_\ell$ as

$$\underbrace{\frac{d\Gamma}{dw}\big(B \to D^{(*)}\ell\nu\big)}_{\text{Experiment}} = \Bigg[\underbrace{K_1^{D^{(*)}}(w)}_{\text{Known factors}} \times \underbrace{|F(w)|^2}_{\text{Theory}} + \underbrace{K_2^{D^{(*)}}(w,m_\ell)}_{\text{Known factors}} \times \underbrace{|F_2(w)|^2}_{\text{Theory}}\Bigg] \times |V_{cb}|^2\,. \tag{2.157}$$

where m_ℓ is lepton mass, $K_{1,2}^{D^{(*)}}(w)$ include known factors (kinematic factors, constants, etc.) defined in the theory, $F_{1,2}(w)$ are the decay amplitudes that can be computed from theory; and the term $K_2^{D^{(*)}}(w,m_\ell)|F_2(w)|^2$ is proportional to m_ℓ^2 so it contributes meaningfully only for tau lepton. In this equation, we can experimentally measure the $d\Gamma/dw$; and decay amplitudes and form factors can be calculated from LQCD, therefore, they can be compared with each other. However, there are some challenges: The LQCD predictions are well-defined in high-q^2 region whereas experimental measurements less precise due to low statistics since the decay rate is constrained by phase space. In addition, LQCD calculations are easier for $B \to D\ell\nu$

since they only have two form factors whereas $B^0 \to D^{*-}\ell^+\nu_\ell$ has four form factors (one Vector, two Axial-vector, one Pseudo-scalar) and features large error but for the experimental point of view, it is the opposite. There is a better signal-to-noise ratio in $B^0 \to D^{*-}\ell^+\nu_\ell$ whereas larger background contamination is present in $B \to D\ell\nu$. Although experimentally challenging, precise differential measurements are indispensable for probing hadronic structure and testing LQCD predictions. In recent years, several high-precision measurements of the differential decay rate as a function of the recoil parameter w have been reported. For the scope of this discussion, we restrict ourselves exclusively to those measurements which include the fully unfolded and efficiency-corrected spectra in their publications, as these are essential for direct, unbiased theoretical comparisons and global fits. Within this criteria, three key measurements are highlighted:

1) **LHCb [4]** performed a measurement of the differential decay rate shape in w for the $B_s \to D_s^*\mu\nu$ decay using an integrated luminosity of 1.7 fb^{-1}. The unfolded and efficiency-corrected decay rate shape in multiple w bins is shown in Fig. 2.8.

2) **Belle II [5]** reported the measurement of the differential decay rate shape in w for $B^0 \to D^{*-}\ell^+\nu_\ell$ using both electron and muon modes with an integrated luminosity of 189 fb^{-1}. The unfolded and efficiency-corrected shape is shown in Fig. 2.9.

3) **Belle [6]** recently published a comprehensive measurement of the $B^0 \to D^{*-}\ell^+\nu_\ell$ differential shapes using the full Belle data sample of 711 fb^{-1}. Alongside the angular distributions, they provided the fully unfolded, 1D efficiency-corrected differential decay rate in w as shown in Fig. 2.10.

All of these measurements are performed across the full q^2 range. By fitting these unfolded spectra to different form factor parametrisations, they provide experimental tests for LQCD predictions.

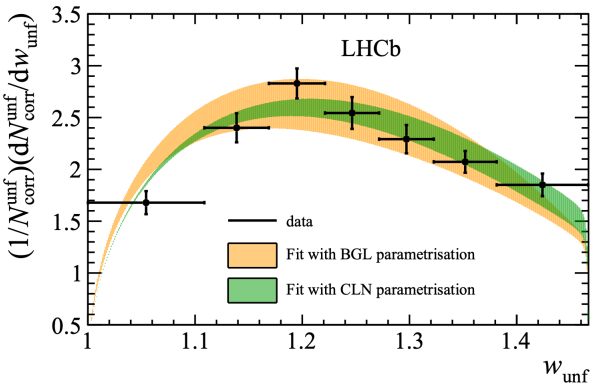


Figure 2.8: Unfolded normalised differential decay rate of $B_s \to D_s^* \mu\nu$ with the fit superimposed for the CLN parametrisation (green), and BGL (orange). The band in the fit results includes both the statistical and systematic uncertainty on the data yields. Image taken from Ref. [4].

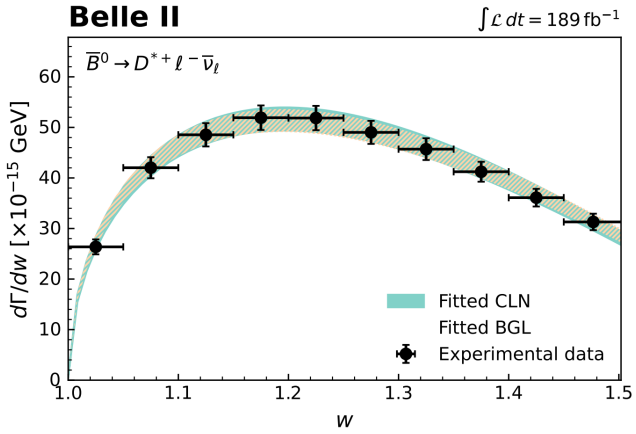


Figure 2.9: Comparison of the fitted partial decay rates with 1σ uncertainties in the BGL and CLN parametrizations to the unfolded experimental data (shown as points with error bars). Note that the BGL (hatched) band almost completely overlaps the CLN (solid) band. Image taken from Ref. [5].

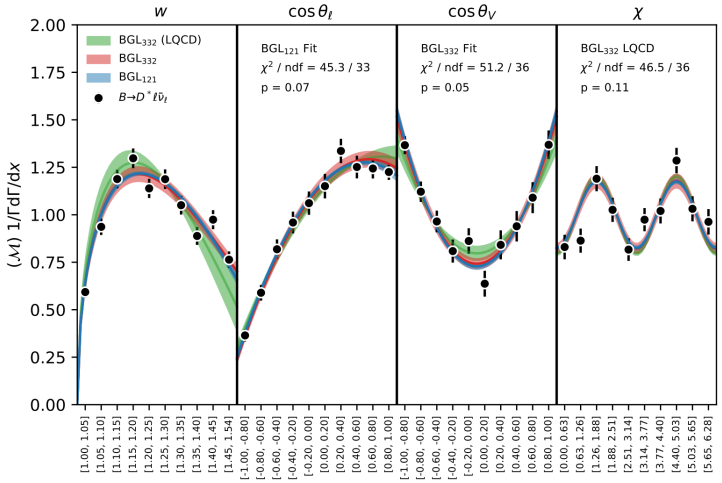


Figure 2.10: One-dimensional projections of the normalised differential decay rates for $B \to D^* \ell \bar{\nu}_\ell$. The panels display, from left to right, the kinematic recoil w, the lepton helicity angle $\cos\theta_\ell$, the hadron helicity angle $\cos\theta_V$ (equivalent to the $\cos\theta_D$ notation used in this work), and the azimuthal angle χ. The unfolded data points are shown in black. The coloured bands represent the fit results and their associated uncertainties for different BGL parametrisation configurations: a lower-order BGL_{121} fit (blue), a higher-order BGL_{332} fit (red), and a BGL_{332} fit incorporating LQCD constraints (green). Image taken from Ref. [6].

In recent full-kinematic-range calculations [7] based on the heavy-HISQ approach [95, 96], the HPQCD collaboration, provide the vector, axial, and tensor form factors for both $B_s \to D_s^* \mu\nu$ and $B^0 \to D^{*-} \mu^+ \nu_\mu$ decay modes across the full q^2 range. The form factor definitions given in Ref. [7] are based on HQET basis and same as in Eq. 2.114. The paper uses correlator fits where they fit to lattice data with specific correlator functions defined in Eqs. 2.155 and 2.156, and then extracts the form factors from these fits (For more details, see Ref. [7]). These results are obtained using multiple lattice spacings and physical quark masses, allowing controlled systematic uncertainties. The form factors for both SM and tensor current are shown in Figs. 2.11, 2.12.

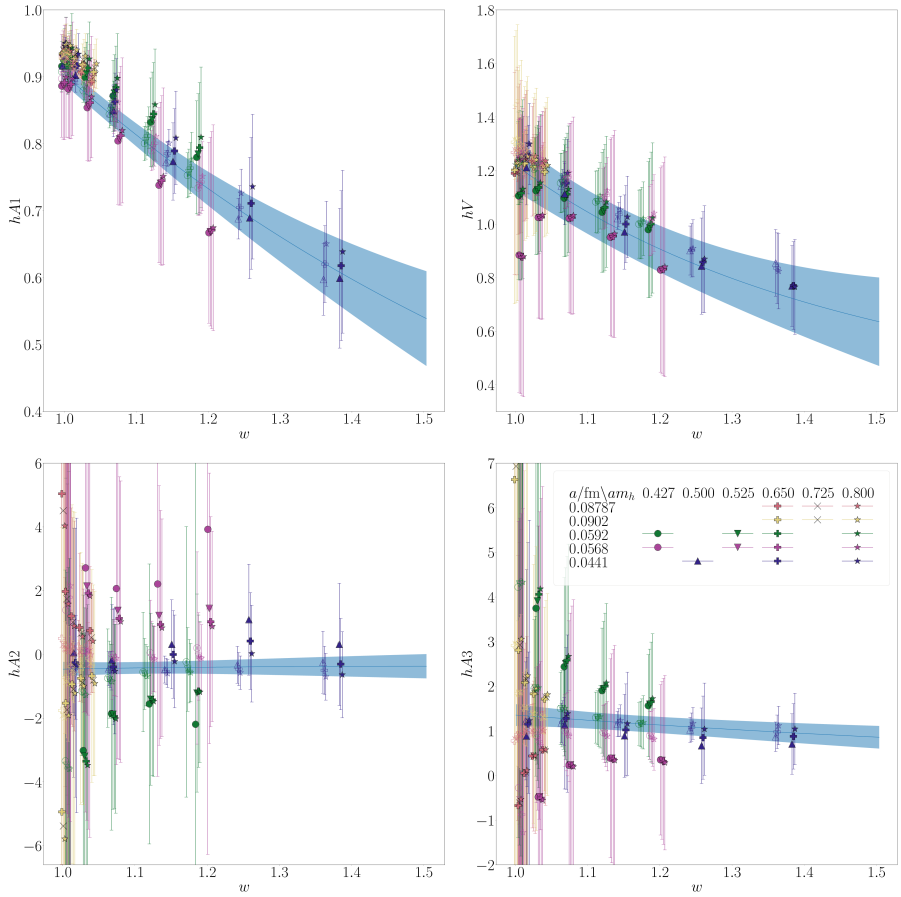


Figure 2.11: The points show LQCD results in Ref. [7] for each SM form factor for both $B \to D^*$ (filled points) and $B_s \to D_s^*$ (empty points) as a function of the recoil parameter, w. The legend gives the mapping between symbol colour and shape and the set of gluon field configurations used, as given by the lattice spacing, and the heavy quark mass in lattice units. The blue curve with error band is the result of correlator fit in the continuum limit and with the physical b quark mass for the decays.

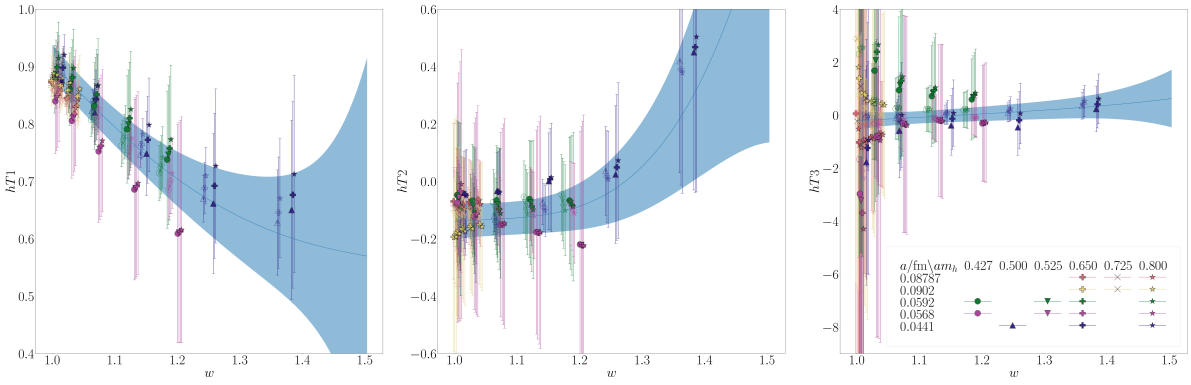


Figure 2.12: The points show LQCD results in Ref. [7] for each tensor form factor for both $B \to D^*$ (filled points) and $B_s \to D_s^*$ (empty points) as a function of the recoil parameter, w. The legend gives the mapping between symbol colour and shape and the set of gluon field configurations used, as given by the lattice spacing, and the heavy quark mass in lattice units. The blue curve with error band is the result of correlator fit in the continuum limit and with the physical b quark mass for the decays. Image taken from Ref. [7].

The paper also computes their results to the specific FF parametrisation BGL for the physical continuum (vanishing lattice spacing and physical quark masses). They fit synthetic data points generated at $w = 1.025$, $w = 1.225$, and $w = 1.425$ for each $B \to D^*$form factor in the helicity basis, defined in Eq. 2.100, using the BGL parametrisation. The result of each BGL FF parameter can be found in TABLE XIV in Ref. [7]. Then, they use their form factors (in physical continuum as described in Section IV F) together with the untagged data, $B^0 \to D^{*-}\ell^+\nu_\ell$ for $\ell = e, \mu$ from Belle [22] in order to extract $|V_{cb}|$. Their lattice-only normalised differential decay rates for $B \to D^*$ and $B_s \to D_s^*$ are shown in Figs. 2.13 and 2.14 respectively, together with the experimental data points for each bin from LHCb [4] and Belle [5], where they note a difference in shape between their results and the binned data.

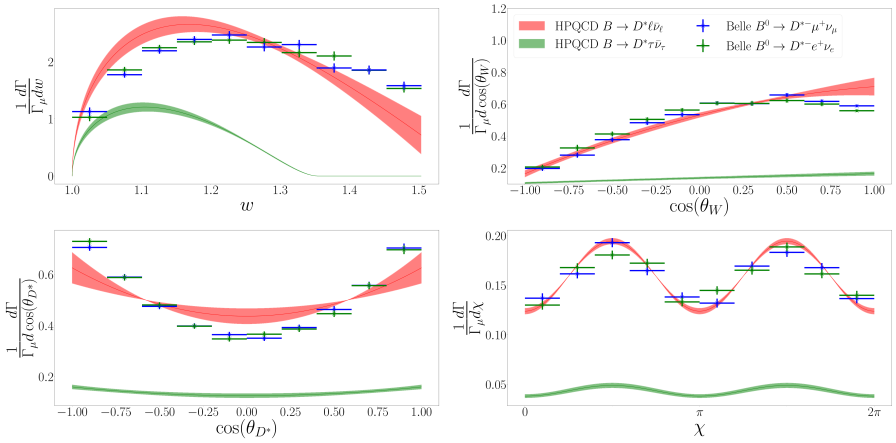


Figure 2.13: The lattice-only normalised differential decay rates for $B^0 \to D^{*-}\ell^+\nu_\ell$, with respect to the angular variables defined in Fig. 2.6, are shown as the red bands. We also include binned untagged data for e/μ from Belle. Note the clear difference in shape, particularly for the differential rate with respect to w. The tauonic differential decay rates are shown in green. Image taken from Ref. [7].

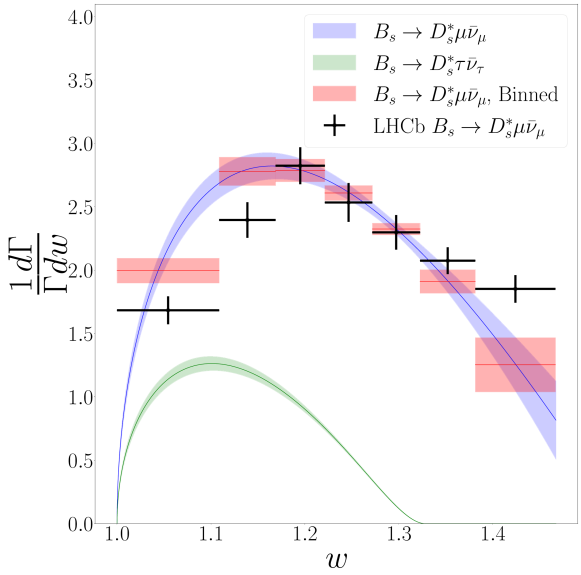


Figure 2.14: The normalised differential decay rate for $B_s \to D_s^* \ell \nu$ with respect to w is shown as the blue band. The binned data from LHCb is also shown. Here, they note that a similar difference in shape between SM theory and experiment to that seen for Belle data in Fig. 2.13. The semi-tauonic mode is plotted as the green band. Image taken from Ref. [7].

2.6 Summary

Semileptonic b-hadron decays provide a means of testing the SM through measurements of branching fractions, differential decay rates and angular observables. The measurements of $R(D)$ and $R(D^*)$ reviewed in this chapter exhibit a combined tension with SM predictions, although its origin remains unresolved. Possible NP contributions must therefore be considered alongside statistical fluctuations, underestimated experimental or theoretical uncertainties, and potential biases. Meanwhile, advances in lattice QCD and experimental measurements of differential distributions provide complementary information on hadronic form factors. The differences between some predicted and measured distributions discussed above highlight the importance of further experimental tests and careful treatment of these uncertainties.

This motivates the study of the angular and kinematic distributions of $B^0 \to D^{*-}\mu^+\nu_\mu$ decays presented in this thesis. These distributions provide sensitivity both to the hadronic form factors and to possible non-SM contributions to the underlying weak interaction, offering information beyond that available from integrated decay rates alone. The form-factor parametrisations and effective-Hamiltonian framework introduced in this chapter provide the theoretical basis for the measurements presented in Chapters 4 and 5, allowing the data to be interpreted within the SM and used to constrain possible NP contributions.

Chapter 3

The LHCb experiment and Upgrade II

This chapter will introduce The Larger Hadron Collider Beauty (LHCb) experiment. The analyses described in this thesis – the New Physics search in Ch. 4 and the differential measurement in Ch. 5 – uses data collected from proton-proton (p-p) collisions at LHCb. Each analysis uses different set of data taking years, 2011–2012 (Run 1) and 2016–2018 (Run 2), therefore detector conditions and software infrastructure during these periods will be discussed with greater details. There will be an additional section describing the future LHCb detector with upcoming enhancements as its relation to the work presented in section 3.4 – the simulation of new detector in upgraded LHCb detector.

3.1 The LHC

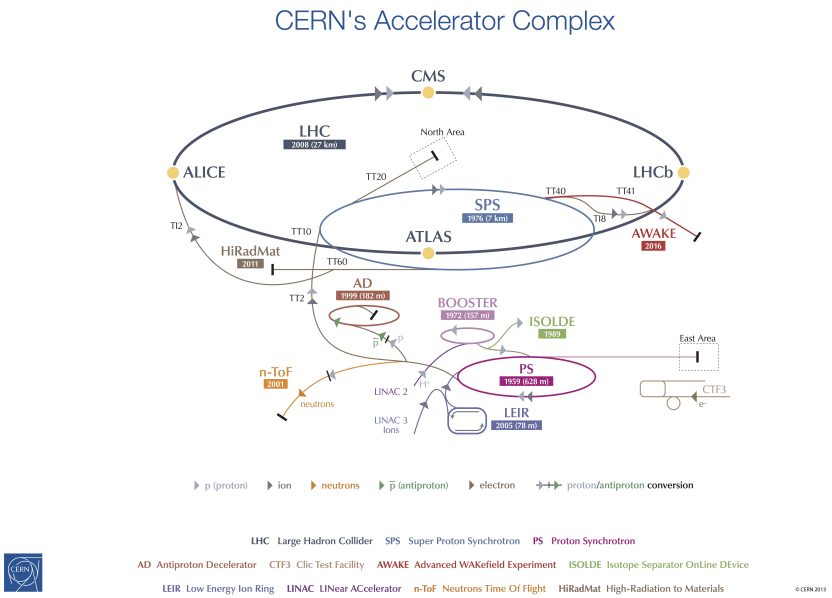


Figure 3.1: An schematic drawing [8] of the accelerator complex, where stages of accelerators are used to accelerate protons before feeding into the LHC.

The Large Hadron Collider (LHC) at CERN is a circular superconducting synchrotron with a circumference of 26.7 km, designed to accelerate and collide beams of protons or heavy ions at the highest achievable energies with 14 TeV centre of mass energy. The accelerator is installed in the former Large Electron–Positron Collider (LEP) tunnel and employs superconducting dipole magnets operating at fields of up to 8.3 T to guide two counter-rotating beams along separate beam pipes [97]. The LHC constitutes the final stage of CERN's accelerator complex (See Fig. 3.1), receiving beams from the injector chain composed of Linear Accelerator (Linac4), the Proton Synchrotron Booster (PSB), the Proton Synchrotron (PS), and the Super Proton Synchrotron (SPS) [98]. Before injection into the LHC, proton beams are prepared through CERN's multi-stage injector chain, which progressively increases the beam energy while preserving beam quality. The initial protons are produced from hydrogen gas, which is ionised in a plasma source to generate negatively charged hydrogen ions (H^-) that are extracted and injected into Linac4. These ions are accelerated by Linac4 to an energy of 160 MeV and subsequently stripped of their electrons before injection into PSB, where the proton beam is accelerated to 2 GeV.

The beam is then transferred to PS, which accelerates it further to 26 GeV and performs essential manipulations such as bunch splitting and longitudinal shaping. Subsequently, the beam is injected into SPS, where it is accelerated to 450 GeV and prepared for transfer to the LHC. Once injected, the beams circulate in the LHC and are ramped to their final energy before being brought into collision at the experimental interaction points. Each of the two counter rotating beams travelling in its own vacuum pipe, contains many packets of tightly packed protons called *bunches*. These bunches are spaced by 25 ns and each bunch crossing can result in $\sim$ 60-150 proton-proton (p-p) interactions simultaneously called *pile-up*.

Since the start of physics operation in 2010, the LHC has been operated in a sequence of multi-year running periods, referred to as *runs*, separated by long shutdowns (LS) dedicated to consolidation, maintenance, and upgrades of the accelerator complex and experimental detectors. The first physics run, **Run 1** (2010–2012), delivered proton–proton collisions at centre-of-mass energies of 7 and 8 TeV with peak instantaneous luminosity, $\mathcal{L} \approx 7.7 \times 10^{33} \mathrm{cm}^{-2}\mathrm{s}^{-1}$. This period was followed by **Long Shutdown 1 (LS1)** from 2013 to 2014, during which the LHC was prepared for higher-energy operation.

The subsequent **Run 2** period (2015–2018) marked the beginning of operation at a centre-of-mass energy of 13 TeV. During this run, the LHC achieved a substantial increase in instantaneous and integrated luminosity, supported by improvements in beam intensity, optics, and operational efficiency. Run 2 established the operational baseline for high-luminosity proton–proton collisions and provided large datasets for all four major experiments with $\mathcal{L} \approx 2 \times 10^{34} \mathrm{cm}^{-2}\mathrm{s}^{-1}$.

The **Long Shutdown 2 (LS2)**, which took place between 2019 and 2022, programme focused on improving machine reliability, upgrading cryogenic and powering systems, and increasing beam brightness through significant upgrades to the injector chain, in particular the commissioning of Linac4 and related improvements to the PS complex [99].

Following LS2, the LHC entered its third operational period (Run 3) in July 2022 and got extended to June 2026. During **Run 3**, the LHC operates primarily with proton–proton collisions at a centre-of-mass energy of 13.6 TeV, representing the highest collision energy achieved so far.

The LHC hosts four major experiments installed at its interaction points. The ATLAS and CMS detectors are general-purpose experiments designed to operate at the highest achievable luminosities, enabling precision measurements of the Stan-

dard Model and searches for new phenomena [100], [101]. The ALICE experiment is optimised for the study of strongly interacting matter in heavy-ion collisions and operates primarily during dedicated Pb–Pb and proton–ion running periods [102]. The LHCb experiment [9] is dedicated to precision measurements in flavour physics and CP violation, covering the forward pseudo-rapidity region and operating at a lower instantaneous luminosity than ATLAS and CMS. In addition to these experiments, several smaller detectors [103] are installed at specific locations around the LHC ring to address specialised physics goals.

The performance of the LHC during Run 3 has benefited from progressive improvements in beam intensity, optics, and operational efficiency. Proton–proton operation is typically conducted with a 25 ns bunch spacing, and the delivered luminosity has steadily increased as operational experience has been accumulated. The differing requirements of the experiments are accommodated through techniques such as luminosity levelling [104], which allows the instantaneous luminosity at each interaction point to be independently optimised while maintaining global machine stability .

Unlike the general-purpose detectors at the LHC, LHCb intentionally limits its collision rate via a luminosity levelling. By adjusting the transverse overlap of the colliding beams, the instantaneous luminosity was held constant at approximately $4 \times 10^{32}\,\mathrm{cm}^{-2}\mathrm{s}^{-1}$ throughout Run 2. This is double the original design specification of the detector and matches the peak levelled luminosity achieved at the end of Run 1, ensuring a stable number of visible interactions per bunch crossing ($\mu \approx 1.1$) for optimal vertex resolution and tracking performance.

The operational conditions of the LHC during Run 1 and Run 2 define the experimental environment in which the data analysed in this thesis were collected. A clear understanding of the accelerator's design, operating modes, and performance evolution is therefore essential for the interpretation of detector operation and physics results.

3.2 The LHCb detector in Run 1 and Run 2

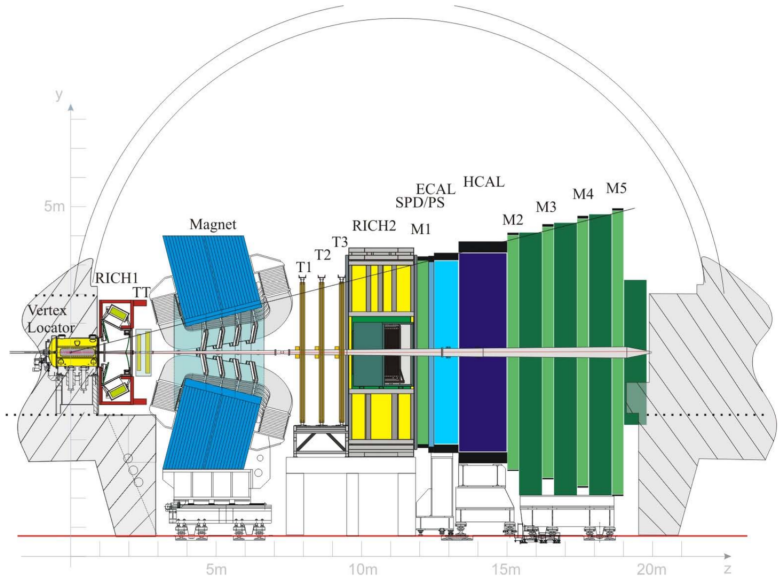


Figure 3.2: A side view of the Run 1-2 LHCb detector, containing layers of sub-detectors covering a region close to the proton beams, with the proton collisions occurring on the left [9].

The LHCb detector [9] is a single-arm forward spectrometer designed for precision studies of heavy-flavour hadrons produced in proton–proton collisions at the LHC. It is optimised for the kinematic region in which b- and c-hadrons are predominantly produced, covering the pseudo-rapidity range $2 < \eta < 5$. During Run 1 of the LHC (2011–2012), the detector operated at a centre-of-mass energy of 7 TeV and 8 TeV, recorded an integrated luminosity of ~ 3 fb^{-1}; while Run 2 (2015–2018), the detector operated at a centre-of-mass energy of 13 TeV and recorded an integrated luminosity of ~ 6 fb^{-1}, enabling a wide range of precision measurements and searches for physics beyond the Standard Model.

The LHCb detector (See Fig. 3.2) consists of several sub-systems arranged along the beam direction, each optimised to perform a specific task in the reconstruction and identification of charged and neutral particles. A high-precision vertex detector located close to the interaction point provides accurate measurements of primary and secondary vertices. This is followed by tracking stations placed upstream and downstream of a dipole magnet, which allow momentum reconstruction with excellent resolution. Particle identification is achieved through dedicated sub-detectors,

including ring-imaging Cherenkov detectors, calorimeters, and a muon system. A multi-level trigger system selects events of interest in real time, reducing the data rate to a manageable level for offline processing.

In the following sections, the individual sub-detectors of LHCb as they were operated during Run 1-2 are described, together with the trigger architecture and the track reconstruction algorithms employed in the experiment.

3.2.1 The Vertex Locator (VELO)

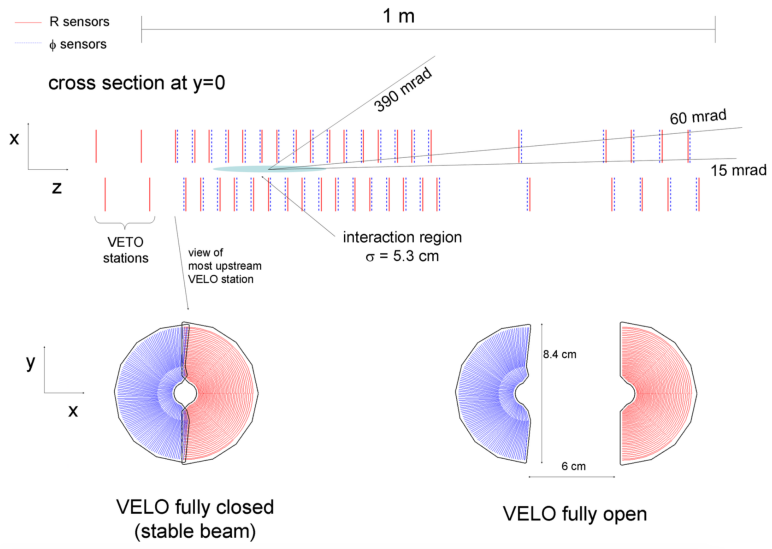


Figure 3.3: The top shows the layout of the modules along the proton beam, with the proton-proton collision region shown in blue. The bottom shows two modules from opposite halves when the VELO is closed (left) and opened (right); for each module, only either the R (red) or Φ (blue) layer of silicon strip sensor is shown. Reproduced from [10].

The Vertex Locator (VELO) is a silicon microstrip detector that surrounds the proton–proton interaction region of the LHCb experiment and is designed to perform precise measurement of primary and secondary vertices, as well as impact parameters – distance between particle trajectory and vertex – for charged tracks. Accurate vertexing is essential for the identification of heavy–flavour hadron decays, which typically originate a measurable distance from the proton–proton collision point.

During Run 1 and Run 2, the VELO consisted of two retractable halves, each containing 21 measurement modules arranged along the beam direction, for a total of 42 modules [10]. Each module was formed by a pair of semi-circular silicon

microstrip sensors, one measuring the radial coordinate (R) and the other the azimuthal coordinate (Φ), mounted back-to-back on a common support (See Fig. 3.3). The microstrip pitch varied from approximately 40–100 µm across the active area, yielding fine spatial granularity. The sensors employed oxygenated n-type silicon operating at a 40 MHz sampling rate matched to the LHC bunch crossing frequency.

To minimise multiple scattering and improve impact parameter resolution, the VELO operated in a secondary vacuum separated from the LHC beam vacuum by a thin corrugated aluminium RF foil of approximately 300 µm thickness [10]. During physics data taking, the active sensor edges were positioned as close as 7–8 mm from the LHC beam axis, significantly closer than the aperture required during injection and beam tuning. To accommodate this, the two VELO halves were retracted by about 29 mm in the horizontal plane during injection and only closed around the beam once stable-beam conditions were declared. The motion system utilised radiation-hard stepper motors and position encoding, achieving a reproducibility of better than 10 µm and symmetric closing to within a few micrometres, which was critical for alignment and stable operation.

3.2.2 Tracking Stations

Charged-particle momentum measurement in the LHCb experiment is performed by a system of tracking detectors located both upstream and downstream of the dipole magnet as indicated in Fig. 3.4. Together with VELO, these detectors provide precise reconstruction of particle trajectories and momenta, which is essential for invariant mass measurements and decay-time determinations in heavy-flavour physics.

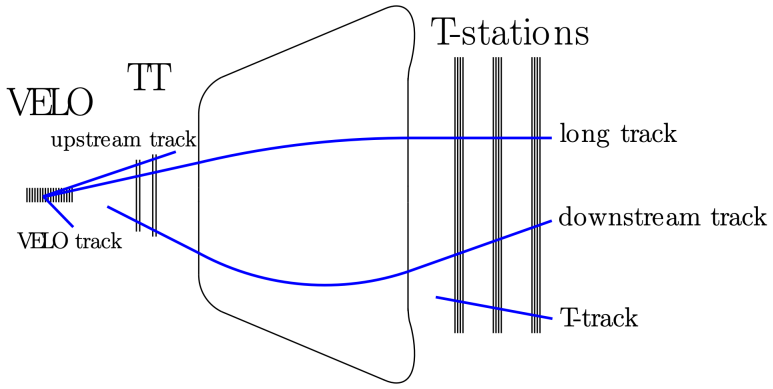


Figure 3.4: Sketch [11] of the different tracking detectors and types of tracks within LHCb.

3.2.2.1 TT

Upstream of the dipole magnet, tracking is performed by *Tracker Turicensis* (TT), a silicon microstrip detector, positioned between the VELO and the dipole magnet. The TT consists of four detection layers arranged in two stations, each composed of two silicon planes. Two middle layers are tilted along the x-axis with angles of $\pm 5^{\circ}$ that provide two-dimensional position measurements (See Fig. 3.5) – stereo layers –. The detector covers the full acceptance of the LHCb spectrometer and is optimised for track matching between the VELO and the downstream tracking stations [9]. The TT sensors are based on p-on-n silicon technology with a strip pitch of 183 µm, providing a spatial resolution of order 50 µm .

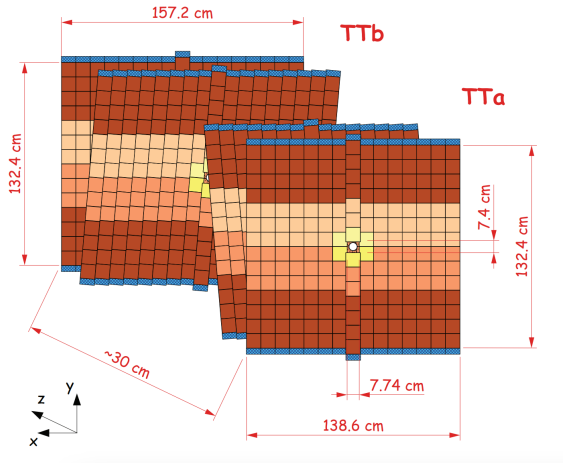


Figure 3.5: Layout of the TT, the four layers are shown. Image taken from Ref. [12].

3.2.2.2 T-stations

Downstream particle tracking is performed by three tracking stations as indicated in Fig. 3.4, denoted T1, T2, and T3. Each station is composed of two distinct detector technologies arranged according to the radial distance from the beam line. In the high-occupancy region close to the beam pipe, the *Inner Tracker* (IT) (See Fig. 3.6) employs silicon microstrip detectors using the same sensor technology as TT, while in the outer region the *Outer Tracker* (OT) (See Fig. 3.7) uses straw-tube drift chambers. This hybrid layout allows efficient tracking over the full detector acceptance while maintaining manageable channel counts and occupancies. The IT consists of silicon microstrips with pitch of 198 µm arranged in four layers (two vertical and two stereo ones) per station.

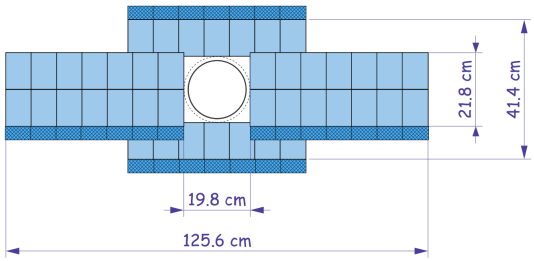


Figure 3.6: Layout of the first IT station. Only the first layer is shown. In light blue are the sensors. Image taken from Ref. [12].

The Outer Tracker (OT) has been positioned in three station as part of downstream tracking along with IT but with a different detector technology. The OT is composed of straw tubes filled with a gas mixture of $Ar/CO_2/O_2$, with a straw diameter of 4.9 mm and lengths of up to 2.4 m [13]. Similar to TT, middle two layers have stereo angle (tilted) $\pm 5^{\circ}$, positioned along the z-axis. Charged particles ionise the gas as they traverse the straws, and the resulting drift time (below 50 ns) of the electrons is used to reconstruct the hit position. The OT provides single-hit resolutions of approximately 200 µm and covers the majority of the tracking acceptance. Its large active area and relatively low material budget make it well suited for efficient tracking of particles with moderate to high transverse momentum.

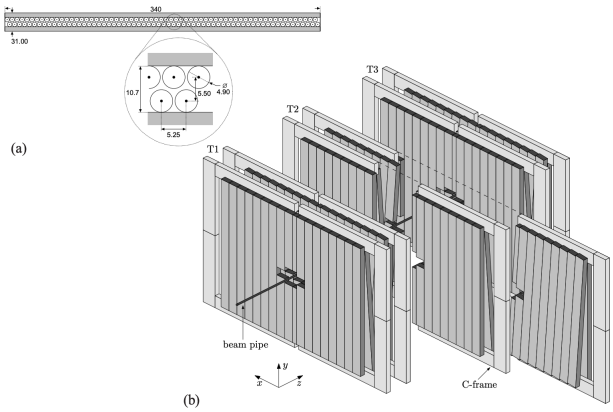


Figure 3.7: (a) Module cross section. (b) Arrangement of OT straw-tube modules in layers and stations. Image taken from Ref. [13].

Combined information from the VELO, TT, and T stations allows precise determination of track parameters. During Run 1-2, the LHCb tracking system achieved a momentum resolution of approximately 0.5% at low momentum, degrading to about 1% at 200 GeV/c. Track reconstruction efficiencies exceed 95% for charged particles within the detector acceptance with ∼10-12% fake rate, providing a robust foundation for the physics analyses presented in this thesis.

3.2.3 RICH

Particle identification (PID) in the LHCb experiment is primarily provided by two Ring-Imaging Cherenkov (RICH) detectors, which allow separation of charged hadrons (pions, kaons, and protons) over a wide momentum range. The RICH system exploits the emission of Cherenkov radiation by charged particles traversing dielectric media at velocities exceeding the local speed of light, with the Cherenkov angle providing a measure of the particle velocity. Combined with the momentum measured by the tracking system, this information enables determination of the particle mass. Cherenkov photons are reflected by a system of spherical and flat mirrors (See Fig. 3.8) onto arrays of Hybrid Photon Detectors (HPDs), which provide single-photon sensitivity and precise spatial resolution. The reconstructed Cherenkov rings are associated with charged tracks, and likelihood-based algorithms are used to compute particle identification variables for different mass hypotheses. These variables play a central role in suppressing background and enhancing signal purity in heavy-flavour analyses.

The LHCb RICH system consists of RICH1, located upstream of the dipole magnet, and RICH2, positioned downstream of the magnet. This configuration allows efficient PID across the full detector acceptance. RICH1 is optimised for low momentum (1–60 GeV/c) particles and employs two radiators: C4F10 gas. RICH2 is optimised for higher-momentum (15–100 GeV/c) tracks and uses C4F4 gas as radiator. Together RICH1 and RICH2 provides excellent π-K separation in the momentum range from 2 to 100 GeV/c [9].

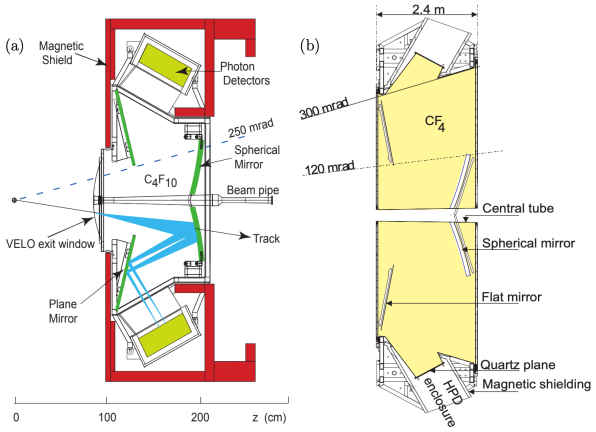


Figure 3.8: The optical system of (a) RICH1 and (b) RICH2. Image taken from Ref. [14].

3.2.4 Calorimeters

The calorimeters [9] are positioned downstream of the magnet after RICH2 (See Fig. 3.2) and performs several tasks from identification of electrons and photons to measuring position and energy of charged hadrons enabling different sub-systems. The calorimeters also perform first level trigger (Level-0) decision for hadrons after 4 µs of the interaction.

The calorimeter system consists of four sub-systems arranged sequentially along the beam direction with different lateral segmentation according to their respective hit density: a Scintillating Pad Detector (SPD), a Preshower detector (PS), an Electromagnetic Calorimeter (ECAL), and a Hadronic Calorimeter (HCAL) (See Fig. 3.9). Together, these detectors provide complementary information for particle identification and energy measurement.

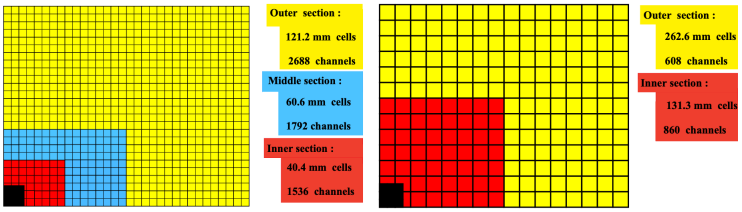


Figure 3.9: Lateral segmentation of the SPD/PS and ECAL (left) and the HCAL (right). One quarter of the detector front face is shown. In the left figure the cell dimensions are given for the ECAL. Image taken from Ref. [9].

The SPD and PS are sampling detectors based on scintillator pads read out by photomultiplier tubes. The SPD is primarily used to distinguish charged particles from neutral ones, while the PS provides early discrimination between electromagnetic and hadronic showers. These detectors are particularly important for electron and photon identification and contribute to the first level trigger decision.

The ECAL is a shashlik-type sampling calorimeter composed of alternating layers of lead absorber and plastic scintillator tiles, with wavelength-shifting fibres used to collect scintillation light. It is optimised for the detection and energy measurement of electrons and photons, achieving an energy resolution of approximately $\frac{\sigma_E}{E} = \frac{(69\pm5)\%}{E/GeV} \oplus (9\pm2)\%$. The ECAL provides precise spatial and energy information that is essential for reconstructing electromagnetic objects and neutral mesons. The HCAL is a sampling calorimeter based on iron absorbers and scintillator tiles and is designed to measure the energy of hadrons with $\frac{\sigma_E}{E} = \frac{(8.2\pm0.4)\%}{E/GeV} \oplus (0.87 \pm 0.07)\%$. While its energy resolution is coarser than that of the ECAL, the HCAL provides valuable information for hadron identification and plays an important role in triggering on high-transverse-energy hadronic activity.

3.2.5 Muon system

The muon system [9] is designed to provide efficient identification of muons and to supply fast information for the first level trigger. The muon system is located at the downstream end of the detector.

The system consists of five muon stations, denoted M1–M5, arranged along the beam direction and interleaved with iron absorbers that act as a hadron filter. Stations M2–M5 are located downstream of the hadronic calorimeter, while station M1 is placed in front of the calorimeters as it can be seen from Fig. 3.10. This configuration allows efficient discrimination between muons and hadrons, as only muons

typically penetrate the full absorber depth. Each muon station is divided into four regions (R1-R4 in Fig. 3.10) of increasing granularity towards the beam pipe in order to accommodate the strong variation in particle flux.

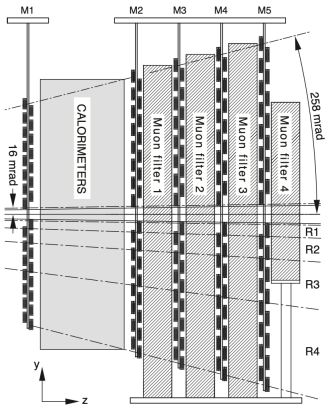


Figure 3.10: Side view of the muon system [9].

The muon detectors provide discrete spatial measurements of charged-particle trajectories, delivering binary hit information to both the trigger system and the data acquisition chain.

Muon triggering is based on stand-alone track reconstruction within the muon system and on an estimate of the transverse momentum of the candidate. Trigger algorithms require the presence of aligned hits across all five muon stations. The first three stations (M1–M3), which feature finer segmentation in the bending plane, are used to determine the track direction and to estimate the transverse momentum with a resolution of approximately 20%. The M4 and M5 primarily serve to confirm the penetration of particles through the absorber material and thereby enhance muon identification.

The detectors are based primarily on Multi-Wire Proportional Chambers (MWPCs), which provide fast response times and good spatial resolution. In the innermost, highest-rate region of the first station, Gas Electron Multiplier (GEM) detectors are employed to ensure reliable operation under high occupancy conditions.

The muon system provides coarse but fast position measurements, which are combined with tracking information to identify muon candidates. The system achieved a muon identification efficiency of 99% in Run 1 and 97.4% in Run 2 with misidentification rate of $\leq 1\%$ [105, 106] .

3.2.6 Particle identification

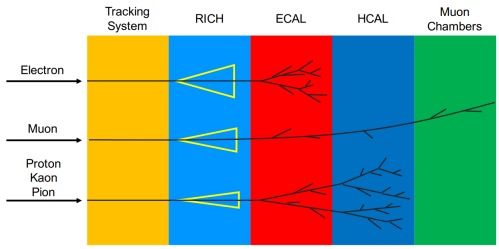


Figure 3.11: The typical signals left by different particle species on different sub-detector components. A straight line corresponds to a track and a bunch of scattered lines corresponds to a particle shower. The differences between the particles species are used for their identification. [15].

As mentioned in previous sections, separation of different species of particles at the LHCb experiment performed by several sub-detectors: two RICH detectors, the calorimeters and the muon system. To quantify the combined information on particle identification from these detectors, there are several Particle identification (PID) [9] variables using likelihood-based variables. For each reconstructed charged track, the detector responses are evaluated under several particle hypotheses (electron, muon, pion, kaon, and proton), and corresponding likelihoods $\mathcal{L}_h$ are assigned. Discriminating PID variables are typically formed as differences in logarithmic likelihoods between two hypotheses, denoted $DLL(h_1 - h_2) = ln\mathcal{L}_{h_1} - ln\mathcal{L}_{h_2}$ and generically the reference particle is π. There are also machine learning based PID algorithms [15] developed by the collaboration i.e. decision trees and artificial neural-networks to handle the non-trivial correlations of these PID variables.

3.2.7 The Trigger System

The LHCb experiment employs a dedicated trigger system designed to reduce the event rate from the LHC bunch-crossing frequency to a level suitable for permanent storage, while retaining events of high physics interest. The trigger operates by applying a sequence of selection algorithms to each event, exploiting partial or full detector information depending on the trigger stage.

During Run 1, the LHCb trigger system operated as a strictly synchronous pipeline consisting of one hardware and two software levels. The initial Level-0 (L0) hardware trigger utilised custom electronics to identify high transverse energy

and momentum signatures from the calorimeters and muon stations, reducing the 40 MHz bunch-crossing rate to 1 MHz. These accepted events were then immediately processed by the High Level Trigger (HLT) without intermediate disk buffering, where HLT1 performed a partial track reconstruction to reduce the rate to roughly 43 kHz, and HLT2 executed a full event reconstruction using pre-calculated calibration constants to achieve a final storage rate of approximately 3 kHz.

A single trigger selection algorithm is conventionally referred to as *line*, and the complete trigger configuration consists of a collection of such lines targeting different physics signatures. The major difference in Run 1 and Run 2 is the trigger architecture which can be seen from Figs. 3.12, 3.13. Compared to Run 1, the Run 2 trigger employs real-time detector calibration and alignment and the full reconstruction in the trigger stage while enabling the final signal selection at the trigger level with ∼33% more signal efficiency and a reduction of 27% in fake tracks [11].

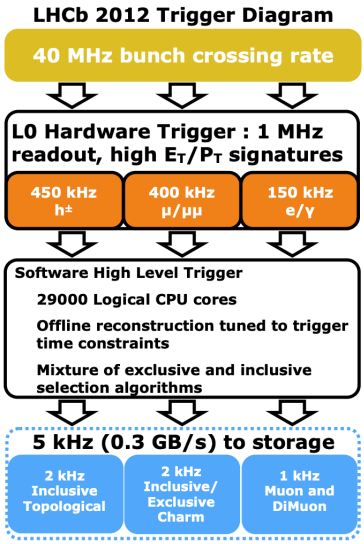


Figure 3.12: Overview of the LHCb trigger system during Run 1 [11].

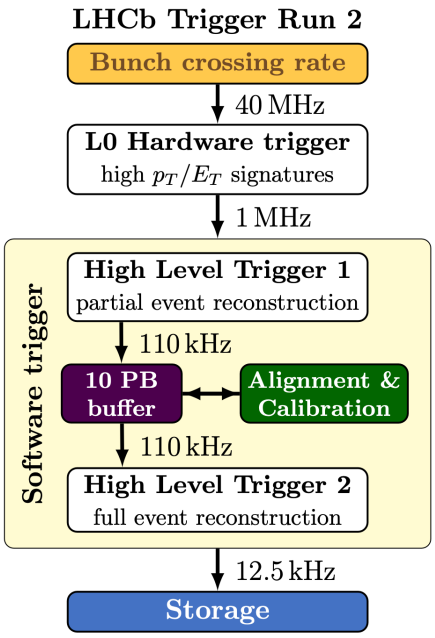


Figure 3.13: Overview of the LHCb trigger system during Run 2 [11].

During Run 2, the LHCb trigger system consisted of two sequential stages: a hardware-based trigger, known as the Level-0 (L0) trigger, followed by a software-based High Level Trigger (HLT), which was further subdivided into HLT1 and HLT2.

3.2.7.1 Hardware (L0) Trigger

The Level-0 trigger is implemented in custom hardware electronics and operates synchronously with the LHC bunch crossings at a rate of 40 MHz. Its primary purpose is to reduce the event rate to approximately 1 MHz, compatible with the readout bandwidth of the detector. During Run 1, the L0 hardware trigger thresholds were tuned to ensure the output rate remained below the 1 MHz readout limit. These requirements were explicitly tightened between the 2011 and 2012 data-taking periods to compensate for the increase in centre-of-mass collision energy from 7 TeV to 8 TeV. For the muon system, the single-muon transverse momentum (p_{T}) threshold was set to approximately 1.48 GeV/c in 2011 and subsequently raised to 1.76 GeV/c in 2012. In the calorimeter system, the transverse energy (E_{T}) threshold for hadron candidates increased from roughly 3.5 GeV to 3.7 GeV, while the corresponding thresholds for electron and photon candidates were raised from 2.5 GeV to 3.0 GeV.

The L0 trigger uses information from the calorimeter and muon systems. The L0-calorimeter trigger is based on transverse energy measurements from SPD, PS,

ECAL, and HCAL. Trigger decisions are formed according to the transverse energy (E_{T}) thresholds and the additional information from SPD and PS to distinguish electron, photon and hadron candidates. The thresholds can be seen in Tab. 3.1 for different data taking years during Run 2.

L0 trigger	2015	2016	2017	SPD threshold
Hadron	> 3.6 GeV	> 3.7 GeV	> 3.46 GeV	< 450
Photon	> 2.7 GeV	> 2.78 GeV	> 2.47 GeV	< 450
Electron	> 2.7 GeV	> 2.4 GeV	> 2.11 GeV	< 450
Muon	> 2.8 GeV	> 1.8 GeV	> 1.35 GeV	< 450
Muon high p_T	> 6.0 GeV	> 6.0 GeV	> 6.0 GeV	none
Dimuon	> 1.69 GeV^2	> 2.25 GeV^2	> 1.69 GeV^2	< 900

Table 3.1: L0 trigger E_T/p_T and SPD thresholds for 2015, 2016, and 2017.

In parallel, the L0-muon trigger exploits hit information from the muon stations to identify muon candidates with high transverse momentum. Muon trigger primitives [11] are formed by searching for straight-line track segments aligned across all five muon stations, allowing a rapid estimate of the muon transverse momentum.

3.2.7.2 High Level Trigger (HLT): HLT1 and HLT2

Events accepted by the L0 trigger are processed by the High Level Trigger, which is executed on a large computing farm and performs fully software-based event reconstruction. The HLT is divided into two stages, HLT1 and HLT2, each with increasing reconstruction complexity and selectivity.

HLT1 reconstructs the trajectories of charged particle with $p_T > 500$ MeV/c traversing the full LHCb tracking system, called long tracks as indicated in Fig. 3.4. Additionally, muon identification and primary vertex (PV) reconstruction are performed in this stage. HLT1 applies inclusive selections based on track and vertex properties and reduces the event rate by approximately an order of magnitude. The sequence of HLT1 algorithms to reconstruct the long tracks and vertices is shown in Fig. 3.14.

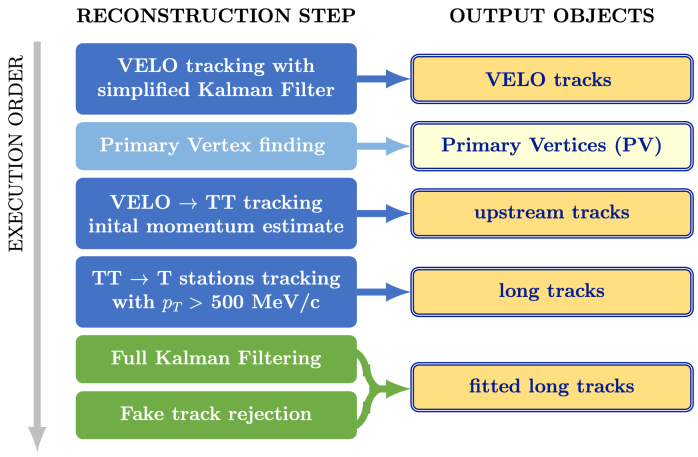


Figure 3.14: Sketch of the HLT1 track and vertex reconstruction sequence [11].

Pattern recognition: Track reconstruction in HLT1 contains three main steps: Reconstruction of VELO tracks, their extrapolation to the TT stations to match to upstream tracks and as final step, their extension to the T stations to produce long tracks. Kalman filtering is used to fit the long tracks and to reject the fake tracks. The positions of the PVs are determined through the set of fitted VELO tracks.

High-momentum tracks leave hits in the VELO which can be combined as a straight line, then these hits are extrapolated to form an upstream track along with at least three hits found in the TT as shown in Fig. 3.4. The TT has capability to reject low p_T tracks with a relative resolution of about 20%. In order to form the long tracks, cluster of hits in the IT and OT with certain properties to be matched to VELO tracks is searched. The plane of search window in the IT and OT is defined by the projection of hits for a given slope and upstream position of a single hit in the IT and OT while keeping the momentum fixed. Then, the cluster of hits in this search plane is checked to define the final long tracks.

One of the key ingredients to the software trigger performance is the reduction of fake tracks. Fake tracks are the reconstructed tracks that do not correspond to the trajectory of a true particle but rather they are formed by the combination of unrelated hits from separate particles or from detector noise, and they are commonly referred as *ghost* tracks. In order to increase the efficiency and purity of the track candidates, two artificial neural nets were implemented in the pattern recognition [107] with variable called *ghost probability* [108] where fake –ghost– tracks are rejected at the early stage without actually fitting the track candidate – due to computational expense and time constraints – but rather by evaluating neural

networks on the basic features of the track candidate.

Between HLT1 and HLT2, real-time detector calibration and alignment constants are derived from the dedicated samples selected by HLT1 and applied, ensuring that the subsequent reconstruction is performed with conditions equivalent to those used offline. The main tasks of alignment and calibration can be listed as following:

- the VELO alignment followed by the tracking stations alignment,
- the Muon stations alignment
- mirror alignment for rotations around local axes in both RICH detectors
- global time calibration of the OT,
- calorimeters calibration

The HLT2 stage executes a full event reconstruction, including tracking, vertexing, particle identification, and decay reconstruction, using algorithms closely matched to those employed in offline analysis. HLT2 selections are organised into inclusive and exclusive trigger lines targeting specific decay modes or physics signatures. The output of HLT2 defines the final dataset written to permanent storage, with an event rate of a few kHz.

The HLT2 stage takes the full information of fitted tracks provided by HLT1 and performs the additional steps of patterns recognition –which did not happen due to time constraint in HLT1 stage i.e. reconstruction of lower momentum tracks and new search window defined by maximal possible deflection of a particle with p_T >80 MeV/c – in Fig. 3.15 to identify the long and downstream tracks with the most precise momentum estimate possible. Then, full reconstruction of neutral particles is performed. Finally, HLT2 exploits full particle identification using RICH 1-2 and calorimeters in addition to the muon identification done by HLT1.

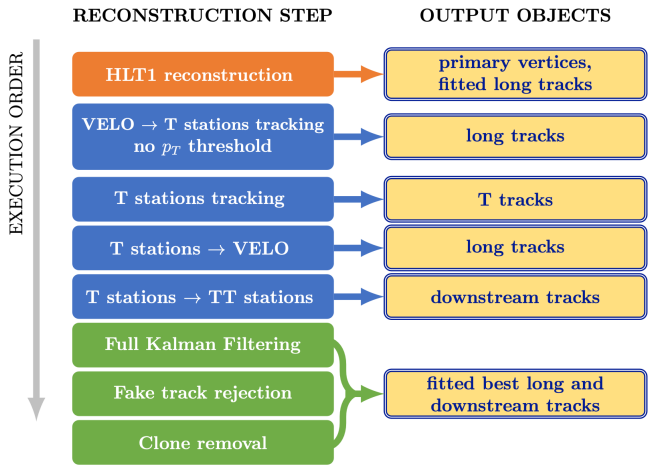


Figure 3.15: Sketch of the HLT2 track and vertex reconstruction sequence [11].

3.3 HL-LHC and Upgrade II

The HL-LHC is an upgrade of the LHC designed to significantly increase its luminosity ($\sim$7.5 $\times 10^{34}\text{cm}^{-2}\text{s}^{-1}$), allowing it to collect about 10 times more data than the original machine. It aims to deliver an integrated luminosity of around 3000–4000 fb^{-1}.

The main goal of the HL-LHC is to improve the precision of measurements—especially of the Higgs boson—and to enhance sensitivity to rare processes and potential new physics beyond the SM. To handle the much higher collision rates, major upgrades are being made to the accelerator and the detectors.

The LHCb Upgrade II is the second major phase of enhancements to the LHCb detector, planned to fully exploit the physics potential of the HL-LHC. While the first major upgrade (Upgrade I) was completed during Long Shutdown 2 and prepared the experiment for Run 3 operation at increased luminosity, Upgrade II is intended to prepare the experiment for operation beyond Run 4 at the highest instantaneous luminosities foreseen at the HL-LHC. The framework for this stage of the project is defined in [16], and approved in 2022.

3.3.1 Motivation and physics case

The primary aim of Upgrade II [109] is to accumulate an unprecedented dataset corresponding to an integrated luminosity of approximately 300 fb^{-1} over the period of the HL-LHC. Operating at instantaneous luminosities up to $1.5 \times 10^{34}\,\text{cm}^{-2}\text{s}^{-1}$ will allow LHCb to extend its sensitivity to rare processes and precision measurements across heavy-flavour, electroweak, and beyond the SM. For flavour physics observables, the increased data sample and improved detector performance will significantly enhance statistical precision and reduce systematic limitations, nearly doubling the new physics mass reach for equivalent couplings compared to the pre-HL-LHC era.

3.3.2 Challenges and detector upgrades for HL-LHC

Operating at the HL-LHC will subject the detector to substantially higher particle fluxes and occupancy than in previous runs. To maintain and improve performance under these conditions, substantial redesigns and technology advancements are required across the detector. Upgrade II must cope with increased multiplicities, high

radiation conditions, and the need for improved spatial and time resolution, while keeping material budgets and readout bandwidths within practical limits. Achieving the physics goals will also require enhanced online reconstruction and triggers that are capable of delivering high-quality data in environments with significantly higher pile-up than currently experienced.

The plan of the detector upgrades foreseen for Upgrade II is to keep the existing structure of the spectrometer while keeping up with HL-LHC challenges and maintaining the current arrangement of sub-systems as shown in Fig. 3.16. The tracking stations will consist of VELO and Upstream Tracker (UT), placed in upstream direction of the magnet; Mighty Tracker (MT) placed in downstream of the magnet. The MT is composed of a silicon tracker part in the inner region, and a SciFi tracker part for its outer region. Differently from Upgrade I, there will be additional tracking components on the magnet side walls, namely, Magnet Stations (MS). The PID will be performed by RICH 1-2, ECAL and 4 muon stations (M2-M5). The existing HCAL previous to Upgrade II is replaced by neutron shielding which features a time-of-flight detector, namely, TORCH placed in front of RICH2.

Time precision in the detectors is a new essential attribute for Upgrade II, and this will be applied to many sub-systems, i.e. the VELO, RICH, ECAL and TORCH. This new feature providing time resolution order of 10^{-11} s per particle will help immensely the correct vertex association of the charged tracks and photons, and suppress combinatorial background. The detector design presented for Upgrade II will satisfy the performance expectation from Upgrade I, but in a 7.5 times higher pile-up environment while providing an opportunity for more physics access. In order to cope with the challenges of this new environment, a number of breakthrough technologies and certain novel designs are required i.e. extensive use of Monolithic Active Pixel Sensor technologies (MAPS), the use of timing pixel detectors, namely as promising candidates, LGADs, 3D pixels, and high time resolution in photon detectors with silicon photomultipliers (SiPMs) or Microchannel Plate Photomultipliers (MCP-PMTs).

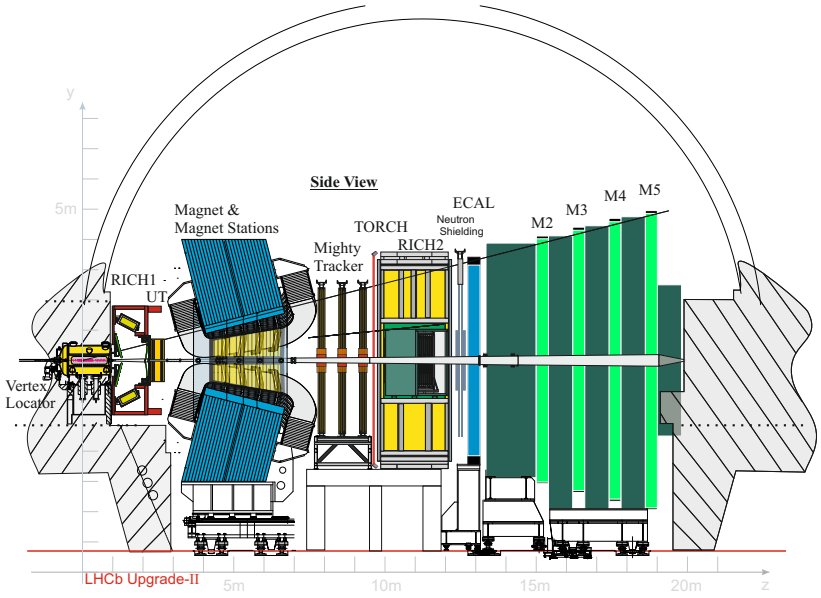


Figure 3.16: View of LHCb detector in Upgrade II [16].

The Upgrade II programme encompasses a wide range of detector developments and the main ones can be summarised:

Tracking System: One of the key requirements of the LHCb physics program is the efficient reconstruction of charged particles in the real-time software trigger, as well as, to be able to correctly associate tracks from secondary vertices to primary vertices with high-precision. In order to satisfy the performance level in track reconstruction and vertex association previous to the HL-LHC, the VELO needs to transform to a 4D tracking detector with high granularity spatial detection and additional time information of resolution better than 50 ps. This will enable to cope with high track density while mitigating inefficiency of track reconstruction due to the high pile-up. The high track density brought by HL-LHC requires the usage of pixel detectors for both upstream tracker and central region of downstream trackers. The UT detector helps reduce the rate of fake track matches between the VELO and downstream tracks in the MT, and it improves momentum resolution for the long tracks. To maintain the track reconstruction efficiency at high occupancies, the downstream tracking system will be redesigned as well with enhanced granularity.

Particle Identification: The particle identification systems will be enhanced to preserve separation power at higher event rates. For example, the RICH detectors are expected to adopt more granular and faster photon detectors, such as SiPMs, to

handle increased Cherenkov photon rates with improved time and spatial resolution. Consideration is also being given to novel PID technologies such as the TORCH time-of-flight detector to extend low-momentum hadron identification.

Calorimetry: Plans include the development of a high-precision electromagnetic calorimeter with excellent timing capabilities and finer segmentation, necessary to deal with dense particle environments and overlapping energy deposits. These advances will enhance photon and electron reconstruction and improve pile-up rejection at the highest luminosities.

Trigger and Electronics: The online data acquisition and trigger infrastructure will be further evolved to handle the vastly increased data flow. This includes readout electronics capable of coping with high rates, precision timing information, and sophisticated real-time reconstruction strategies to maintain efficient event selection without overwhelming storage and computing resources.

Upgrade II is planned for installation during Long Shutdown 4 (LS4), currently scheduled for the early 2030s. The upgraded detector is expected to begin data taking with the HL-LHC from Run 5 onward, extending LHCb's physics reach deep into the 2030s.

3.4 Mighty Tracker

The downstream tracking system contains three tracking stations (T1-T3) and the information provided by them is essential to maintain the efficient track reconstruction, especially to provide a precise estimate of particle momenta combined with the VELO and UT. In Upgrade I, Run 3, only the SciFi tracker is used as the downstream tracker read out by SiPM. However, with the high occupancy and large radiation brought by HL-LHC, the performance of the SciFi will significantly degrade. In order to recover this performance decrease in Upgrade II, the downstream tracker will combine the improved granularity and the radiation resistant silicon technologies around the beam pipe with scintillating fibres in the outer tracker region, in a detector referred as Mighty Tracker (MT).

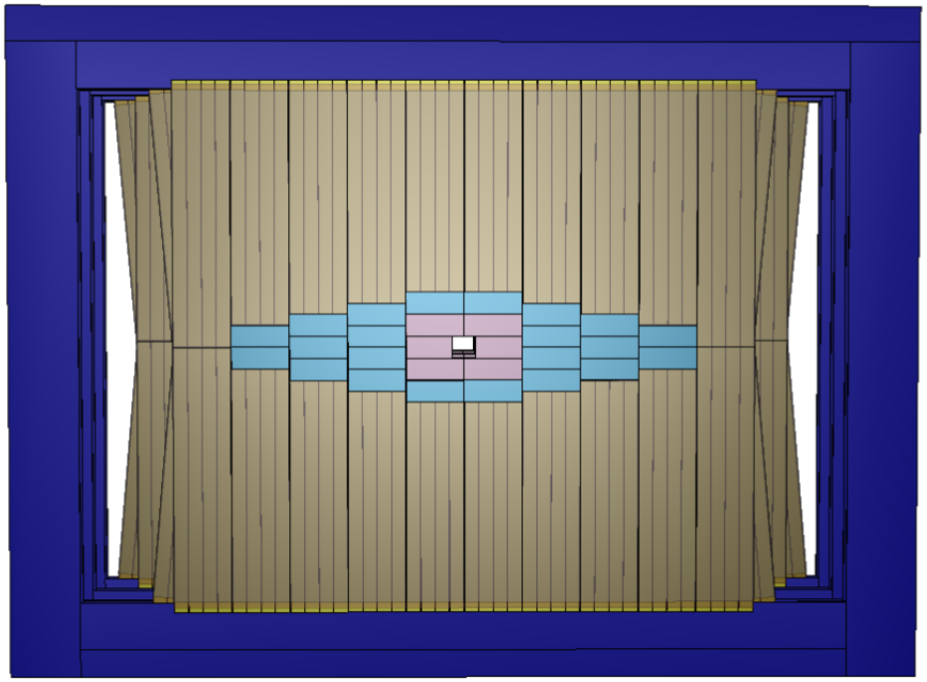


Figure 3.17: View of Mighty Tracker for Upgrade II [16]. The region near the beam pipe is covered with HV-CMOS sensors (in the colours of pink and light blue). The outer region use scintillating fibre technology.

Each MT station (See Figs. 3.17) is composed of four SciFi layers in the outer region and two of the layers are positioned vertically (X-layers) while the other two are tilted by $\pm 5^{\circ}$ (U and V layers). Each of 12 SciFi layers have up to 6 modules to ensure the detector coverage, and each model contain eight arrays of scintillating fibres, 2.4 m long and 250 µm in diameter (See Fig. 3.18 and 3.19). There are 128-channel SiPMs at each end of a fibre with a mirror placed at the opposite end maximising the light yield. These SiPM channels provide a hit-position resolution of better than 100 µm. The SiPM signals are read and digitised by 64-channel ASIC running at 40 MHz, and the clustering is done by Field Programmable Gate Arrays (FPGAs).

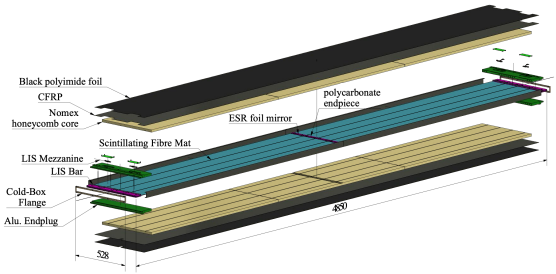


Figure 3.18: View of the components and dimensions of a SciFi module. This example corresponds to one of the most external modules in a station where the scintillating fibre arrays (fibre mats) cover the full area. For modules sharing detection area with the MT MAPS detector, the scintillating fibre mats are shorter and the ESR foil mirrors are placed closer to the extremities of the module [16].

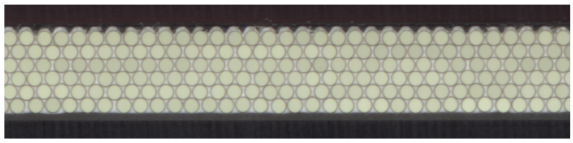


Figure 3.19: Optical scan of a six-layer array of densely packed 250 µm diameter scintillating fibres [16].

The inner part of the MT (MightyPix, MP) will be equipped with HighVoltage - Monolithic Active Pixel Sensors (HV-MAPS) and high granularity pixels (50 µm × 150 µm) will help the pattern recognition and thus the real-time track reconstruction. The inner MT consists of 3 pairs of layers, each layer pair placed in a separate MT station and they are equipped by the MAPS. Each layer has 28 modules covering a total area of $28 \times 0.108\,\mathrm{m}^2 = 3.0\,\mathrm{m}^2$ per layer (See Fig. 3.20). Each module has a sandwich structure (See Fig. 3.21): Cooling pipes are embedded in carbon foam, enclosed by carbon fibre plates. On the outside, readout flex tapes are glued, and on top of them a matrix of HV-CMOS pixel chips is mounted and wire-bonded. The chips are arranged with slight overlaps so that there are no gaps in active silicon coverage.

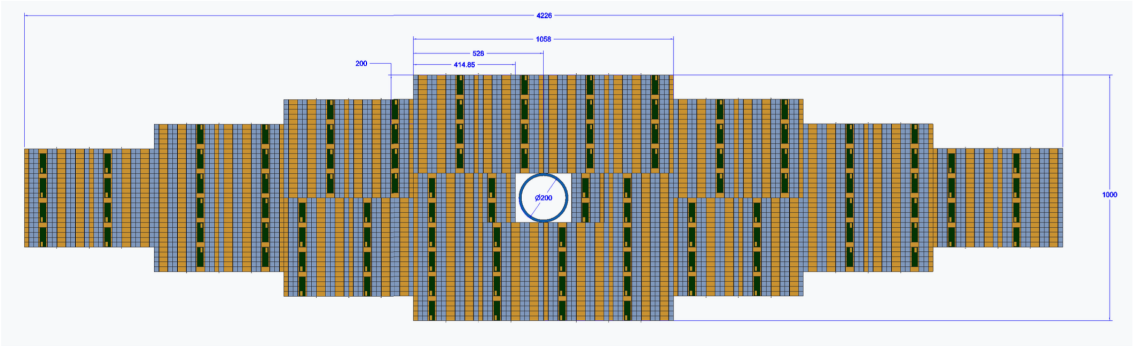


Figure 3.20: The overall design and dimensions of the one Silicon panel -Mighty Pixel (MP)- (28 modules) [16].

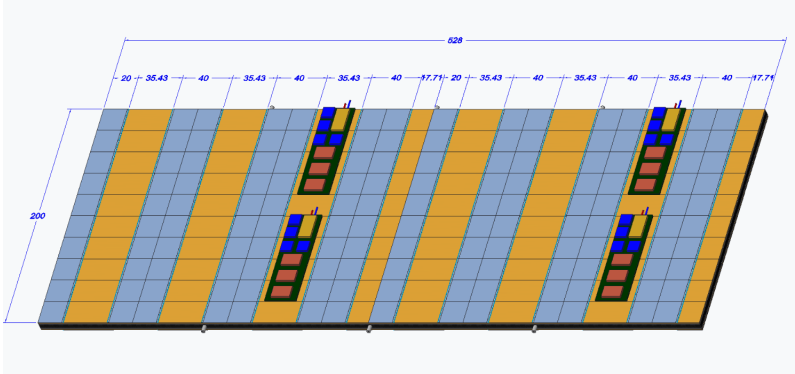


Figure 3.21: Mighty tracker module layout, with the grey rectangles representing MAPS chips. The underlying kapton tapes can be seen in the gaps between the MAPS chips. The other side of the module has an offset arrangement of the chip to provide full coverage of the plane. The service hybrids are also visible with red and blue rectangles representing the readout components [16].

3.4.1 Mighty Tracker Simulation

Detector simulation as a general concept is crucial in particle physics as it can help optimise detector performance, enable detector response to be understood, and validate detector models before the actual construction. Hence, to optimise the design of the MT, simulation is essential.

We can summarise the LHCb software simulation and processing chain in three main steps:

- **Event generation & Detector simulation**: The GAUSS [110] framework manages the creation of simulated events and is conceptually split into two phases as event generation and detector simulation

  - *Event Generation:* First, primary proton-proton (p-p) collisions are generated using PYTHIA [111], tuned to specific LHCb configurations. The decays of unstable particles, particularly B and D hadrons, are handled by EVTGEN [112], while final-state QED radiation is generated using PHOTOS [113].
  - *Detector Simulation:* The generated particles are then propagated through the detector material using the GEANT4 [114] toolkit. This step simulates physics interactions between the particles and the detector material. The output of GAUSS consists of Monte-Carlo (MC) truth information of particles and energy deposits left in the detector volumes.

- **Digitisation**: The `Boole` application bridges the gap between the simulation and what the actual detector hardware records. It converts the continuous energy deposits into discrete detector responses to mimic the real read-out electronics. This stage needs to account for electronic noise, dead or inefficient channels, cross-talk between neighbouring sensors, and *spill-over* events (signals left over from previous or subsequent bunch crossings).

- **Reconstruction & Selection**: Following digitisation, the data is passed to the `Moore` application, which handles both event reconstruction and the software trigger selection (from Run 3 onwards). During reconstruction, electronic signals are translated back into physical objects e.g. particle hits, tracks. This involves pattern recognition to find particle trajectories, Kalman filter algorithms to precisely determine momentum, and to locate primary p–p collision points and secondary decay vertices. `Moore` also aggregates data from the RICH, Calorimeter, and Muon systems to perform Particle Identification (PID), assigning probability likelihoods to each reconstructed track.

3.4.2 Digitisation of MightyPix

The digitisation of the MightyPix (MP) requires dedicated event model classes that are capable of simulating the full detector response chain, from the initial energy deposit to the final detector readout and clustering stage (See Fig. 3.22). This section describes the software architecture and data structures developed to support this process, ensuring a consistent and traceable link between simulated particles and reconstructed detector signals.

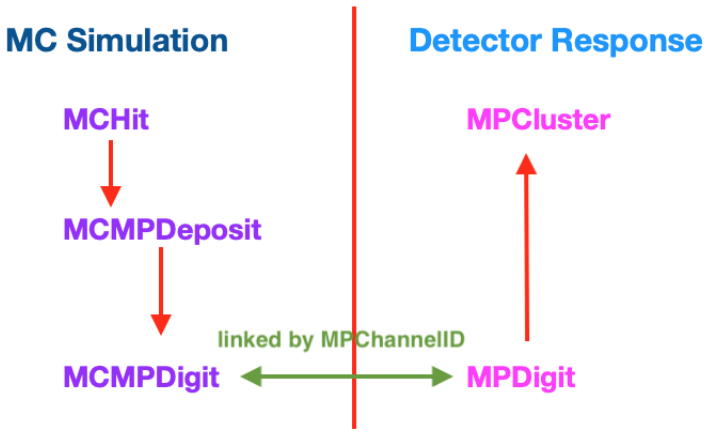


Figure 3.22: A diagram of the digitization chain of algorithms.

The first step in the digitisation chain is the recording of energy deposits produced by simulated MC particles traversing the detector. These deposits are represented by the `MCMPDeposit` class. Each `MCMPDeposit` object stores the originating MC hit (`MCHit`) with its three-dimensional (3D) coordinate (in the detector sector), the corresponding deposited charge, the associated MP channel identification (`MPChannelID`) and the time of the deposit. These objects are held in a *SmartRefVector* - storing only object references for memory management - to be passed onto `MCMPDigit` class. This structure ensures that MC hit information is preserved at the earliest stage of the simulation and transferred accurately to the next stages. To bridge the gap between individual energy deposits and the detector response, the `MCMPDigit` class acts as an intermediate MC truth container. It aggregates the spatial and temporal information of all `MCMPDeposit`s occurring within the same physical pixel channel during a given event, prior to the modelling of the detector electronics response.

A crucial aspect of the digitisation model is the association between MC truth information and the physical detector channels. This link is provided by the `MPChannelID` class which is built on top of `eLHCbID`, extending its functionality to overcome limitations of the standard `LHCbID`. While LHCbID provides 28 bits for channel encoding, the MT geometry requires 33 bits to fully describe its segmentation (see Tab. 3.2).

The detector electronics response is modelled by the `MPDigit` class, and this class simulates the response of the MP sensors. The algorithm operates on the list of `MCMPDigit` objects, and for each object above the sensor threshold (from detector

Table 3.2: Bit-packing allocation and hierarchy for the `MPChannelID` within the Mighty Tracker geometry.

Geometric Hierarchy Level	**Maximum Count**	**Bits Required**
Layer	6	**3 bits**
Module	28	**5 bits**
Ladder	20	**5 bits**
Sensor	14	**4 bits**
Column	116	**7 bits**
Row	320	**9 bits**
Total Channel Payload $3 + 5 + 5 + 4 + 7 + 9 = 33$		**33 bits**

calibrations bookkeeping), performs the electronics response modelling and conversion into final readout digits. For each `MCMPDigit` with a signal, a corresponding `MPDigit` object is produced. The `MPDigit` therefore represents the realistic detector output after sensor processing, including the effects encoded in the response model. The use of `MPChannelID` ensures that the produced digits retain a direct and traceable connection to both the detector geometry and the originating MC information.

The final stage of the digitisation chain is clustering. The `MPDigit` objects serve as input to a clustering algorithm, foreseen to be implemented in the `MPCluster` class. The purpose of clustering is to group neighbouring pixel hits and reconstruct spatial charge distributions while providing higher-level objects suitable for pattern recognition and tracking. Although the `MPDigit` and `MPCluster` classes are still under development, their roles in the digitisation sequence are clearly defined.

3.4.3 A Fast-Tracking Model in MightyPix (MP)

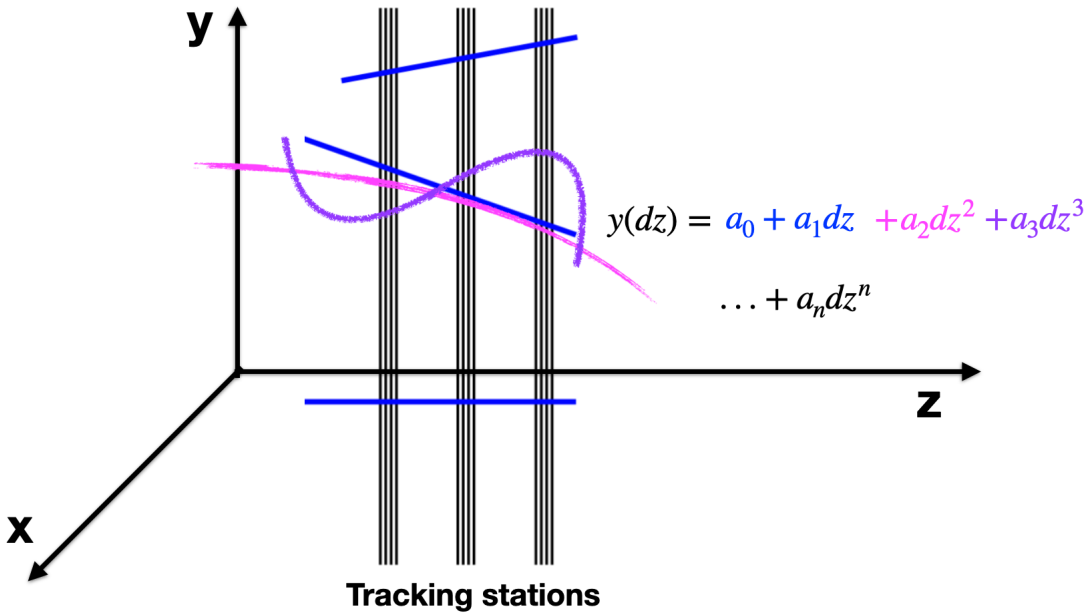


Figure 3.23: An illustrative sketch to show how polynomial function can be used for different track models using LHCb coordinate system where z is the direction of beam line, y is in the magnetic field direction and x is the bending plane with dz the distance of z to the the centre of the T station.

Following the development of the event model classes and dedicated monitoring algorithms, a fast and efficient track model was developed for preliminary tracking studies of MightyPix (MP) as an original work. The primary goal was to construct a computationally lightweight fitting procedure capable of providing reliable track parameter estimation while enabling detailed studies of parameter correlations and track fit quality.

The track model is formulated as a linear function in the fit parameters. A particle trajectory is approximated independently in the x–z and y–z planes using a polynomial expansion as shown in Fig. 3.23,

$$x(dz) = \sum_{k=0}^{n} a_k dz^k, \quad y(dz) = \sum_{k=0}^{n} b_k dz^k \tag{3.1}$$

where dz is $z - z_0$ and z_0 chosen as the centre of the T station (8500 mm), a_k and b_k are the fit parameters, n is adjustable depending on the required model complexity.

The optimal set of parameters is obtained by minimising a standard χ^2 function

$$\chi^2 = \sum_i \frac{(x_i - x(z_i))^2}{\sigma_i^2} \tag{3.2}$$

where i represents the number of measurements. Analogously similar expression for $y(z)$ can be written for tracks in $y-z$ plane independently from the track fitting in $x-z$ plane. Since the model is linear in the fit parameters, the minimisation leads to a system of linear equations

$$M\vec{p} = \vec{v} \tag{3.3}$$

where M is a matrix, p is the vector of fit parameters, v is constructed from the measurements. The matrix M is symmetric and positive definite by construction, properties that are exploited in the numerical solution. Several matrix decomposition techniques are available to solve the linear system. In this implementation, *Cholesky Decomposition* was chosen because it is numerically stable, fast and computationally efficient, and it exploits the symmetry of the matrix. The symmetric positive-definite matrix M is decomposed as $M = LL^T$ where L is a lower triangle matrix. To further optimise memory usage, the matrix is stored in packed form, keeping only one triangular half. This reduces memory consumption by a factor of two for each measurement.
Tracks are fitted separately in the two transverse planes using *cheated* tracks – omitting full track reconstruction step–, where MC truth information is used to associate the `MCParticle` objects directly with corresponding `MCHit` measurements. The resulting fit parameters are stored in tuples for detailed offline analysis.
This framework enables studies of:

- Diagnostics for fit quality i.e. dependence of χ^2 on model to compare different degrees of polynomial,
- Numerical results of track parameters for preliminary estimations which can be used in pattern recognition,
- Correlations between track parameters

3.4.3.1 An example case study

In this work, the maximum degree of polynomial n in Eq. 3.1 is chosen as 4 since the parametrisation is designed to retain physically meaningful coefficients such as intercept, slope, and curvature, while allowing extension to higher-order terms if required. The track fit algorithm ran over 10^4 events from a simulation sample of inclusive minimum-bias p–p collision data generated at Run 5 conditions within the MP geometrical acceptance. The χ^2 and χ^2 probability distributions are examined to assess statistical stability of the fit. The uniform χ^2 probability distributions shown in Fig. 3.24 demonstrate the statistical stability of the fits, confirming the absence of over-fitting or model deficiencies, and the absence of significant correlations in different planes confirms the consistency and independence of the fits. Furthermore, the Gaussian residuals centred around zero in both the $x-z$ and $y-z$ planes (Fig. 3.26) confirm that the reconstructed track parameters are unbiased. Correlations between track parameters are explored both within a single plane and across planes, and they are shown in Fig. 3.27, Fig. 3.28, Fig. 3.29 respectively. The numerical results from this track fit are reported in Tab. 3.3.

While evaluating a single fourth-degree polynomial model allows for an initial assessment of how higher-order coefficients contribute to the track geometry, a rigorous optimization of the tracking parametrisation requires systematically analysing fit quality metrics—such as the χ^2 probability distribution—as a function of the polynomial degree. This systematic approach identifies the configuration that yields an optimal balance between reconstruction accuracy and over-fitting. Consequently, this polynomial tracking framework serves as a fast, numerically robust, and flexible tool for preliminary MightyPix (MP) performance studies, offering clear diagnostics for interpreting geometric effects, model limitations, and parameter correlations.

Coefficient	μ_X	μ_Y
$a0$	-4.5962	-5.8582
$a1$	-0.0024	-6.4170e-04
$a2$	-5.6243e-07	1.6173e-08
$a3$	5.9154e-11	-1.0980e-10
$a4$	5.9259e-13	1.3907e-13

Table 3.3: Mean (μ) values of the track fit parameters for the $x-z$ and $y-z$ planes.

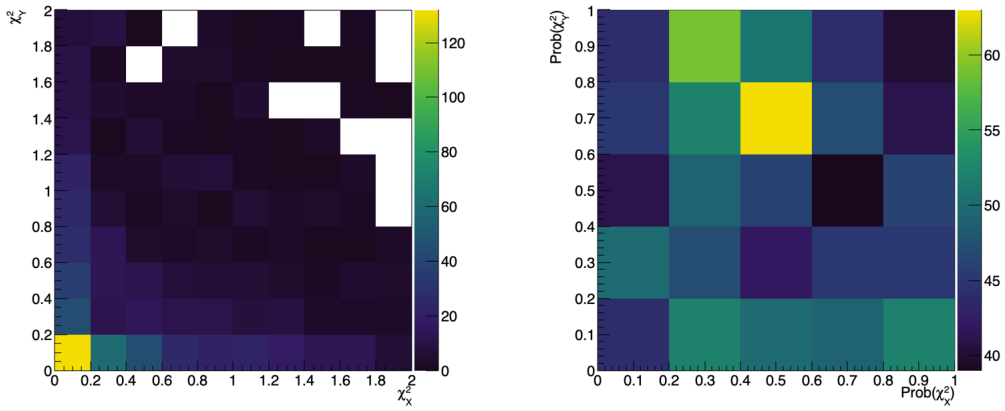


Figure 3.24: Correlations between χ^2_X, χ^2 distribution in the $x-z$ plane and χ^2_Y, χ^2 distribution in the $y-z$ plane; χ^2 probability distribution in the $x-z$ plane and in the $y-z$plane.

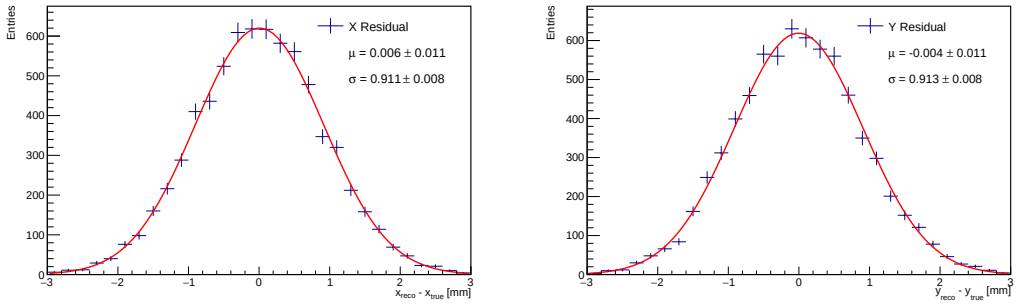


Figure 3.25: The residual distributions ($x_{reco} - x_{true}$) of tracks in the $x-z$ plane (left) and $y-z$ plane (right), fitted with Gaussian function reporting μ (mean) and σ (standard deviation).

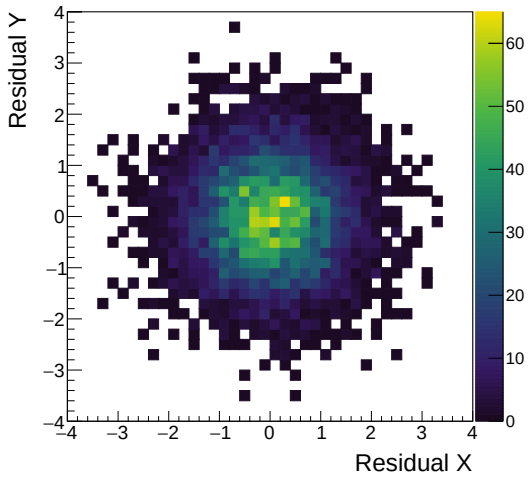


Figure 3.26: The correlation between the residual distributions in the x-z plane and in the y-z plane.

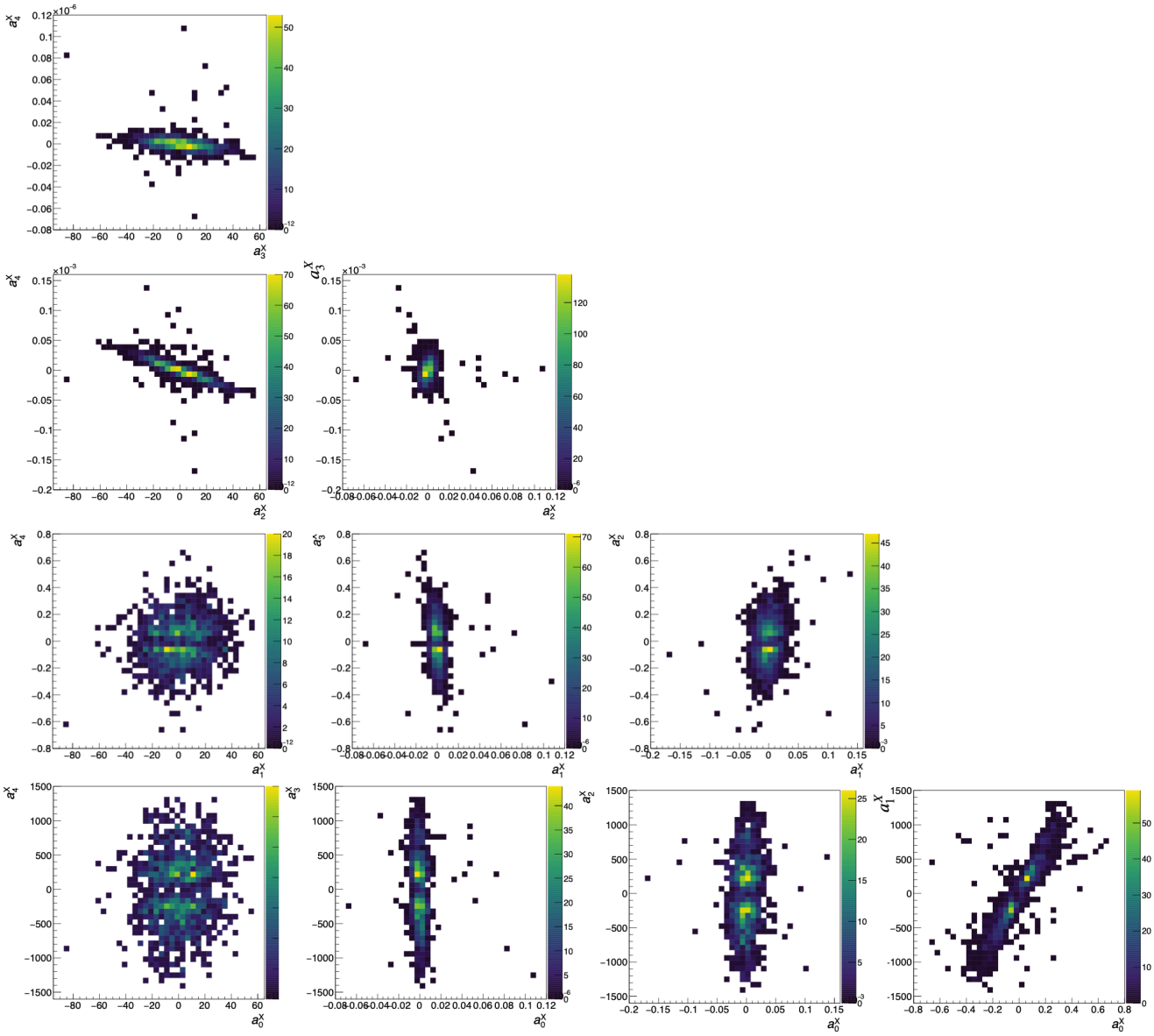


Figure 3.27: The correlation between track fit parameters in $x - z$ plane showing relation between different orders of contribution.

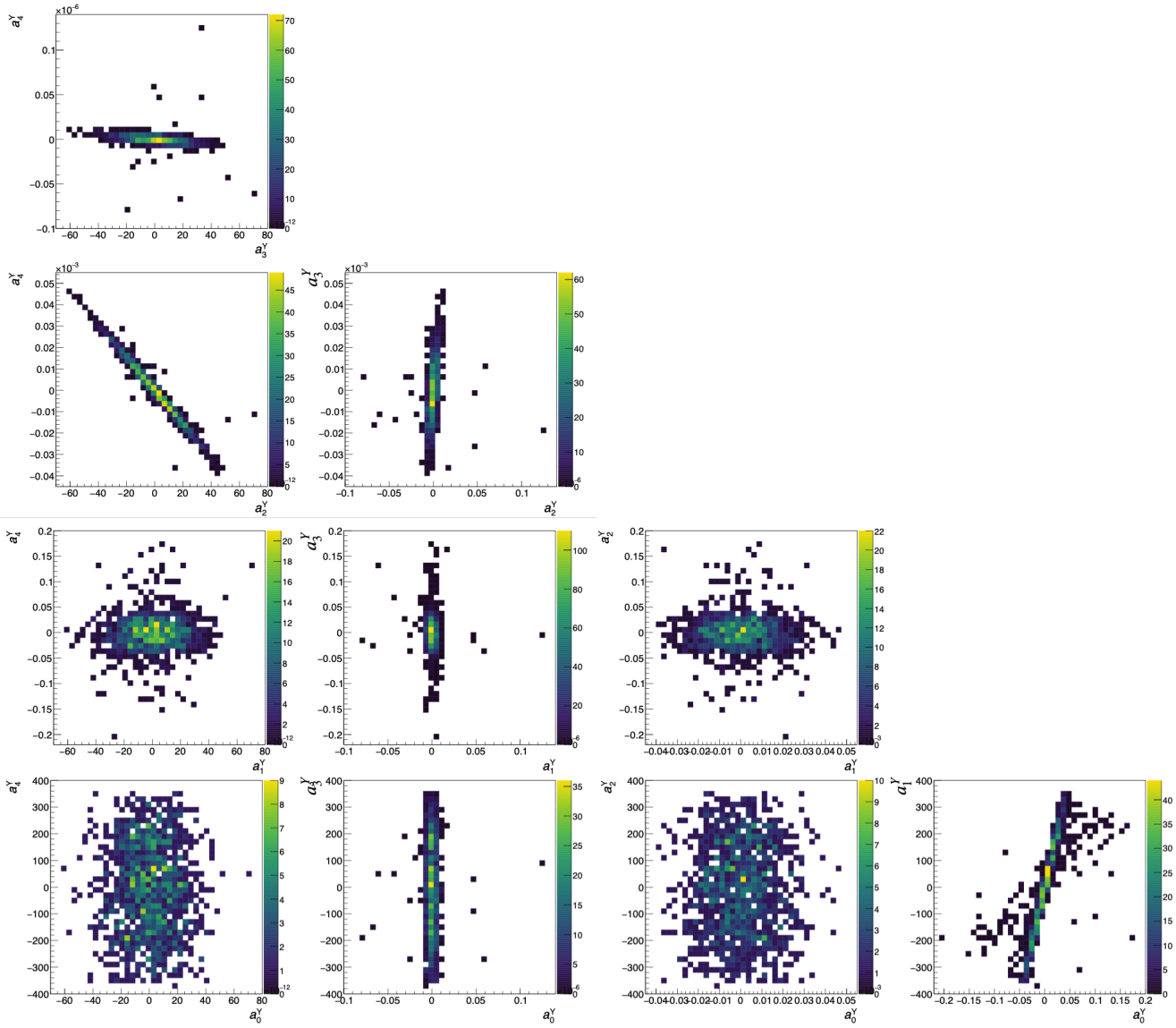


Figure 3.28: The correlation between track fit parameters in $y - z$ plane showing relation between different orders of contribution.

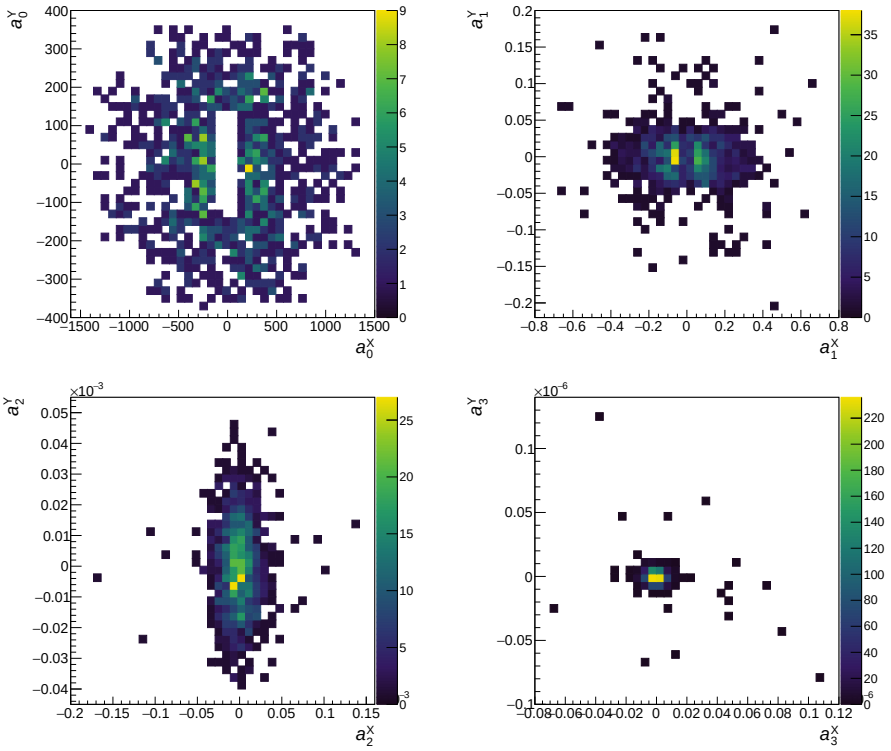


Figure 3.29: The correlation between same order terms of $x - z$ plane and $y - z$ plane.

Track fit parameter correlations in the $x - z$ plane

Correlation studies of the track fit parameters (a_n) indicate that in the $x - z$ plane, a quadratic polynomial with parameters –a_0, a_1, a_2– provides an optimal and sufficient description of the track geometry. If we explore the correlations between all combinations of available parameters in Fig. 3.27, we can iteratively evaluate terms ($a_0 \to a_1 \to a_2 \to a_3 \to a_4$) by assessing whether they form expected geometric pattern and their total spatial contribution across the tracking volume ($\Delta y = a_n \cdot dz^n$) exceeds a meaningful physical threshold defined by the 50 μm pixel width of MP sensors.

Let us start with base terms of the quadratic model –a_0, a_1, a_2– and explore relation between them. In this context, from Fig. 3.27, a strong linear correlation between the base parameters a_0 (intercept) and a_1 (slope) is observed, which is a mathematically expected consequence of the fundamental track trajectory. The second-degree coefficient, a_2 (curvature), also exhibits meaningful correlations with a_0 and a_1 in Fig. 3.27, confirming its necessary contribution for describing the track's parabolic deflection in the magnetic field. However, extending the fit to a higher-degree poly-

nomial may result in over-fitting. The correlations between the higher-order terms (a_3, a_4) and the base parameters generally show uniform, featureless distributions, indicating they provide no additional geometric information i.e. the plots of a_4 vs. $a_0(a_1)$ show uniform distribution whereas a_3 vs. $a_0(a_1, a_2)$ vertical line indicating a_3 is independent from rest of the parameters. While a negligible line-like correlation between a_2 and a_4 is observed, its magnitude ($\sim 10^{-12}$) is vanishingly small.

Track fit parameter correlations in the $y - z$ plane

In the $y - z$ plane, a simple linear model (a_0, a_1) seems adequate for track representation. To verify this by repeating same exercise done in $x - z$ plane, the relation between base terms $-a_0, a_1-$ is checked and it confirms that expected geometric pattern seen in Fig. 3.28; then, we iteratively evaluate the contribution of higher-order terms ($a_2 \rightarrow a_3 \rightarrow a_4$). In Fig. 3.28, the distributions of a_2 versus both a_0 and a_1 are uniform, signifying that a quadratic term does not contribute geometrically. Continuing to higher orders, a_3 and a_4 similarly demonstrate uniform distributions and complete independence from a_0 and a_1 as it can be seen from Fig. 3.28. This confirms that coefficients beyond a_1 lack physical meaning, proving that the linear parameters a_0 and a_1 are fully sufficient to describe the unbent $y - z$ plane tracks. While the $y - z$ plane tracks are fundamentally described by a linear model, two distinct correlation seen in the plots of a_4 vs. a_2 and a_0 vs. a_1 needs to be commented.

The diagonal correlation seen in the plot of a_4 vs. a_2 in Fig. 3.28 is not a physical phenomenon, but rather a mathematical artifact of the fitting procedure. When using a standard power basis (i.e. dz^n in Eq. 3.1) instead of orthogonal polynomials i.e. Chebyshev polynomials, the even-powered symmetric terms (z^2 and z^4) are naturally coupled. As the fitting algorithm minimises the residual noise, it is forced to algebraically trade off these coefficients against one another. If the fit slightly overestimates the curvature (a_2), it compensates by driving a_4 in the opposite direction.

In contrast to the numerical artifact above, the double-slope structure in the plot of a_0 vs. a_1 is a direct physical consequence of the detector geometry and track kinematics. In the $y - z$ plane, there is no magnetic deflection, meaning particles travel in straight lines originating from the primary collision vertex region near $z = 0$. Consequently, the spatial intercept (a_0) measured at a downstream reference plane is inherently tied to the track's slope (a_1). The visible double structure arises

from the geometric acceptance of the detector—specifically the split between the upper and lower modules of the tracking stations. Particles traversing the upper detector half ($+y$) exhibit positive slopes and positive intercept, while those in the lower half ($-y$) mirror this with negative slopes and intercepts, cleanly segregating the data into two distinct, physically correlated kinematic bands.

3.4.3.2 Summary and Outlook

The development of the MightyPix baseline digitisation and the associated polynomial fast-track reconstruction algorithm provides a crucial foundation for preliminary Mighty Tracker performance studies. Looking forward, the immediate next step is the integration of these stand-alone frameworks into the full LHCb simulation chain as the detector geometry is finalised. Ultimately, this work serves as the computational stepping stone for the high-performance tracking algorithms that will be strictly necessary to handle the extreme data-rate conditions of the HL-LHC.

Chapter 4

New physics search in $B^0 \to D^{*-}\mu^+\nu_\mu$

This chapter will give the overview of the New Physics search in $B^0 \to D^{*-}\mu^+\nu_\mu$ using Run 1 dataset while introducing the necessary tools to explore the full angular structure of the particular decay channel i.e. the reconstruction and re-weighting techniques. This chapter will also serve as the introduction of the analysis tools that is also used in Ch. 5, i.e. decay of $B^0 \to D^{*-}\mu^+\nu_\mu$ and its angular structure, selection strategy, sample compositions and background modelling.

4.1 An Overview

This measurement introduces a novel approach to measure New Physics (NP) contributions directly from the data, rather than deriving them in a subsequent phenomenological interpretation. This allows the experimental effects to be varied consistently with the NP contributions and form-factor parameters, reducing the model dependence of their determination. The analysis exploits the differential decay rate of $B^0 \to D^{*-}\mu^+\nu_\mu$ as formulated in Eq. 4.1, a function of the decay angles (See Fig. 2.6) and the squared momentum transferred to the lepton pair, q^2. This strategy maximises both the phenomenological consistency of the measured parameters and the sensitivity to NP interactions, while simultaneously improving the determination of the hadronic dynamics of the decay.

$$\frac{\mathrm{d}^4\Gamma(B^0 \to D^{*-}\ell^+\nu_\ell)}{\mathrm{d}q^2\,\mathrm{d}\cos\theta_\ell\,\mathrm{d}\cos\theta_{D^*}\,\mathrm{d}\chi} \propto |V_{cb}|^2 \sum_i H_i(q^2) f_i(\theta_\ell, \theta_{D^*}, \chi). \tag{4.1}$$

This decomposition originates from the effective Hamiltonian, $\mathcal{H}_{\text{eff}} = \sum_k C_k O_k$, where the short-distance interactions (including New Physics couplings) are encoded in the Wilson coefficients, C_k, and the long-distance hadronic dynamics in the operators, O_k (See section 2.3). The terms $f_i(\theta_\ell, \theta_{D^*}, \chi)$ act as a set of purely geometric angular basis functions, fixed by the spins of the initial and final state particles. The physical sensitivity to New Physics and hadronic form factors is contained entirely within the q^2-dependent coefficients, $H_i(q^2)$, which are constructed from the underlying helicity amplitudes. Because different effective operators (such as scalar or tensor interactions) project onto different helicity states, they dictate which angular basis functions contribute to the total decay rate and with what relative strength. Consequently, a simultaneous analysis of the full multi-dimensional angular distribution and the q^2 spectrum is required to disentangle New Physics couplings from the hadronic effects.

This analysis uses the Run 1 LHCb dataset, consisting of p–p collision data collected in 2011 and 2012, at the centre of mass energy of 7 TeV and 8 TeV respectively. In order to select the $B^0 \to D^*\ell\nu$, the D^* meson is reconstructed via the decay chain $D^{*+} \to D^0\pi^+$ and $D^0 \to K^-\pi^+$.
The kinematics of the process is characterized by the q^2 and the three angles defined and shown as in Fig. 2.6, and the m^2_{miss} variable is used for discriminating between signal and the backgrounds. The q^2 and m^2_{miss} are calculated as

$$q^2 = (p_B - p_{D^*})^2, \tag{4.2}$$

$$m^2_{miss} = (p_B - p_{D^*} - p_\mu)^2, \tag{4.3}$$

where p_B, p_{D^*} and p_μ are the four-momenta of the D^*, the B^0 and the μ.

Due to the neutrinos escaping detection at LHCb, the signal $B^0 \to D^*\mu\nu$ and the associated $B^0 \to D^*\tau\nu$ decays cannot be fully reconstructed. Instead, they must be selected inclusively from the class of decays with the visible final state $D^*\mu X$, where X represents any undetected particle combination. Because the B^0 meson momentum is only partially reconstructed, the missing mass squared, m^2_{miss} (defined in Eq. 4.3), serves as the primary kinematic discriminant. For the signal $B^0 \to D^*\mu\nu$ decay containing a single neutrino, m^2_{miss} peaks sharply at approximately zero. Conversely, the τ final state involves three neutrinos, resulting in a broad distribution that extends to large, positive m^2_{miss} values.

The inclusive nature of the $D^*\mu X$ selection naturally introduces substantial back-

ground contamination. This background composition can be broadly categorised into three main physical sources, each exhibiting characteristic kinematic distributions:

- **Feed-down from higher-mass states ($B \to D^{**}\mu\nu$):** This constitutes the dominant background. It occurs when a heavier D^{**} resonance decays to a D^*, emitting soft pions or photons that are not reconstructed. Because these undetected particles carry away momentum, this background mimics the signal topology but shifts towards higher m^2_{miss} values and softer muon momenta.
- **Double-charm decays ($B \to D^* D_{(s)} X$):** These processes mimic the signal when the second charm hadron decays semileptonically, or when one of its hadronic decay products is misidentified as a muon. While generally possessing larger missing mass than the signal, they form a significant high-m^2_{miss} tail in the data sample.
- **Combinatorial and Misidentification backgrounds:** These arise from random combinations of tracks that coincidentally form a D^* vertex (Wrong Sign –WS–), and from prompt hadrons (such as kaons or pions) that are falsely identified as muons (MisID).

To isolate the signal and suppress these distinct background components, the offline selection applies targeted topological, kinematic, and particle identification (PID) requirements. Geometric criteria, such as the flight distance significance (χ^2_{FD}) of the B and D^0 vertices, are heavily utilized to reject prompt combinatorial backgrounds originating directly from the primary vertex. Stringent PID requirements are placed on the muon candidate to drastically reduce the hadron-to-muon misidentification rate. Finally, to combat the dominant feed-down and double-charm backgrounds, isolation algorithms are employed. By vetoing candidates that possess additional charged tracks originating from the reconstructed B decay vertex [115], the selection efficiently suppresses background processes with higher track multiplicities while preserving a high signal efficiency. To extract the signal and the corresponding backgrounds, trigger, stripping and offline selections are applied as in Tables 4.1, 4.3, 4.5, respectively.

The D^0 is reconstructed using the K and π tracks originating from the same vertex and each of them satisfying the PID, momentum, and track properties (IP cuts); then D^0 is combined with soft pion candidates to form the D^* with $D^{*+} \to$

$D^0\pi^+$ decay imposing PID, track and vertex property cuts on D^0. The $D^{*+}\mu^-$ pair is formed with muon candidates passing `IsMuon` along with PID and momentum requirements. The specific momentum and transverse-momentum requirements for muon as $p > 6000$ MeV/c and $p_T > 1200$ MeV/c are imposed to remove most of the particles misidentified as muon, which most frequently have a momentum in the range of 3000 – 6000 MeV/c. The p_T requirement on the muon also helps reducing $B \to D^*DX$ and $B^0 \to D^*\tau\nu$ backgrounds. A mass cut on B^0 meson is applied to remove contributions of $B \to D^*DX$ and $B^0 \to D^*\tau\nu$ backgrounds.

The cut on D^0 and D^* mass is imposed to remove substantial amount of combinatorial background (See Fig. 4.1). This pair $D^{*+}\mu^+$ are random combinations of D^* with muon tracks coming from other decays in the event and $D^0\ \pi^+\mu^+$ consisting of random combinations of D^0 and pions in the event. Another important variable to separate signal from the combinatorial is the impact parameter (IP), $\log(\mathrm{IP}_{D^0}) >$ -3.5 and $\mathrm{IP}^2_\chi > 9$ cuts are imposed on D^0. The wrong sign events distribution presents a double peak structure, depending on whether D^0 meson points back to the PV (prompt) whereas the same structure but with a reduced prompt component is seen for the right sign events (See Fig. 5.2). Therefore the cut on $\log(\mathrm{IP}_{D^0}) >$ -3.5 helps reducing likely contribution from wrong sign samples to the right sign samples.

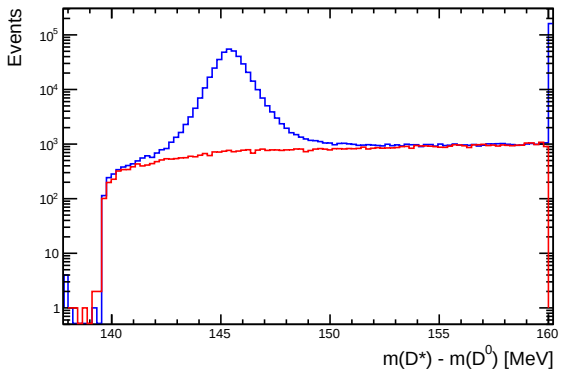


Figure 4.1: $m(D^*) - m(D^0)$ distribution for the signal candidates of $D^{*+}\mu^-$ (blue) and the wrong sign $D^0\pi^+\mu^+$ candidates (red). A cut is placed in the offline selection at $m(D^*) - m(D^0) < 147$ and > 144 MeV.

This analysis makes use of a five-dimensional fit to the three angles (Fig. 2.6), q^2 and m^2_{miss} to determine the data sample composition and measure the effective New Physics (NP) Wilson coefficients and the hadronic form factors parameters.

To account for neutrinos not being detected at LHCb a technique to evaluate the reconstructed variables used in fitting is presented in section 4.2.

The signal can be re-weighted to a particular NP scenario using the HAMMER software, which allows measuring NP or SM effects. The re-weighting process is explained in section 4.3. All the background components modelled in this analysis can be seen along with signal in Tab. 4.12.

In order to understand the selection lines listed in the selection tables, the following information is provided where everywhere in the list PV stands for a primary vertex and SV for secondary vertex:

- **IP**: Distance of the particle track to the primary vertex.
- $\boldsymbol{\chi^2_{\text{IP}}}$: Difference between the χ^2 of the PV reconstructed with and without the track IP under consideration.
- $\boldsymbol{\chi^2_{\text{track}}}$: χ^2 of the track, calculated through the difference between measured track coordinates and the fitting model.
- $\boldsymbol{\chi^2_{\text{track}}}$/ndf: χ^2 divided by the degrees of freedom of the track fit.
- $\boldsymbol{\chi^2_{\text{vertex}}}$/ndf: χ^2 of the vertex calculated during vertex fitting. The vertex can refer to a PV or a decay vertex of the corresponding particle.
- **PV/ndf**: number of degree of freedom in fit to PV.
- **FD**: Flight distance — the distance between the primary vertex and the particle decay.
- $\boldsymbol{\chi^2_{\text{FD}}}$: Flight distance significance — the significance of the particle's flight distance (separation between the decay vertex and its associated primary vertex), expressed as

$$\chi^2_{\text{FD}} = \Delta\mathbf{x}^T \left(C_{\text{DV}} + C_{\text{PV}}\right)^{-1} \Delta\mathbf{x}, \quad \text{with } \Delta\mathbf{x} = \mathbf{x}_{\text{DV}} - \mathbf{x}_{\text{PV}},$$

  where $\mathbf{x}_{\text{DV}}$ and $\mathbf{x}_{\text{PV}}$ are the vertex positions and C_{DV} and C_{PV} are their covariance matrices, with correlations between the two vertex estimates neglected. Larger values indicate a more significant flight distance from the PV.
- **GEC**: The Global Event Cut is a selection requirement applied in the trigger system to remove time-consuming events in reconstruction.

- **nSPDhits**: Number of hits in the SPD detector. This variable is used in the GEC selection cuts to reduce event complexity.
- **nPV**: Number of primary vertices.
- **isMuon**: Boolean flag from the "IsMuon" algorithm indicating muon identification, and the requirements can be seen in Tab. 4.4.
- **GhostProb**: A multivariate classifier using kinematic and reconstruction variables to identify ghost (fake) tracks.
- **DLL**x: A particle identification variable equal to the difference in the log-likelihood (DLL) under the hypothesis of particle type x with respect to the particle type π.
- **DOCA** : Distance of the closest approach between two tracks.
- **ProbNN**: A multivariate variable combining tracking and PID information into a single probability value for each particle hypothesis.
- **DIRA**: Angle between the line from the PV to the SV of the particle and the sum of the decay product momenta.
- **nTracks**: Total number of tracks in the event.
- $\langle \boldsymbol{m} \rangle$: Mass of the particle according to the value given in the PDG.
- **Triggered on signal (TOS)**: a positive trigger decision using information from the signal candidate alone.
- **Trigger Independently of Signal (TIS)**: a positive trigger decision using information exclusively from the rest of the event.
- **Trigger on both (TOB)**: a positive trigger decision using the information from the entire event, allowing to have a mixture of signal and non signal information.

Variable	Selection
`B_L0Global_TIS or Dst_L0HadronDecision_TOS`	
`Hlt2CharmHadD02HH_D02KPi`	TOS
`Hlt1TrackAllL0` (K or π)	TOS

Table 4.1: Trigger selection.

Variable	`Hlt2CharmHadD02HH_D02KPi`
χ^2_{track}/ndf	< 3
Track p_t [MeV]	> 800
Track p [MeV]	> 5000
> 1 Track p_t [MeV]	> 1500
χ^2_{vertex}/ndf	< 10
$FD\chi^2$	> 40
DIRA	> 0.99985
D p_t [MeV]	> 2000
D mass interval [MeV]	1815-1915

Table 4.2: Selection for the `Hlt2CharmHadD02HH_D02KPi` trigger line.

Event Level Cuts	Variable	Selection
GEC	nSPDhits	< 600
PV cut	nPV	> 0
Particle cuts	Variable	Selection
μ	isMuon	True
	$IP\chi^2$	> 45
	GhostProb	< 0.5
	PIDμ	> 2
	p	> 3 GeV
K, π	p_t	> 300 MeV
	$IP\chi^2$	> 2 GeV
	isMuon	False
	DLLK	> 4(K), $< 2(\pi)$
	GhostProb	< 0.5
D^0	$\lvert p_t(\pi)\rvert + \lvert p_t(K)\rvert$	> 1.4 GeV
	χ^2_{fit}/DOF	< 4
	DIRA	> 0.9998
	FDχ^2	> 250
	m - $< m >$	< 80 MeV
B	m	< 10 GeV
	χ^2_{fit}/DOF	< 6
	DIRA	> 0.9995

Table 4.3: Stripping selection.

p_{track} [GeV]	Hits in muon stations
3 - 6	M2, M3
6 - 10	M2, M3 and M4 or M5
>10	M2, M3, M4, M5

Table 4.4: `IsMuon` algorithm hit requirements in the muon stations based on the momentum of the particle track.

Particle	Variable	Selection
K	p_t	$>$ 800 MeV
	p	$>$ 3000 MeV
	$IP\chi^2$	$>$ 45
	DLLk	$>$ 4
π	p_t	$>$ 1200 MeV
	p	$>$ 3000 MeV
	$IP\chi^2$	$>$ 45
	DLLk	$<$ 2
D^0	p_t	$>$ 2000 MeV
	$\log(D^0 IP)$	$>$ -3.5
	$IP\chi^2$	$>$ 9
	mass interval	1845 - 1890 MeV
μ	p	$>$ 6000 MeV
	p_T	$>$ 1200 MeV
	DLLmu	$>$ 2
	$m(D^*) - m(D^0)$	147 MeV
	$m(B)$	2500-5200 MeV
	B Isolation BDT	$<$ 0.15

Table 4.5: Offline selection.

4.2 Neutrino reconstruction

With the signal decay $B^0 \to D^*\mu\nu$ having one neutrino that escapes the LHCb detection, B^0 meson momentum cannot be reconstructed fully and, there are two approaches used in this analysis to estimate B^0 momentum: One is constructing an approximate rest frame for the B meson, and second is solving a full quadratic equation then, choosing a random solution. Therefore, the resolution of the fit variables depending on B^0 momentum will be affected by the approach and we need to account for it. These two approaches are presented and their resolutions are

compared here. The B rest frame approach is used for calculating the m^2_{miss} fitting variable and the second one is used to calculate the rest of four fitting variables.

4.2.1 Approximate B rest frame

An approximate rest frame for the B meson is constructed assuming that the proper velocity of the part of the decay that is detected (D^*l referred as Y) along the z-axis is equal to the proper velocity of the B meson along the same axis.

$$p_z^B = \frac{m_B}{m_Y} p_z^Y. \tag{4.4}$$

The vector that defines the B momentum direction can be constructed from the position of the primary and the secondary vertex

$$p_{\mathrm{B_{dir}}} = \mathrm{SV(position)} - \mathrm{PV(position)}. \tag{4.5}$$

The angles of the direction vector with each of the x, y and z axis can be calculated

$$\cos(\alpha_{\mathrm{x}}) = \mathrm{p_{xB_{dir}}}/|\mathrm{p_{B_{dir}}}|, \tag{4.6}$$
$$\cos(\alpha_{\mathrm{y}}) = \mathrm{p_{yB_{dir}}}/|\mathrm{p_{B_{dir}}}|, \tag{4.7}$$
$$\cos(\alpha_{\mathrm{z}}) = \mathrm{p_{zB_{dir}}}/|\mathrm{p_{B_{dir}}}|. \tag{4.8}$$

These angles can be used to compute the reconstructed components of the B momentum. Using this geometry the magnitude of the B momentum is given by the formula

$$|p_B| = \frac{m_B}{m_Y} p_z^Y \sqrt{1 + \tan^2(\alpha_z)}. \tag{4.9}$$

Using Eq. 4.9 and Eqs. 4.6 - 4.8 the components of the reconstructed B momentum are given as

$$p_x = \cos(\alpha_{\mathrm{x}})|\mathrm{p_B}|, \tag{4.10}$$
$$p_y = \cos(\alpha_{\mathrm{y}})|\mathrm{p_B}|, \tag{4.11}$$
$$p_z = \cos(\alpha_{\mathrm{z}})|\mathrm{p_B}|. \tag{4.12}$$

4.2.2 Full quadratic equation

The kinematic properties of decays with single unreconstructed particle can be reconstructed via solving a quadratic equation for the components of the B momentum. We decompose the visible momentum (D^*l) into components transverse and along the flight vector of the B meson ($p^{\perp}_{D^*l}$ and $p^{\parallel}_{D^*l}$). With an assumption of the single massless unreconstructed particle for the B meson final state we can derive the quadratic equation in $p^{\parallel}_{miss}$ as:

$$p^{\parallel}_{miss} = -a \pm \sqrt{r} \tag{4.13}$$

where

$$a = \frac{p^{\parallel}_{D^*l}(m^2 - m^2_{D^*l} - 2(p^{\perp}_{D^*l})^2)}{2((p^{\perp}_{D^*l})^2 - E^2_{vis})} \tag{4.14}$$

$$r = \frac{E^{\parallel}_{D^*l}(m^2 - m^2_{D^*l} - 2(p^{\perp}_{D^*l})^2)}{4((p^{\perp}_{D^*l})^2 - E^2_{vis})^2} + \frac{(E_{D^*l}p^{\perp}_{D^*l})^2}{(p^{\perp}_{D^*l})^2 - E^2_{vis}} \tag{4.15}$$

By defining the axis of the B meson flight direction as the vector connecting the primary and secondary vertices, the perpendicular component of the B meson momentum is, by definition, zero ($p^{\perp}_B = 0$). Consequently, the transverse momentum of the missing neutrino must exactly balance the transverse momentum of the visible $D^*\ell$ system ($p^{\perp}_{\nu} = p^{\perp}_{D^*\ell}$). The total momentum of the B meson is therefore entirely longitudinal along its flight axis. Enforcing the nominal B meson mass constraint yields a quadratic equation for this parallel momentum, which provides two possible mathematical solutions:

$$p^+ = p^{\parallel}_{D^*\ell} - a + \sqrt{r}, \tag{4.16}$$

$$p^- = p^{\parallel}_{D^*\ell} - a - \sqrt{r}. \tag{4.17}$$

Generically, one of these solutions is chosen randomly to resolve the ambiguity.

With the estimate of B momentum using the two approaches, the variables of interest are calculated: θ_l, θ_d, χ and q^2. The results for the three angles and the q^2 are shown on Fig. 4.2. It can be seen that quadratic approach yields a better resolution in θ_l and χ. In order to benefit from the better resolution, the second approach is chosen for the calculation of angles and the q^2 variable.

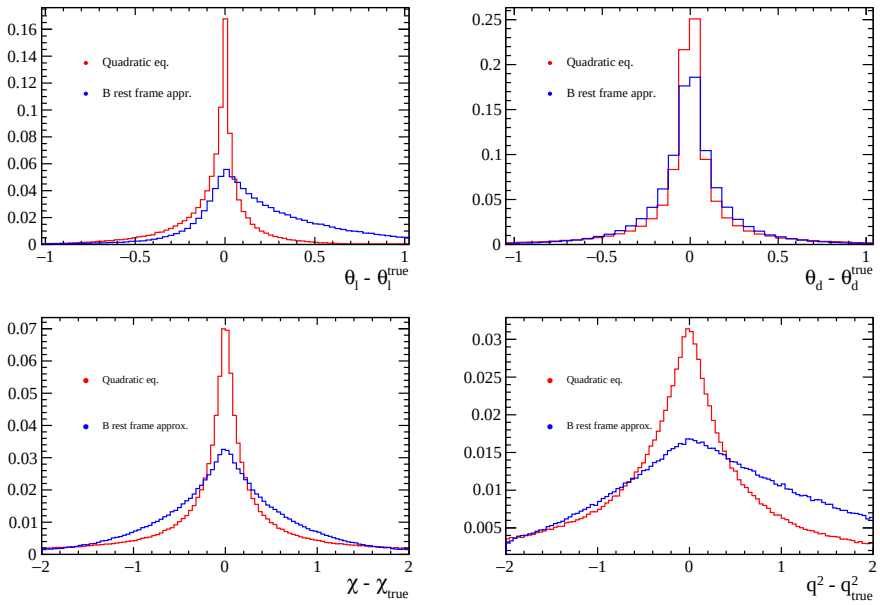


Figure 4.2: Resolution of θ_l (top left), θ_d (top right), χ (bottom left) and q^2 (bottom right) for two types of neutrino reconstruction. The quadratic equation approach (red) and B rest frame approximation (blue) are compared. The quadratic approach yields a better resolution in the θ_l and χ.

To be noted is that there are cases when the solution of the equation is negative (Eq. 4.15) which arise from events that are poorly reconstructed. In this case it is not possible to evaluate Eqs. 4.16 and 4.17 and therefore we impose $r = 0.0$ in order to obtain unique solution. In Fig. 4.3 the resolution of the variables is compared for the case when we exclude the events where the solution is negative. We observe no significant difference as compared to the current approach.

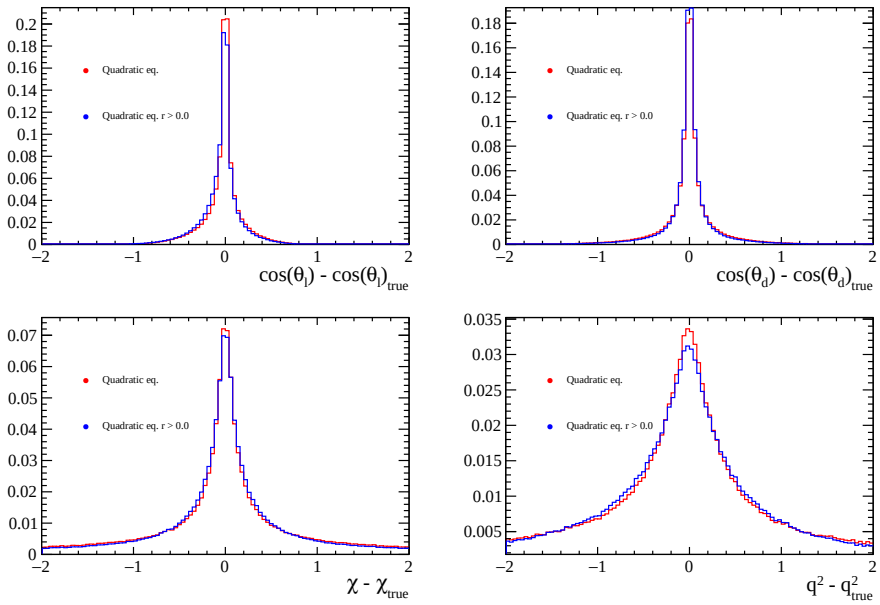


Figure 4.3: Resolution of θ_l (top left), θ_d (top right), χ (bottom left) and q^2 (bottom right) for the two cases when the events with $r = 0.0$ are accepted (red) and discarded (blue).

4.3 Reweighting for different form factor parametrisations and/or New Physics

This analysis performs the first measurement of the Wilson coefficients for New Physics scenarios and therefore relies on producing Monte Carlo (MC) templates that are used in the fits to extract these theoretically defined parameters. The fitting procedure uses histograms of the fit variables that are sensitive to a specific theoretical model that introduces NP. The NP couplings modify the templates for the signal and possibly the background distributions. In order to have a consistent interpretation of NP in data, for each NP Wilson coefficient considered dedicated MC samples are required for each model. Therefore the MC samples with different models need to be generated many times to try to account for all the possible models which is computationally expensive. A smart solution for these difficulties is the HAMMER (Helicity Amplitude Module for Matrix Element Reweighting) library [116], which incorporates a specific reweighting procedure that can be applied to any large MC sample to any NP model. The reweighting is done by using tensorial calculations and introduces a NP scenario to the samples by assigning them a

certain operator contracted with a corresponding Wilson coefficient (See Eq. 2.51 for definitions of Wilson coefficients). It can also be interfaced to any analysis framework giving the analyst control over the type of NP and the hadronic form factor parametrization. The reweighting can be used in a form of event weights or a set of variables can be reweighted in a form of histogram. Using HAMMER we are able to produce templates for different NP theoretical model for semi-leptonic b-hadron decays and use them further in the fitting procedure. In this section an overview of the reweighting procedure is given.

Let us consider a MC sample that consists of events (indexed by i), weights (w_i) and truth-level kinematics q_i. We would like to reweight this sample from an 'old' theory to a 'new' theory that results in a new differential rate. We can define the ratio of the 'old' and 'new' decay rate as

$$r_i = \frac{d\Gamma_i^{\text{new}}/dPS}{d\Gamma_i^{\text{old}}/dPS}, \tag{4.18}$$

where Γ is the decay rate and PS is denoted as phase space. The value of this ratio is used to apply the mapping of the weight as $w_i \mapsto r_i w_i$. The 'old' or the input theory is normally the SM, which is tied with a certain form factor parametrization. The 'new' rate consists of a theory that involves NP, a different hadronic model or a combination of both. The HAMMER software is able to perform reweighting of processes that can be explained with a theory, where the Lagrangian can be specified as a sum of SM and NP operators which is given as

$$\mathcal{L} = \sum_i c_i \mathcal{O}_i, \tag{4.19}$$

where $\mathcal{O}_i$ are the basis of operators and c_i are the Wilson coefficients of the SM and the NP.

The NP operators and coupling conventions that can be used in HAMMER are given in Table 4.6. The amplitude of each of these processes can be written in a tensorial form as

$$M(q) = \sum_{\alpha,i} c_\alpha F_i(q) A_{\alpha i}(q) \tag{4.20}$$

where F_i stands for the form factors and $A_{\alpha i}$ is the NP amplitude tensor. The

Current	WC tag	WC	4-Fermi/$(i2\sqrt{2}V_{cb}G_F)$
SM	SM	1	$[\bar{c}\gamma^\mu P_L b][\bar{l}\gamma_\mu P_L \nu]$
Vector	${}^*V_{\mathrm{qLlL}}$	$\chi_L^V \lambda_L^V$	$[\bar{c}\chi_L^V\gamma^\mu P_L b][\bar{l}\lambda_L^V\gamma_\mu P_L\nu]$
Vector	${}^*V_{\mathrm{qRlL}}$	$\chi_R^V \lambda_L^V$	$[\bar{c}\chi_R^V\gamma^\mu P_R b][\bar{l}\lambda_L^V\gamma_\mu P_L\nu]$
Vector	V_{qLlR}	$\chi_L^V \lambda_R^V$	$[\bar{c}\chi_L^V\gamma^\mu P_L b][\bar{l}\lambda_R^V\gamma_\mu P_R\nu]$
Vector	V_{qRlR}	$\chi_R^V \lambda_R^V$	$[\bar{c}\chi_R^V\gamma^\mu P_R b][\bar{l}\lambda_R^V\gamma_\mu P_R\nu]$
Scalar	${}^*S_{\mathrm{qLlL}}$	$\chi_L^S \lambda_L^S$	$[\bar{c}\chi_L^S\gamma^\mu P_L b][\bar{l}\lambda_L^S\gamma_\mu P_L\nu]$
Scalar	${}^*S_{\mathrm{qRlL}}$	$\chi_R^S \lambda_L^V$	$[\bar{c}\chi_R^V\gamma^\mu P_R b][\bar{l}\lambda_L^S\gamma_\mu P_L\nu]$
Scalar	S_{qLlR}	$\chi_L^S \lambda_R^s$	$[\bar{c}\chi_L^S\gamma^\mu P_L b][\bar{l}\lambda_R^S\gamma_\mu P_R\nu]$
Scalar	S_{qRlR}	$\chi_R^S \lambda_R^S$	$[\bar{c}\chi_R^V\gamma^\mu P_R b][\bar{l}\lambda_R^S\gamma_\mu P_R\nu]$
Tensor	${}^*T_{\mathrm{qLlL}}$	$\chi_L^T \lambda_L^s$	$[\bar{c}\chi_L^T\gamma^\mu P_L b][\bar{l}\lambda_L^S\gamma_\mu P_L\nu]$
Tensor	S_{qRlR}	$\chi_R^T \lambda_R^T$	$[\bar{c}\chi_R^V\gamma^\mu P_R b][\bar{l}\lambda_R^S\gamma_\mu P_R\nu]$

Table 4.6: NP operator basis and coupling conventions as given in HAMMER. The lower index of λ denotes the helicity of the neutrino and the lower index of χ is the helicity of the b quark. The Wilson coefficients considered in this analysis are marked with (*).

differential rate can be written now as

$$\frac{d\Gamma}{dPS} = \sum_{\alpha,i,\beta,j} c_\alpha c_\beta^\dagger F_i F_j^\dagger(q) A_{\alpha i} A_{\beta i}^\dagger(q) \tag{4.21}$$

$$= \sum_{\alpha,i,\beta,j} c_\alpha c_\beta^\dagger F_i F_j^\dagger(q) W_{\alpha i\beta j} \tag{4.22}$$

The weight tensor is defined as the product of the amplitude

$$W = AA^\dagger \tag{4.23}$$

and the object $\sum_{ij} F_i F_j^\dagger W_{\alpha i\beta j}$ is independent of the Wilson coefficients and it can be contracted with a choice of NP to generate an event weight. In a general region of phase space the rate can be written as

$$\Gamma_\Omega^s = \sum_{\alpha,\beta} c_\alpha c_\beta^\dagger \int_\Omega dPS \sum_{ij} F_i F_j^\dagger(q) W_{\alpha i\beta j}(q) \tag{4.24}$$

This integral generates a NP-generalized tensor and once computed can be con-

tracted with any choice of Wilson coefficients. In this way HAMMER provides efficient reweighting by computing the NP and FFs generalized objects and contracting them after with the NP and form factor choice to calculate the event weight. In this analysis we fit for the Wilson coefficients with left handed neutrinos only, marked with (*) in Table 4.6.
Beside the variation of the Wilson coefficients the variation in the form factor parametrization is also generalized in HAMMER. The form factor parametrization having a parameter set μ can be linearized around a best-fit point μ^0 so that

$$F_i(q,\mu) = F_i(q,\mu^0) + \sum_a F'_{ia}(q,\mu)e_a \tag{4.25}$$

where a represents the indices that can be varied and the variation is e_a. The function $F'_{i,a}$ can also be considered as the perturbation of F_i in e_a. The above equation can also be rewritten in the form

$$\sum_a \zeta_a \Phi_{i,a} = F_i + \sum_{a'} F'_{ia'} e_{a'} \tag{4.26}$$

with vectors $\zeta_a \equiv (1, e_a)$ and $\Phi_{i,a+1} \equiv (F_i, F'_{i,a})$. Using this the differential decay rate becomes

$$\frac{d\Gamma^s}{dPS} = \sum_{\alpha,a,\beta,b} c_\alpha c_{\beta\dagger} \zeta_a \zeta_b^\dagger \mathcal{U}^s_{\alpha a \beta b} \tag{4.27}$$

$$\mathcal{U}^s_{a\alpha b\beta} \equiv \sum_{ij} \Phi_{ia} \Phi^\dagger_{jb}(q) W^s_{\alpha i \beta j}(q) \tag{4.28}$$

where $\mathcal{U}$ is the weight tensor generalized for the FFs and the NP. Therefore the integral in any part of the phase space, Ω, is

$$\Gamma^s_\Omega = \sum_{a,\alpha,b,\beta} c_\alpha c^\dagger_\beta \zeta_a \zeta_b^\dagger \int_\Omega \mathcal{U}_{a\alpha b\beta} dPS. \tag{4.29}$$

The amplitude tensor can be written with the Wilson coefficients and the FF linearisation which can be contracted with the choice of NP of FFs with ζ_a representing the FF uncertainties or FF eigenvectors. If we have a case when an overall ratio of rates needs to be computed $\Gamma^{\text{old}}/\Gamma^{\text{new}}$, HAMMER needs to compute the two

different rates. In that case the generalized tensor for the weight looks like

$$\frac{d\Gamma^{\text{new}}dPS}{dPS} \Big/ \frac{d\Gamma^{\text{old}}dPS}{dPS}, \tag{4.30}$$

with the denominator having no NP and FF variation. The NP and FF rate tensors $\Gamma^{\text{old,new}}$ should be computed once for each sample and in general these require integration over the whole phase space.
The weights generated with the procedure described are produced per event for the input process that is specified in the initialization. The initialization refers to the input FF parametrization, which corresponds to the FF parametrization that was used to simulate the sample that needs to be reweighted. During the reweighting process HAMMER also permits performing calculations with the resulting NP and FF weight tensors. These usually are connected to different binning to integrate the phase space and as well as adding some detector simulation effects. The histograms that can be generated this way have NP and FF generalized tensors as bin entries. After storing these objects contraction with NP and FF generates the event weights or the histogram bin weights. HAMMER provides an interface to save and reload any weight tensor or weighted histogram to allow for quicker reprocessing the weights for the new theory.

4.4 Sensitivity to New Physics scenarios

Using the HAMMER software different physics scenarios that contain different operators in effective Hamiltonian (See Eq. 2.53) are introduced. Table 4.6 shows the possible New Physics operators that can be obtained from HAMMER. Visualising the change in the signal template assuming different values of the Wilson coefficients provides information on the sensitivity we have to the specific Wilson coefficient or Wilson coefficient combination. Based on that the effect of several NP scenarios on the signal template using the BLPR form factor parametrisation is presented. The templates are plotted for a number of values in the range [-1.0, 1.0] for the real part of the Wilson coefficient. The fit performed on data allows to vary the Wilson coefficients in the range [-1.0, 1.0] which is justified by several theory papers which predict the values of the NP Wilson coefficients [35], [33], [79]. The analysis in this thesis estimates the size of NP using only the information based on the shape of the fitting variables.

4.4.1 Vector operator

The vector operator is defined as

$$[\bar{c}\chi^V_{\mathrm{L,R}}\gamma^\mu P_{L,R}b][\bar{l}\lambda^V_{\mathrm{L,R}}\gamma_\mu P_{\mathrm{L,R}}\nu] \tag{4.31}$$

where χ^i_j and λ^i_j are the NP couplings to the quark and lepton currents, which can be complex numbers. The lower index of λ denotes the ν helicity and the lower index of χ is the helicity of the b quark, both can be of left or right. In the case of the decay $B^0 \to D^*\mu\nu$, first we are interested in the right handed b quark and the left handed neutrinos in both the real and imaginary part of the operator. We use V_{qRlL} as the notation for this and respectively for the rest of the NP operators. Fig. 4.4 shows the sensitivity of the signal template when it is reweighted with a specific value of the real part of the V_{qRlL} Wilson coefficient.

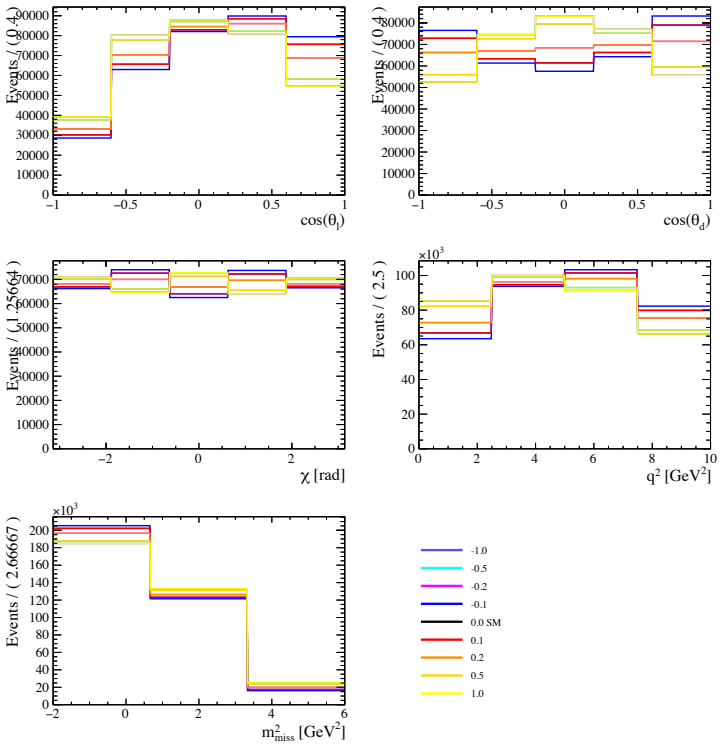


Figure 4.4: Plots of distribution of the fitting variables for values in the range [-1.0, 1.0] for the real part of the right handed vector operator.

The variation in shape is the most prominent for the three angles and the q^2. The variable m^2_{miss} is not expected to be sensitive to these variations. It is included in the fit due to its powerful signal to background discrimination and not to enhance the NP sensitivity. The shape of the rest of the variables deviates the most at the edges of the [-0.5, 0.5] interval, for the large values of the Wilson coefficients. The shape variations are smaller for the lower values of coefficients. This is significant enough to be able to proceed into one of the fitting configurations. Similarly the variation in the fitting variables is observed for the imaginary part of V_{qRlL}, shown on Fig. 4.5.

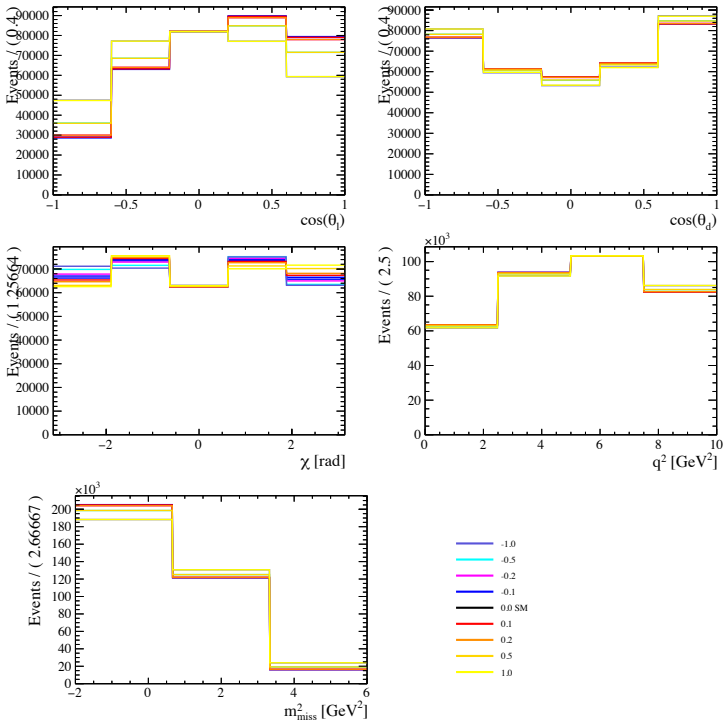


Figure 4.5: Plots of distribution of the fitting variables for values in the range [-1.0, 1.0] for the imaginary part of the right handed vector operator.

4.4.2 Tensor operator

The tensor operator is defined as

$$[\bar{c}\chi^T_{\mathrm{L,R}}\sigma^{\mu\nu}P_{\mathrm{L,R}}b][\bar{l}\lambda^T_{\mathrm{L,R}}\sigma_{\mu\nu}P_{\mathrm{L,R}}\nu], \tag{4.32}$$

where $\sigma^{\mu\nu} = \frac{i}{2}[\gamma^\mu, \gamma^\nu]$. The fit variables show a sizeable variation (shown in Fig. 4.6 and Fig. 4.7), which is measured in one of the fit configurations later.

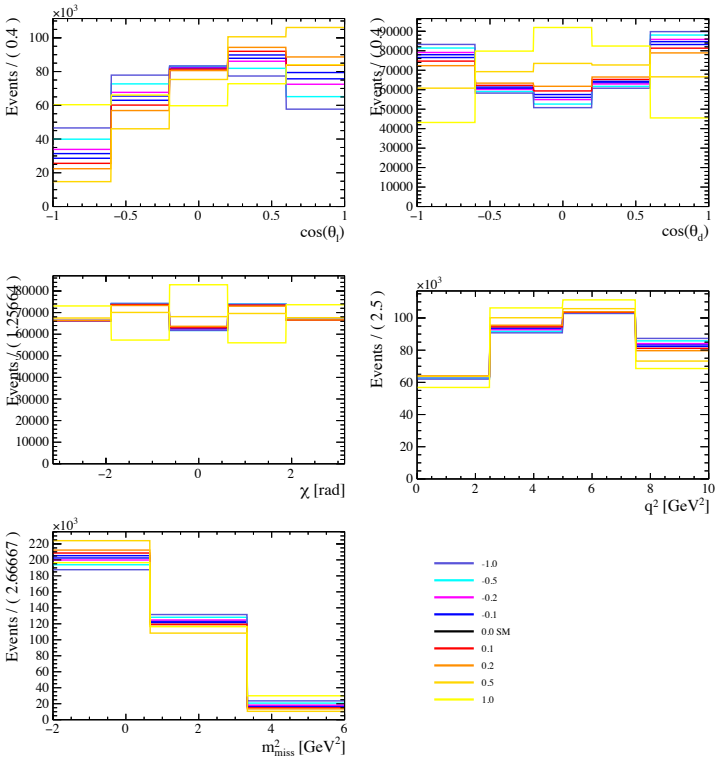


Figure 4.6: Plots of distribution of the fitting variables for values in the range [-1.0, 1.0] for the real part of the left handed tensor operator.

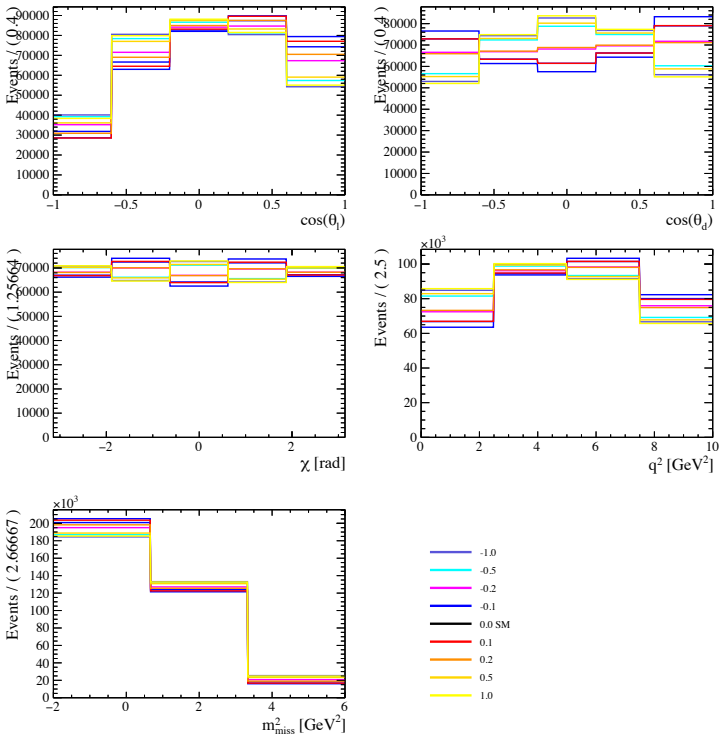


Figure 4.7: Plots of distribution of the fitting variables for values in the range [-1.0, 1.0] for the imaginary part of the left handed tensor operator.

4.4.3 Scalar operator

The scalar operator is defined as

$$[\bar{c}\chi^V_{\mathrm{L,R}}\gamma^\mu P_{\mathrm{L,R}}b][\bar{l}\lambda^S_{\mathrm{L,R}}\gamma_\mu P_{\mathrm{L,R}}\nu] \tag{4.33}$$

The scalar operator is expected to pair less with the lighter leptons since its effective coupling is directly proportional to lepton mass [117] and the sensitivity of the signal template to this operator is significantly smaller, shown in Fig. 4.8 and Fig. 4.9. Due to the low sensitivity of the single scalar operator it is expected that the uncertainty measured in the fit to be larger than the one for the vector and tensor contribution.

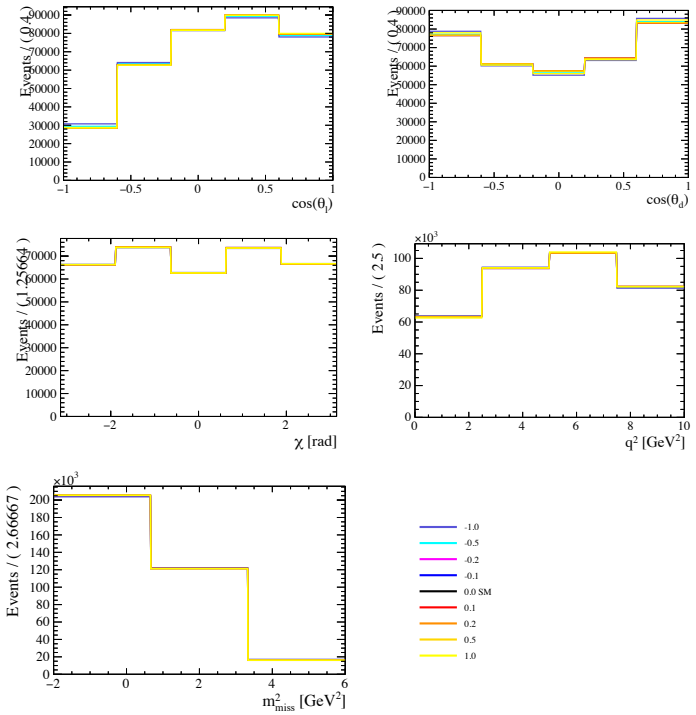


Figure 4.8: Plots of distribution of the fitting variables for values in the range [-1.0, 1.0] for the real part of the left handed scalar operator.

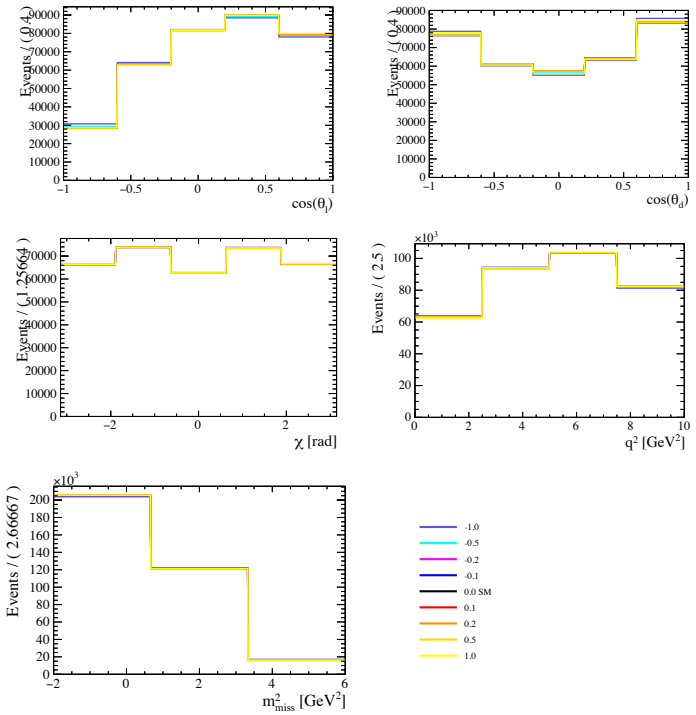


Figure 4.9: Plots of distribution of the fitting variables for values in the range [-1.0, 1.0] for the imaginary part of the left handed scalar operator.

4.5 Fit model

The implementation of the fit to data uses RooFit [118] and HAMMER to manage the various templates and their normalizations. An interface between HAMMER and RooFit is used to be able to float the hadronic form factor parameters and Wilson coefficients in the fit [119]. A variation of the interface between HAMMER and RooFit documented in Ref. [119] was developed and used to enable five-dimensional templated fit. The fit is based on the maximum likelihood method

in five-dimensional binned data with the following binning scheme:

- $\cos(\theta_l)$, five equal bins in the range [-1,1].
- $\cos(\theta_d)$, five equal bins in the range [-1,1].
- χ, five equal bins in the range $[-\pi, \pi]$ rad.
- q^2, four equal bins in the range [0.0, 10.0] GeV^2.
- m^2_{miss}, three equal bins in the range [-2.0, 6.0] GeV^2.

While the ranges of $\cos\theta_l$, $\cos\theta_d$ and χ cover the full angular phase space and the q^2 range covers the full kinematic range; the $m^2_{\rm miss}$ range is chosen to include the signal peak near zero and the background contributions at higher values. The combination of bin numbers was tested by examining the distribution of signal statistics across the bins and the sensitivity of the signal shape to NP contributions, as illustrated in section 4.4.

The fitter extracts the contributions of signal, feed-down from semileptonic decays from each of several excited charm states as well as higher charm states, combinatorial (same sign combinations of D^* and μ) and D^* Combinatorial (a fake D^* made with a D^0 combined with a wrong sign π), backgrounds from particles mis-identified as muons, Wilson coefficients and hadronic form factor parameters that correspond to the signal variation. The relative contributions of the signal and background components are determined from the fit to data. No independent pre-fit yield predictions are used in this fit; the initial yield values serve as starting points for the minimisation. The fit can be run in several different configurations according to the form factor parametrisation used for the signal. Central values of the form factor parameters in HAMMER (See Tables 4.7, 4.8, 4.9, 4.10) are used for each parametrisation and the offset of these values is measured in the fit. The fitter is configured to vary FF offsets Δp_i relative to the reference form-factor parameter values $p_i^{\rm ref}$, as required by the HAMMER interface used in this analysis; the physical parameter values are reconstructed as $p_i = p_i^{\rm ref} + \Delta p_i$.

The fit templates and their shapes are summarized in Tab. 4.12. The parameters in the fit model are: The yields for the signal and background processes, the hadronic form factor (FF) parameters and Wilson coefficients for $B^0 \to D^*\mu\nu$ and the hadronic form factor parameters for each of the $B \to D^{**}$ background contributions. Since $B^0 \to D^*\mu\nu$ and $B^0 \to D^*\tau\nu$ are described with the same form

Parameters	Values (as in HAMMER)
ρ^2	1.24
$\chi_2(1)$	-0.06
$\chi_2'(1)$	0.0
$^\dagger\chi_3'(1)$	0.05
$\eta(1)$	0.30
$\eta'(1)$	-0.05
$^\dagger V_{20}$	7.5

Table 4.7: BLPR form factor parameters with central values obtained from [2]. Parameters that are not floated in the fit in this analysis are noted with † in the table (The explanation is given in 4.5.1.4).

Parameters	Values (as in HAMMER)
ρ^2	1.207
R_1	1.401
R_2	0.854
R_0	1.15

Table 4.8: CLN form factor parameters with central values from [3].

factor parametrization their corresponding parameters are floated and shared between these two components. Similarly, for the D^{**} states the BLR form factor parameters are floated and shared between the excited states. Gaussian constraints are applied on the values of the BLR parameters corresponding to the measured values from the $R(D^0)$ vs $R(D^*)$ analysis [115] as in Tab. 4.11.

Parameters	Values
a_0	0.00038
a_1	0.026905
a_2	0.0
$^\dagger b_0$	0.00055
b_1	-0.0020370
b_2	0.0
c_1	-0.0020370
c_2	0.005353
d_0	-0.007
d_1	0.036

Table 4.9: BGL form factor parameters with central values as given in HAMMER. Parameters that are not floated in the fit in this analysis are noted with † in the table (The explanation is given in 4.5.1.1).

Parameters	Values
t_1	0.7
t'	-1.6
τ_1	-0.5
τ_2	2.9
zt_1	0.7
ζ'	0.2
ζ_1	0.6

Table 4.10: BLR form factor parameters with central values as given in HAMMER.

$B \to D^{**}$ FF	value	uncertainty
t_1	1.0	fixed
t'	-1.18	$\pm$ 0.18
τ_1	0.62	$\pm$ 0.41
τ_2	0.93	$\pm$ 0.31
zt_1	1.0	fixed
ζ'	-1.36	$\pm$ 0.21
ζ_1	0.61	$\pm$ 0.33

Table 4.11: BLR FF parameters results from the $R(D^0)$ vs $R(D^*)$ analysis. These values are used for applying a Gaussian constraint to the fit parameters for the D^{**} background contributions.

Component	Shape	Parameter
$B^0 \to D^*\mu\nu$	MC + HAMMER reweight	$N_{D^*\mu}$, WCs and FF parameters
$B^0 \to D^*\tau\nu$	MC + HAMMER reweight	$N_{D^*\tau}$ and FFs
$B^0 \to D_1\mu\nu$	MC + HAMMER reweight	$N_{D_1(2420)^+}$ and FFs
$B^0 \to D_1^{'}\mu\nu$	MC + HAMMER reweight	$N_{D_1^+}$ and FFs
$B^0 \to D_2^*\mu\nu$	MC + HAMMER reweight	$N_{D_2^*(2460)^+}$ and FFs
$B_s \to D_{s2}^*\mu\nu$	MC + HAMMER reweight	$N_{D_{s2}(2573)^*}$ and FFs
$B^+ \to D_1\mu\nu$	MC + HAMMER reweight	$N_{D_1(2420)^0}$ and FFs
$B^+ \to D_1^{'}\mu\nu$	MC + HAMMER reweight	$N_{D_1(2430)^0}$ and FFs
$B^+ \to D_2^*\mu\nu$	MC + HAMMER reweight	$N_{D_2^*(2460)^0}$ and FFs
$B_s \to D_{s1}\mu\nu$	MC + HAMMER reweight	$N_{D_{s1}(2536)^+}$ and FFs
$B \to D^{**}(\text{Higher})\mu\nu$	MC	$N_{D^{**}(Higher)}$
$B \to D^{**}\tau\nu$	MC	$N_{D^{**}\tau}$
$B \to D^{*+}D(X_c \to \mu\nu X)$	MC	N_{DDX}
MisID	Data	N_{MisID}
Combinatorial	Data	N_{comb}
D^* Combinatorial	Data	N_{D^*comb}

Table 4.12: Fit components summary and their corresponding parameters. The shape of the fit templates can be taken directly from simulation (MC), simulation and additional weights from HAMMER or from data which is stated in the second column. The third column lists the associated fit parameters to each of the components where N_i corresponds to the measured yield, WCs are the Wilson coefficients and FFs are the form factor parameters.

4.5.1 Blinded fit results and sensitivity

Before the NP measurements are performed, a SM fit using the BLPR, BGL and CLN form factor parametrisation is done. The values of the form factor parameters are extracted in each of the SM fits and presented as part of the results of this analysis. The systematic uncertainties are as well computed for each of the fit configurations separately.

This analysis focuses on directly measuring the Wilson coefficients using different configurations according to the different assumptions about the nature of the NP contribution. Results for the signal template receiving one contribution from NP by measuring the real and imaginary part of the contributing Wilson coefficient are given. The fitter is run considering one Wilson coefficient contribution for the operators shown in Tab. 4.13, having one contribution corresponding to each row of the table. When a choice of the operator is made, the rest of the NP contributions are set to zero. This approach makes an assumption about the NP structure, further the fits using this strategy are identified as single-parameter fits. The single-parameter fits are useful to understand if the NP nature is due to one single operator and the precision we can have given the assumption, given in Tab. 4.13. Furthermore results when considering together the scalar, vector and tensor operator are reported and this is referred to as the multi-parameter fit. The multi-parameter fit configuration is achieved by floating a reparametrisation as given in Eq. 4.35 and discussed later.

Current	WC tag	WC	4-Fermi/$(i2\sqrt{2}V_{cb}G_F)$
SM	SM	1	$[\bar{c}\gamma^\mu P_L b][\bar{l}\gamma_\mu P_L \nu]$
Vector	VqRlL	$\chi_R^V \lambda_L^V$	$[\bar{c}\chi_R^V\gamma^\mu P_R b][\bar{l}\lambda_L^V\gamma_\mu P_L \nu]$
Scalar	SqLlL	$\chi_L^S \lambda_L^S$	$[\bar{c}\chi_L^S\gamma^\mu P_L b][\bar{l}\lambda_L^S\gamma_\mu P_L \nu]$
Tensor	TqLlL	$\chi_L^T \lambda_L^s$	$[\bar{c}\chi_L^T\gamma^\mu P_L b][\bar{l}\lambda_L^S\gamma_\mu P_L \nu]$

Table 4.13: NP operator basis and coupling conventions as given in HAMMER.

The NP results all use the BLPR form factor parametrisation for the signal. The values of the Wilson coefficients and the corresponding BLPR form factor parameters are blinded values in the analysis.

The blinding is implemented by assigning a blinding shift to the Wilson coefficient and the form factor parameters according to which the fitted values of the Wilson coefficients are shifted when displayed in the final fit result. In the next

sections the blinded results from the single and multi parameter NP scenario, and from the SM fit results are shown.

4.5.1.1 Results for SM fit using BGL

The signal template shape is obtained using the BGL form factor parametrisation with the option of varying its parameters. The central values of the parameters of interest are given in Tab. 4.9. The fitter is run in a SM scenario to measure the offset of these values with the b_0 parameter fixed to the value of 0.012 (the value comes from the measured value in the $R(D^0)$-$R(D^*)$ measurement [115]) to fix the normalisation. All the form factor parameters are shared except for the helicity suppressed parameters d_0 and d_1 which are fitted separately for the $B^0 \to D^*\mu\nu$ and the $B^0 \to D^*\tau\nu$ template. In the next section the determination of the nominal fit BGL configuration is explained.

4.5.1.2 Truncation order estimation for the BGL parametrisation

Since the BGL parameters are outcome of series of different order the choice of fitting particular order of parameters depends on the sensitivity of the data. To be able to choose between the alternative fit models consisting of different order of parameters in the BGL series we use the Bayesian Information Criterion (BIC) [120]. The BIC can be defined as

$$\mathrm{BIC} = \chi^2 + \mathrm{kln(n)}, \tag{4.34}$$

where k is the number of model parameters, n is the sample size which for a binned fit is the number of bins. The χ^2 values reported in Tab. 4.14 are evaluated over the five-dimensional binning using minimiser's χ^2 function with Poisson data errors. The statistic is defined as $\chi^2 = \sum_i [n_i - \mu_i(\hat{\boldsymbol{\theta}})]^2/\sigma_i^2$, where n_i and μ_i are the observed and fitted expected bin yields, respectively, and σ_i is the asymmetric Poisson uncertainty selected in the direction of the prediction. The model comparison assesses the relative preference among the tested form-factor truncations; it does not, by itself, establish the absolute goodness of fit.

To be able to compare the different models involves calculating the BIC for different order combination of the parameters. The BGL fit to the data has been evaluated for all the combinations of the parameters from Table 4.9 and the BIC was calculated. The model with the lowest BIC is initially considered as the *best*.

The difference between the BIC (Δ BIC) of a particular model and the *best* model (with the lowest BIC) can be used as an argument against the other model. If Δ BIC is between 2 and 6 [120] one can say that we have a good argument in favour of the *best* model. If the Δ BIC is between 6 and 10 it represents a strong argument in favour of the *best* model. For Δ BIC larger than 10 very strong argument in favour of the *best* model. If Δ BIC is less than 2 it's too small to be significant or considered. In Tab. 4.14 a summary of evaluating the BIC and the Δ BIC is given for 10 models with the lowest BIC of all possible combinations of parameters.

Parameter	Order of fitting									
a	**2**	2	2	2	2	2	2	2	2	2
b	**2**	2	2	2	2	2	2	2	2	2
c	**2**	1	2	1	2	1	2	1	2	1
d	**0**	0	2	2	2	2	1	1	1	1
$d\,\tau$	**0**	0	2	2	1	1	1	1	0	0
χ^2	1814.17	1834.72	1804.31	1821.34	1805.42	1821.95	1809.8	1826.16	1814.98	1833.14
N fit par.	**5**	4	9	8	8	7	7	6	6	**5**
N bins	**1500**	1500	1500	1500	1500	1500	1500	1500	1500	**1500**
BIC	2004.31	2017.55	2023.70	2033.42	2017.50	2026.72	2014.57	2023.62	2012.44	2023.29
Δ BIC	**0.0**	13.23	19.39	29.12	13.19	22.41	10.26	19.30	8.12	18.97

Table 4.14: Summary of the BIC values for several fitting models that use the combination of fitting parameters as stated in the order of fitting in the table. There is a separate d parameter that we fit for the muonic and tauonic template.

The nominal fit configuration was chosen to be the one that provides the lowest BIC having two a and b parameters (b_0 is fixed for normalisation) two c parameters (shown in bold in Table 4.14). The next configurations with the lowest BIC is the one with Δ BIC value of 8.12. This one is used to evaluate the systematic uncertainty of the parameters due to the truncation of the series, discussed later in section 4.7.

The results of the fit of the above chosen nominal configuration are given in Tab. 4.15 and the correlations between the form factor parameters are shown in Tab. 4.16. The fit projections in the five fitting variables are shown in Fig. 4.10.

Parameters	Fit value ± Uncertainty
Δa_0	0.0007 ± 0.0000
Δa_1	-0.0285 ± 0.0009
Δb_1	0.0017 ± 0.0002
Δc_1	0.0004 ± 0.0001
Δc_2	-0.0046 ± 0.0011
$\Delta\tau_1$	1.3400 ± 0.3720
$\Delta\tau_2$	-2.0300 ± 0.3100
$\Delta t'$	0.6980 ± 0.1600
$\Delta\zeta_1$	0.2660 ± 0.3030
$\Delta\zeta'$	-1.4700 ± 0.2060
N $D_1(2420)^+$	10500.0 ± 2160.0
N $D_1(2420)^0$	0.0 ± 2.8
N D_1^+	5480.0 ± 3747.3
N $D_1(2430)^0$	0.0 ± 3605.8
N $D_2^st(2460)^+$	3290.5 ± 1440.2
N $D_2^st(2460)^0$	169.5 ± 708.8
N D^*DX	5100.0 ± 591.0
N $D^*\mu$	220000.0 ± 1130.0
N $D^*\tau$	5800.0 ± 1130.0
N $D_{s1}(2536)^+$	1320.0 ± 936.0
N $D_{s2}^*(2573)^+$	2450.0 ± 914.0
N D^{**}(Higher)	824.0 ± 1240.0
N $D^{**}\tau$	2530.0 ± 772.0
N MisID	1080.0 ± 288.0
N Comb	365.0 ± 304.0
N D^* comb	6350.0 ± 982.0

Table 4.15: Values of the parameters and statistical uncertainty determined by the fit to Run 1 data using the SM scenario with the BGL form factor parametrisation.

Parameter	Δa_0	Δa_1	Δb_1	Δc_1	Δd_0
Δa_0	1.000	-0.914	0.496	0.354	-0.273
Δa_1	-0.914	1.000	-0.556	-0.227	0.151
Δb_1	0.496	-0.556	1.000	0.583	-0.476
Δc_1	0.354	-0.227	0.583	1.000	-0.972
Δc_2	-0.273	0.151	-0.476	-0.972	1.000

Table 4.16: Correlation coefficients of the form factor parameters determined by the fit to Run 1 data in the SM scenario with the BGL form factor parametrisation.

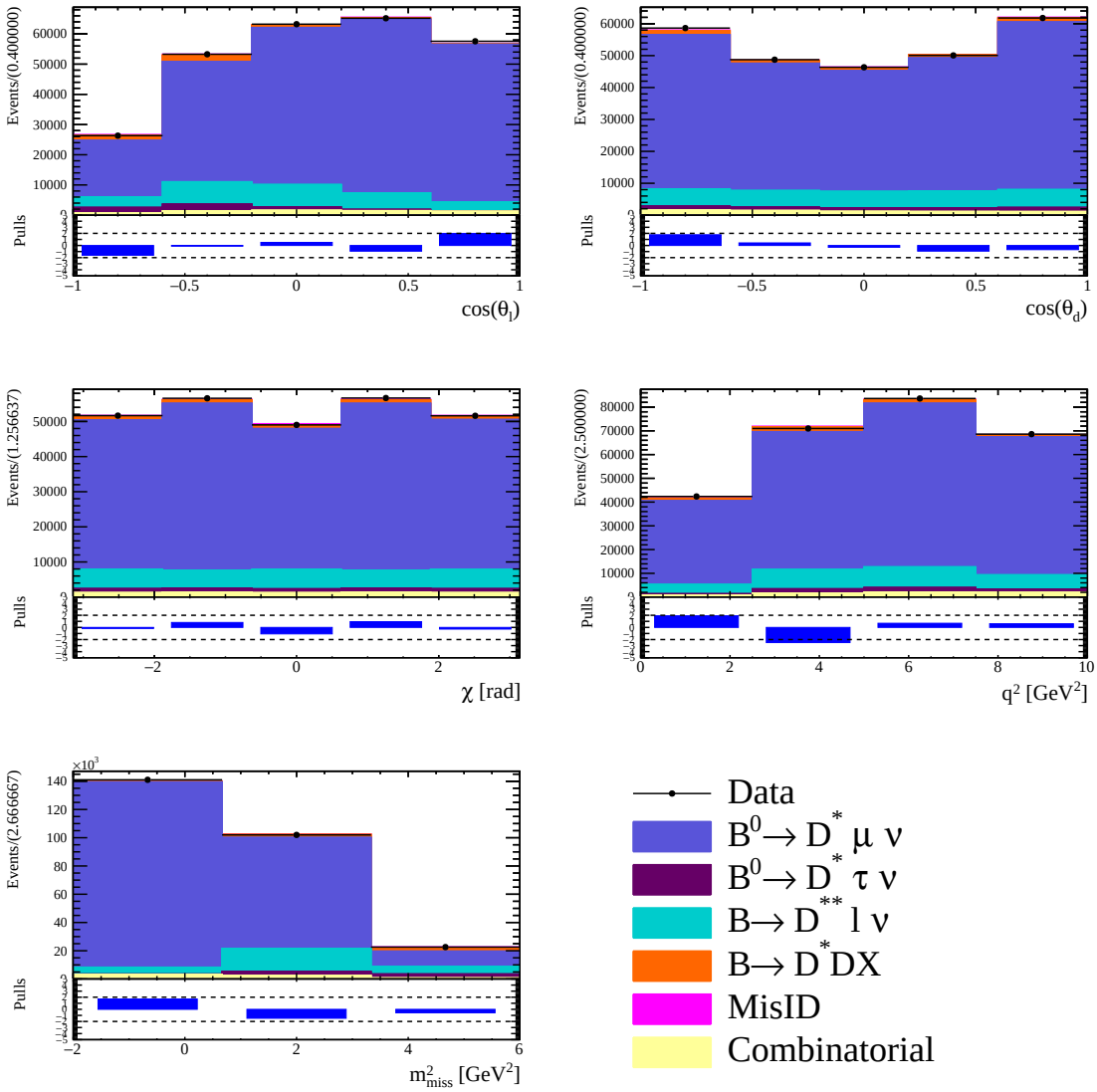


Figure 4.10: Fit projections of the fitting variables for the SM fit with BGL form factor parametrisation. The signal ($B^0 \to D^*\mu\nu$) is shown in purple and rest of the backgrounds in different colours. The black points represent the data.

4.5.1.3 Results for SM fit using CLN

In this SM fit configuration the CLN form factor parametrisation is used to model the signal template. The measured offsets of the central values and the yields for this configuration are shown in Tab. 4.17. Correlations between the form factor parameters are shown in Tab. 4.18.

Parameters	Fit value ± Uncertainty
ΔR_1	-0.0981 ± 0.0324
ΔR_2	0.0055 ± 0.0141
$\Delta\rho^2$	0.0039 ± 0.0198
$\Delta\tau_1$	1.3600 ± 0.3710
$\Delta\tau_2$	-2.0400 ± 0.3090
$\Delta t'$	0.6910 ± 0.1610
$\Delta\zeta_1$	0.2780 ± 0.3030
$\Delta\zeta'$	-1.4700 ± 0.2060
N $D_1(2420)^+$	10400.0 ± 2150.0
N $D_1(2420)^0$	0.0 ± 2.8
N D_1^+	5400.0 ± 3699.2
N $D_1(2430)^0$	0.0 ± 3564.0
N $D_2^st(2460)^+$	3291.2 ± 1372.4
N $D_2^st(2460)^0$	228.8 ± 642.7
N D^*DX	5060.0 ± 590.0
N $D^*\mu$	221000.0 ± 1120.0
N $D^*\tau$	5630.0 ± 1130.0
N $D_{s1}(2536)^+$	1130.0 ± 937.0
N $D_{s2}^*(2573)^+$	2570.0 ± 912.0
N D^{**}(Higher)	737.0 ± 1230.0
N $D^{**}\tau$	2630.0 ± 768.0
N MisID	1140.0 ± 288.0
N Comb	362.0 ± 302.0
N D^* comb	6430.0 ± 980.0

Table 4.17: Values of the parameters and statistical uncertainty determined by the fit to Run 1 data using the SM scenario with the CLN form factor parametrisation.

Parameter	ΔR_1	ΔR_2	$\Delta\rho^2$
ΔR_1	1.000	0.663	-0.612
ΔR_2	0.663	1.000	-0.774
$\Delta\rho^2$	-0.612	-0.774	1.000

Table 4.18: Correlation coefficients of the form factor parameters determined by the fit to Run 1 data in the SM scenario with the CLN form factor parametrisation.

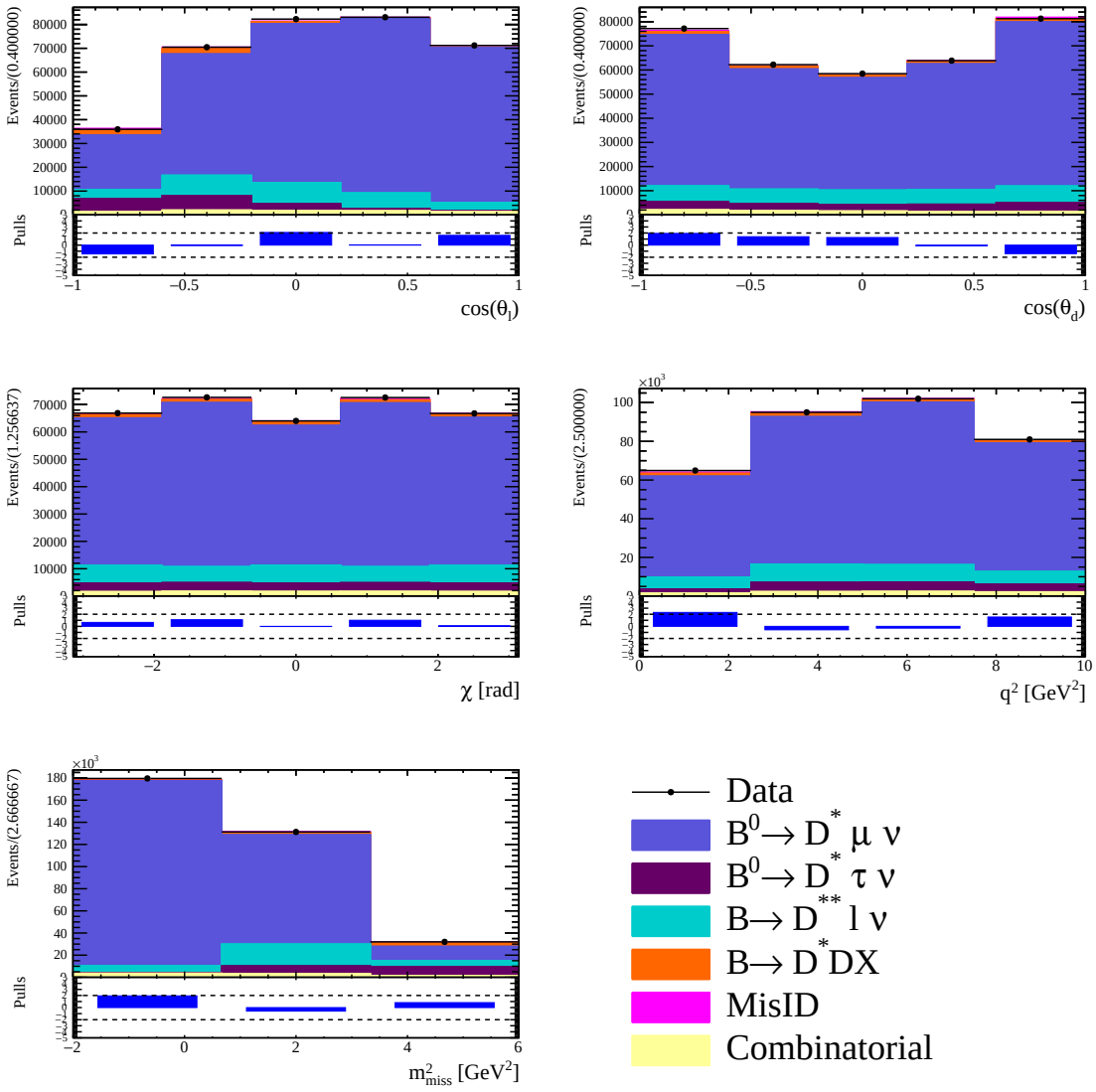


Figure 4.11: Fit projections for the SM fit with the CLN form factor parametrisation. The signal ($B^0 \to D^*\mu\nu$) is shown in purple and rest of the backgrounds in different colours. The black points represent the data. The rest of the fit configurations show similar fit quality.

4.5.1.4 Results for SM fit using BLPR

The fit was run using the BLPR form factor parametrisation to describe the signal template. When using the BLPR parametrisation, we fix the parameters $\Delta\chi'_3(1)$ and ΔV_{20}, since they are not directly present in the decay rate expression for $B^0 \to D^*\ell\nu$ as calculated from Ref. [2]. In addition this has been verified when plotting the change of the signal template shape with various values of $\Delta\chi'_3(1)$ and ΔV_{20}.

It can be seen in Fig. 4.12 and Fig. 4.13 that the signal template does not show any sensitivity to these two parameters, as expected from the theory calculation in Ref. [2].

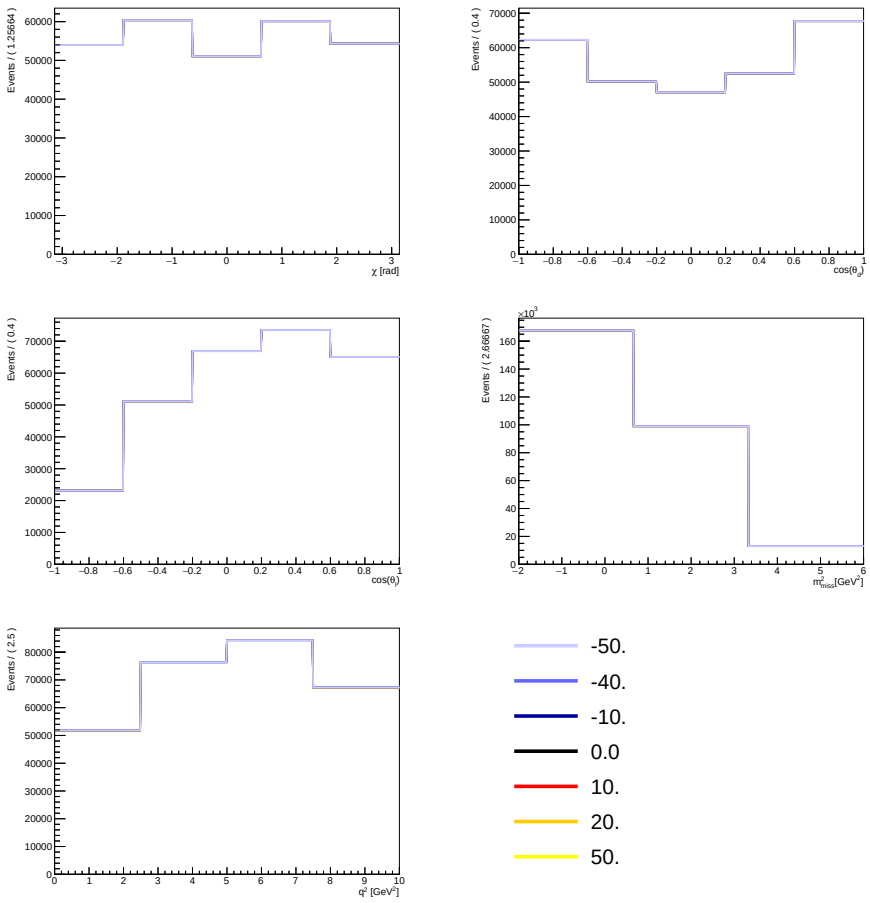


Figure 4.12: Template shapes for the five fitting variables overlayed for different values of the ΔV_{20} parameter. It can be seen that there is no change in the template under this parameter.

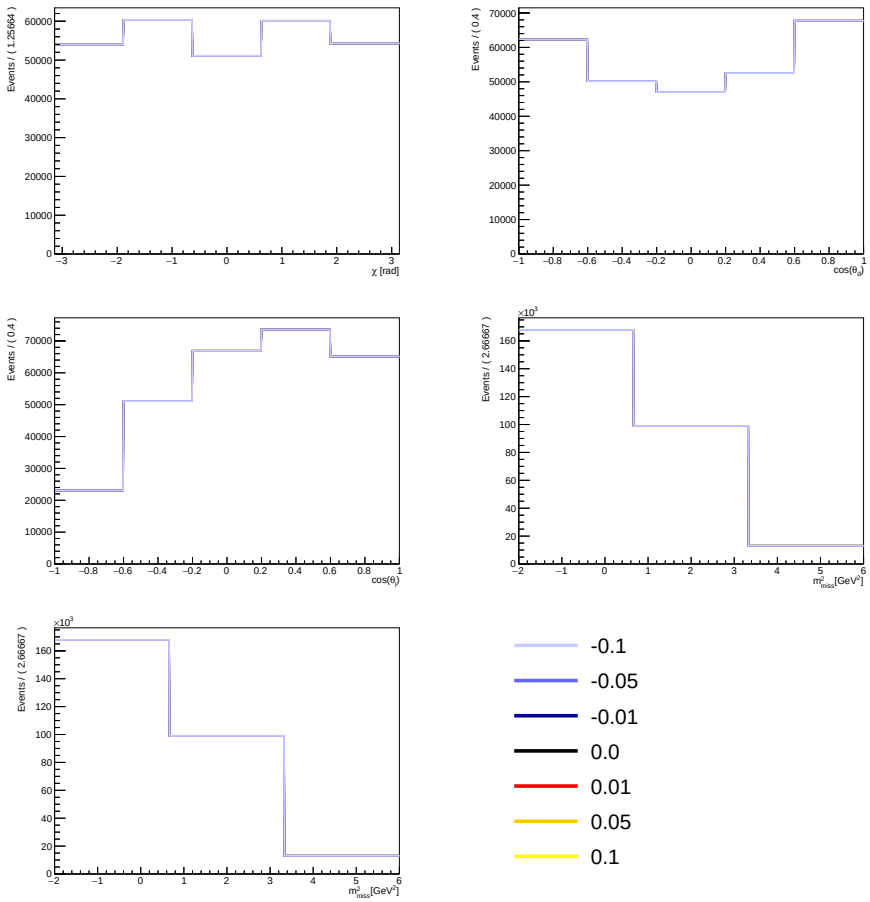


Figure 4.13: Template shapes for the five fitting variables overlayed for different values of the $\Delta\chi_3(1)'$ parameter. It can be seen that there is no change in the template under this parameter.

This configuration of BLPR form factor parameters is further used in the case of the NP scenarios. The fitted values of the parameters are given in Table 4.19 with the correlation coefficients of the form factors in Table 4.20. Projections of the fitting variables are shown in Fig. 4.14.

Parameters	Fit value ± Uncertainty
$\Delta\rho^2$	-0.0821 ± 0.0285
$\Delta\chi_2(1)$	-0.0504 ± 0.1150
$\Delta\chi_2'$	0.3820 ± 0.1770
$\Delta\eta(1)$	0.1250 ± 0.1360
$\Delta\eta(1)'$	-0.5920 ± 0.5150
$\Delta\tau_1$	1.3100 ± 0.3760
$\Delta\tau_2$	-2.0300 ± 0.3090
$\Delta t'$	0.7120 ± 0.1620
$\Delta\zeta_1$	0.2660 ± 0.3040
$\Delta\zeta'$	-1.4700 ± 0.2060
N $D_1(2420)^+$	10500.0 ± 2170.0
N $D_1(2420)^0$	0.0 ± 2.8
N D_1^+	5560.0 ± 3870.4
N $D_1(2430)^0$	0.0 ± 3736.3
N $D_2^st(2460)^+$	3221.7 ± 2164.9
N $D_2^st(2460)^0$	148.3 ± 1766.8
N D^*DX	5190.0 ± 590.0
N $D^*\mu$	220000.0 ± 1130.0
N $D^*\tau$	5700.0 ± 1130.0
N $D_{s1}(2536)^+$	1470.0 ± 949.0
N $D_{s2}^*(2573)^+$	2430.0 ± 916.0
N D^{**}(Higher)	764.0 ± 1230.0
N $D^{**}\tau$	2550.0 ± 776.0
N MisID	1080.0 ± 287.0
N Comb	371.0 ± 303.0
N D^* comb	6240.0 ± 983.0

Table 4.19: Values of the parameters and statistical uncertainty determined by the fit to Run 1 data using the SM scenario with the BLPR form factor parametrisation.

Parameter	$\Delta\rho^2$	$\Delta\chi_2(1)$	$\Delta\chi_2'$	$\Delta\eta(1)$	$\Delta\eta(1)'$
$\Delta\rho^2$	1.000	-0.280	-0.681	-0.273	0.826
$\Delta\chi_2(1)$	-0.280	1.000	0.111	-0.678	-0.331
$\Delta\chi_2'$	-0.681	0.111	1.000	0.323	-0.847
$\Delta\eta(1)$	-0.273	-0.678	0.323	1.000	-0.381
$\Delta\eta(1)'$	0.826	-0.331	-0.847	-0.381	1.000

Table 4.20: Correlation coefficients of the form factor parameters determined by the fit in the SM scenario with the BLPR form factor parametrisation.

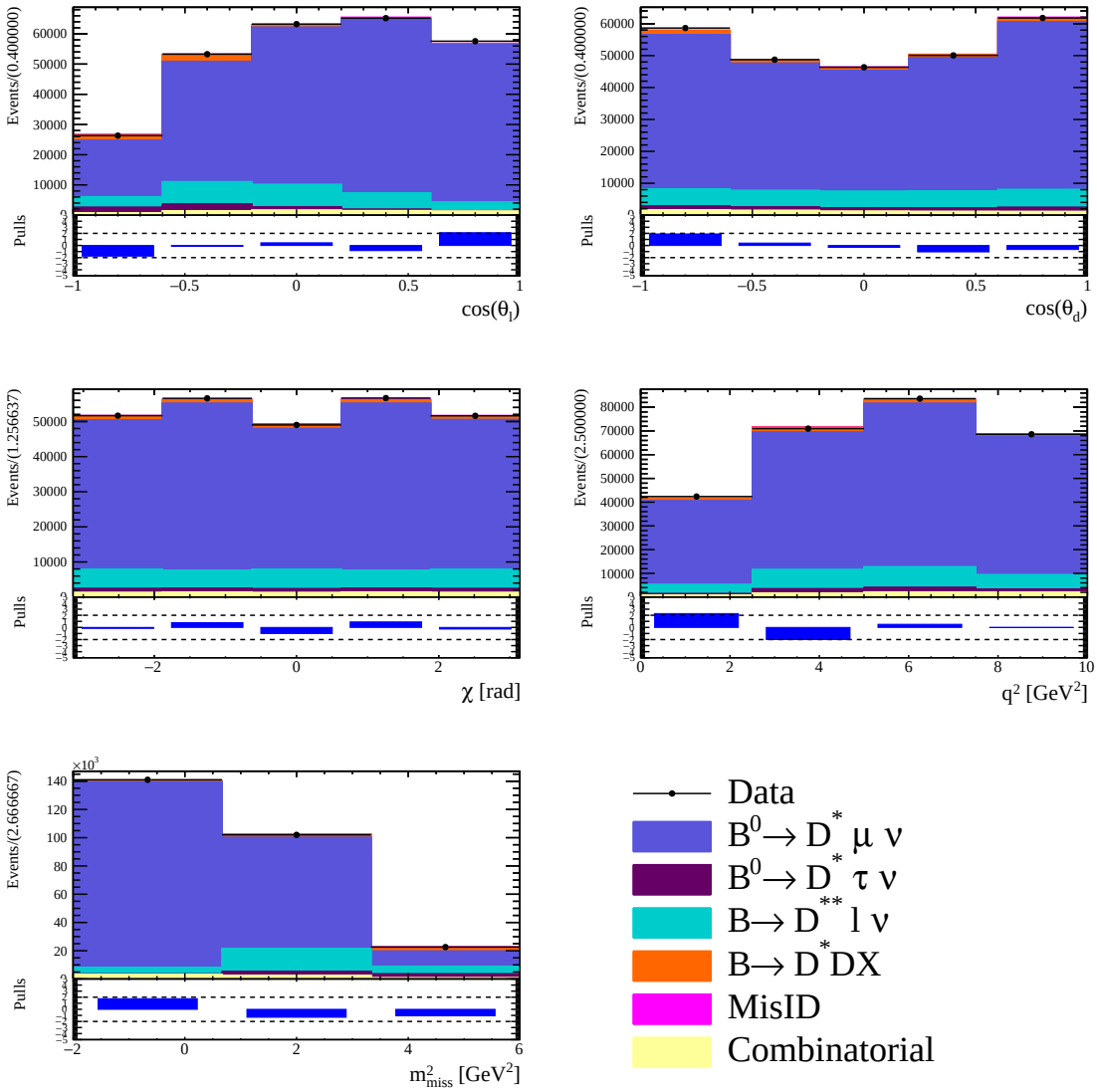


Figure 4.14: Fit projections for the SM fit with the BLPR form factor parametrisation. The signal ($B^0 \to D^*\mu\nu$) is shown in purple and rest of the backgrounds in different colours. The black points represent the data. The rest of the fit configurations show similar fit quality.

4.5.1.5 Results for NP fit with V_{qRlL} contribution

In this configuration the right handed vector contribution is added to the signal template. The fit is varying the Wilson coefficient value of this operator for its real and imaginary part while floating the BLPR form factor parameters. As difference to the other single WC fit configurations, the $\chi_2(1)$ parameter is fixed since it is one of the parameters that is highly correlated with real part of the V_{qRl} (see Fig. 4.15).

This was seen in the fit to data and further studied in toys.

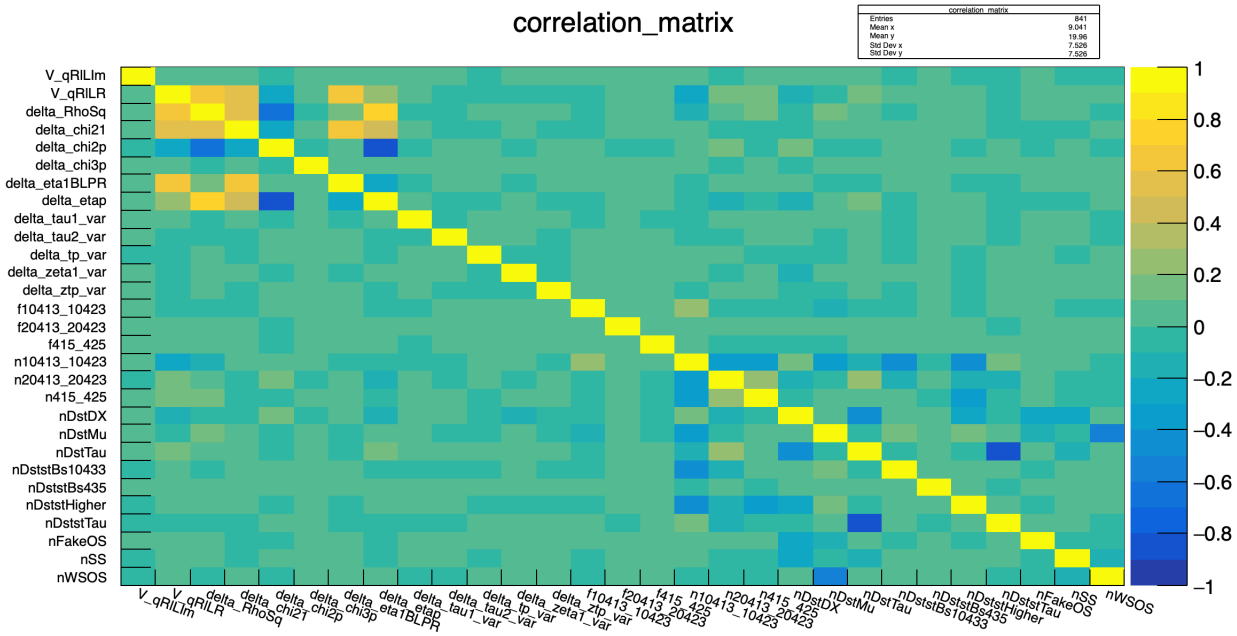


Figure 4.15: Correlation matrix for the New Physics V_{qRl} toy fit.

Furthermore it was cross checked that the $\chi_2(1)$ is not having enough sensitivity for the signal template for V_{qRlL} and therefore fixed in the fit to data. In Fig. 4.16 the change of the template shape for different values of $\chi_2(1)$ are shown, resulting with no sensitivity.

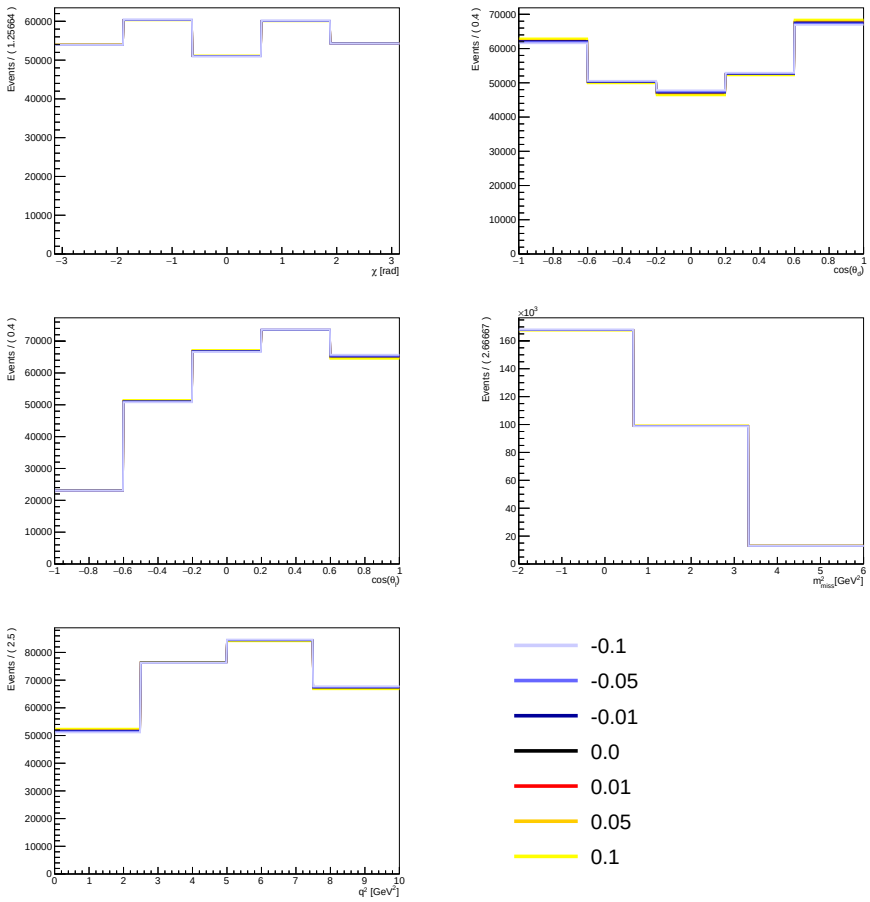


Figure 4.16: Template shapes for the five fitting variables overlayed for different values of the $\Delta\chi_2(1)$ parameter. The range of values determined in a way that it will cover all the possible fitted values seen in toys. It can be seen that there is only some slight variation in the template for $cos\theta_l$, $cos\theta_d$ and q^2.

Here the blinded values of the Wilson coefficients are reported. The fit results are shown in Tab. 4.21. The correlations between the real and imaginary part of V_{qRlL} are shown in Table 4.22.

Parameter	Fit value ± uncertainty
$V_{qRlL}Im$	xxx ± 0.0127
$V_{qRlL}Re$	xxx ± 0.0080
$\Delta\rho^2$	xxx ± 0.0298
$\Delta\chi'_2$	xxx ± 0.1760
$\Delta\eta(1)$	xxx ± 0.1150
$\Delta\eta(1)'$	xxx ± 0.4890
$\Delta\tau_1$	1.3200 ± 0.3750
$\Delta\tau_2$	-2.0200 ± 0.3090
$\Delta t'$	0.7220 ± 0.1620
$\Delta\zeta_1$	0.2750 ± 0.3040
$\Delta\zeta'$	-1.4700 ± 0.2060
N $D_1(2420)^+$	10200.0 ± 2160.0
N $D_1(2420)^0$	0.0 ± 2.8
N D_1^+	5600.0 ± 4382.4
N $D_1(2430)^0$	0.0 ± 4267.2
N $D_2^st(2460)^+$	3493.0 ± 1444.3
N $D_2^st(2460)^0$	157.0 ± 735.8
N D^*DX	5180.0 ± 590.0
N $D^*\mu$	220000.0 ± 1130.0
N $D^*\tau$	6140.0 ± 1120.0
N $D_{s1}(2536)^+$	1560.0 ± 948.0
N $D^*_{s2}(2573)^+$	2400.0 ± 916.0
N D^{**}(Higher)	706.0 ± 1240.0
N $D^{**}\tau$	2490.0 ± 767.0
N MisID	424.0 ± 181.0
N Comb	458.0 ± 305.0
N D^* comb	6430.0 ± 983.0

Table 4.21: Values of the parameters determined by the fit to Run 1 data using the NP scenario including V_{qRlL} with the BLPR form factor parametrisation.

Parameter	V_{qRlL}Im	V_{qRlL}Re	$\Delta\rho^2$	$\Delta\chi_2'$	$\Delta\eta(1)$	$\Delta\eta(1)'$
V_{qRlL}Im	1.000	0.026	0.000	0.008	0.013	-0.010
V_{qRlL}Re	0.026	1.000	0.394	-0.075	0.479	-0.099
$\Delta\rho^2$	0.000	0.394	1.000	-0.654	-0.343	0.702
$\Delta\chi_2'$	0.008	-0.075	-0.654	1.000	0.442	-0.851
$\Delta\eta(1)$	0.013	0.479	-0.343	0.442	1.000	-0.811
$\Delta\eta(1)'$	-0.010	-0.099	0.702	-0.851	-0.811	1.000

Table 4.22: Correlation coefficients of the form factor parameters determined by the fit in the NP scenario including V_{qRlL} with the BLPR form factor parametrization.

4.5.1.6 Results for NP fit with S_{qLlL} contribution

In this configuration the left handed scalar contribution is added to the signal template. The fit is varying the Wilson coefficient value of this operator for its real and imaginary part and floating the BLPR form factor parameters. The blinded values of the Wilson coefficients are reported. The fit results are shown in Tab. 4.23 with the correlations between the real and imaginary part of S_{qLlL} shown in Tab. 4.24.

Parameter	Fit value ± uncertainty
$S_{qLlL}Im$	xxx ± 0.1750
$S_{qLlL}Re$	xxx ± 0.1270
$\Delta\rho^2$	xxx ± 0.0275
$\Delta\chi'_2$	xxx ± 0.1750
$\Delta\eta(1)$	xxx ± 0.1010
$\Delta\eta(1)'$	xxx ± 0.4860
$\Delta\tau_1$	1.1400 ± 0.3920
$\Delta\tau_2$	-2.0600 ± 0.3100
$\Delta t'$	0.6840 ± 0.1660
$\Delta\zeta_1$	0.2890 ± 0.3030
$\Delta\zeta'$	-1.4600 ± 0.2050
N $D_1(2420)^+$	10800.0 ± 2130.0
N $D_1(2420)^0$	0.0 ± 2.8
N D_1^+	5740.0 ± 4125.0
N $D_1(2430)^0$	0.0 ± 4012.3
N $D_2^st(2460)^+$	3562.6 ± 1414.8
N $D_2^st(2460)^0$	227.4 ± 649.3
N D^*DX	5250.0 ± 588.0
N $D^*\mu$	220000.0 ± 1130.0
N $D^*\tau$	6250.0 ± 1130.0
N $D_{s1}(2536)^+$	748.0 ± 913.0
N $D^*_{s2}(2573)^+$	2320.0 ± 918.0
N D^{**}(Higher)	888.0 ± 1250.0
N $D^{**}\tau$	2310.0 ± 771.0
N MisID	432.0 ± 181.0
N Comb	473.0 ± 304.0
N D^* comb	6210.0 ± 992.0

Table 4.23: Values of the parameters determined by the fit using the NP scenario including S_{qLlL} with the BLPR form factor parametrisation.

Parameter	S_{qLlL}Im	S_{qLlL}Re	$\Delta\rho^2$	$\Delta\chi_2'$	$\Delta\eta(1)$	$\Delta\eta(1)'$
S_{qLlL}Im	1.000	0.061	0.005	-0.021	0.077	-0.017
S_{qLlL}Re	0.061	1.000	0.016	0.049	-0.107	0.044
$\Delta\rho^2$	0.005	0.016	1.000	-0.677	-0.653	0.807
$\Delta\chi_2'$	-0.021	0.049	-0.677	1.000	0.531	-0.859
$\Delta\eta(1)$	0.077	-0.107	-0.653	0.531	1.000	-0.871
$\Delta\eta(1)'$	-0.017	0.044	0.807	-0.859	-0.871	1.000

Table 4.24: Correlation coefficients of the form factor parameters determined by the fit in the NP scenario including S_{qLlL} with the BLPR form factor parametrisation.

4.5.1.7 Results for NP fit with T_{qLlL} contribution

In this configuration the left handed tensor contribution is added to the signal template. The fit is varying the Wilson coefficient value of this operator for its real and imaginary part and floating the BLPR form factor parameters. The blinded values of the Wilson coefficients are reported. The fit results are shown in Tab. 4.25 with the correlations between the real and imaginary part of T_{qLlL} shown in Tab. 4.26.

Parameter	Fit value ± uncertainty
$T_{qLlL}Im$	xxx ± 0.0118
$T_{qLlL}Re$	xxx ± 0.0075
$\Delta\rho^2$	xxx ± 0.0292
$\Delta\chi_2'$	xxx ± 0.1770
$\Delta\eta(1)$	xxx ± 0.1000
$\Delta\eta(1)'$	xxx ± 0.4880
$\Delta\tau_1$	1.1200 ± 0.3940
$\Delta\tau_2$	-2.0500 ± 0.3100
$\Delta t'$	0.6720 ± 0.1670
$\Delta\zeta_1$	0.2860 ± 0.3030
$\Delta\zeta'$	-1.4600 ± 0.2050
N $D_1(2420)^+$	10500.0 ± 2100.0
N $D_1(2420)^0$	0.0 ± 2.8
N D_1^+	5860.0 ± 4269.5
N $D_1(2430)^0$	0.0 ± 4160.6
N $D_2^st(2460)^+$	3405.6 ± 1415.6
N $D_2^st(2460)^0$	194.4 ± 634.1
N D^*DX	5320.0 ± 587.0
N $D^*\mu$	221000.0 ± 1200.0
N $D^*\tau$	6230.0 ± 1120.0
N $D_{s1}(2536)^+$	888.0 ± 912.0
N $D_{s2}^*(2573)^+$	2370.0 ± 915.0
N D^{**}(Higher)	847.0 ± 1160.0
N $D^{**}\tau$	2310.0 ± 771.0
N MisID	431.0 ± 181.0
N Comb	481.0 ± 304.0
N D^* comb	6190.0 ± 1010.0

Table 4.25: Values of the parameters and statistical uncertainty determined by the fit to Run 1 data using the NP scenario including T_{qLlL} with the BLPR form factor parametrisation.

Parameter	T_{qLlL}Im	T_{qLlL}Re	$\Delta\rho^2$	$\Delta\chi_2'$	$\Delta\eta(1)$	$\Delta\eta(1)'$
T_{qLlL}Im	1.000	0.058	0.001	0.000	0.011	-0.005
T_{qLlL}Re	0.058	1.000	0.336	-0.145	0.055	0.110
$\Delta\rho^2$	0.001	0.336	1.000	-0.684	-0.602	0.796
$\Delta\chi_2'$	0.000	-0.145	-0.684	1.000	0.528	-0.866
$\Delta\eta(1)$	0.011	0.055	-0.602	0.528	1.000	-0.860
$\Delta\eta(1)'$	-0.005	0.110	0.796	-0.866	-0.860	1.000

Table 4.26: Correlation coefficients of the form factor parameters determined by the fit in the NP scenario including T_{qLlL} with the BLPR form factor parametrisation.

4.5.1.8 Results for NP fit with scalar, vector and tensor contribution (Reel parts only)

In this configuration the left handed scalar and tensor contribution together with the right handed vector are added to the signal template. The fit is varying only the real parts of the Wilson coefficients in the BLPR form factor parametrization. The blinded values of the Wilson coefficients are reported. The fit results are shown in Table 4.27 with the correlations between real parts of the Wilson coefficients in Table 4.28.

Parameter	Fit value ± uncertainty
$S_{qLlL}Re$	xxx ± 0.1240
$T_{qLlL}Re$	xxx ± 0.0062
$V_{qRlL}Re$	xxx ± 0.0080
$\Delta\rho^2$	xxx ± 0.0309
$\Delta\chi_2'$	xxx ± 0.1770
$\Delta\eta(1)$	xxx ± 0.1160
$\Delta\eta(1)'$	xxx ± 0.4850
$\Delta\tau_1$	1.1100 ± 0.3940
$\Delta\tau_2$	-2.0600 ± 0.3120
$\Delta t'$	0.6730 ± 0.1670
$\Delta\zeta_1$	0.2830 ± 0.3040
$\Delta\zeta'$	-1.4600 ± 0.2050
N $D_1(2420)^+$	10700.0 ± 2220.0
N $D_1(2420)^0$	0.0 ± 2.8
N D_1^+	5590.0 ± 3930.5
N $D_1(2430)^0$	0.0 ± 3801.2
N $D_2^st(2460)^+$	3344.0 ± 1458.5
N $D_2^st(2460)^0$	176.0 ± 661.8
N D^*DX	5280.0 ± 591.0
N $D^*\mu$	221000.0 ± 1220.0
N $D^*\tau$	6290.0 ± 1130.0
N $D_{s1}(2536)^+$	869.0 ± 912.0
N $D_{s2}^*(2573)^+$	2400.0 ± 913.0
N D^{**}(Higher)	941.0 ± 1220.0
N $D^{**}\tau$	2340.0 ± 764.0
N MisID	428.0 ± 181.0
N Comb	469.0 ± 303.0
N D^* comb	6020.0 ± 1030.0

Table 4.27: Values of the parameters and statistical uncertainty determined by the fit to Run 1 data using the NP scenario including real parts only of the Wilson coefficients using the BLPR form factor parameterization.

Parameter	$S_{qLlL}Re$	T_{qLlL}Re	$V_{qRlL}Re$	$\Delta\rho^2$	$\Delta\chi_2'$	$\Delta\eta(1)$	$\Delta\eta(1)'$
$S_{qLlL}Re$	1.000	-0.067	-0.027	-0.008	-0.130	0.175	0.034
T_{qLlL}Re	-0.067	1.000	-0.063	0.266	-0.109	-0.010	0.101
$V_{qRlL}Re$	-0.027	-0.063	1.000	0.362	-0.062	0.472	-0.109
$\Delta\rho^2$	-0.008	0.266	0.362	1.000	-0.648	-0.321	0.698
$\Delta\chi_2'$	-0.130	-0.109	-0.062	-0.648	1.000	0.397	-0.846
$\Delta\eta(1)$	0.175	-0.010	0.472	-0.321	0.397	1.000	-0.785
$\Delta\eta(1)'$	0.034	0.101	-0.109	0.698	-0.846	-0.785	1.000

Table 4.28: Correlation coefficients of the form factor parameters determined by the fit in the NP scenario with the real parts only of the Wilson coefficients using the BLPR form factor parameterization.

4.5.1.9 Results for NP fit with scalar, vector and tensor contribution (Reel and Imaginary parts)

Here, we present results from a multi-parameter scenario which is based on the NP parametrisation given in Ref. [121]. The NP contributions in $B \to D^*\ell\nu$ decays can be written using the effective field theory with the effective Hamiltonian given in Eq. 2.50 and the corresponding NP operators defined in Eq. 2.51. We can group the $B \to D^*\ell\nu$ Wilson coefficients in four combinations such as:

$$C_V^l = C_{V_R}^l + C_{V_L}^l, \quad C_A^l = C_{V_R}^l - C_{V_L}^l, \quad C_P^l = C_{S_R}^l - C_{S_L}^l, \quad C_T^l, \tag{4.35}$$

where the combination $C_S^l = C_{S_R}^l + C_{S_L}^l$ enters only in $B \to D\ell\nu$. Following Ref. [121], the minimal number of parameters to parametrise the Wilson coefficients is five, however, since the overall phase is unobservable, one can choose one of the complex coefficients to be real and positive. The results are presented when the tensor WC is chosen to be real and positive. Other WCs such as the vector and the scalar were also tested for this choice in toys studies and the toys are also documented in Appendix B.7.1. We observe the best results from toys when we make the assumption of real and positive WC on the tensor. The toys are summarized in section 4.6.1.6 while here the blinded results are presented. Following Eq. 4.35, the sum and difference of the right handed and left handed scalar WCs are introduced as fitting parameters (C_p and C_s). They are defined as

$$C_pRe = S_{qRlL}Re - S_{qLlL}Re \quad C_pIm = S_{qRlL}Im - S_{qLlL}Im \tag{4.36}$$

$$C_sRe = S_{qRlL}Re + S_{qLlL}Re \quad C_sIm = S_{qRlL}Im + S_{qLlL}Im \tag{4.37}$$

The sum (C_sRe and C_sIm) is fixed to an arbitrary number while the difference is a floating parameter during fitting. For the rest of the Wilson coefficients we impose the real and positive tensor and no constraint on the vector Wilson coefficient. The blinded fit results are given in Tab. 4.29 and the correlations in Tab. 4.30.

Parameter	Fit value ± uncertainty
C_pIm	xxx ± 0.1320
C_pRe	xxx ± 0.1230
$T_{qLlL}Re$	xxx ± 0.0058
$V_{qRlL}Im$	xxx ± 0.0128
$V_{qRlL}Re$	xxx ± 0.0080
$\Delta\rho^2$	xxx ± 0.0309
$\Delta\chi_2'$	xxx ± 0.1770
$\Delta\eta(1)$	xxx ± 0.1180
$\Delta\eta(1)'$	xxx ± 0.4900
$\Delta\tau_1$	1.1100 ± 0.3950
$\Delta\tau_2$	-2.0600 ± 0.3100
$\Delta t'$	0.6740 ± 0.1670
$\Delta\zeta_1$	0.2830 ± 0.3050
$\Delta\zeta'$	-1.4600 ± 0.2060
N $D_1(2420)^+$	10700.0 ± 2230.0
N $D_1(2420)^0$	0.0 ± 2.8
N D_1^+	5490.0 ± 3843.6
N $D_1(2430)^0$	0.0 ± 3711.2
N $D_2^st(2460)^+$	3384.2 ± 2793.1
N $D_2^st(2460)^0$	155.8 ± 2457.5
N D^*DX	5340.0 ± 590.0
N $D^*\mu$	221000.0 ± 1220.0
N $D^*\tau$	6260.0 ± 1120.0
N $D_{s1}(2536)^+$	844.0 ± 918.0
N $D_{s2}^*(2573)^+$	2480.0 ± 919.0
N D^{**}(Higher)	1040.0 ± 1250.0
N $D^{**}\tau$	2220.0 ± 782.0
N MisID	428.0 ± 181.0
N Comb	469.0 ± 305.0
N D^* comb	5980.0 ± 1030.0

Table 4.29: Values of the parameters determined by the fit to Run 1 data using the multi-parameter NP scenario with the BLPR form factor parametrisation.

Parameter	$CpIm$	$CpRe$	T_{qLlL}Re	V_{qRlL}Im	V_{qRlL}Re	$\Delta\rho^2$	$\Delta\chi'_2$	$\Delta\eta(1)$	$\Delta\eta(1)'$
$CpIm$	1.000	-0.198	0.010	0.091	-0.057	-0.027	0.035	-0.186	0.072
$CpRe$	-0.198	1.000	-0.040	-0.028	0.041	0.010	0.114	-0.110	-0.054
T_{qLlL}Re	0.010	-0.040	1.000	-0.022	0.044	-0.256	0.102	-0.011	-0.088
V_{qRlL}Im	0.091	-0.028	-0.022	1.000	0.024	0.005	0.006	0.001	-0.001
V_{qRlL}Re	-0.057	0.041	0.044	0.024	1.000	0.365	-0.059	0.473	-0.114
$\Delta\rho^2$	-0.027	0.010	-0.256	0.005	0.365	1.000	-0.649	-0.315	0.694
$\Delta\chi'_2$	0.035	0.114	0.102	0.006	-0.059	-0.649	1.000	0.400	-0.845
$\Delta\eta(1)$	-0.186	-0.110	-0.011	0.001	0.473	-0.315	0.400	1.000	-0.789
$\Delta\eta(1)'$	0.072	-0.054	-0.088	-0.001	-0.114	0.694	-0.845	-0.789	1.000

Table 4.30: Correlation coefficients of the parameters determined by the fit in the multi-parameter NP scenario with the BLPR form factor parametrization.

4.6 Toy studies

To validate the fit setup, a number of pseudo-experiments (toys) were performed. Toy data is generated for three different hadronic form factor parametrizations (CLN, BGL, BLPR) according to the different configurations of the fit. All the toy studies are set to use the set of parameters and fitting ranges consistent with the final fit to data in the respective configuration. Each toy fit is performed in the following steps:

- Generation of fit parameter values: The values for the yields of the signal and backgrounds are generated according to a Poisson distribution centred at the nominal fit results. The form factor parameters are generated using a uniform distribution within the statistical uncertainty of the fit to data.

- The fit model is built according to the generated parameters in the previous step and pseudo data is generated according to this model. The setup uses the templates as described in section 4.5.

- Generation of constraint terms: The mean values of gaussian constraint terms are generated from a gaussian distribution with mean and standard deviation of the nominal constraint term.

- The pseudo data is fitted with the model as described in Tab. 4.12 in ~ 1000 pseudo experiments (toys) for each of the configurations.

The pull distributions of the toys are analysed for all of the fit parameters. The pull is defined as following,

$$\text{pull}(X_n) = \frac{X_n^{final} - X_n^{true}}{\sigma(X_n)},$$

where X_n^{final} is the final value of the parameter after fitting, X_n^{true} is the parameter's generated value and $\sigma(X_n)$ is the statistical uncertainty on the fit parameter. The pulls are fitted with a Gaussian distribution from which the mean and the standard deviation are extracted. A convergence rate is calculated by considering converged fits for which the covariance matrix is declared positive defined at the end of the fit and as well the minimization has converged.

4.6.1 Toy fit results

In this section the pull distributions of the fit parameters, as well as the results of their Gaussian fits are given. In each of the fit configurations a summary plot showing the values of the mean and the standard deviation of the pulls for each fit parameter is given. In each of the toy configurations the form factor parameters for the backgrounds of type $B \to D^{**}\mu\nu$ are Gaussian constrained with the values given in Tab. 4.11. The standard deviations of the pull distributions of these parameters reflect the uncertainty of the constraint. We do not see any significant biases in any of the fit parameters, in the respective fit configuration studied. In some of the configurations a 10% bias or underestimate of the uncertainty can be seen. This will be accounted for when reporting the final fit results after unblinding. The results are summarized in the next three sections divided by fit configuration of the form factor parametrisation of the signal template. In all the plots below, only the converged toys are shown.

4.6.1.1 CLN toy studies

1000 toys were fitted in the CLN configuration (see Tab. 4.17 for the list of parameters and starting values) reporting a convergence rate of 99% . The summary plot of the fit parameters is given in Fig. 4.17. The ρ^2 and R_2 form factor parameters show a small bias and the uncertainties are well estimated.

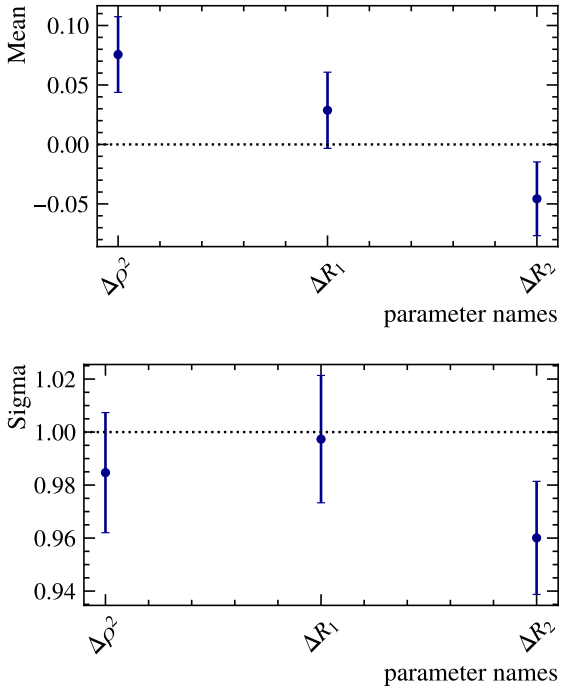


Figure 4.17: Summary plots of the mean values and standard deviations of the pull distributions within the CLN fit configuration.

4.6.1.2 BGL toy studies

The BGL toys were evaluated in the BGL configuration (see Tab. 4.9 for the list of BGL parameters available in HAMMER) labelled as nominal fit according to the BIC criterion explained in section 4.5.1.2 and compared in Tab. 4.14 to the alternative choices of BGL parameters considered (see Tab. 4.15 for the list of parameters and starting values). 1000 toys are displayed with a convergence rate of 100% and the summary plots of the parameters are given in Fig. 4.18. The fit is well behaved as seen from the mean and the mean and the standard deviation of the pulls.

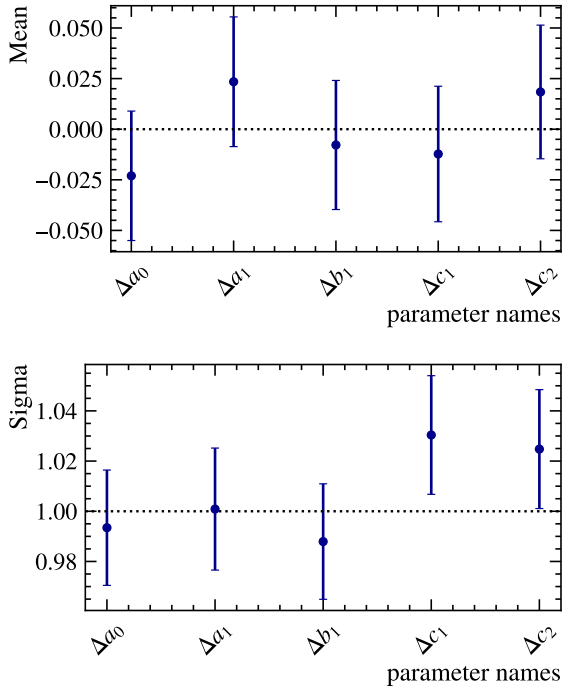


Figure 4.18: Summary plots of the mean values and standard deviations of the pull distributions within the BGL fit configuration.

4.6.1.3 BLPR toy studies

This section covers the toy studies regarding the BLPR form factor parametrization and the several configurations with the Wilson coefficients. The toys are separately produced in a SM scenario where the Wilson coefficients (WCs) are fixed to 0.0; and NP toys where the WCs are floated in the fit, vector (V_{qRl}), scalar (S_{qLl}) and tensor (T_{qLl}) individually and all of them together in the multi-parameter scenario.

4.6.1.4 BLPR SM toy studies

The BLPR form factor parametrisation was used to perform the SM toy studies. 1000 toys were fitted reporting a convergence rate of 91%. The summary plots are given in Fig. 4.19. The non-convergent fits were examined as a function of the generated parameter values, and no clear dependence or clustering in particular parameter regions was observed. The fit is showing biased pulls of order 0.1 or less for the $\Delta\rho^2$, and $\Delta\eta_p$ parameters and well estimated uncertainties.

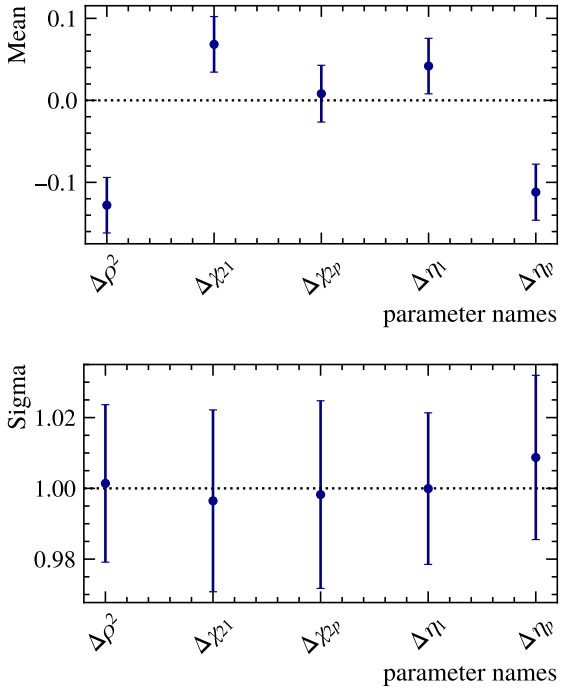


Figure 4.19: Summary plots of the mean values and standard deviations of the pull distributions within the BLPR fit configuration.

4.6.1.5 BLPR NP toy studies

In this section, the NP toys are presented as separated into two main categories: toys with single WC floating (where the real and imaginary parts of the WC are fit parameters separately) and the toys containing multiple WCs. For the case of multiple WCs, all WCs - vector (V_{qRl}), scalar (S_{qLl}) and tensor (T_{qLl}) - are generated and floated at the same time. The single WC toys are generated using a uniform distribution within the ranges listed in Tab. 4.31 which are the values of the statistical uncertainties of the WCs in some of the preliminary fits. Furthermore we consider generation of these toys for the multi-parameter WC scenario summarised later in 4.6.1.6. In all the results presented here only the converged NP toys are considered.

	Central Generation Value	Generation interval	Fitting Range
$V_{qRlL}Im$	0.0	± 1.11e-02	[-1,1]
$V_{qRlL}Re$	0.0	± 4.04e-02	[-1,1]
$S_{qLlL}Im$	0.0	± 1.64e-01	[-1,1]
$S_{qLlL}Re$	0.0	± 2.23e-01	[-1,1]
$T_{qLlL}Im$	0.0	± 6.17e-01	[-1,1]
$T_{qLlL}Re$	0.0	± 1.00e-01	[-1,1]

Table 4.31: WCs generation and fitting interval in the BLPR NP toys.

$\mathbf{V}_{qRlL}$ toys:

1000 toys were fitted reporting a convergence rate of 99%. A summary plot of the mean and standard deviations of the pull distributions is shown in Fig. 4.20. An example likelihood scan from the toys is given in Fig. 4.21.

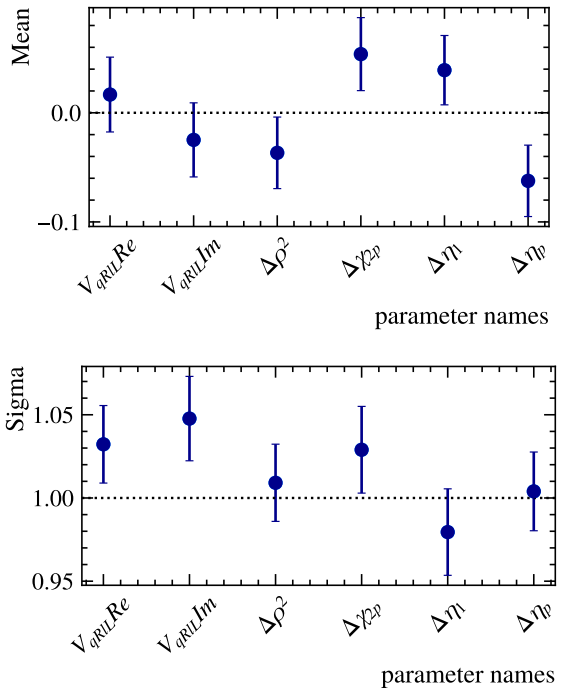


Figure 4.20: Summary plot of the mean values and standard deviations of the pull distributions in single WC-V_{qRlL} scenario. The respective WC and the form factor parameters from the signal are shown.

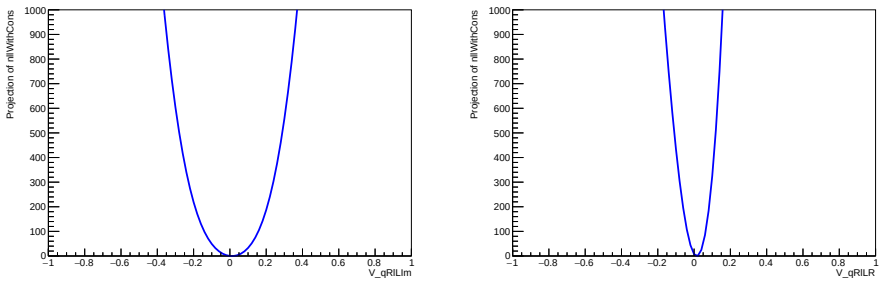


Figure 4.21: Likelihood scans of V_{qRlL}. Fitted values: V_{qRlL}Re = 0.01482, V_{qRlL}Im = 0.01108; generated values : V_{qRlL}Re = 0.01953, V_{qRlL}Im=0.007845

S_{qLlL} toys:

1000 toys were fitted reporting a convergence rate of 99%. A summary plot of the mean and standard deviations of the pull distributions is shown in Fig. 4.22. Biases are observed in the S_{qLlL} real and imaginary parts and as well as largely overestimated uncertainty for the Im(S_{qLlL}) WC. When MINOS is enabled for the asymmetric uncertainties we see improvement in the coverage for Im(S_{qLlL}) (plot in the appendix in Fig. A.1), however still observe overestimation for this parameter. Previous sensitivity studies (See section 4.4) demonstrate that the signal exhibits limited sensitivity to scalar operator contributions, leading to relatively flat regions in the likelihood profile along these parameter directions that can cause unreliable error estimations and systematic biases. An example likelihood scan from the toys is given in Fig. 4.23.

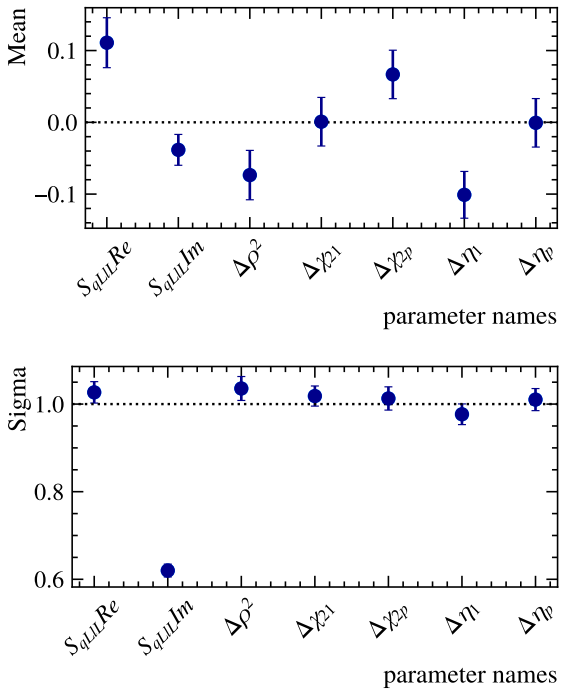


Figure 4.22: Summary plot of the mean values and standard deviations of the pull distributions in single WC-S_{qLlL} scenario. The respective WC and the form factor parameters from the signal are shown.

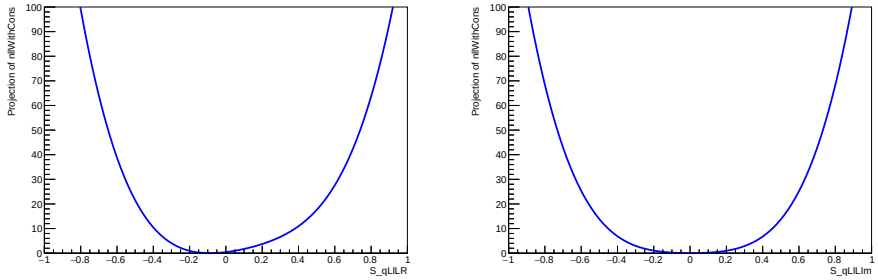


Figure 4.23: Likelihood scans of S_{qLlL}. Fitted values: S_{qLlL}Re = -0.08892, S_{qLlL}Im = 0.004298; generated values : S_{qLlL}Re = 0.004271, S_{qLlL}Im=0.02892.

$\mathbf{T}_{qLlL}$ toys:

1000 toys were fitted reporting a convergence rate of 90%. The summary plots are shown in Fig. 4.24. We observe biases for the T_{qLlL}Re parameter. The biases arise due to existing double solutions in the likelihood of the imaginary part for various points in the Wilson coefficients space. An example likelihood scan from the toys is given in Fig. 4.25.

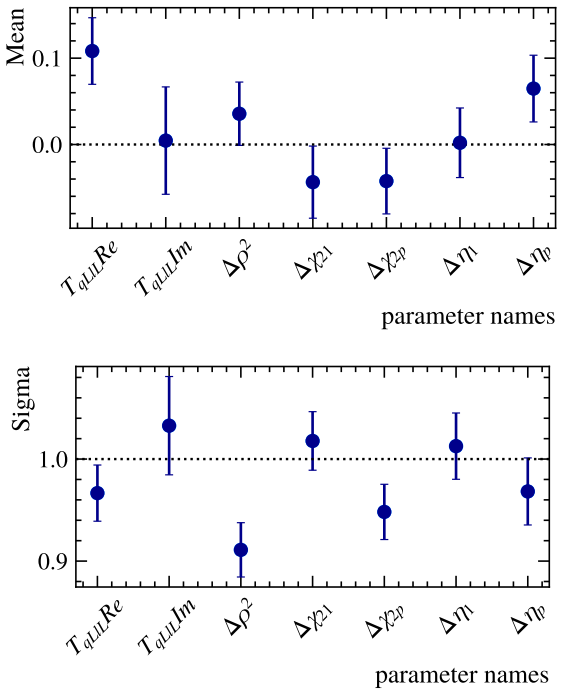


Figure 4.24: Summary plot of the mean values and standard deviations of the pull distributions in single WC-T_{qLlL} scenario. The respective WC and the form factor parameters from the signal and the backgrounds are shown.

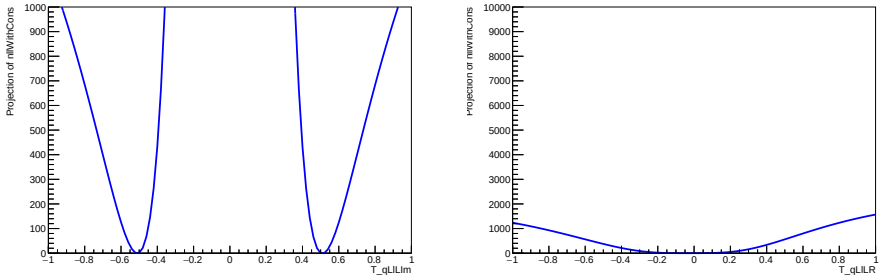


Figure 4.25: Likelihood scans of T_{qLlL}. Fitted values: T_{qLlL}Re = -0.04603, T_{qLlL}Im = 0.51; generated values : T_{qLlL}Re = -0.09512, T_{qLlL}Im=-0.5028.

4.6.1.6 Toys with multiple WCs

The first test in the multi-WC toy configuration was done when fixing the imaginary parts and floating together the real parts of the vector (V_{qRl}), scalar (S_{qLl}) and tensor (T_{qLl}). The toys are run with the fixed generation values of 0.1 (arbitrary chosen within the measurement range). The pull distributions are given in Fig. 4.26 where we see a well behaved fit.

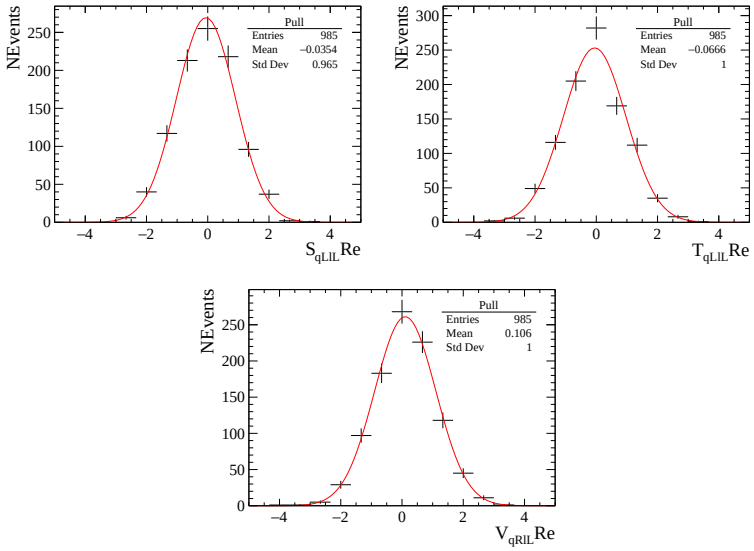


Figure 4.26: Pull distributions in the real-only WC scenario.

In addition, we consider a scenario where also the imaginary parts of right handed vector and scalar WCs are floating (explained in section 4.5.1.9). Toys were generated at a fixed value of 0.1 (arbitrarily chosen) with the fitting ranges as in Tab. 4.32. A set of 1000 toys were fitted reporting a convergence rate of 99% with the summary plots of summary of the pull distributions shown in Fig. 4.27. This configuration shows pulls with well estimated uncertainties and no significant biases. An example likelihood scan of the Wilson coefficients is shown in Fig. 4.28. This configuration is considered as the nominal multi-parameter Wilson coefficient scenario that is used for the final results in the analysis. Other configurations where the real and positive WC assumption is made differently were tested in Appendix B.7.

	Central Generation Value	Starting value	Fitting Range
$V_{qRlL}Im$	0.1	0.1	[-1, 1]
$V_{qRlL}Re$	0.1	0.1	[-1, 1]
C_pIm	0.0	0.0	[-2.2, 1.8]
C_pRe	0.0	0.0	[-2.2, 1.8]
C_sIm	0.2	0.2	fixed
C_sRe	0.2	0.2	fixed
$T_{qLlL}Im$	0.0	0.0	fixed
$T_{qLlL}Re$	0.1	0.1	[0, 1]

Table 4.32: Wilson coefficients used in this parametrization shown here along with their generation and starting values and fitting intervals.

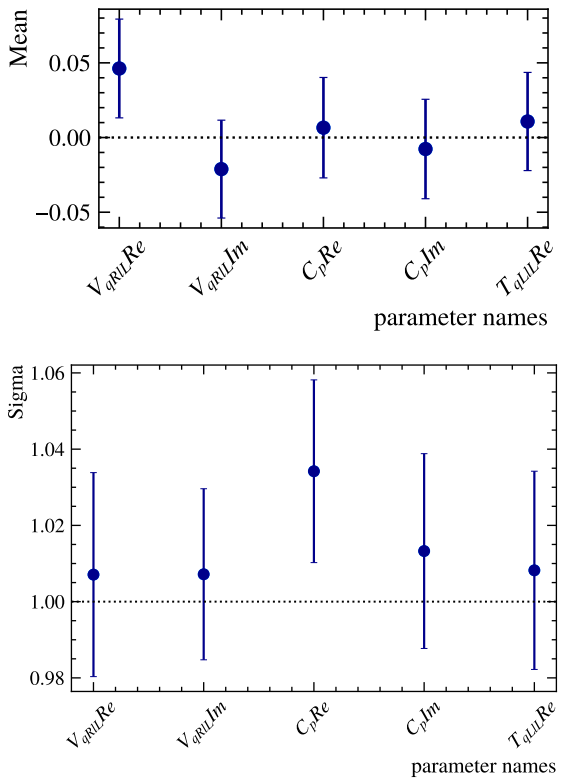


Figure 4.27: Summary plot of the mean values and standard deviations of the pull distributions of the Wilson coefficients from Tab. 4.32.

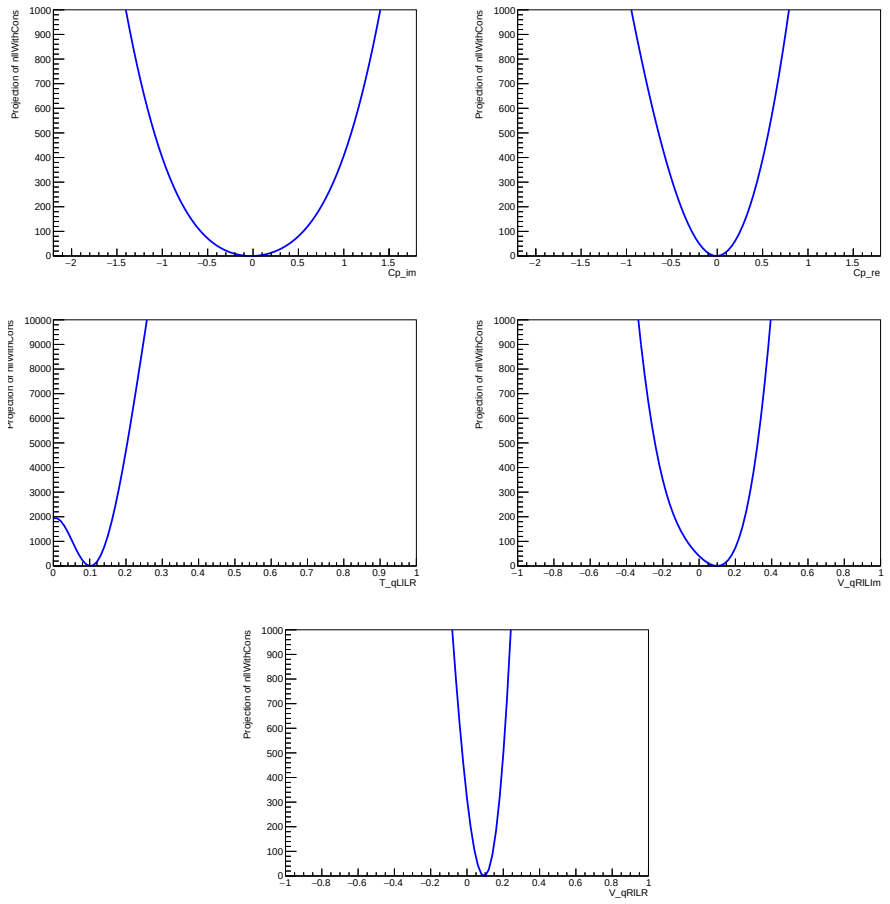


Figure 4.28: Likelihood scans of WCs when they generated and fitted as in Tab. 4.32 and the fitted values: V_{qRlL}Re = 0.094, V_{qRlL}Im = 0.099, T_{qLlL}Re = 0.102 C_pRe = -0.007 , C_pIm = -0.02.

4.6.2 Summary on the pseudo-experiment studies

For the SM form factor fits, all the parameters show well estimated uncertainties and unbiased behaviour, except for the $\bar{\rho}_*^2$ and $\eta(1)'$ BLPR parameters, where corrections are applied to account for biases of the order 10% of the statistical uncertainty.

In configurations where a single Wilson coefficient is extracted at a time, the fits for V_{RL} yield unbiased central values with exact uncertainty coverage. However, this is not the case for the S_{LL} and T_{LL} coefficients, which exhibit non-Gaussian behaviour in their imaginary components. To ensure accurate frequentist coverage for both the real and imaginary parts of S_{LL} and T_{LL}, a two-dimensional Feldman-Cousins scan is employed.

In scenarios where multiple Wilson coefficients are extracted simultaneously, the

pseudo-experiments indicate a Gaussian likelihood but reveal biases in the fitted central values. Relying on the Gaussian nature of the likelihood, the statistical uncertainties are scaled to ensure that the 1σ intervals encompass 68% of the generated true values. The inherent biases are evaluated using residual distributions, defined as the difference between the fitted and generated values. To correct for these shifts, the mode of the multidimensional residual distribution is evaluated via kernel density estimation (KDE). Finally, a systematic uncertainty is assigned to this correction procedure, defined as the deviation between the mean of the residual distribution and the KDE-extracted mode.

4.7 Systematic uncertainties

The systematic uncertainties that affect this measurement include the limited size of the simulated samples used for the fit templates, residual differences between simulation and data, choice of fixed form-factor parameters, modelling of background components, and Coulomb corrections. In the BGL form factor fit a systematic uncertainty is also associated to the truncation of the BGL form-factor parameters series. The NP Wilson coefficient measurement is also affected by the NP contributions assumed in $B^0 \to D^{*-}\tau^+\nu_\tau$ decays. In addition, the multi Wilson coefficient scenario is affected by the bias correction, discussed in section 4.6.1.5, and a systematic uncertainty is assigned to this correction.

Tab. 4.33 shows the size of each contribution to the total systematic uncertainty for each parameter in the three SM form-factor fits, while Tab. 4.34 shows the size of each contribution to the total systematic uncertainty for each parameter in the five NP scenarios.

The systematic uncertainty arising from the finite statistical precision of the Monte Carlo simulation is evaluated utilizing a bootstrap resampling technique [122]. Ensembles of alternative templates are generated by repeatedly drawing candidates from the nominal simulated samples with replacement. The data fit is subsequently performed using these alternative templates, and the systematic uncertainty is assigned as the standard deviation of the resulting parameter distributions.

To account for potential residual discrepancies between the data and the simulation, an additional systematic uncertainty is assessed by introducing alternative simulation corrections. This is achieved through a multistage reweighting procedure. Building upon the baseline correction, alternative binning schemes and correction

Table 4.33: Systematic uncertainties affecting the measurement of hadronic form-factor parameters. The total systematic uncertainties are obtained assuming no correlations among the contributions. For comparison, the statistical uncertainties are also reported.

	Uncertainties (10^{-3})								**Uncertainties** (10^{-2})				
	CLN			BGL					BLPR				
Systematic source	R_1	R_2	ρ^2	a_0	a_1	b_1	c_1	c_2	$\bar{\rho}^2_*$	$\chi_2(1)$	$\chi_2'(1)$	$\eta(1)$	$\eta(1)'$
Simulation sample size	13	12	16	<1	19	4	1	22	2.4	8.7	15	10	42
Simulation corrections	47	29	18	2	10	30	4	5	2.5	27	15	34	18
BGL truncation	–	–	–	<1	17	6	<1	4	–	–	–	–	–
Fixed d_i parameters	–	–	–	<1	5	<1	<1	9	–	–	–	–	–
Fixed b_0 parameter	–	–	–	<1	3	<1	<1	4	–	–	–	–	–
Fixed R_0 parameter	1	1	3	–	–	–	–	–	–	–	–	–	–
Fixed χ_3' parameter	–	–	–	–	–	–	–	–	<0.1	3.4	1.6	1.8	9
MisID model	4	1	1	<1	16	<1	<1	10	0.1	1.8	0.3	3.2	0.5
Physics bkg. model	<1	<1	<1	<1	<1	<1	<1	<1	<0.1	0.2	0.2	0.2	0.6
Coulomb correction	<1	<1	<1	<1	<1	<1	<1	<1	<0.1	0.3	0.2	0.5	0.6
Total systematic	49	31	30	2	31	31	7	26	4	29	21	36	47
Stat. uncertainty	32	14	20	1	22	4	1	26	3	12	18	14	52

variables are applied, and the fit is repeated. At each successive stage, supplementary weights are derived from three-dimensional histograms constructed from combinations of variables—such as the B^0-meson flight distance, final-state transverse momentum, and impact-parameter χ^2—to match the data-fit agreement.

The nominal fit model assumes Standard Model for the $B^0 \to D^*\tau\nu$ background. To estimate the impact of neglecting potential NP contributions in this mode, the data fit is repeated 1000 times, fixing the NP Wilson coefficients in the $B^0 \to D^{*-}\tau^+\nu_\tau$ model to random values. These values are sampled from regions theoretically compatible with current $R(D)$ and $R(D^*)$ measurements [52]. The standard deviation of the parameter distributions resulting from these alternative fits defines the assigned systematic uncertainty.

The systematic uncertainty associated with the truncation order of the BGL form-factor parametrisation is evaluated through a dedicated pseudo-experiment study. A set of toys is generated using the baseline fit model and subsequently fitted with an expanded model that includes one additional higher-order term in the a, b, and c expansion series. The systematic uncertainty for each parameter is defined as the deviation between the mean of the fitted parameter distribution in the alternative toys and its baseline generation value.

The impact of fixing specific form-factor parameters—specifically b_0 and d_i in

Table 4.34: Systematic uncertainties affecting the measurement of the NP Wilson coefficients. The total systematic uncertainties are obtained assuming no correlations among the contributions.

		Uncertainties (10^{-3})								
Systematic source	Sim. size	NP in $B \to D^*\tau\nu$	Sim. corr.	Fixed χ'_3	Fixed $\chi_2(1)$	MisID model	Bkg. model	Coulomb corr.	Bias corr.	Total syst.
Single WC fit										
$\mathcal{R}e(S_{LL})$	81	71	16	27	40	29	2	4	–	119
$\mathcal{I}m(S_{LL})$	27	18	32	60	50	< 1	1	3	–	91
$\mathcal{R}e(V_{qRL})$	6	4	5	< 1	< 1	4	< 1	< 1	–	10
$\mathcal{I}m(V_{RL})$	10	1	7	1	2	1	< 1	< 1	–	12
$\mathcal{R}e(T_{LL})$	4	4	2	< 1	2	3	< 1	< 1	–	7
$\mathcal{I}m(T_{LL})$	1	< 1	< 1	< 1	< 1	< 1	< 1	< 1	–	1
Multiple WC fit										
$\mathcal{R}e(C_P)$	81	22	37	13	15	12	1	< 1	109	144
$\mathcal{I}m(C_P)$	74	23	7	47	57	1	1	< 1	69	127
$\mathcal{R}e(V_{RL})$	6	5	5	2	3	< 1	< 1	< 1	1	10
$\mathcal{I}m(V_{RL})$	10	1	7	< 1	3	1	< 1	< 1	2	13
$\mathcal{R}e(T_{LL})$	4	4	2	6	6	1	< 1	< 1	2	11
Multiple $\mathcal{R}e$ WC fit										
$\mathcal{R}e(S_{LL})$	89	13	38	32	8	13	1	< 1	142	176
$\mathcal{R}e(V_{RL})$	6	4	5	< 1	< 1	1	< 1	< 1	< 1	9
$\mathcal{R}e(T_{LL})$	4	4	2	3	2	1	< 1	< 1	2	7

the BGL framework, and χ'_3 and $\chi_2(1)$ in the BLPR formalism—is evaluated by performing alternative fits. In these variations, the fixed parameters are sampled within their respective uncertainties as reported in Refs. [123], [41], and [17].

Misidentification backgrounds, predominantly hadrons misidentified as muons, are susceptible to imperfect modelling. This associated uncertainty is quantified by replacing the nominal background shape with an alternative model that incorporates track momentum smearing, which accounts for the kinematic effects of in-flight pion and kaon decays.

Uncertainties related to the shape parametrisation of the physical backgrounds, primarily the highly excited $B \to D^{**}\mu^+\nu_\mu$ and double-charm $B \to D^{*-}(H_c \to \mu^+X)(X')$ decays, are propagated by performing 1000 alternative fits. These fits utilise varied template shapes bounded by the uncertainties measured in Ref. [124]. The standard deviation of the resulting fit values is assigned as the *physics bkg. model* systematic uncertainty, as detailed in Tab. 4.33.

The effect of neglecting Coulomb interaction corrections in the simulated samples is assessed by reweighting the signal template candidates according to Eq. 16 of

Ref. [125]. The observed parameter shifts between the nominal and alternatively weighted templates are taken as the systematic uncertainty.

In summary, for the Standard Model form-factor fits, the dominant systematic contributions arise from the limited simulated sample sizes and the residual data-simulation differences. The correlations between parameters induced by each systematic source are explicitly evaluated and incorporated into the total correlation matrix presented in Tab. 4.35. For the extraction of the NP Wilson coefficients, the hierarchy of systematic uncertainties is scenario-dependent, but is typically dominated by the finite simulation size and bias corrections (where applicable), followed by the NP contributions in the τ mode and data-simulation discrepancies.

4.8 Unblinded results and conclusion

This section presents the conclusion on the measurement of hadronic form-factor (FF) parameters and New Physics (NP) Wilson coefficients (WCs) in $B^0 \to D^{*-}\mu^+\nu_\mu$ decays. The analysis is based on a five-dimensional binned likelihood fit to 3 fb^{-1} of LHCb data. Notably, this work provides the first direct measurement of NP WCs along with the hadronic FF parameters for $B^0 \to D^{*-}\ell^+\nu_\ell$ at LHCb. The results achieve improved precision and remain compatible with both existing measurements and theoretical predictions.

The FF parameters are extracted using three distinct parametrisations—BGL, BLPR, and CLN—which yield mutually consistent results. The measured values for the FFs are summarized in Tab. 4.35. To validate the results, the extracted FFs are compared against various theoretical frameworks and experimental datasets. Fig. 4.29 illustrates the comparison between the results obtained using CLN, BGL and BLPR parametrisations, all converted to the BGL basis (Eq. 2.100). To ensure a consistent comparison with lattice predictions at zero recoil ($w = 1$), the BLPR form factors are rescaled following the procedure in Ref. [17] using the lattice value from Ref. [126]. A noticeable tension exists between the CLN and BLPR results for $f(q^2)$, which is likely a consequence of the restrictive assumptions inherent to the CLN parametrisation. Furthermore, while the BGL and CLN fits are insensitive to $\mathcal{F}_2(q^2)$ (See section 4.5.1.2), the BLPR fit incorporates this term through parameters in the helicity-suppressed amplitude (Eq. 2.114).

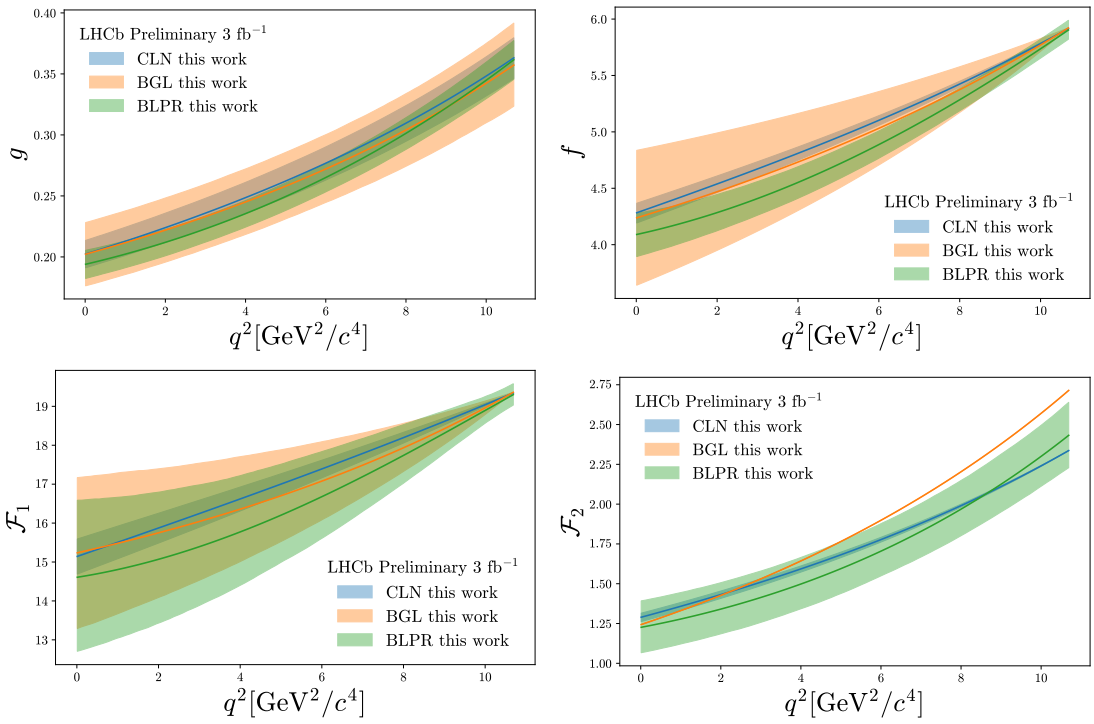


Figure 4.29: Comparison of the results obtained in this form-factor measurement using CLN (blue), BGL (orange), and BLPR (green) parametrisations. The uncertainty bands are derived assuming that systematic uncertainties are uncorrelated. The BGL form-factor basis is used. The BGL form-factor parameters associated to $\mathcal{F}_2$ are fixed in this measurement and therefore the uncertainty band is not available.

The BGL results are further compared to recent LQCD calculations in Fig. 4.30. Across the full q^2 range, the form factors $f(q^2)$ and $g(q^2)$ appear generally compatible with predictions from HPQCD [7], Fermilab-MILC [127], and JLQCD [128]. However, for $\mathcal{F}_1(q^2)$, this measurement shows significantly better agreement with the Fermilab-MILC and JLQCD results than with those from HPQCD. Detailed comparisons for the BLPR and CLN cases are provided in Appendix D.

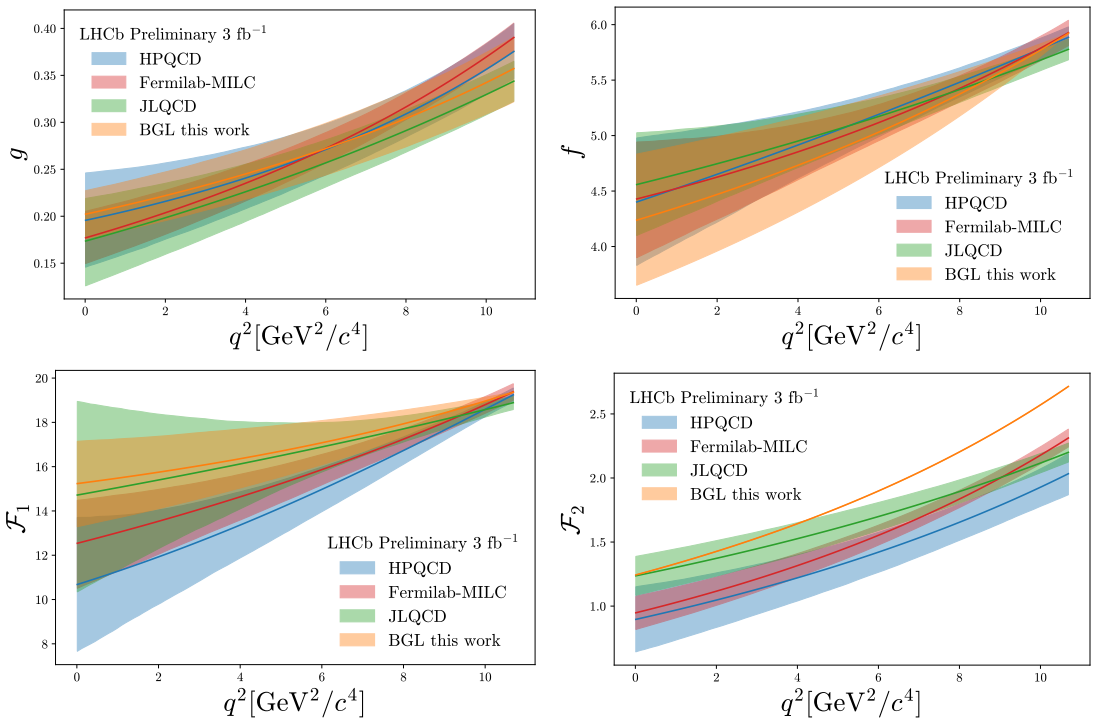


Figure 4.30: Comparison of the results obtained in this form-factor measurement using the BGL parametrisation (orange) to lattice QCD calculations from HPQCD (blue), Fermilab-MILC (red) and JLQCD (green). The uncertainty bands for this work are derived assuming that systematic uncertainties are uncorrelated. The results are compared in the BGL form-factor basis. The form-factor parameters associated to $\mathcal{F}_2$ in the BGL parametrisation are fixed (see Tab. 4.9) in this measurement therefore there is no uncertainty band.

Finally, the consistency of this work with complementary experimental datasets is shown in Fig. 4.31. The angular observables A_{FB}, $\tilde{F}_{\mathrm{L}}$, and F_{L}—calculated using the FF parameters determined in Ch. 4—show excellent agreement with the results of the BLPR fit to Belle data [17, 129, 130]. The latter combines Belle's detector-corrected distributions with constraints from lattice data [126, 131] and QCD sum rules [132–134]. Additionally, Fig. 4.32 shows the comparison of decay rate density in w computed from BGL fit results with different LQCD predictions and Belle-Belle II HFLAV average results [52], where systematics uncertainties included.

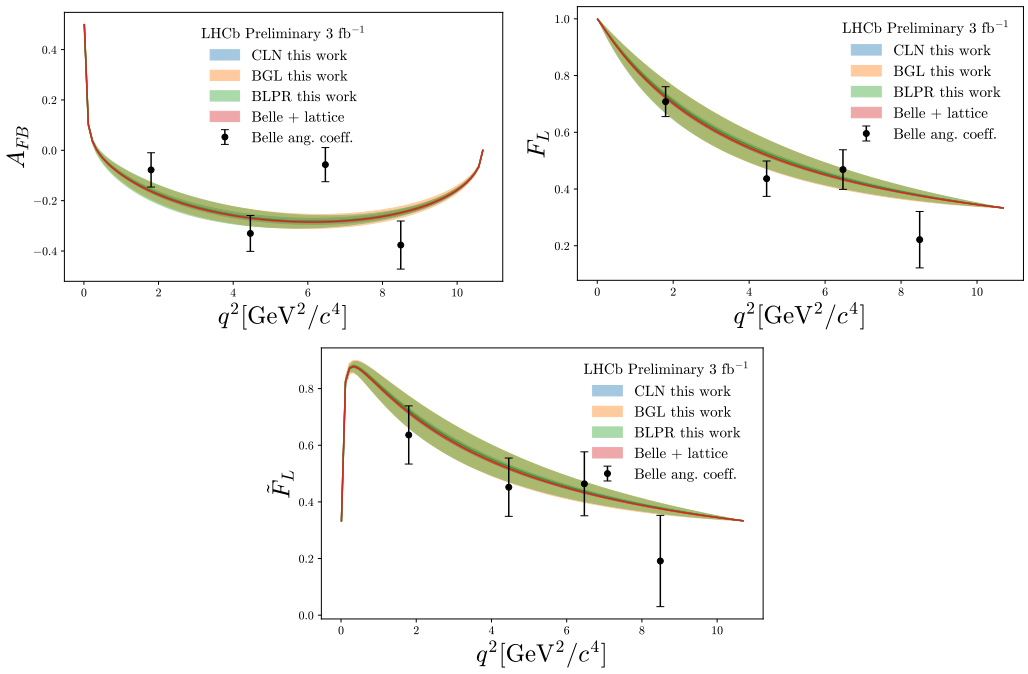


Figure 4.31: Distribution of forward-backward asymmetry of the muon (A_{FB}), longitudinal polarisation of D^* (F_{L}) and polarisation of the muon ($\tilde{F}_{\mathrm{L}}$) estimated using the values of hadronic form-factors parameters measured in this analysis. The results for various form-factor parametrisations are compared with Belle results from Ref. [17] (red) and Ref. [18] (black points). The uncertainty bands for CLN, BGL and BLPR form-factor parametrisations from this work are derived assuming that systematic uncertainties are uncorrelated.

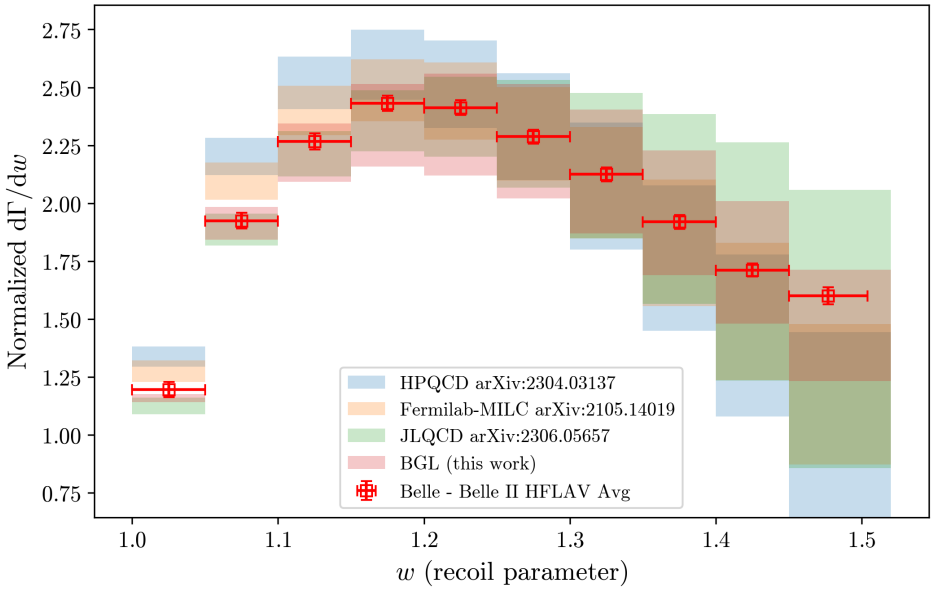


Figure 4.32: Normalised decay rate of $B^0 \to D^{*-}\mu^+\nu_\mu$ in w compared, with the total uncertainties.

Table 4.35: Standard Model fit results. On the left measured values are reported alongside the statistical and systematic uncertainties. On the right the statistical correlation matrix is shown.

CLN parametrisation					
		Statistical correlations			
			R_1	R_2	ρ^2
R_1	1.303 ± 0.032 (stat) ± 0.049 (syst)	R_1	1.00	0.66	-0.61
R_2	0.859 ± 0.014 (stat) ± 0.031 (syst)	R_2		1.00	-0.77
ρ^2	1.211 ± 0.020 (stat) ± 0.030 (syst)	ρ^2			1.00

BGL parametrisation							
		Statistical correlations					
			a_0	a_1	b_1	c_1	c_2
a_0	0.026 ± 0.001 (stat) ± 0.002 (syst)	a_0	1.00	-0.91	0.50	0.35	-0.27
a_1	-0.039 ± 0.022 (stat) ± 0.031 (syst)	a_1		1.00	-0.56	-0.23	0.15
b_1	-0.008 $\pm$ 0.004 (stat) $\pm$ 0.031 (syst)	b_1			1.00	0.58	-0.48
c_1	-0.001 ± 0.001 (stat) ± 0.007 (syst)	c_1				1.00	-0.97
c_2	0.019 ± 0.026 (stat) ± 0.026 (syst)	c_2					1.00

BLPR parametrisation							
		Statistical correlations					
			$\bar{\rho}^2_*$	$\chi_2(1)$	$\chi_2^{'}(1)$	$\eta(1)$	$\eta(1)'$
$\bar{\rho}^2_*$	1.28 ± 0.03 (stat) ± 0.04 (syst)	$\bar{\rho}^2_*$	1.00	-0.28	-0.68	-0.27	0.83
$\chi_2(1)$	-0.11 ± 0.12 (stat) ± 0.29 (syst)	$\chi_2(1)$		1.00	0.11	-0.68	-0.33
$\chi_2^{'}(1)$	0.38 ± 0.18 (stat) ± 0.20 (syst)	$\chi_2^{'}(1)$			1.00	0.32	-0.85
$\eta(1)$	0.43 ± 0.14 (stat) ± 0.36 (syst)	$\eta(1)$				1.00	-0.38
$\eta(1)'$	-0.52 ± 0.52 (stat) ± 0.47 (syst)	$\eta(1)'$					1.00

The measured values for the NP Wilson coefficient parameters, for the five scenarios considered, are reported in Tab. 4.36. The results are consistent with zero, in agreement with the SM predictions. The statistical correlations among the Wilson coefficients in the five scenarios considered are given in Tab. 4.37.

To guarantee proper frequentist uncertainty coverage for the real and imaginary components of the S_{LL} and T_{LL} NP Wilson coefficients, a two-dimensional Feldman-Cousins scan is executed for their respective independent fits. The resulting 1σ, 2σ, and 3σ confidence contours are presented in Fig. 4.33. This computationally intensive procedure is not required for the V_{RL} coefficient, as dedicated pseudo-experiments confirm unbiased central values and accurately estimated uncertainties under the standard likelihood approximation. Consequently, the explicit 68% confidence intervals derived from the Feldman-Cousins method are reported for the isolated S_{LL} and T_{LL} results in Tab. 4.36.

The extracted parameters can be directly compared to the recent phenomenolog-

Table 4.36: NP Wilson coefficient fit results for the five NP scenarios considered.

Single WC fit	
$\mathcal{R}e(S_{LL})$	0.200 ± 0.100 (stat) ± 0.119 (syst)
$\mathcal{I}m(S_{LL})$	0.000 ± 0.200 (stat) ± 0.091 (syst)
$\mathcal{R}e(V_{RL})$	0.000 ± 0.008 (stat) ± 0.010 (syst)
$\mathcal{I}m(V_{RL})$	0.005 ± 0.013 (stat) ± 0.012 (syst)
$\mathcal{R}e(T_{LL})$	0.020 ± 0.008 (stat) ± 0.007 (syst)
$\mathcal{I}m(T_{LL})$	$0.000\ ^{+0.014}_{-0.016}$ (stat) ± 0.001 (syst)
Multiple WC fit	
$\mathcal{R}e(C_P)$	$0.048\ ^{+0.123}_{-0.147}$ (stat) ± 0.144 (syst)
$\mathcal{I}m(C_P)$	$0.082\ ^{+0.118}_{-0.128}$ (stat) ± 0.127 (syst)
$\mathcal{R}e(V_{RL})$	0.000 ± 0.008 (stat) ± 0.010 (syst)
$\mathcal{I}m(V_{RL})$	0.009 ± 0.013 (stat) ± 0.013 (syst)
$\mathcal{R}e(T_{LL})$	$0.019\ ^{+0.006}_{-0.007}$ (stat) ± 0.011 (syst)
Multiple $\mathcal{R}e$ WC fit	
$\mathcal{R}e(C_P)$	$0.028\ ^{+0.162}_{-0.126}$ (stat) ± 0.176 (syst)
$\mathcal{R}e(V_{qRlL})$	-0.001 ± 0.008 (stat) ± 0.009 (syst)
$\mathcal{R}e(T_{qLlL})$	$0.020\ ^{+0.006}_{-0.009}$ (stat) ± 0.007 (syst)

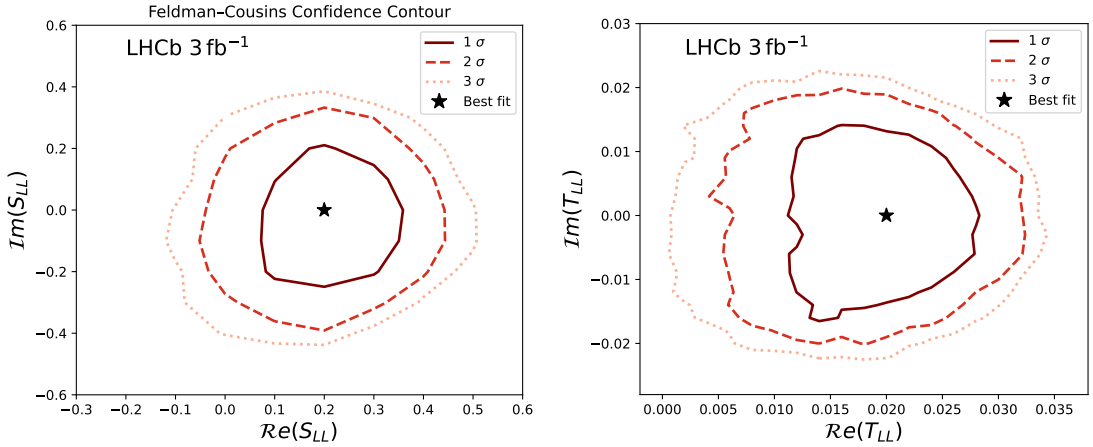


Figure 4.33: The 1, 2 and 3σ confidence contours for S_{LL} and T_{LL} NP Wilson coefficients, obtained with a two-dimensional Feldman-Cousins scan for the real and imaginary part of each WC.S_{qLlL} and T_{qLlL} correspond to the results of the single WC scenario in Table 4.36.

ical analysis presented in Ref. [19], as illustrated in Fig. 4.35. While the measured NP Wilson coefficients exhibit excellent compatibility with these prior findings, the present analysis achieves superior precision in the determination of the vector and scalar Wilson coefficients. This improvement is fundamentally driven by the method-

Table 4.37: Statistical correlations among the Wilson coefficients for the different NP scenarios.

Single WC fit					
	$\mathcal{R}e(S_{LL})$	$\mathcal{I}m(S_{LL})$			
$\mathcal{R}e(S_{LL})$	1.0	0.061			
$\mathcal{I}m(S_{LL})$		1.0			
	$\mathcal{R}e(V_{RL})$	$\mathcal{I}m(V_{RL})$			
$\mathcal{R}e(V_{RL})$	1.0	0.061			
$\mathcal{I}m(V_{RL})$		1.0			
	$\mathcal{R}e(T_{LL})$	$\mathcal{I}m(T_{LL})$			
$\mathcal{R}e(T_{LL})$	1.0	0.058			
$\mathcal{I}m(T_{LL})$		1.0			
Multiple WC fit					
	$\mathcal{I}m(C_P)$	$\mathcal{R}e(C_P)$	$\mathcal{R}e(T_{LL})$	$\mathcal{I}m(V_{RL})$	$\mathcal{R}e(V_{RL})$
$\mathcal{I}m(C_P)$	1.000	-0.198	0.010	0.091	-0.057
$\mathcal{R}e(C_P)$		1.000	-0.040	-0.028	0.041
$\mathcal{R}e(T_{LL})$			1.000	-0.022	0.044
$\mathcal{I}m(V_{RL})$				1.000	0.024
$\mathcal{R}e(V_{RL})$					1.000
Multiple $\mathcal{R}e$ WC fit					
	$\mathcal{R}e(S_{LL})$	$\mathcal{R}e(V_{RL})$	$\mathcal{R}e(T_{LL})$		
$\mathcal{R}e(S_{LL})$	1.000	-0.067	-0.027		
$\mathcal{R}e(V_{RL})$		1.000	-0.063		
$\mathcal{R}e(T_{LL})$			1.0		

ological differences between the two approaches. The study in Ref. [19] relies on a combined phenomenological fit, incorporating Belle II measurements of angular coefficients evaluated in discrete q^2 bins [18] alongside LQCD inputs from the HPQCD, JLQCD, and Fermilab-MILC collaborations. In contrast, the framework developed in this work leverages the full multi-dimensional kinematic space of the helicity angles and q^2, enabling a comprehensive and more sensitive determination of the New Physics contributions directly from the data.

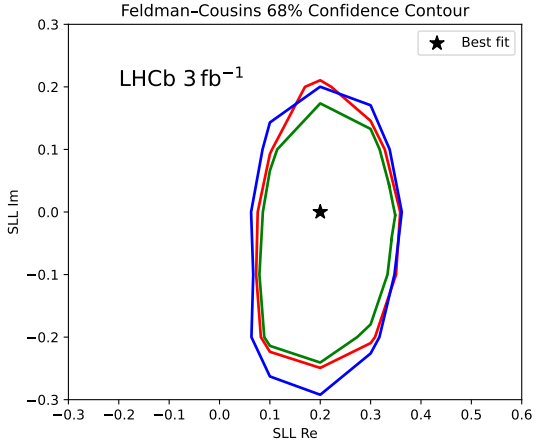


Figure 4.34: Three 68% confidence contours for the S_{LL}, obtained assuming different values for the BLPR form factor parameter $\eta(1)$. The contours are obtained with a two-dimensional Feldman-Cousins scan for the real and imaginary part of the WC parameter. $\eta(1)$ is fixed to $\pm 1\sigma$ of the SM fit value for each alternative contour in blue and green respectively. The similarity of the contours shows that the NP parameters determination is uncorrelated to the hadronic form factors.

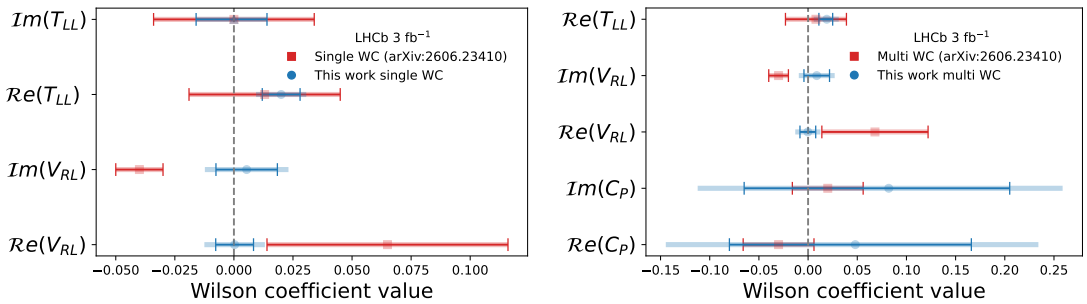


Figure 4.35: Comparison of NP Wilson coefficients measured when fitting one Wilson coefficient at a time (left) and determining multiple NP Wilson coefficients (right) to the results of the recent analysis reported in Ref. [19].

Chapter 5

Differential decay rate shape measurement of $B^0 \to D^{*-}\mu^+\nu_\mu$

This chapter presents my second measurement, the differential decay rate shape of $B^0 \to D^{*-}\mu^+\nu_\mu$ as the same decay channel in the analysis of new physics search described in Ch. 4. Consequently, frequent references will be made to the previous chapter, as the theoretical formalism, analysis methodology and tools are shared while explaining the additional concepts specific to this analysis methodology and Run 2 datasets used.

5.1 Motivation and analysis overview

The differential decay rate in w provides direct sensitivity to the hadronic form factors [7] governing the semileptonic transition and allows for precise tests of theoretical predictions from Lattice QCD (LQCD). Especially, for the low w region (high q^2), LQCD predictions are well defined [20] (See Fig. 5.1), and where LHCb, thanks to high statistics and forward boost, benefits from substantially better sensitivity than Belle [5], which previously performed the same measurement. The present data from Belle and Belle II show significant disagreement with the most recent LQCD calculations, as pointed in [135]. Hence, a high precision determination of spectrum differential decay rate is paramount to understand the source of these discrepancies (See section 2.5.2), and will also serve as an essential input to global semileptonic fits.

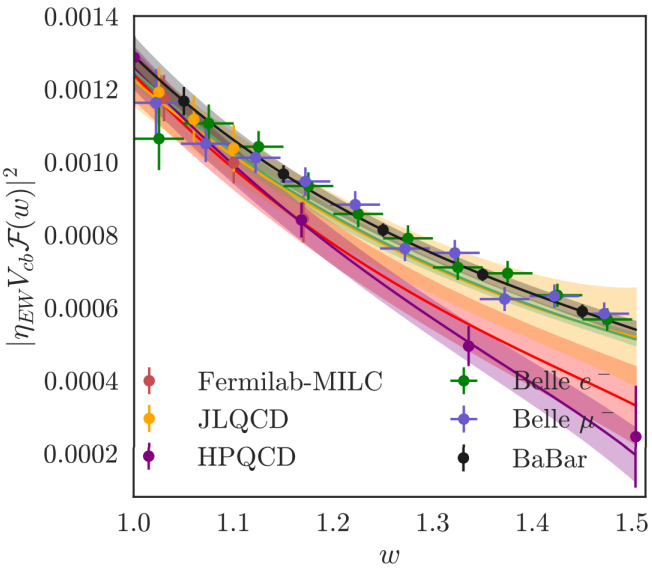


Figure 5.1: Comparison of the shapes of the decay amplitude for the different calculations and experiments. Image taken from [20].

The goal of this analysis is to obtain an unfolded and efficiency-corrected differential decay rate in the hadron recoil parameter w using same 10-bins binning scheme as Belle II measurement [5] for future comparison. For each w bin, a fit to the $m^2_{miss} = (P_B - P_{D^*\ell})^2$ is performed to extract the sample composition. The MC signal m^2_{miss} template is reweighted by BGL FF parametrisation. For the one-dimensional fits to m^2_{miss}, a novel framework referred as `HAMMER-PyHf` has been adopted. This fit framework is a combination of `PyHf`(`Python` based `HistFactory` [136]) and HAMMER [116], and it is built upon model-agnostic likelihoods reweighting scheme called `redist` [137] where the template shapes are varied with the model defined. The fitter enables a reliable signal estimate which will be unfolded and efficiency corrected. To mitigate the unconstrained kinematics due to the missing particle, the neutrino in the decay channel, a Gaussian Precess Regression is implemented to predict the B-meson momentum. By using this machine-learning–based approach, we obtain a significantly better resolution ($\sim$20% improvement in w comparing to random solution case in section 4.2), which enhances the precision of the extracted decay-rate shape. The unfolded and efficiency corrected 1D spectrum in w is measured, and will be compared to both Belle results and state-of-the-art LQCD predictions. To avoid experimenter bias, the values of the efficiencies measured to correct the w spectrum are currently not displayed (blinding), and not included in this thesis. It has been proposed to extend this one-dimensional differential decay rate measurement to a

four-dimensional one, for extracting the angular coefficients [138].

This analysis uses the same decay mode $B^0 \to D^{*-}\mu^+\nu_\mu$ with D^* decaying into $D^0\pi^+$ and D^0 reconstructed through $D^0 \to K\pi$ final state as my previous measurement in Ch. 4 . As a reminder to section 2.4, it is useful to re-define the certain variables of interest including kinematics variables to be used in the fit and one-dimensional (1D) decay rate expression to be measured in this analysis. The kinematics of the process is characterised with the $q^2(\propto w)$ and m^2_{miss}variables calculated as

$$q^2 = (p_B - p_{D^*})^2; \quad w = \frac{m_B^2 + m_{D^*}^2 - q^2}{2m_B m_{D^*}} \tag{5.1}$$

$$m^2_{miss} = (p_B - p_{D^*} - p_\mu)^2 \tag{5.2}$$

where p_B, p_{D^*}, p_μ are the 4-momenta of the D^*, B^0 and the μ. When m^*_D and angles are integrated in 2.56, the differential decay rate expression in w becomes as following

$$\frac{d\Gamma(B^0 \to D^* l\nu_l)}{dw} = \frac{G_F^2 |V_{cb}||\eta_{EW}|^2 m_{D^*}\sqrt{w^2-1}\, q^2}{48\pi^3}\left(1 - \frac{m_\mu^2}{q^2}\right)^2 \tag{5.3}$$

$$\times \left[(|H_+|^2 + |H_-|^2 + |H_0|^2)\left(1 + \frac{m_\mu^2}{2q^2}\right) + \frac{3}{2}\frac{m_\mu^2}{q^2}|H_t|^2\right] \tag{5.4}$$

where $H_{\pm,0,t}$ are helicity amplitudes described in section 2.4 (See Eqs. 2.69, 2.68, 2.70) and they are parametrised by the BGL form factors described in section 2.4.1.1. In this analysis, the differential spectrum in Eq. 5.3 is measured while accounting for w resolution and efficiency effects.

5.2 Datasets and Simulation

This analysis uses the Run 2 sample of p–p collisions collected by the LHCb experiment at a centre-of-mass energy of 13 TeV, corresponding to an integrated luminosity of approximately $\sim$6 fb^{-1}. The *nominal* sample consists of events that have correct relative electric charges of the final state particles D^* and μ as opposite charges –*right sign* (RS)–. However, there might be random combinations of final state particles with unphysical event with D^{*+} and μ^+ or D^{*-} and μ^- and therefore they must be accounted for the background modelling. This type of sample is

called *wrong sign* (WS). In addition to *wrong sign* samples, a MisID (mis-identified) sample is selected to model the contributions from misidentified hadrons (largest contribution from kaons and pions) and electrons as muons.

5.2.1 Simulation

Simulation samples are essential for this analysis, as collision data alone cannot provide a complete description of the underlying processes. Monte Carlo (MC) samples therefore play a fundamental role in this analysis. Specifically, they are used to evaluate the signal selection efficiencies, construct the probability density templates required for the maximum likelihood fit, model detector resolution effects, and assess various sources of systematic uncertainty. The full LHCb simulation chain has already been described in section 3.4.1 where all sub-detectors systems described in section 3.2. However, for this analysis, in order to reduce computing time and storage requirements, *Tracker-Only* simulated samples are used, in which only the tracking detectors (described in section 3.2.2) are fully simulated. The necessary information missing from the sub-detectors, trigger and PID, are emulated in the samples; the emulation procedure is explained in section 5.4.

The decay modes are simulated under detector conditions corresponding to Run 2 for each data-taking year, with the number of generated events listed in Tab. 5.1. In all modes, the D^*decays via $D^*\to D^0(\to K\pi)\pi_s$, and the τ decays through $\tau \to \mu\nu\nu$, with charge conjugation implied throughout.

Modes	Cocktail Notes	Size (16/17/18)
$B^0 \to D^*\mu\nu$	Single Mode	24M/23M/28M
$B^0 \to D^*\tau\nu$	Single Mode	8.8M/9.4M/12M
$B^0 \to D^{**+}\mu\nu$	D_1^+, $D_1^{\prime+}$, D_2^{*+}	4.8M/4.4M/6M
$B^+ \to D^{**0}\mu\nu$	D_1^0, $D_1^{\prime 0}$, D_2^{*0}	7.2M/7.4M/9M
$B_s^0 \to D_{s2}^*\mu\nu$	$D_{S1}^{\prime+}$, D_{S2}^{*+}	780K/830K/1.1M
$B^0 \to D^{**}\tau\nu$	$D_1^{\prime+}, D_0^{*+}, D_1^+, D_2^{*+}$	36K/46K/54K
$B^+ \to D^{**}\tau\nu$	$D_0^{*0}, D_1^0, D_1^{\prime 0}, D_2^{*0}$	94K/92K/130K
$B^0 \to D^{*+}(X_c \to \mu\nu X)$	$D_0^{*+}, D_1^+, D_1^{\prime+}, D_2^{*+}$	6.6M/6.8M/8.8M
$B^+ \to D^*(X_c \to \mu\nu X)$	$\bar{D}_1^{\prime 0}, \bar{D}_1^0, \bar{D}_2^*, D^+, D^{*+}, D_{s1}^{\prime+}$	3.4M/4.2M/3.6M
$B^0 \to D_2(2460)^*\mu\nu$	$D^*(2S)^-, D(2S)^-, D(2750)^-, D(3000)^-$	2.4M/2.6M/4.8M
$B^+ \to D_2(2460)^*\mu\nu$	$D^*(2S)^0, D(2S)^0, D(2750)^0, D(3000)^0$	2.4M/2.4M/3.4M

Table 5.1: Simulated decay modes, cocktail notes (mixture of several states of the particle) and sample sizes used in this analysis are given.

5.3 Candidate selection

This section explains how the signal candidates are chosen and distinguished from backgrounds. A selection procedure is implemented and applied to data samples consecutively - the trigger, stripping and additional offline - in order to reduce the background. This particular list of selections inspired from the measurement presented in Ch. 4 since both analyses use same signal decay channel. The list of abbreviations used in selection requirements and the sample composition have already been explained in section 4.1.

5.3.1 Trigger

The LHCb trigger system selects events through three successive stages: L0, HLT1 and HLT2, as described in Sections 3.2.7.1 and 3.2.7.2. The trigger selection used in this analysis is constrained by the pre-filtering already applied to the available data sample during the tuple production, which restricted the trigger selections that could be used. Consequently, events are required to satisfy either L0Global TIS or L0Hadron TOS on the D^0 candidate, followed by HLT1TrackMVA TOS on a K or π track from the D^0 decay. This strategy was adopted to accommodate the existing data selection, and its suitability is supported by previous validation of charm-hadron-based trigger strategies in Run 1 angular analysis and in muonic $R(D^*)$ analyses. Furthermore, the presented signal trigger strategy, selecting the charm hadron, has the advantage of permitting a possible future $|V_{\rm cb}|$ determination, which could use $B^0 \to D^{*-}\pi^+$ decays as normalisation channel. This decay mode, with Branching Fraction known at 2.6% level [29], and about 30K signal candidates reconstructed in the (pre-scaled) MisID line in roughly a third of the LHCb Run 2 data sample, offering the prospect of a competitive $|V_{\rm cb}|$ measurement to be studied in the future.

At HLT2, the B^0 candidate is required to satisfy the semileptonic `Hlt2XcMuXForTauB2XcMu` line. The requirements at each stage are detailed below:

- L0 trigger requires the events to pass at least one of
  - **L0Global TIS**: Triggered exclusively by any particle other than the signal candidate

  - **L0Hadron TOS**: Triggered on D^0, with $D^0 \to K^-\pi^+$, from the signal candidate

- HLT1 trigger requires the events to pass
  - **HLT1TrackMVA TOS**: Triggered on π or K tracks from D^0 as non linear combination of IP χ^2 and p_T above a certain threshold for single track of K or π

- HLT2 trigger requires
  - The B^0 candidate must pass the `Hlt2XcMuXForTauB2XcMu` line requirements listed in Tab. 5.2

Particle	Variable selection
K, π	$p_T > 200$ MeV/c $p > 5000$ MeV/c Max$p_T > 800$ MeV/c DLLK$< 4(K), < 2(\pi)$
D^0	DIRA > 0.999 $p_T > 2000$ MeV/c Mass 1815-1915 MeV/c^2 $\chi^2_{\text{vertex}}/\text{ndf} < 10$ $\text{FD}_{\chi^2} > 25$ Sum track $p_T > 2500$ MeV/c Child pair DOCA < 0.1mm
μ	$\text{IP}^2_\chi > 16$ isMuon $= 1$
D^0 μ	$\chi^2_{\text{vertex}}/\text{ndf} < 15$ DIRA > 0.999 DOCA < 0.5 mm $\text{FD}_{\chi^2} > 50$

Table 5.2: `Hlt2XcMuXForTauB2XcMu` selection variables and the cuts.

To reject a sample of decays with a particle incorrectly identifies as signal muon (MisID), to be used in background modelling in this analysis (as mentioned in section 4.1), the additional HLT2 line `Hlt2XcFakeMuForTauB2XcMu` is used. This trigger line has the same requirements as the `Hlt2XcMuXForTauB2XcMu` however, it is not requiring the events to pass `isMuon`.

5.3.2 Centralised offline selection: Stripping

After the trigger-level selections applied to the events, a set of centralised offline selections by the LHCb experiment are imposed on the selected events, known as *stripping*. The selection requirements applied at stripping level are summarised in Table 5.3. The selection is built by using combinations of well-identified and reconstructed D^0 candidates with μ of both positive and negative charge. For the sample containing particles misidentified as muons, we use the `b2D0MuXFakeB2DMuNuForTauMuLine` stripping line. This differs from the signal and combinatorial sample (random particle combination) lines, mainly in the PID requirements of muon.

Event Level Cuts	Variable	Selection
GEC	nSPDhits	< 600
PV cut	nPV	≥ 1
Particle	Variable	Selection
μ	$IP\chi^2$	> 16
	GhostProb	< 0.5
	DLLμ	> 2
	p	> 3 GeV/c
K, π	p_T	> 300 MeV/c
	p	> 2 GeV/c
	$IP\chi^2$	> 0
	DLLK	> 4(K), $< 2(\pi)$
	GhostProb	< 0.5
D^0	$\lvert p_t(\pi)\rvert + \lvert p_t(K)\rvert$	> 2.5 GeV/c
	χ^2_{vertex}/ndf	< 4
	DIRA	> 0.999
	FDχ^2	> 25
	Mass	1785-1945 MeV/c^2
D^0 μ	Mass	< 10 GeV/c^2
	χ^2_{vertex}/ndf	< 6
	DIRA	> 0.999

Table 5.3: Stripping selection.

5.3.3 Reconstruction and offline selection

Additional offline selections are applied that are designed specifically for the final state particles in signal decay (to make sure that they are reconstructed with good accuracy). These selection cuts are listed in the Tab. 5.4.

Particle	Variable	Selection
K	p_T	$>$ 800 MeV
	p	$>$ 3000 MeV
	$IP\chi^2$	> 45
	DLLk	> 4
π	p_T	$>$ 1200 MeV
	p	$>$ 3000 MeV
	$IP\chi^2$	> 45
	DLLk	< 2
D^0	p_T	$>$ 2000 MeV
	$\log(D^0 IP)$	$>$ -3.5
	$IP\chi^2$	> 9
	$FD\chi^2$	> 250
	mass interval	1845 - 1890 MeV
μ	p	$>$ 6000 MeV
	p_T	$>$ 1200 MeV
	DLLmu	> 2
	isMuon	$= 1$
	$m(D^*) - m(D^0)$	144 - 147 MeV
	$m(B)$	2500-5200 MeV
	B Isolation BDT	< 0.15
π_s	$IP\chi^2$	> 0
	Ghost probability	< 0.25

Table 5.4: Offline selection. The slow-pion (π_s) requirements are applied during tuple production.

The D^0 is reconstructed using the K and π tracks originating from the same vertex and each of them satisfying the PID, momentum, and track properties (IP cuts); then D^0 is combined with soft pion candidates to form the D^* with $D^{*+} \to D^0\pi^+$ decay imposing PID, track and vertex property cuts on D^0. During the tuple production, the slow pion is required to satisfy $IP\chi^2 > 0$ and a track ghost probability below 0.25, where the ghost probability estimates how likely the reconstructed track is to be fake. The $D^{*+}\mu^-$ pair is formed with muon candidates passing `IsMuon` along with PID and momentum requirements. The specific momentum and transverse-momentum requirements for muon as $p > 6000$ MeV/c and $p_T > 1200$ MeV/c are imposed to remove most of the particles misidentified as muon, which most frequently have a momentum in the range of 3000 – 6000 MeV/c, the p_T requirement on the muon also helps reducing $B \to D^*DX$ and $B^0 \to D^*\tau\nu$ backgrounds (as we saw with Run 1 analysis). A mass cut on B^0 meson is applied to remove contribu-

tions of $B \to D^*DX$ and $B^0 \to D^*\tau\nu$ backgrounds. The cut on D^0 and D^* mass is imposed to remove substantial amount of combinatorial background. This pair $D^{*+}\mu^+$ are random combinations of D^* with muon tracks coming from other decays in the event and D^0 $\pi^+\mu^+$ consisting of random combinations of D^0 and pions in the event. Another important variable to separate signal from the wrong sign combinatorial is the IP, $\log(\mathrm{IP}_{D^0})$ > -3.5 and $\mathrm{IP}^2_\chi > 9$ cuts are imposed on D^0. Fig. 5.2 shows a double-peaked distribution for the wrong-sign sample, associated with whether the D^0 candidate points back to the PV and is therefore compatible with prompt production. A similar structure, with a smaller prompt component, is observed in the right-sign sample. The requirement $\log(IP_{D^0}) > -3.5$ suppresses candidates compatible with prompt D^0 production and helps reduce the combinatorial background, which is estimated using the wrong-sign sample.

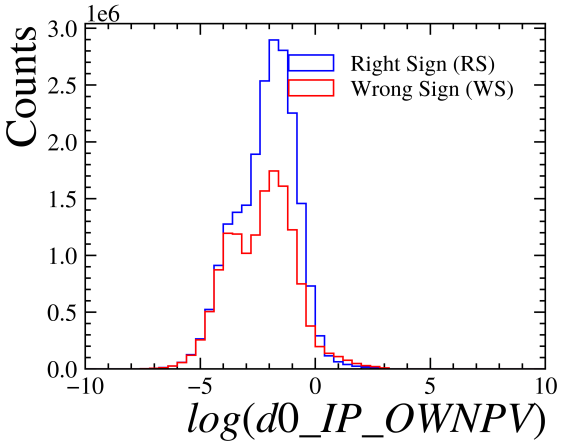


Figure 5.2: D^0 impact parameter with respect to the best PV in right-sign and wrong-sign samples compared.

Track isolation Multivariate Analysis tool: To further improve the signal separation from background events containing additional final-state particles, a Boosted Decision Tree (BDT) isolation algorithm is applied. The primary objective of this Multivariate Analysis (MVA) is to classify whether an arbitrary track in the event is dynamically *associated* with the reconstructed B candidate or if it is an unrelated (*unassociated*) track from the rest of the event. The classifier takes several track and vertex properties as inputs in Tab. 5.5, re-evaluating the vertex fit by temporarily including the track in question. The separation power is driven by training the BDT on known *associated* tracks (e.g., from higher mass states like $B \to D^{**}\mu\nu$) against *unassociated* tracks from background processes. In the context of this analysis, the

isolation of the B candidate is quantified by the highest MVA score assigned to any extra track in the event. A cut is placed on the BDT isolation variable of < 0.15, which represents the MVA values for the highest valued track in the event. This requirement guarantees that the most *associated-like* extra track is still predominantly background-like, confirming the isolation of our signal topology. This isolation algorithm and the specific cut taken from Ref. [115].

Track properties	Vertex properties
$\chi^2_{IP}(PV)$	χ^2_{FD}
$\chi^2_{IP}(SV)$	$\Delta\chi^2_{FD}$
p_T	
$\cos(D^*\mu, \text{track})$	

Table 5.5: Input variables for the isolation MVA.

5.3.4 Gaussian Process Regression to reconstruct neutrinos

It is well known that the reconstruction of b-hadron momentum in semi-leptonic decays can be done up to quadratic ambiguity (See Eqs. 4.16 and 4.16) due to a undetected neutrino. Many analyses in this category used a random solution out of two possibilities as described in section 4.2. However, there can be several kinematic properties of the visible system that help to estimate the more likely solution i.e. linear regression [139] in which the flight direction of b-hadron is used to estimate the b-hadron momentum.

In this analysis, the method of Gaussian Process Regression (GPR) [140] is adopted to choose the most likely solution for B^0 meson to resolve the quadratic ambiguity (See Eq. 4.16 and 4.16). GPR is a non-parametric Bayesian approach that avoids the rigid assumptions of linear models (e.g. $f(x) = mx + c$), allowing the data to define the underlying functional form.

5.3.4.1 Gaussian process

A Gaussian Process (GP) defines a distribution over functions such that any finite subset of the domain follows a multivariate Gaussian distribution. A central component of the GP is the covariance function (or kernel), which encodes the relationship between observations. A common choice for the kernel is the Squared Exponential (SE) kernel, also known as the Radial Basis Function (RBF) kernel

$$k(x, x') = \sigma_f^2 \exp\left[\frac{-(x - x')^2}{2l^2}\right] + \sigma_n^2 \delta(x, x') \tag{5.5}$$

where $x^{(\prime)}$ are observations, σ_f^2 represents the signal variance, l is the characteristic length-scale (quantity of differential smoothness of a function), and σ_n^2 accounts for Gaussian noise in the observations. In the context of modelling these kinematic distributions, the hyper-parameters of the Gaussian process kernel possess direct physical interpretations:

- **Signal Variance (σ_f^2):** This parameter determines the average amplitude of the function's variation from its mean. Physically, it dictates the overall vertical scale of the kinematic structures being modelled, ensuring the GP can capture the full height of kinematic peaks or resonant structures.
- **Length-scale (l):** This parameter defines the characteristic *memory* or

smoothness of the process in the kinematic phase space. A large l implies a slowly varying, highly correlated background distribution, whereas a smaller l allows the model to capture sharper, localised physical features such as kinematic edges or rapid threshold turn-ons.

- **Noise Variance (σ_n^2):** This term accounts for the uncorrelated, random fluctuations in the observations. In this analysis, it physically represents the statistical uncertainty inherent in the finite Monte Carlo samples, as well as unresolved detector resolution effects.

Regression and Scalability: In the context of machine learning, regression is the task of predicting a continuous target variable (such as the B^0 momentum) from a set of input features (the visible kinematic properties). To achieve this, a model must be *trained* on a dataset of known inputs and targets, learning the underlying mapping so it can generalize and make accurate predictions on new, unseen data. For a set of N training points, the joint distribution of the observed values y and the predicted values f_* is given by

$$\begin{bmatrix} \mathbf{y} \\ \mathbf{f}_* \end{bmatrix} \sim \mathcal{N}\left(\mathbf{0}, \begin{bmatrix} K(X,X) + \sigma_n^2 I & K(X,X_*) \\ K(X_*,X) & K(X_*,X_*) \end{bmatrix}\right) \tag{5.6}$$

where $K(X,X) + \sigma_n^2 I$ is the covariance of the training data including the measurement noise (i.e. uncertainty in our MC or detector resolution), $K(X_*,X_*)$ is the covariance of the test points, and $K(X,X_*)$ represents the cross-covariance between the training data and the test data.

The conditional distribution (the posterior) derived from the joint covariance matrix in Eq. 5.6 is also gaussian and given as

$$f_*|y \sim \mathcal{N}(\mu_*, \Sigma_*) \tag{5.7}$$

where μ_* is the mean and Σ_* is the covariance of the prediction, and they are explicitly defined as

$$\mu_* = K(X_*,X)[K(X,X) + \sigma_n^2 I]^{-1} \tag{5.8}$$

$$\Sigma_* = K(X_*,X_*) - K(X_*,X)[K(X,X) + \sigma_n^2 I]^{-1} K(X,X_*) \tag{5.9}$$

The primary bottleneck in exact GPR is the inversion of the $N \times N$ covari-

ance matrix, which scales with a computational complexity of $\mathcal{O}(N^3)$ and memory requirements of $\mathcal{O}(N^2)$. Given that our signal MC sample consist of $\sim$ 2 million events, exact GPR is computationally prohibitive. To address this, we utilise the `GPflow` library [141], which implements Sparse Variational Gaussian Process Regression (SVGP) [142] –sGPR–. The sparse approach approximates the full posterior by introducing M *inducing points* (where $M \ll N$), which act as a representative *active set* of the data. By optimising the location and values of these inducing points, sGPR reduces the computational complexity to $\mathcal{O}(NM^2)$.

5.3.4.2 Implementation on $B^0 \to D^{*-}\mu^+\nu_\mu$ decay

Building on the theoretical framework of Gaussian processes, this section details the practical application of sGPR to the specific kinematics of the $B^0 \to D^{*-}\mu^+\nu_\mu$ decay to predict B^0 meson momentum. The primary objective is to move beyond a simple choice between the two quadratic solutions and utilise the full visible kinematic information to estimate the most probable B meson momentum. The mean function (μ_*) in Eq. 5.8 represents the predicted value, which is then used to resolve the quadratic ambiguity, serving as a statistically driven selection for the B^0 momentum. A unique advantage of GPR is the predictive variance (Σ_*) defined in Eq. 5.9. Unlike a standard neural network or linear regression, GPR provides a per-event uncertainty that quantifies exactly how much the model *trusts* its own prediction. As demonstrated in Fig. 5.3, sGPR is highly effective at predicting the most likely solution for b-hadron momentum as it is not dependent on rigid assumptions for the underlying function of the distributions, yielding a significant resolution improvement in P_{Λ_b} compared to linear regression [139]. This superior performance stems from the model's ability to capture complex, non-linear correlations that linear approaches fundamentally overlook.

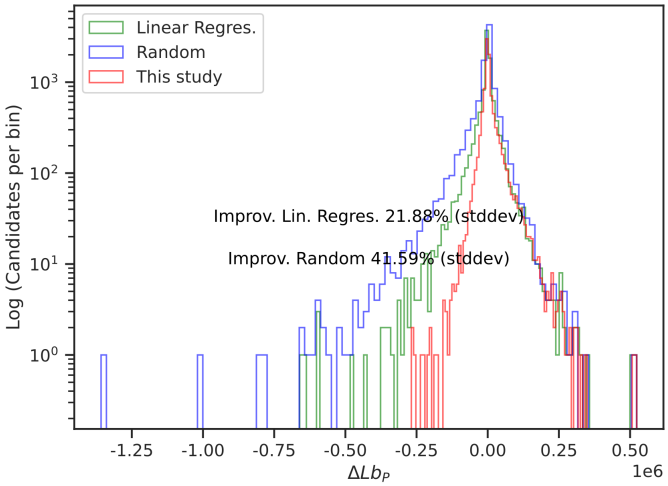


Figure 5.3: Distribution of the b-hadron momentum residuals ($\Delta = P_{b_{reco}} - P_{b_{true}}$). The label *This study* in the legend indicates the GPR application to the $\Lambda_b \to \Lambda_c\mu\nu$ decay channel, showing a narrower and more centred peak compared to the *random solution* and linear regression approaches. The respective improvements written on the plot as 41.59% and 21.88%. Image taken from LHCb-ANA-2024-058 (in preparation).

To implement the sGPR model for the B meson system, several hyper-parameter (training variables) choices were optimised. We adopt the *Matérn* covariance function [143] as a flexible general class of kernels. This choice is based on dedicated studies performed for the $\Lambda_b \to \Lambda_c\mu\nu$ analysis (LHCb-ANA-2024-058 in preparation). Furthermore, we utilise a linear model (linearity between observation and the prediction function) as the mean function, allowing the GP to focus on modelling the non-linear residuals. To ensure computational feasibility without sacrificing accuracy, the number of inducing points was fixed at 4000, providing a robust approximation of the underlying function across the large dataset.

The training sample (input features) is derived from MC sample for $B^0 \to D^{*-}\mu^+\nu_\mu$ after all selection stages applied. To teach the topology of our kinematic space by encapsulating all the necessary information for the sGPR to model the prediction of true magnitude of B^0 meson spatial momentum, the following kinematic variables are trained:

- spatial components of D^*meson momentum vector
- spatial components of μ momentum vector
- spatial components of B^0 meson flight distance vector

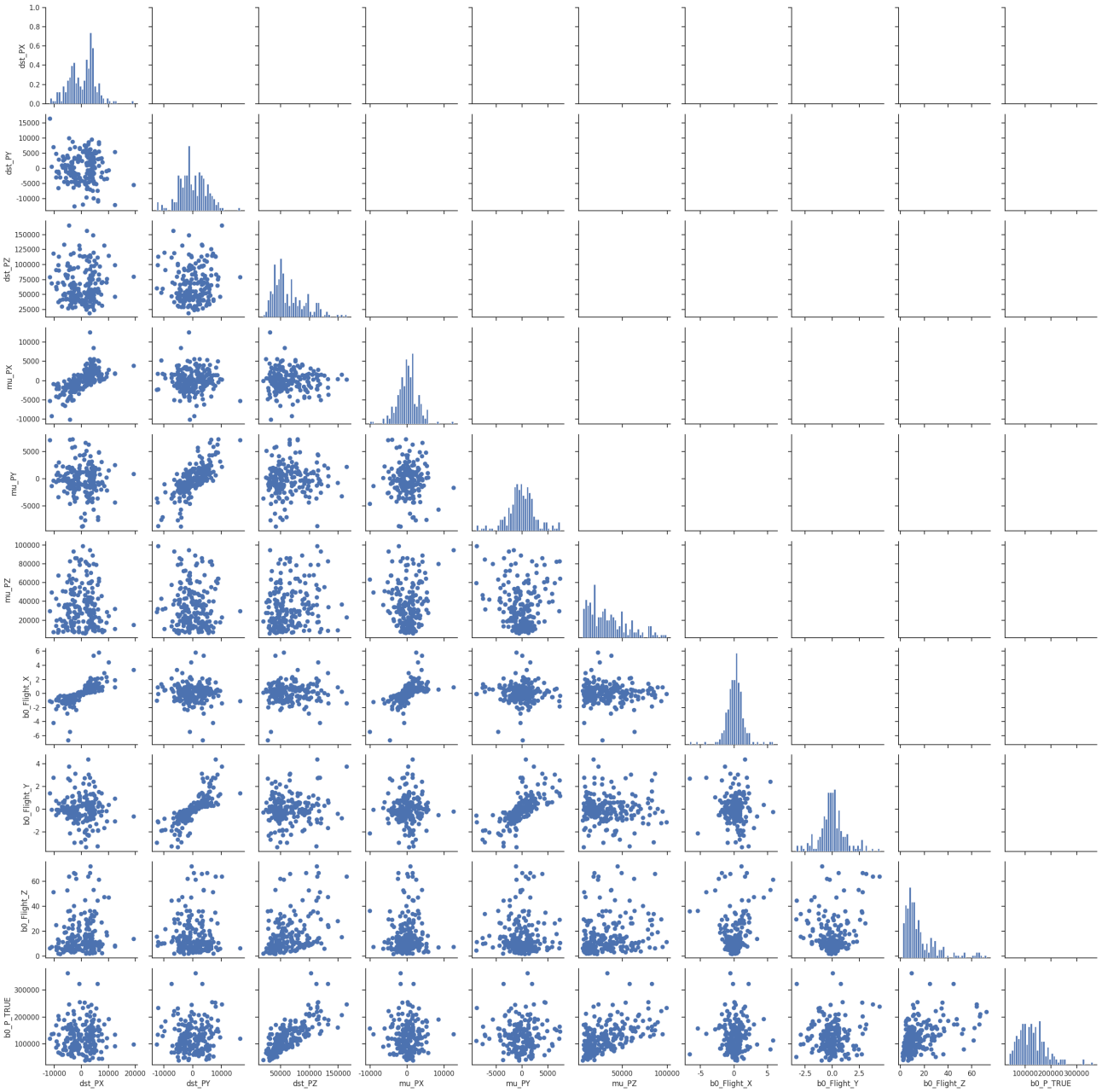


Figure 5.4: Correlation of training variables and target variable in 2016 signal MC sample with magnet up polarisation.

To ensure the success of choice of training variables, it is crucial to understand the distributions and correlations of these variables across the phase space. Fig. 5.4 presents a scatter matrix (pair-plot) illustrating the one-dimensional distributions of each variable on the diagonal and the pairwise two-dimensional correlations on the off-diagonal plots.

The bottom row of Fig. 5.4 displays the relationship between the nine training variables (from left to right, `dst_P(X/Y/Z)`, `mu_P(X/Y/Z)` and `b0_Flight_(X/Y/Z)`) and the target variable (`b0_P_TRUE`). There is a clear positive, roughly linear correlation between the true B^0 momentum and the longitudinal components of the visible system (`dst_PZ`, `mu_PZ`, and `b0_Flight_Z`). This strong baseline correlation mathematically justifies the architectural choice to use a linear model as the mean function for the sGPR, as discussed previously. The linear mean function easily captures this dominant trend. The off-diagonal scatter plots of Fig. 5.4 reveal dependencies between the training variables themselves. For instance, there are visible correlations between the transverse flight distances (`b0_Flight_X`, `b0_Flight_Y`) and the corresponding transverse momenta of the D^* and μ. While a standard linear regression would struggle with the complex multicollinearity and the non-linear Heterogeneous distributions of the transverse components, the sGPR utilises the *Matérn* covariance kernel to effectively map these subtle, multidimensional cross-correlations.

To evaluate the predictive power of the sGPR, the correlation and distribution of the estimated B^0 momentum ($b0_P_Estm$) are compared against the true MC value ($b0_P$_TRUE). This comparison is performed for both the small training subset (200 events) and the large test sample ($\sim$ 1.5 million events), as shown in Fig. 5.5. The top row of Fig. 5.5 displays the correlation matrices for the training and test samples. The estimated and true B^0 momenta exhibit similar correlations in both samples, indicating comparable predictive performance on the training and test data. This is consistent with generalisation to unseen events and provides no indication of substantial overtraining according to this metric. The bottom row of Fig. 5.5 compares the logarithmic (log) scale distributions of the target and predicted momentum. The histogram shows that the sGPR (in red) roughly follows the target distribution (in green), though with expected statistical fluctuations due to the very small sample size of 200 events. In the high-statistics test sample, the predicted distribution (beige) shows excellent agreement with the target distribution (blue) across the entire momentum range.

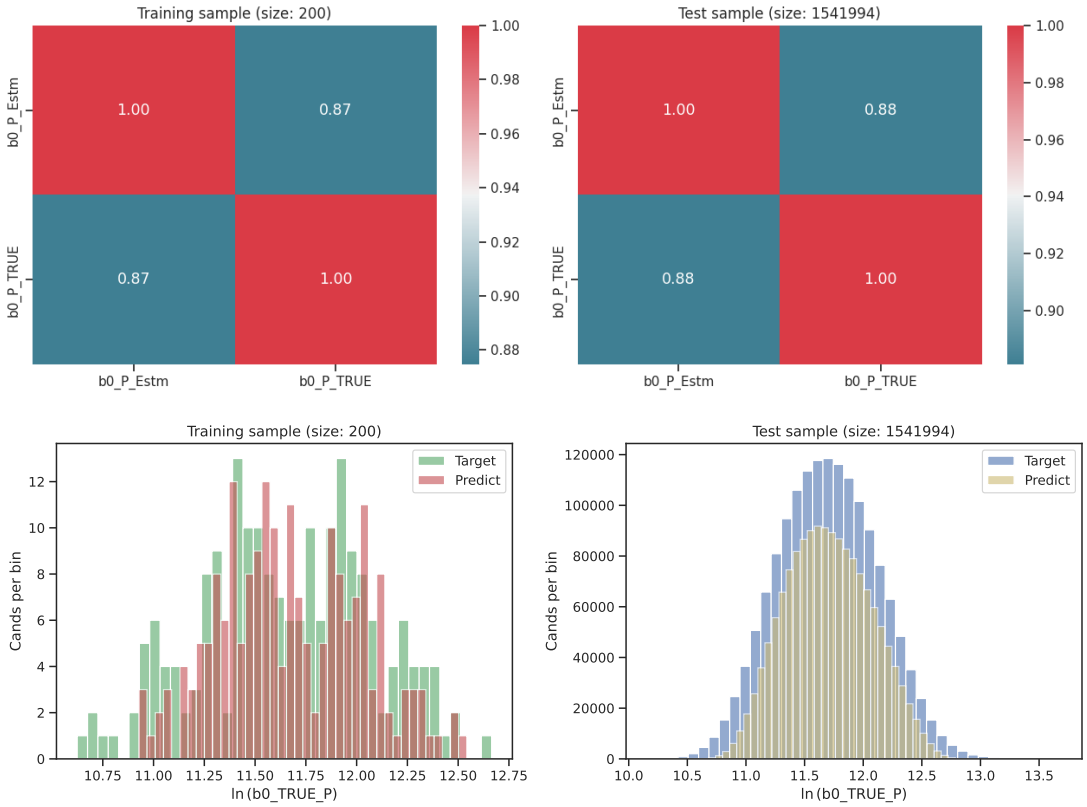


Figure 5.5: Correlations between prediction and the target variable in training (left) and test (right) samples (top-row). The distribution of true log-scaled B^0 momentum overlay with sGPR predictions (bottom-row).

In order to evaluate sGPR performance in reconstructing B^0 meson momentum, the results are compared against MC truth information and random solution approximation presented in section 4.2. The top panel of Fig. 5.6 displays the momentum distributions on a logarithmic scale. The sGPR prediction (Pred, red) shows a significantly better agreement with the MC truth (True, blue) compared to the random-solution reconstruction (Reco, green). Specifically, the random solution tends to overpopulate the high-momentum tail (above 0.4 GeV), a bias that is effectively corrected by the sGPR model. The bottom-left panel shows the residual distribution for the regressed variable, $\Delta b0_P = P_{estimated} - P_{true}$ and for the randomly choses solution $\Delta b0_P = P_{reco} - P_{true}$. The sGPR method achieves a resolution improvement of 39.18% relative to the random solution. The predicted residuals (red) exhibit a much narrower peak centred at zero, whereas the reconstructed residuals (green) show a broad distribution with a significant shoulder in the negative region, corresponding to cases where the incorrect quadratic solution was chosen.

The bottom-right panel illustrates the resolutions, defined as $\Delta b0_P / b0_{P_{True}}(\%)$. The residual asymmetry can arise from the two-fold kinematic ambiguity in the momentum reconstruction, since selecting the incorrect solution need not produce symmetrically distributed upward and downward errors. The sGPR method mitigates this effect, but the available information does not allow the ambiguity to be resolved perfectly for every event, leaving some residual asymmetry. The logarithmic vertical scale highlights the remaining tails.

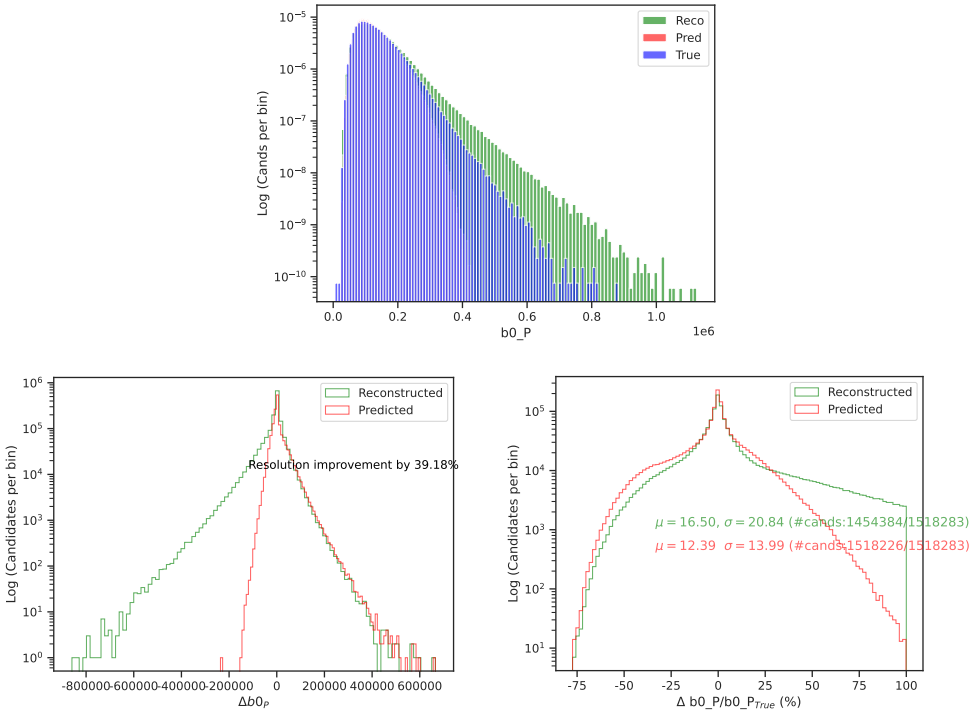


Figure 5.6: Top comparison of B^0 momentum reconstruction using sGPR (Pred in red), random solution (Reco in green), and MC truth (True in blue). Bottom-left: Momentum residuals. Bottom-right: Fractional momentum residuals with statistical summary.

The ultimate objective of improving the B^0 momentum resolution is to achieve a more precise measurement of the differential decay rate, $d\Gamma/dw$. Therefore, the performance of the reconstruction is evaluated on the parameter of interest, w. This parameter is computed using the GPR prediction of the B^0 momentum, and the results are compared against the MC truth and the random-solution reconstruction in Fig. 5.7. As seen in the distributions (top panel), the GPR prediction (red) maps the MC truth (blue) with high fidelity across the entire physically allowed phase space ($1.0 < w \lesssim 1.5$). In contrast, the standard random-solution approach (green)

suffers from noticeable shape distortions, artificially migrating events toward the high-w tail. Accurately capturing this shape is critical, as distortions in the w spectrum directly translate into systematic uncertainties in the $d\Gamma/dw$ measurement. The bottom left panel shows the residual distribution, $\Delta w = w_{predicted} - w_{true}$. By applying the sGPR model, we achieve a 19.35% improvement in the resolution compared to the random solution. The broad, asymmetric shoulders seen in the standard reconstruction—caused by selecting the incorrect quadratic root—are heavily suppressed by the GPR. This improvement is further confirmed by the fractional residuals ($\Delta w/w_{True}$) in the bottom right panel.

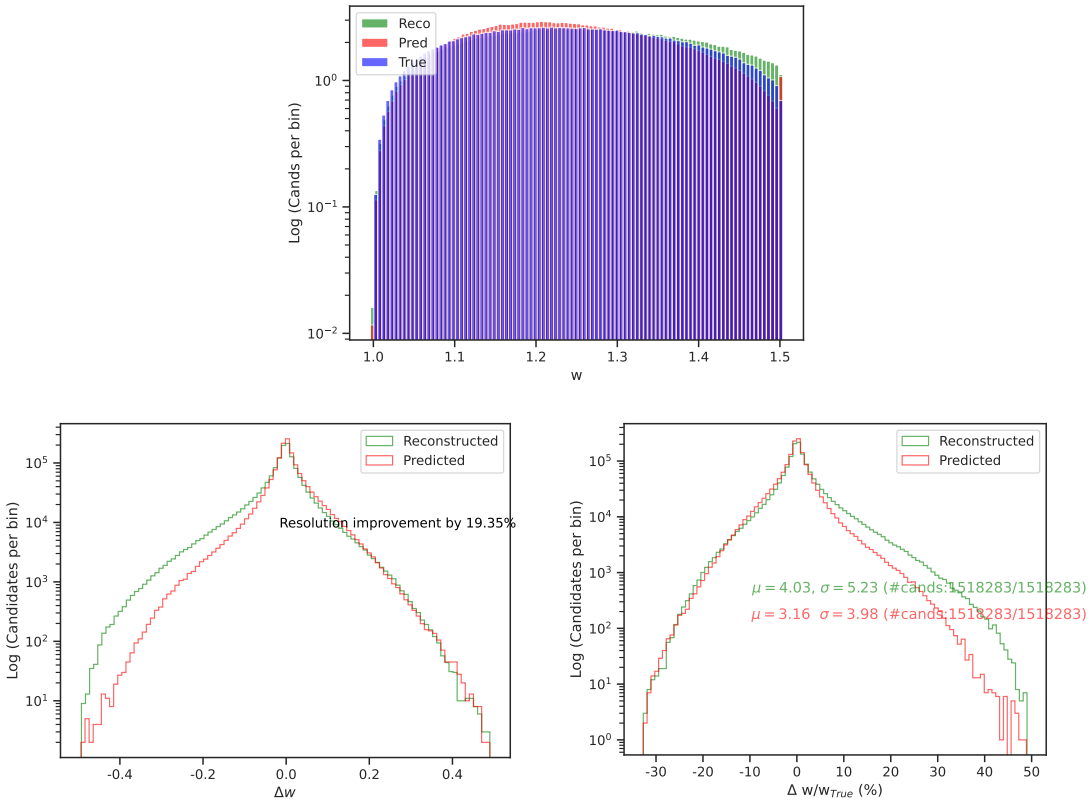


Figure 5.7: In top row, the w momentum distributions are compared between GPR prediction (red) and random solution (green) approximation compared with MC true (blue) distribution. In bottom row, w residual and resolutions are compared and the improvement in resolution with respect to the random approximation written on the residual plot.

The results are shown in this section based on 2016 MC signal with magnet up polarisation. The remaining Run 2 samples can be found in Appendix E.

5.4 Trigger and PID emulation for tracker-only MC samples

Tracker-only simulation is a fast simulation technique that turns off the Cherenkov emission in the RICH, shower development in the Calorimeter and interactions in the Muon systems. Around 85% of the simulation time is taken by simulating the response of RICH and Calorimeter systems. Therefore, tracker-only simulation is $\sim$ 8 times faster than full simulation. However, we need to add information missing from these systems in order to be able to use these samples (For more details, See [50]). For Run 2, since the HLT2 selection is very well reproduced by offline selections, we only need the emulation of the L0 (both TIS - TOS) and HLT1 (TOS) triggers used in our selections described in section 5.3.1.

- L0Global TIS or L0Hadron TOS
- HLT1Track: HLT1TrackMVA, which utilises the MVA method (BDT) based on input parameters of IP χ^2 and p_T above a certain threshold for single track

In addition to the trigger decisions, the PID information needs to be emulated as well since RICH, calorimeters and muon system which performs PID are missing in tracker-only simulation.

5.4.0.1 L0 Trigger emulation

L0 Hadron TOS emulation: An event passes the L0 Hadron trigger selection when an E_T energy deposit exceeds a certain threshold in a 2x2 cluster on HCAL (See section 3.2.7.1 and Tab. 3.1). If it is a TOS decision, it has to be triggered by $D^0 \to K\pi$. To emulate this requirement on tracker-only simulation samples, we use the similar strategy as in Ref. [50], where the response of the L0 Hadron trigger is modelled by using a XGBoost multivariate algorithm [144]. The output of this algorithm is used to obtain the efficiency of each event passing the trigger line. The XGBoost is trained on a full simulation sample with input variables listed in Tab. 5.6 to give the accurate description of hadronic trigger, then it produces the efficiency of L0 Hadron trigger in each event to be added as weights to the samples. The agreement can be seen in Fig. 5.8 which shows the efficiency comparison of L0 Hadron trigger line between full simulation signal sample (real response) and

tracker-only signal sample (emulated). The L0HadronTOS efficiency appears to be underestimated by the emulation at low $p_T(D^0)$ (below 10 GeV), while appears to be overestimated at high $p_T(D^0)$, with a noticeable disagreement in bins of 30 GeV and 40 GeV. The source and implications of this behaviour are under investigation. However, it is worth noting that because full simulation does not describe real data perfectly, this level of disagreement could be acceptable if it remains smaller than the difference between data and simulation.

Group	Variables
Event-level	nTracks
D^0	p, p_T
K^-, π^+	p, p_T, true E_T, HCAL x-coordinate, HCAL y-coordinate, HCAL region

Table 5.6: Variables used to train XGboost for L0 Hadron emulation where E_T measured by the tracker. HCAL region indicates whether the hits are in the inner or outer region of HCAL.

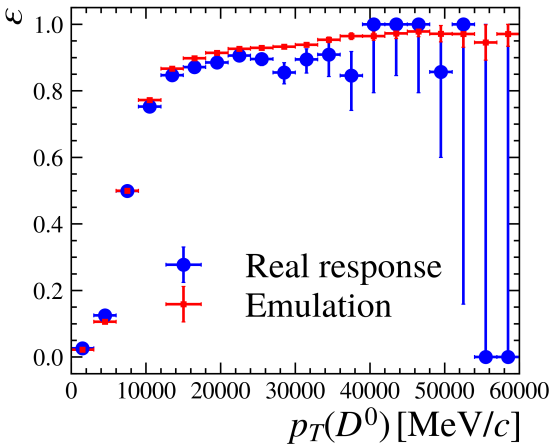


Figure 5.8: The L0HadronTOS efficiency as a function of the reconstructed $P_T(D^0)$. The red line is emulation and the blue line is full simulation.

L0 Global TIS emulation: The L0 hardware trigger fires on general high-p_T signatures without any prior knowledge of specific decay topologies. "Trigger Independent of Signal" (TIS) is a post-reconstruction classification: Once a signal candidate is fully reconstructed, an event is designated as L0 Global TIS if the trigger was satisfied exclusively by particles from the rest of the event, rather than by the signal candidate itself.

The emulation of this trigger line follows the procedure of Ref. [50] using TISTOS method [145]. The TISTOS method extracts the efficiency of TIS from data by using

the events passed L0Muon TOS in the sample $B^+ \to J/\psi K^+$. The TISTOS methods assume that TIS and TOS probabilities are uncorrelated therefore, by isolating a sample of events that are strictly categorized as TIS, the absolute trigger efficiency can then be directly measured as the fraction of these TIS events that also satisfy the TOS condition ($\varepsilon_{\text{TOS}} = N_{\text{TIS\,\&\,TOS}}/N_{\text{TIS}}$). The emulation produces an efficiency histogram of events in $B^+ \to J/\psi K^+$ passing TIS binned in true quantities of B_{P_T} and B_{P_z}, and these efficiencies are assigned to the reference samples as weights to mimic the L0Global TIS decision. The agreement can be seen in Fig. 5.9 which shows the efficiency comparison of L0Global trigger between full simulation signal sample and tracker only signal sample. The emulation underestimates the L0GlobalTIS efficiency in the low $p_T(B^0)$ region, and the source of this disagreement is being investigated for the LHCb analysis

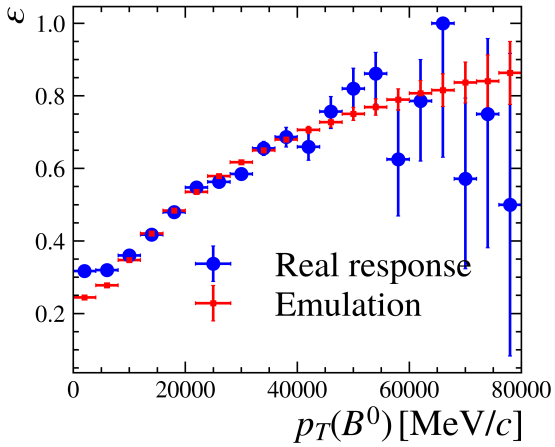


Figure 5.9: The L0GlobalTIS efficiency as a function of the reconstructed $P_T(B^0)$. The red line is emulation and the blue line is full simulation.

5.4.1 HLT1 emulation

The emulation procedure follows the Ref. [50]. The single track line HLT1TrackMVA requires combinations of the D^0 decay products (K, π) to pass a multivariate selection based on the transverse momentum and impact parameter (p_T and IP_{χ^2}) with respect to an associated primary vertex (PV). HLT1 also requires a set of GEC in Tab. 5.7. The emulation uses offline reconstructed tracks of the signal candidate $D^0 \to K\pi$ where HLT1TrackMVA applied separately on the decay products, K and π. The agreement between full simulation signal sample and tracker only signal sample can be seen in Fig. 5.10 which shows the efficiency comparison of HLT1TrackMVA

trigger line. The tracks included in this plot have either L0Hadron TOS or L0GLobal TIS positive decisions, and the disagreement seen in low p_T might be the result of efficiency underestimate seen in previous stages.

GEC
$50 <$ nVeloClusters < 6000
$50 <$ nITClusters < 3000
$50 <$ nOTClusters < 15000

Table 5.7: Global Events cuts applied before the HLT1 reconstructions

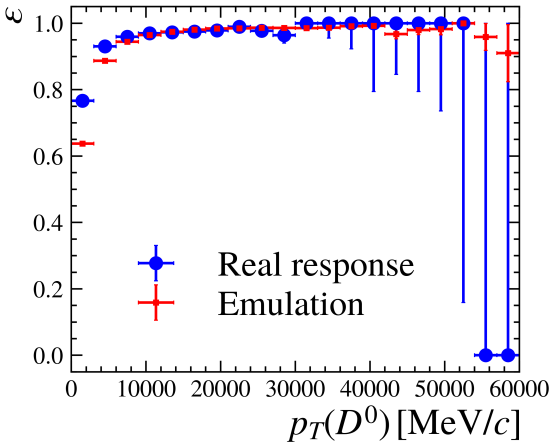


Figure 5.10: The HLT1TrackMVA TOS efficiency as a function of the reconstructed $P_T(D^0)$. The red line is emulation and the blue line is full simulation.

5.4.2 PID emulation

The PID requirements on the muon and the D^* decay products included in the stripping line and the offline selections are emulated with per-event weights derived using PIDCalib2 [146, 147]. The weights are extracted from the three dimensional efficiency histograms in bins of number of tracks (nTracks), pseudo-rapidity (η) and track momentum (P) for each final state particle, π, K and μ in signal decay. These efficiency histograms are data-driven, measured from dedicated calibration samples with our PID selections (K, π, μ), and then applied onto the reference sample. The binning scheme can be seen in Tab. 5.8.

Variable	Binning
nTracks(K, π, μ)	[0, 50, 200, 300, 500]
$\eta(K, \pi, \mu)$	[1.5, 2.375, 3.25, 4.125, 5.0]
P(K, π)	[3.0, 10.45, 17.9, 25.4, 32.9, 40.3, 47.8, 55.2, 62.7, 70.2, 77.6, 85.1, 100.0]
P(μ)	[3,6,10,20,30,40,50,60,70,100]

Table 5.8: The binning scheme used for efficiency histograms produced by PIDCalib2.

5.5 Fitter

This analysis utilizes `HAMMER-Pyhf` [148], a novel framework designed to extract sample compositions through a template-based fit to data. This setup leverages the `redist` environment as an interface between `HAMMER` and the `HistFactory` statistical model [136]. The `redist` framework employs a model-agnostic likelihood approach, which decouples the initial simulation from the final statistical model. This enables the use of templated fits that can dynamically account for various Form Factor (FF) parametrizations or New Physics (NP) effects. Specifically, `HAMMER-Pyhf` modifies the event weights of the baseline probability density function (pdf_{null}) to match an alternative hypothesis (pdf_{alt}) via a weight ratio

$$pdf(C_i, \text{FFs}, \dots) = pdf_{\text{null}} \times \frac{pdf_{\text{alt}}(C_i, \text{FFs}, \dots)}{pdf_{\text{null}}} \tag{5.10}$$

Here, the *pdf* is defined within the Effective Field Theory (EFT) formalism, characterized by Wilson coefficients (C_i) and FF parameters. While pdf_{null} represents the initial physics assumptions of the simulated sample, pdf_{alt} allows for the evaluation of different FF parameter values or NP scenarios without the need for computationally expensive re-simulation. Although the current analysis is performed in one dimension, this framework was adopted to ensure scalability for future multi-dimensional angular coefficient measurements, where the simultaneous variation of complex template shapes is required.

The fit uses one dimensional templates in 20 bins of m^2_{miss} (see Eq. 5.2) for each w (see Eq. 5.1) bin, with w binning scheme and m^2_{miss} range specified in Tab. 5.9. The w bins are defined as in the Belle analysis [22] and cover the full kinematic range. The m^2_{miss} range is chosen to include the signal peak near zero and the background contributions at higher values. The combination of bin numbers was tested by examining the distribution of signal statistics across the bins. Each w bin is fitted independently. The fitter extracts the contributions of signal, feed-down from semileptonic decays from each of several excited charm states as well as higher charm states, and combinatorial background, as introduced in section 4.1.

w Bin	w Range	m^2_{miss} (GeV^2/c^4) Range
1	$1.0 \leq w < 1.05$	[-4.0, 5.5]
2	$1.05 < w \leq 1.10$	[-5.0, 6.0]
3	$1.10 < w \leq 1.15$	[-3.0, 5.5]
4	$1.15 < w \leq 1.20$	[-3.0, 5.0]
5	$1.20 < w \leq 1.25$	[-3.0, 5.0]
6	$1.25 < w \leq 1.30$	[-3.0, 5.0]
7	$1.30 < w \leq 1.35$	[-2.8, 5.0]
8	$1.35 < w \leq 1.40$	[-2.0, 5.0]
9	$1.40 < w \leq 1.45$	[-2.0, 4.1]
10	$1.45 \leq w \leq 1.52$	[-2.0, 3.0]

Table 5.9: Binning in w for 1D fit to m^2_{miss}

5.5.1 Simulation derived templates

In semileptonic analyses, a major source of background arises from *feed-down* processes. Feed-down occurs when a heavier parent state or an intermediate resonance decays into the identical visible final state as the signal candidate, accompanied by additional particles (such as soft pions, kaons, or photons) that fail to be reconstructed or fall outside the detector acceptance. Because these extra particles escape detection, the remaining tracks perfectly mimic the topological signature of the signal.

5.5.1.1 Signal

The $B^0 \to D^{*-}\mu^+\nu_\mu$ is the signal component and its yield is floating and unconstrained in the fit. The FF parametrisation of this mode in the simulation was CLN parametrisation, however, we choose to describe this component with BGL FF parametrisation in our fit. The central values for BGL FF parameters can be found in Tab. 4.9 as implemented in HAMMER. In the fitter, while forming the null-pdf from the template, the certain shifts from the central values denoted by Δ are used, which are reported from Run 1 analysis presented in Ch. 4.

5.5.1.2 Feed down from $B^0 \to D^*\tau\nu$

This decay mode simulation is reweighted with HAMMER using same BGL parameters as in signal to form the templates.

5.5.1.3 Feed down from $B \to D^{**}\mu\nu$

The contribution from this decay mode is modelled in six templates, which include the three different resonances, D_1, D_1', D_2^* for each isospin states of B^0 and B^+. Each of the six different templates are reweighted with BLR FF parametrisation using HAMMER. The central values for BLR FF parameters can be found in Tab. 4.10 as implemented in HAMMER. In the fitter, while forming the null-pdf from these templates, the certain shifts from the central values denoted by Δ are used, which are reported from Run 1 analysis presented in Ch. 4.

The EvtGen issue: A recent study [149] has identified a feature within the EvtGen event generator (mentioned in section 3.4.1) that affects the simulated kinematic distributions of semileptonic B decays proceeding via intermediate resonances. Due to neglected phase-space factors in the sampling algorithm, EvtGen generates an unphysical enhancement in the high-mass tail of the hadronic invariant mass spectrum, which is particularly evident for broad D^{**} states. For this analysis, this effect is isolated entirely to the $B \to D^{**}$ background components. To evaluate the potential impact of this EvtGen modelling issue on the current analysis, a cross-check was performed using a simulated $B \to D_1'\mu\nu$ sample. As illustrated in Fig. 5.11, the application of the corrective reweighting results in a noticeable narrowing of the truth hadronic mass distribution, successfully suppressing the unphysical high-mass tail. However, the reconstructed kinematic variables, most notably the reconstructed recoil parameter (w), appear largely unaffected by the correction. Given that the fit for the signal extraction relies heavily on these reconstructed distributions, the impact of the EvtGen mis-modelling on the final results is expected to be negligible. Consequently, this effect is considered to be well-covered within the systematic uncertainties assigned to the background shapes.

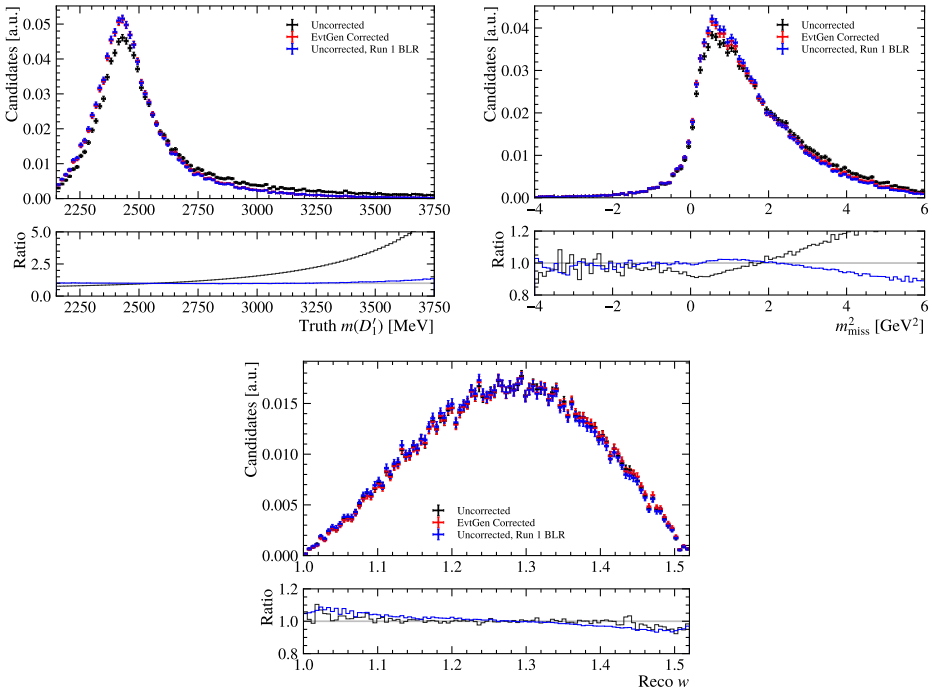


Figure 5.11: Kinematic distributions of $B \to D_1'\mu\nu$ sample overlayed with HAMMER and EvtGen corrections.

5.5.1.4 Feed down from $B^0 \to D^{**}\tau\nu$

This component is not included in the fit since there is only very small size left after the full selection chain. The leftover distribution is not suitable for producing a statistically accurate template shape, which can be seen from Fig. 5.12 along with number of candidates comparison with signal for the first w bin (for rest of the w bins, see Appendix F.1, Fig. F.1).

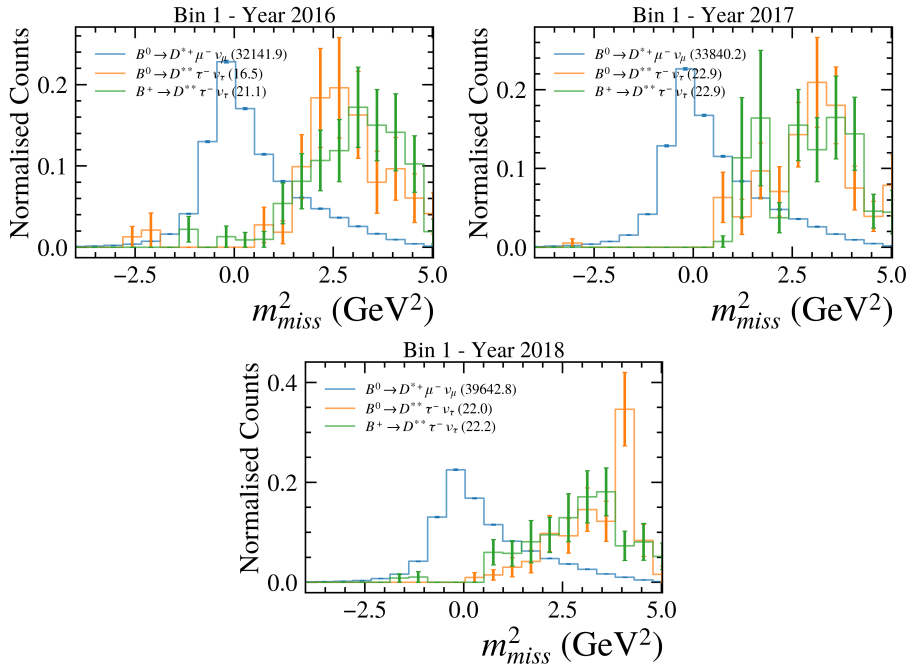


Figure 5.12: The $B \to D^{**}\tau\nu$ template shapes shown for the first w bin laid over signal template shape. Legend shows the number of events for both B meson charges from data taking years 2016/2017/2018

5.5.1.5 Feed down from B_s^0 decays

Decays of B_s mesons may contribute the samples via decay modes of mostly $D_{s1}^+ \to D^{*+}K_s$ and $D_{s2}^+ \to D^0K^+$. This contribution modelled similarly to the $B \to D^{**}\mu\nu$ and two different templates for each D_s state are reweighted in the BLR FF scheme but for the dedicated decay modes for B_s in HAMMER. The BLR FF values are used for forming the templates with the central values in Tab. 4.10 plus the offset values reported as in Tab. 4.15.

5.5.1.6 Higher D^{**} states

The higher D^{**}states are the excited charm stats which are heavier than 3/2 and 1/2 states. This template is formed using a sample of simulated events, which includes several states as cocktail indicated in Tab. 5.1 and the overall yield is floating in the fit.

5.5.1.7 Double charm backgrounds

The double-charms backgrounds consist of feed-down from $B \to D^* DX$ where $X = K, K^*$. This contribution has formed as a single template, where B^0 and B^+ modes are summed according to their contributions in the sample, and overall yield is floating in the fit.

5.5.2 Data derived templates

5.5.2.1 Combinatorial background

There could be random combination of particles which can contribute to the samples, therefore, this contribution needs to be correctly modelled to describe the data accurately. There are two different sources of this type of background considered in this analysis, called combinatorial:

- Wrong sign combinations of D^* and μ (WS Mu)
- A D^* made with a D^0 combined with a wrong sign π (WS Pi)

All these backgrounds are coming from the secondary vertex of the particles. The first type is derived from the data sample with the particle pair, $D^{*+}\mu^+$. The second type is derived from the particle pair, $D^{*+}(\to D^0\pi_s^-)\mu^+$ where soft pion has the wrong sign.

5.5.2.2 Muon MisID

This component is not included in the fit since there is only very small size left after the full selection chain. The leftover distribution is not suitable for producing a statistically accurate template shape, which be seen from Fig. 5.13 along with number of candidates comparison with nominal data sample (for rest of the w bins, see Appendix F.2, Fig. F.2).

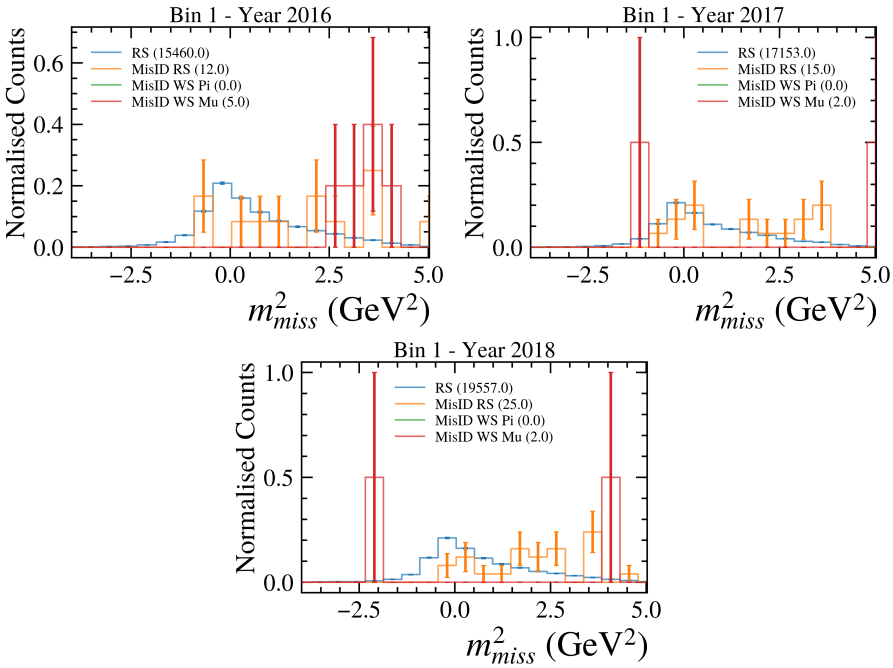


Figure 5.13: The misID template shapes shown in Bin 1 along with signal candidate. Legend shows the number of events for the different types of misID components from data taking years 2016/2017/2018

5.5.3 Fit model structure and parameters

For the fit stability, D^{**} backgrounds are grouped and the sum of the yields is floated for each group: $B \to D^{**}\mu\nu$, $B_s \to Ds^{**}$ and $B \to D^{**}(\text{Higher})\mu\nu$. Each group template is formed by combining the individual templates of the relevant modes as indicated in Tab. 5.10. The grouped templates are re-shaped according to the branching fractions and efficiencies of each mode to form the composition accurately. The overall templates shapes for each group along with its corresponding D^{**} modes are shown in Fig. 5.14 (for rest of the w bins, see Appendix F.3, Fig. F.3).

Group name	Modes summed
$N_{D^{**}}$ $(B \to D^{**}\mu\nu)$	$B^0 \to D_1\mu\nu$
	$B^0 \to D_1^{'}\mu\nu$
	$B^0 \to D_2^{*}\mu\nu$
	$B^+ \to D_1\mu\nu$
	$B^+ \to D_1^{'}\mu\nu$
	$B^+ \to D_2^{*}\mu\nu$
$N_{D_s^{**}}$ $(B_s \to D_s^{**}\mu)$	$B_s \to D_{s1}\mu\nu$
	$B_s \to D_{s2}^{*}\mu\nu$
$N_{D^{**}(\text{Higher})}(B \to D^{**}(\text{Higher}))$	$B^0 \to D^{**}(\text{Higher})\mu\nu$
	$B^+ \to D^{**}(\text{Higher})\mu\nu$

Table 5.10: Description of groups of D^{**}components and corresponding yield parameter in the fit

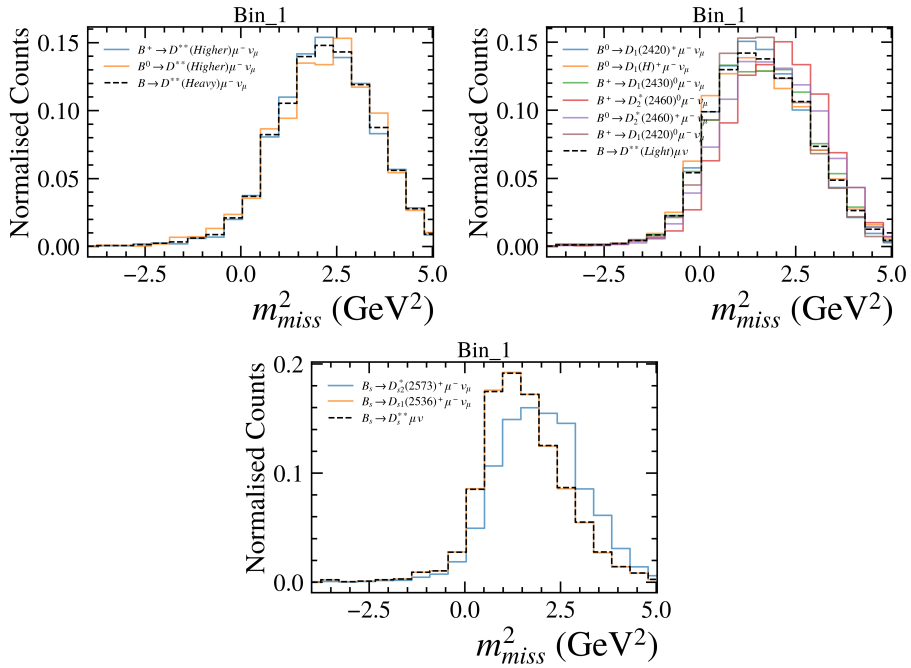


Figure 5.14: Combined D^{**} template shapes (black dashed-line) are shown together with its sub-components described as in Tab. 5.10 for the first w bin.

There are further considerations for the fit stability regarding the reparametrisation of yields of $B^0 \to D^*\tau\nu$ and $B_s \to D_s^{**}\mu$. The yield of $B^0 \to D^*\tau\nu$ component is related to the signal yield from the ratio of

$$\underbrace{\frac{N(B^0 \to D^*\tau\nu)}{N(B^0 \to D^*\mu\nu)}}_{f_\tau} = \underbrace{\frac{BF(B^0 \to D^*\tau\nu)}{BF(B^0 \to D^*\mu\nu)}}_{R(D^*)} \times BF(\tau \to \mu\nu\nu) \times \frac{\epsilon_\tau}{\epsilon_\mu} \tag{5.11}$$

where ratio of branching fractions, $R(D^*)$ is taken as 0.281± 0.013 reported from HFLAV (see Tab. 2.3); the efficiency $\epsilon_{\tau,\mu}$ is the number of events after offline selections in Tab. 5.4 divided by the number of generated events in simulation, and the value of branching fraction of $\tau \to \mu\nu\nu$ is taken from PDG as 0.1739± 0.0004. Therefore, the fraction of $B^0 \to D^*\tau\nu$ events relative to the signal events, f_τ is constrained with a Gaussian distribution to the value 0.0131±0.0031 and then floated in the fit.

In similar formalism, the yield of the component $B_s \to D_s^{**}\mu\nu$ can be related to the yield of $B \to D^{**}\mu\nu$ through the ratio

$$\underbrace{\frac{N(B_s \to D_s^{**}\mu\nu)}{N(B \to D^{**}\mu\nu)}}_{f_{B_s}} = \frac{BF(B_s \to D_s^{**}\mu\nu)}{BF(B \to D^{**}\mu\nu)} \times \frac{\epsilon_{D_s^{**}}}{\epsilon_{D^{**}}} \times \frac{f_s}{f_u + f_d} \tag{5.12}$$

where $BF(B_s \to D_s^{**}\mu\nu)$ is the branching fraction of $B_s \to D_s^{**}\mu\nu$ decay considering the two excited charm-strange states D_{s1} and D_{s2}; $BF(B \to D^{**}\mu\nu)$ is branching fraction of $B^{0,+} \to D^{**}\mu\nu$ decay considering each of B^0 and B^+ mesons decaying to three different D^{**} states (D_1, D_1', D_2^*). The $\epsilon_{D_{(s)}^{**}}$ efficiency of each sample is calculated as the number of selected events divided by the generated number of events in simulation, and $\frac{f_s}{f_u+f_d}$ is the ratio of the B_s, B^+, B^0 production fractions at the LHCb experiment. With the assumption of $f_u \simeq f_d$, the ratio becomes

$$\frac{f_s}{f_u + f_d} \simeq \frac{1}{2}\frac{f_s}{f_d} \tag{5.13}$$

where the value f_s/f_d is measured as 0.2539 ± 0.0079 at LHCb [150].
BF value of B^+ decaying to each $D^{**}(\to D^{*+}\pi)$ state - D_1, D_1', D_2^* - is taken directly from PDG [29]. The $BF(B^0 \to D^{**}(\to D^{*0}\pi)\ell\nu)$ is obtained using isospin relations

$$BF(B^0 \to D^{**}(\to D^{*+}\pi)\ell\nu) = \underbrace{\frac{BF(D^{**} \to D^{*+}\pi)}{BF(D^{**} \to D^{*0}\pi)}}_{0.5,\ \text{isospin symmetry factor}} \times BF(B^0 \to D^{**}(\to D^{*0}\pi)\ell\nu) \tag{5.14}$$

where $BF(B^0 \to D^{**}(\to D^{*0}\pi)\ell\nu)$ is taken from PDG [29].

For the $BF(B_s \to D_s^{**}\mu\nu)$ expression in Eq. 5.12, the D_{s1} contribution can be computed with the value of $BF(B_s \to D_{s1}(\to D^*K_s)\mu\nu)$ as $(2.7 \pm 0.7) \times 10^{-3}$ taken

from the PDG. For the D_{s2} contribution, the branching fraction of the $B_s \to D_{s2}(\to D^{*+}K_s)X\mu\nu$ is corrected through the channel $B_s \to D_{s2}(\to D^0K^+)X\mu\nu$ which has a PDG value of $(2.7 \pm 1.0) \times 10^{-3}$. The desired branching fraction is then expressed

$$BF(B_s \to D_{s2}\mu\nu) = BF(B_s \to D_{s2}(\to \bar{D}^0K^+)X\mu\nu) \times \frac{BF(D_{s2} \to D^*K_S)}{BF(D_{s2} \to D^0K^+)}. \tag{5.15}$$

where the ratio of $BF(D_{s2} \to D^{*+}K_S)/BF(D_{s2} \to D^0K^+)$ can be determined using experimentally measured relative branching-fraction ratios of D_{s2} decays. Explicitly, this ratio can be written as

$$\frac{BF(D_{s2} \to D^{*+}K_S)}{BF(D_{s2} \to D^0K^+)} = \underbrace{\frac{BF(D_{s2} \to D^{*+}K_S)}{BF(D_{s2} \to D^+K_S)}}_{\text{measured by LHCb}} \times \underbrace{\frac{BF(D_{s2} \to D^+K_S)}{BF(D_{s2} \to D^0K^+)}}_{\text{measured by Belle}} \tag{5.16}$$

The value of

$$\frac{BF(D_{s2} \to D^{*+}K_S)}{BF(D_{s2} \to D^+K_S)} = 0.044 \pm 0.005(\text{stat}) \pm 0.011(\text{syst}) \tag{5.17}$$

is measured by the LHCb experiment [151] and the value of

$$\frac{BF(D_{s2} \to D^+K_s)}{BF(D_{s2} \to D^0K^+)} = 0.49 \pm 0.10(\text{stat}) \pm 0.02(\text{syst}) \tag{5.18}$$

as reported from Belle experiment [152].

After plugging the numeric results to the expressions in Eq. 5.12, the ratio of yields $f_{B_s} = N_{D_s^{**}}/N_{D^{**}}$ is evaluated as 0.016±0.004 and floated in the fit with a Gaussian constraint.

Along with the nuisance parameters of $f_\tau = N_{D^*\tau}/N_{D^*\mu}$ and $f_{B_s} = N_{D_s^{**}}/N_{D^{**}}$, the overall fit parameters and the corresponding shapes of the components can be summarised in Tab. 5.11.

Component	Shape	Parameter
$B^0 \to D^*\mu\nu$	MC + HAMMER reweight	$N_{D^*\mu}$
$B^0 \to D^*\tau\nu$	MC + HAMMER reweight	$N_{D^*\tau}$
$B \to D^{**}\mu\nu$	MC + HAMMER reweight	$N_{D^{**}}$
$B_s \to D_s^{**}\mu\nu$	MC + HAMMER reweight	$N_{D_s^{**}}$
$B \to D^{**}(\text{Higher})\mu\nu$	MC	$N_{D^{**}(\text{Higher})}$
$B \to D^{*+}D(X_c \to \mu\nu X)$	MC	N_{D^*DX}
Combinatorial	Data	N_{comb}
D^* Combinatorial	Data	N_{D^*comb}
Nuisance parameter	$\frac{N_{D_s^{**}}}{N_{D^{**}}}$	f_{B_s}
	$\frac{N_{D^*\tau}}{N_{D^*\mu}}$	f_τ

Table 5.11: Fit components summary and their corresponding parameters. The third column lists the associated fit parameters to each of the components where N_i corresponds to the measured yield. Nuisance parameters are used for reparametrisation of the $N_{D^*\mu}$ and $N_{D_s^{**}}$ and they are gaussian constrained (see text for more details).

The template shapes used in each w bin fit can be seen in Fig. 5.15 where there is a good signal-background separation present.

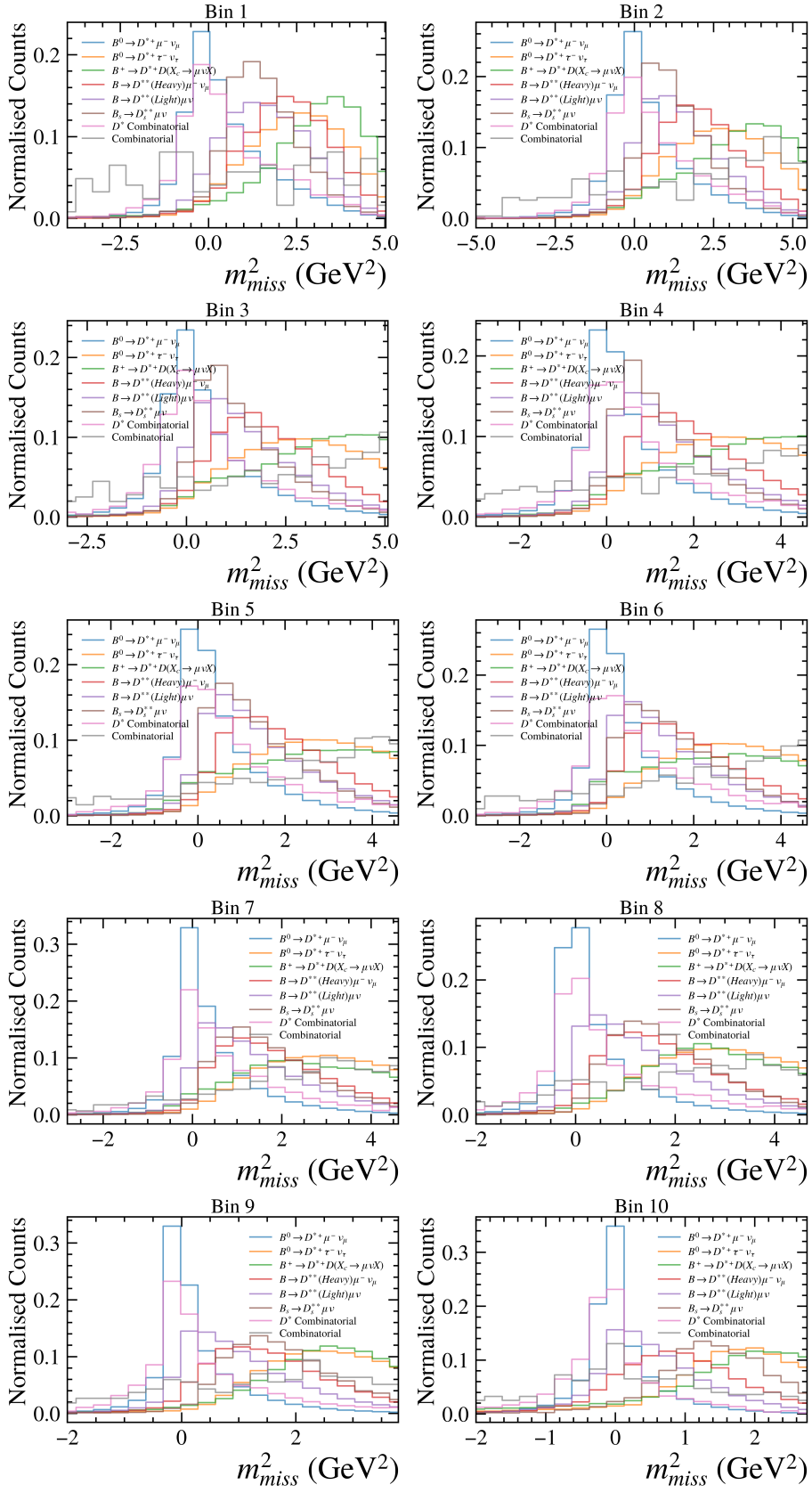


Figure 5.15: The template shapes used in 10 w bin fits shown.

5.5.4 Fit results

The results of the template fit performed in bins of the w are presented in this section. The yields shown (at this stage of the analysis) are raw values extracted directly from the m^2_{miss} fit; no corrections for detector efficiency, bin-to-bin migration (unfolding), or acceptance have been applied.

Fig. 5.16 displays the fit projection in the first w bin as an example, where the model accuracy and the signal domination are evident. The stability of the fit can be seen from the fit projections with the well-behaved *pulls* (pull = $(N^i_{\text{data}} - N^i_{\text{model}})/\sqrt{N^i_{\text{data}}}$). The similar behaviour is observed in across all w bins. The rest of the fit projections and the table of fitted parameters in each w bin are presented in Appendix G. All the fits are converged with a positive-definite covariance matrix.

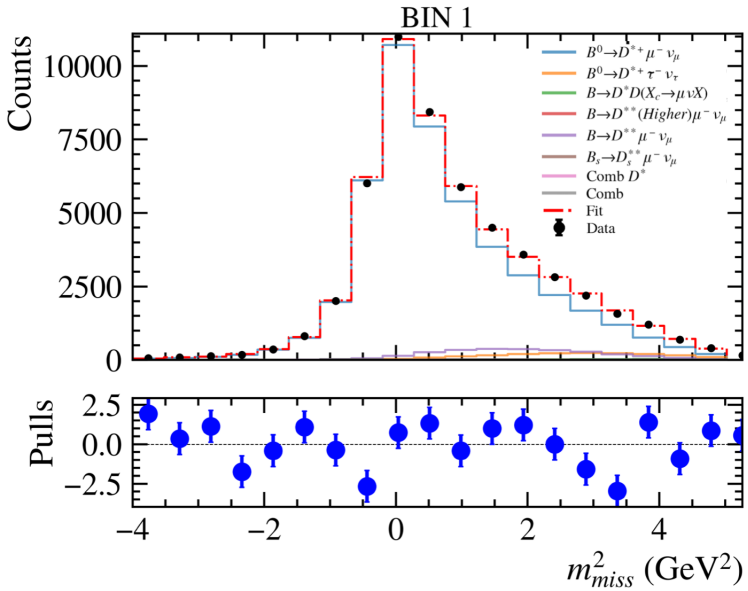


Figure 5.16: The m^2_{miss} fit projection in the first w bin.

Fig. 5.17 displays the fitted yields for the signal $B \to D^*\mu\nu$ candidates in each w bin. The distribution follows the expected kinematic shape, peaking at central values of w and exhibiting high statistical precision across the majority of the range. The corresponding yields for the various background components are shown in Fig. 5.18. It is noted that in specific bins for low-yield components—such as the D^*DX or $B_s \to D_s^*$ contributions—the statistical uncertainties are larger, reflecting the lower occupancy in those regions. These raw signal yields provide the foundation for the subsequent efficiency correction and unfolding procedures required to extract the final differential shape, which will be discussed in section 5.8.

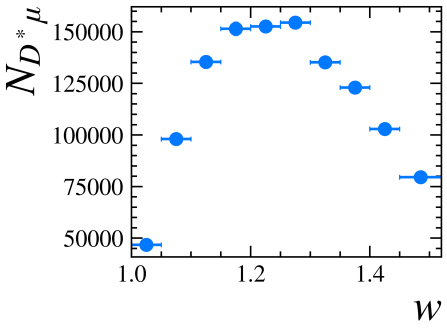


Figure 5.17: The fitted yields of signal component in each w bin

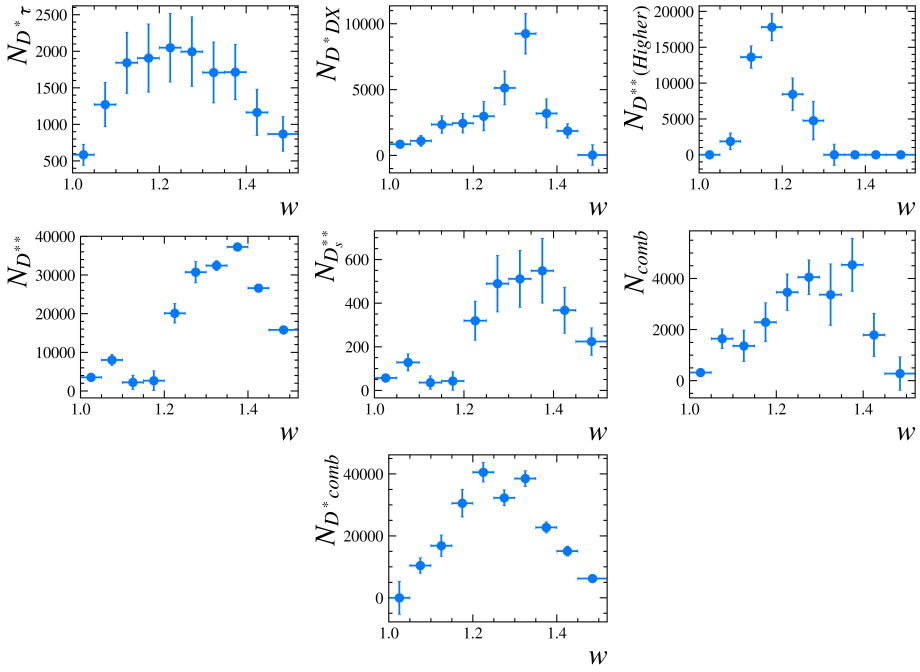


Figure 5.18: Fitted yields of background components in each w bin.

5.6 Corrections to simulation

Most of the fit templates are derived from simulation and therefore rely on an accurate description of the detector response and the underlying physics processes. Although the LHCb simulation framework (see Section 3.4.1) provides a detailed detector model, discrepancies can arise from factors such as detector alignment, local inefficiencies and approximations in the event generators. These discrepancies are addressed through two stages of reweighting. The initial reweighting is incorporated into the templates used in the nominal fit, whereas the final reweighting is used only

to evaluate systematic uncertainties and is not applied in the nominal fit.

- Initial reweighting: These weights are applied when constructing the m^2_{miss} fit templates used in the nominal fit to data. They improve the description of:
  - Event occupancy and B-meson kinematics;
  - Tracking efficiency.
- Final reweighting: This stage addresses residual differences observed in the data/MC comparison after the nominal fit. The comparison uses the fitted component composition, but the remaining discrepancies can reflect both simulation mis-modelling and imperfections in the background composition or shapes. These contributions cannot, in general, be uniquely disentangled from this comparison alone. The final reweighting is therefore treated as an empirical systematic variation probing the sensitivity of the results to residual discrepancies, conditional on the nominal fitted composition. Known modelling uncertainties in the double-charm and D^{**} backgrounds will also assessed through dedicated shape variations, as described in Section 5.9.2.

  Circular feedback into the nominal result is avoided because the final weights extracted from the post-fit comparison are not incorporated into the nominal templates. Instead, their effect is propagated by repeating the fit with the reweighted templates and using the resulting changes in the fitted parameters to evaluate the associated systematic uncertainty. This procedure assesses sensitivity to the residual disagreement; it does not independently validate the fitted background composition.

To validate the efficacy of the applied simulation corrections and the overall background modelling, a *post-fit cocktail* comparison is performed. This procedure evaluates whether the fully corrected simulation accurately describes the observed data when scaled to the results of the primary likelihood fit. Each simulation sample is weighted by the full suite of detector corrections—including tracking efficiency, and B kinematics—and scaled by its respective best-fit yield. Data-driven templates, such as those used to model combinatorial backgrounds, are similarly scaled. These components are then summed to construct a composite model of the expected data. By comparing this post-fit cocktail to the observed data across various distributions, the difference between the simulation and data can be assessed. The agreement in

these distributions, typically quantified by a Data-to-Model ratio consistent with unity, ensures that the final fit will not be biased by the Data-MC difference. The variables in Tab. 5.12 are chosen to ensure the simulation describes the data sample, and avoid potential biases due to mis-modelling reflecting upon detector geometry, trigger variables, track reconstruction of B^0 and D^0 ; and its decay products kinematic and track variables.

The PID-calibration (mentioned in section 5.4) and tracking-calibration weights are data-driven efficiency corrections, distinct from the PID and track-selection requirements imposed during triggering and reconstruction. These weights are applied during the initial reweighting stage. The subsequent final reweighting addresses residual data/MC discrepancies after these corrections have been applied, including possible mis-modelling of selection effects not fully described by the calibration weights. It therefore does not repeat the original PID or tracking-efficiency calibration. Moreover, the final reweighting is used only to evaluate systematic uncertainties and is not applied in the nominal fit.

Particle	Variable
B^0	FD, χ^2_{FD}, χ^2_{vertex}
D^0	FD, χ^2_{FD}, χ^2_{vertex}
D^0, K, π, μ	IP, χ^2_{IP}
D^0, K, π, μ	p, p_T, η
B^0	L0 trigger
Event	nTracks, PV/ndf

Table 5.12: List of variables used in the data/MC corrections. The meaning of the variables is explained at the beginning of section 4.1.

5.6.1 Initial reweighting procedure

The reweighting stage in this section refers to the B kinematic-occupancy and track efficiency corrections. These corrections are included in the m^2_{miss} fit to data, and the final results are derived from this reweighting stage.

5.6.1.1 Tracking efficiency correction

The simulation typically overestimates the probability of reconstructing a track, primarily due to an incomplete modelling of the detector's material budget and the complex dependencies of tracking algorithms on event occupancy. To correct for

these effects, tracking efficiency weights are applied to the simulation during the initial reweighting phase. These corrections are derived using a data-driven tag-and-probe method [153], utilizing high-purity samples of $J/\psi \to \mu^+\mu^-$ decays. In this approach, a muon (Tag) is fully reconstructed using standard tracking and PID criteria, providing a clean reconstruction of the J/ψ decay. The second muon from the decay (Probe) is identified using information independent of the standard tracking system (e.g., using only hits in the Muon Stations or the VELO). By checking how often the *probe* particle is also found by the standard tracking algorithms, the efficiency ε is measured in both data and simulation as a function of the track's kinematics (p and η) and the event occupancy (nTracks). The correction weight ω_{track} is defined as the ratio of these efficiencies

$$\omega_{\text{track}}(p, \eta, \text{nTracks}) = \frac{\varepsilon_{\text{data}}(p, \eta, \text{nTracks})}{\varepsilon_{\text{MC}}(p, \eta, \text{nTracks})} \tag{5.19}$$

These weights are applied to each final-state track in the B candidate decay chain.

5.6.1.2 B occupancy and kinematics corrections

The simulation accuracy depends on physics events generated by Pythia8. The models in Pythia8 governing how a b-quark *fragments* and hadronises into a B^0 or B^+ are phenomenological approximations that often mischaracterise the true transverse momentum (p_T) and rapidity (η) distributions of B mesons produced in p–p collisions. Because critical detector efficiencies—such as trigger acceptance and track reconstruction—are strongly dependent on these kinematics ultimately, they distort the shapes of fit variables. Therefore, we need to account for this by applying data-driven kinematic weights to align the MC samples with the collision data. A control sample $B \to J/\psi K$ decays is used to calculate the corrections to the b-hadron kinematics and occupation. The process begins by performing an unbinned maximum likelihood fit to the B candidate invariant mass spectrum in data using a Double Gaussian function for the signal and an exponential distribution for the combinatorial background. From this fit, the *sPlot* technique [154] is applied to calculate *sWeights* for each event, effectively statistically subtracting the background and isolating the signal-like B kinematics in data.

Subsequently, 2D correction maps are computed to align the simulation with the *sWeighted* data. These maps are derived by taking the ratio of the normalized distributions in data and MC for specific control variables:

- Occupancy Correction: A 2D correction map is generated in the plane of event-level occupancy variables, involving nTracks and the number of degrees of freedom in the fit to determine the position of the PV (PV/ndf).

- Kinematic Correction: A second 2D map is built using the B meson's transverse momentum $p_T(B)$ and the B meson's pseudo-rapidity $\eta(B)$ ($\eta = p_z/|p|$). This step corrects the b-quark fragmentation functions and the hard scattering process modelled in the generator.

The final per-event weight applied to the simulation samples is defined as the product of these two-dimensional correction maps. The impact of this reweighting procedure is illustrated for the $B \to J/\psi K$ sample in Fig. 5.19, where the corrected simulation exhibits significantly improved agreement with the observed data.

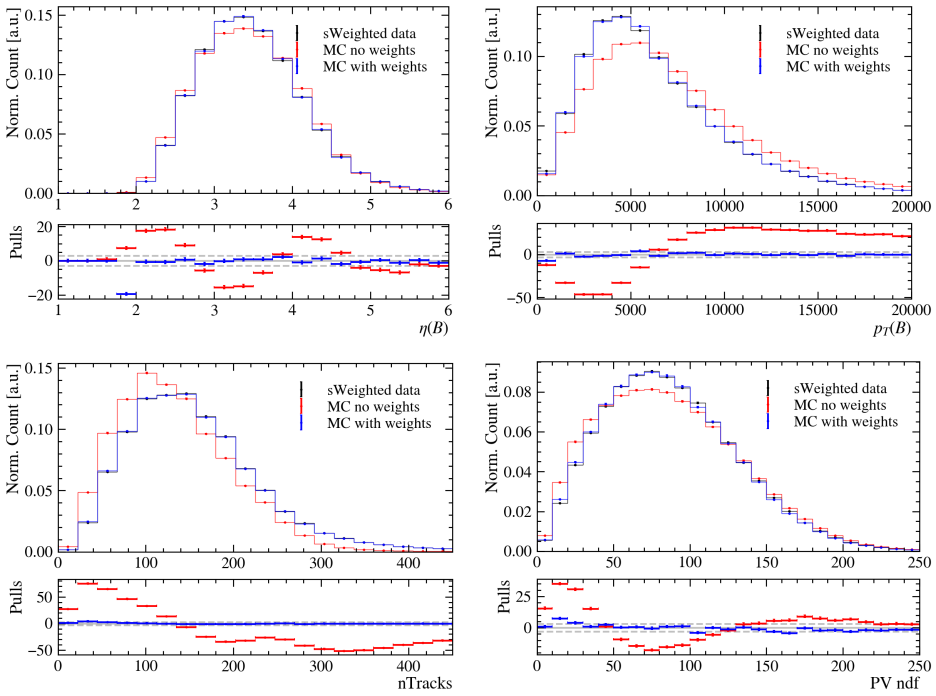


Figure 5.19: The comparison of correction variables for $B \to J/\psi K$ sample.

5.6.2 Final reweighting procedure

The additional set of variables to evaluate data/MC agreement are required for reflecting upon the possible causes on simulation mis-modelling. To account for these effects an iterative, multi-dimensional reweighting procedure is implemented. Each

stage utilizes a three-dimensional histogram (See Tab. 5.13 for the histogram variables) of the ratios computed from collision data and post-fit simulation cocktail (explained in the previous section). Each histogram is taken from signal enriched region ($m^2_{miss}< 0.5$ GeV$^2/c^4$), and the resulting weights from these ratio of histograms are applied on an event-by-event basis to the full sample, to iteratively align the simulation with data.

Since the L0 Global emulation is data-driven, it requires no direct simulation corrections. Conversely, the L0 Hadron emulation relies heavily on simulation. Consequently, the reweighting scheme is explicitly categorized into stages that differentiate between events passing the L0Global TIS trigger decisions and those that do not. The sequential stages are summarized in Tab. 5.13 and motivated as follows:

- Stage 1: Corrects for event occupancies while accounting for correlations with the L0 trigger.
- Stages 2 to 5: Correct for mis-modellings in the L0 Hadron, HLT1, and HLT2 trigger responses, alongside PID and tracking efficiencies.
- Final Stage: Addresses a minor geometric discrepancy in the D^0 direction angle (DIRA), defined as the angle between the D^0 momentum vector and its flight direction from the primary vertex to the decay vertex. This variable is reconstructed online within the HLT2 line and is not superseded by tighter offline selection criteria, making it more susceptible to simulation mis-modelling than pure offline variables.

In this section, for illustration of simulation corrections, the plots are shown for the distributions integrated over all w bins. For the m^2_{miss} fit to be considered in systematics studies in section 5.9.2, the templates are built while accounting for the simulation corrections evaluated for each w bin.

Figs. 5.20, 5.21, 5.22 and 5.23 demonstrate a good data/MC agreement following the final reweighting procedure. Although, there are still some residuals and regional disagreements present. In the low-value region of PV/ndf < 50, the ratio gets slightly below 1.0, whereas in the high end (PV/ndf > 150), the large disagreement is still present from the initial reweighting. The other occupancy variable, nTracks still shows disagreement in region 200–300. This might be due to the fact that PV/ndf is tied to the underlying event multiplicity and pileup environment, which is notoriously difficult for Monte Carlo to simulate perfectly. In the middle region

of IP(B^0) variable (0.5– 1.0 mm), large underestimation by simulation is visible. There is also a slight uniform over-prediction in the ratio panel for FDχ^2(B^0). For D^0 candidate, there is an under-prediction of FDχ^2(D^0) and small variations present in $\eta(D^0)$. For the trigger variables, there is a noticeable disagreement in L0 Hadron variable and this might affect data/MC agreement in variables of D^0 and its decay products. The issue might stem from a not fully accurate description of the L0 trigger in our emulation and is still being investigated.

The disagreements between data and simulation after this stage are taken into account while assigning the systematic uncertainties (See section 5.9.2), where the m^2_{miss} fit is performed with the new updated templates reweighted by the corrections presented in this section. The correction weights obtained at each step deviate from unity by less than 10%.

Variable 1	Binning 1	Variable 2	Binning 2	Variable 3	Binning 3
nTracks	10, 0-400	PV/ndf	10, 0-200	L0Global TIS	2, 0-1
$p_T(D^0)$	40, 2-15 GeV	D^0 η	20, 1.8-5.2	L0Global TIS	2, 0-1
$p_T(K)$	40, 0-10 GeV	K η	20, 1.8-5.2	L0Global TIS	2, 0-1
$p_T(\pi)$	40, 0-10 GeV	π η	20, 1.8-5.2	L0Global TIS	2, 0-1
$p_T(\mu)$	40, 0-10 GeV	μ η	20, 1.8-5.2	L0Global TIS	2, 0-1
log(1 - D^0 DIRA)	40, 20, -14–8.4	-	-	-	-

Table 5.13: Stages of sequential reweighting with each of them representing a 3D histogram with the given binning.

Figs. 5.20 and 5.21 show the data/MC agreement of B^0 and D^0 track geometry and kinematic variables along with occupancy after final reweighting stage.

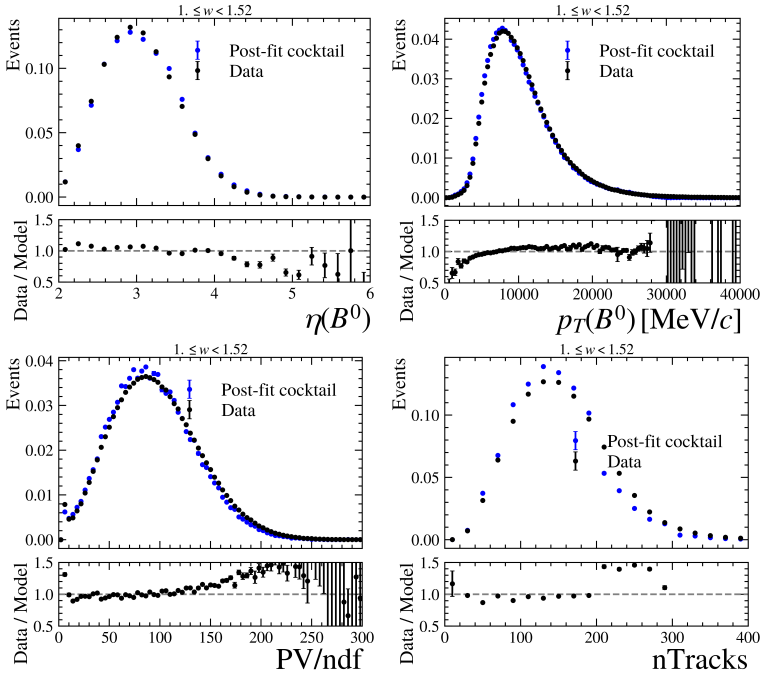


Figure 5.20: B^0 kinematic and occupancy variables comparison between data and simulation after final reweighting stage, where the black markers represent the data, while the blue markers represent the post-fit simulation cocktail. The lower panels display the data-to-model ratio.

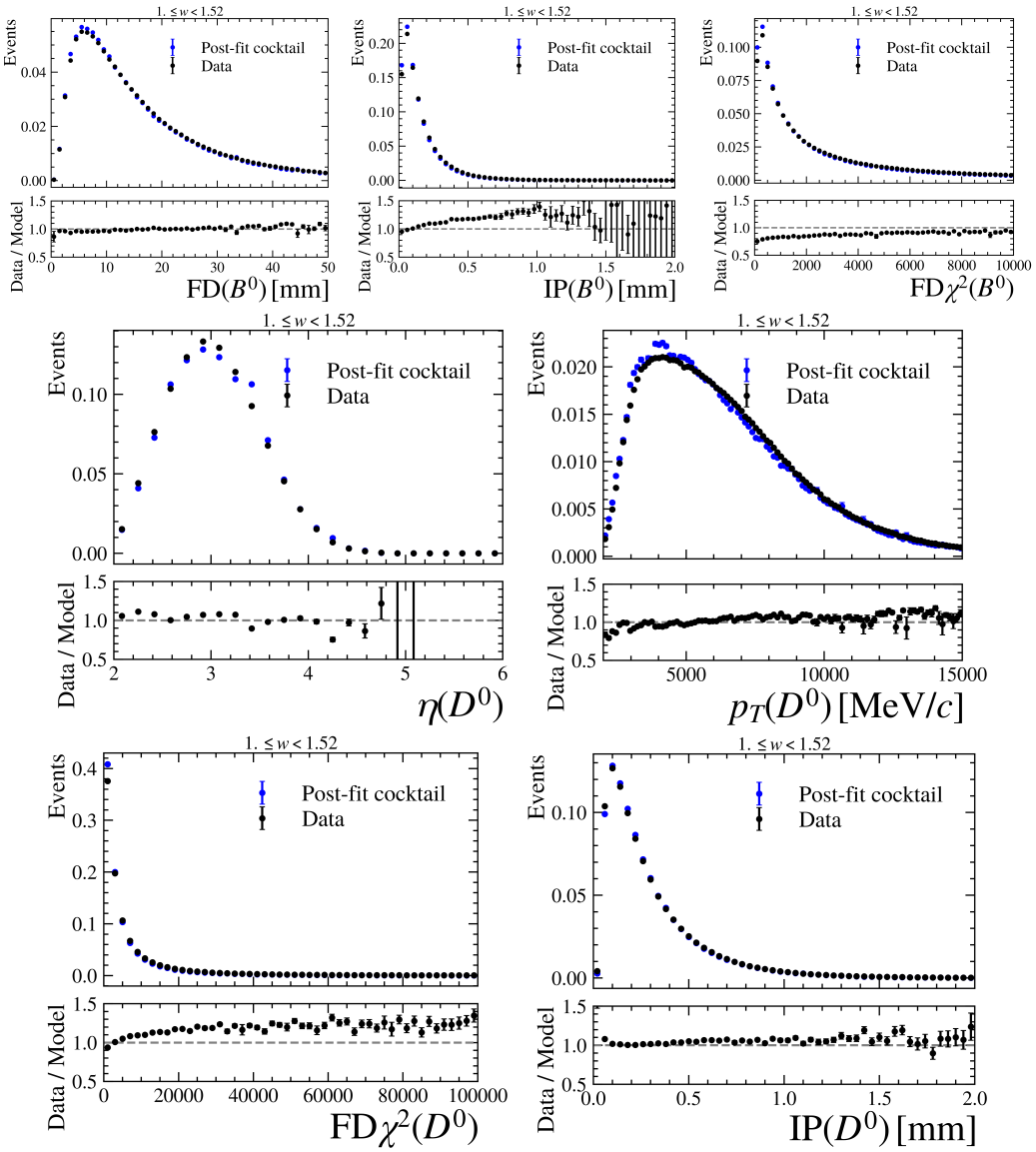


Figure 5.21: The comparison of kinematic and vertex variables of B^0 and D^0 between data and simulation after final reweighting stage across the whole w region, where the black markers represent the data, while the blue markers represent the post-fit simulation cocktail after final reweighting stage. The lower panels display the data-to-model ratio.

Fig. 5.22 shows the data/MC agreement of π, μ and K track geometry and kinematic variables after final reweighting stage. There are some residuals present in kinematics and track variables i.e. a large over-estimation by the model for the momentum of the pion in the region of $p > 60$ GeV, and small but non-uniform under-estimation in IP distributions of K and π.

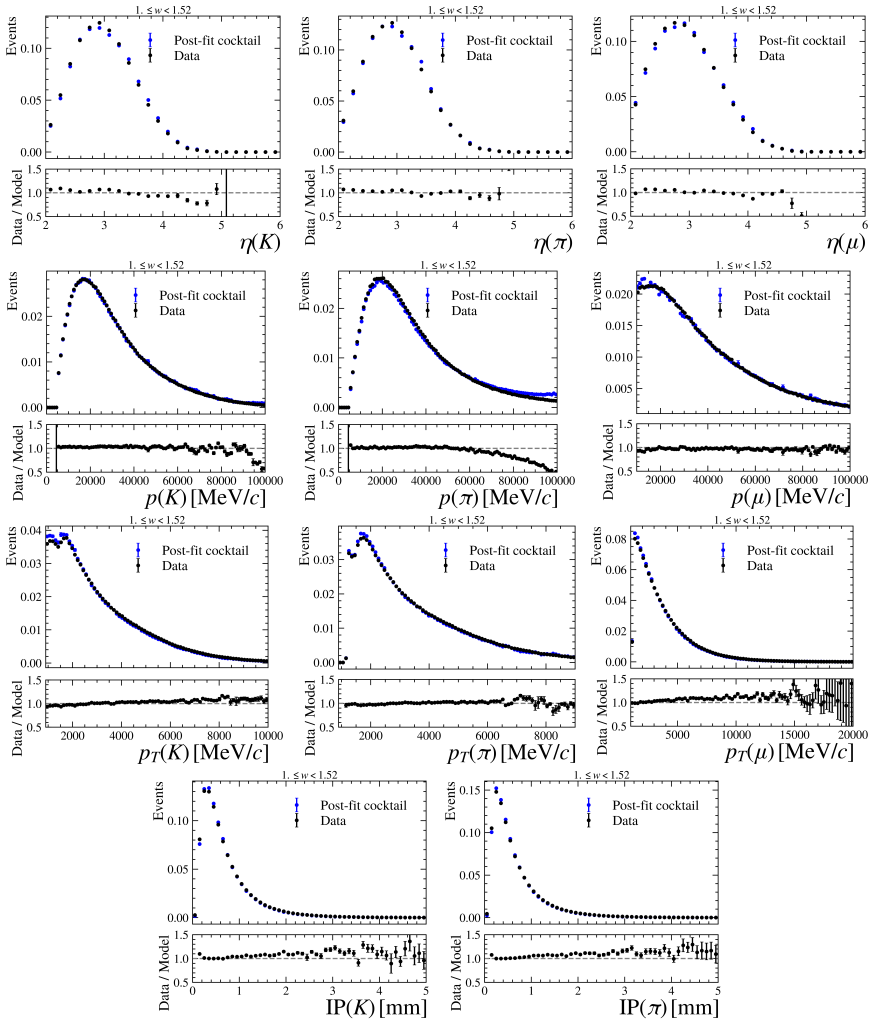


Figure 5.22: The comparison of kinematic and vertex variables for the final-state decay products (K, π, μ) between data and simulation after final reweighting stage across the whole w region, where the black markers represent the data, while the blue markers represent the post-fit simulation cocktail after final reweighting stage. The lower panels display the data-to-model ratio.

Fig. 5.23 shows data/MC agreement of the trigger variables after the final reweighting stage where we see similar agreement in L0 Global as in L0 Hadron.

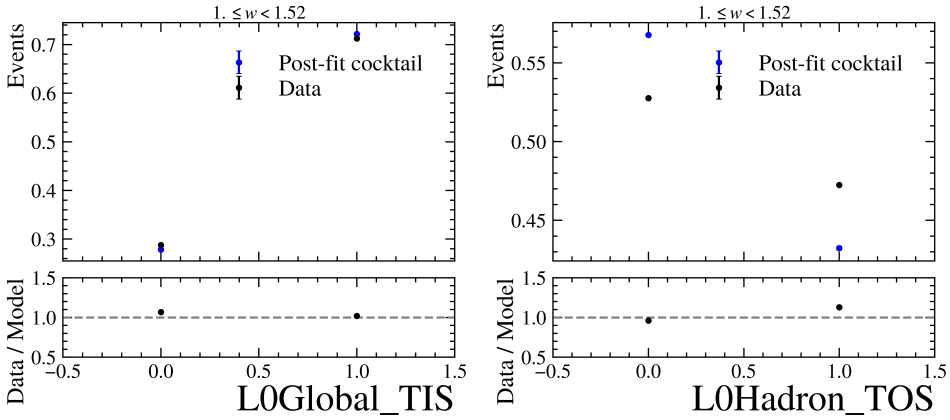


Figure 5.23: Trigger variables comparison between data and simulation after final reweighting stage, where the black markers represent the data, while the blue markers represent the post-fit simulation cocktail. The lower panels display the data-to-model ratio.

5.7 Efficiency correction

A fundamental requirement for interpreting the results after measuring the reconstructed kinematics is accurately translating the observed event yields in bins of w into the true physical distribution. The raw measured spectrum is inherently distorted by partial reconstruction due to the neutrino, detector geometric acceptance, detector resolution, and the analysis-specific kinematic selections required to suppress backgrounds. Crucially, these detector and algorithmic effects are not uniform across the phase space; rather, they introduce a strong, kinematics-dependent bias into the shape of the observed w distribution. To extract a physically meaningful decay rate that can be directly compared with theoretical predictions, the measured spectrum must be corrected for these phase-space-dependent variations, and unfolded, to obtain the spectrum in true w bins (rather than reconstructed w bins).

This analysis requires a precise measurement of all contributions to the detection efficiency as a function of the true hadronic recoil parameter, w_{true}, which is evaluated using simulated events. The total efficiency can be factorized into these distinct contributions

$$\epsilon_{\text{total}} = \epsilon_{\text{generator-level}} \times \epsilon_{\text{selections}} \times \epsilon_{\text{PID}} \times \epsilon_{\text{trigger}} \times \frac{\epsilon_{\text{track}}(\text{data})}{\epsilon_{\text{track}}(\text{MC})} \tag{5.20}$$

where $\epsilon_{\text{generator-level}}$ represents the *generator-level* efficiency, the efficiency of the ge-

ometrical acceptance and generator level cuts, and the remaining terms account for all subsequent selection criteria along with PID-trigger emulation, corresponding FF weight by HAMMER, b-kinematics and occupancy corrections and track efficiency weights, that are used to form the m^2_{miss} fit templates. While the combined selection efficiency—encompassing track reconstruction, PID, stripping, trigger requirements, isolation, and mass cuts—is evaluated using fully simulated MC, the official MC production only stores an integrated retention rate of 0.08 (meaning only 8% of generated events survive the trigger and centralized offline selection filters to be saved to disk). Because it does not preserve the efficiency as a function of w, a dedicated generator-level MC sample, generated without full detector simulation, is required as a baseline. Practically, rather than computing each term in Eq. 5.20 independently as a function of w, the total w-dependent efficiency is derived by comparing the fully selected simulated sample directly to this generator-level baseline

$$\epsilon^i_{\text{total}} = \frac{N^i_{\text{selected}}}{N^i_{\text{generator-level}}} \tag{5.21}$$

The numerator, N^i_{selected}, is the yield in each w_{true} bin (binned as in Tab. 5.9). The selected distributions obtained from the fully simulated dataset (Tab. 5.1) after applying all candidate selection criteria and applying the corresponding weights exactly as used in the m^2_{miss}template fits (See section 5.3). The denominator, $N^i_{\text{generator-level}}$, corresponds to the yield from a separate sample – generator-level samples – produced without detector simulation, binned in w_{true}. The events as a function of w_{true} from both generator-level and full simulation samples are normalised and then divided to get the correct shape for the efficiency corrections. The overall efficiency distribution is multiplied with retention rate of 0.08 since these distributions are taken from two different samples as generator-level and full simulation.

In this analysis, the efficiency is *blinded*, therefore, until the collaboration approval, the exact value of the efficiency is not shown throughout this thesis.

5.8 Unfolded decay rate spectrum

To extract the decay rate spectrum to be compared with theory predictions or any other experimental result, the observed w_{rec} distribution must be translated into the spectrum in the true kinematic variables. This is achieved by unfolding the

measured yields to account for detector resolution and bin migration, correcting for the selection efficiency in bins of w_{true}. The unfolding of the w distribution is performed using the `RooUnfold` package [155], and the unfolded signal yields in w bins can be seen in Fig. 5.25 and reported in Tab. 5.14.

The unfolding process begins by mapping the detector's response using a simulation dataset, where each simulated event's true w value is paired with its reconstructed value. These paired values populate a two-dimensional migration matrix that acts as a blueprint of how the detector distorts the underlying physics, and can be defined as

$$m_{i,j} = \frac{n(i,j)}{N(j)}, \qquad N(j) = \sum_i n(i,j), \tag{5.22}$$

where $N(j)$ is the total number of selected simulated signal events in true-w bin j, summed over the displayed reconstructed-w bins, and $n(i,j)$ is the subset reconstructed in bin i. Both quantities are evaluated after applying the full selection criteria described in Section 5.3. Thus, $\sum_i m_{i,j} = 1$ for each populated true-w bin. The resulting conditional migration probabilities are shown in Fig. 5.24.

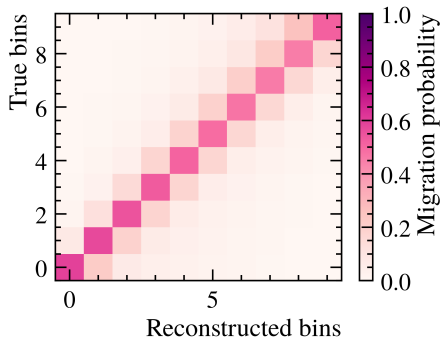


Figure 5.24: Migration matrix $m_{i,j}$ showing the probability of reconstruction in w_{rec} bin i conditional on true-w bin j for selected simulated signal events. Each row, corresponding to a true-w bin, is normalised to unity.

The true kinematic distribution is inferred from the raw collision data using the Iterative Bayesian Unfolding algorithm [156]. Rather than performing a direct and often unstable matrix inversion, this method utilises Bayes' theorem iteratively alongside the detector response matrix to probabilistically correct for finite resolution smearing and bin migration. Using the migration matrix as a conditional probability template ($P(\text{reco}|\text{true})$) along with a prior estimate of the spectrum shape, the al-

gorithm calculates an unfolding matrix. This unfolding matrix maps the observed counts in the smeared, reconstructed bins back to their most likely origin in the true physical bins. The process is executed iteratively over $n_{\text{iter}} = 4$ (regularisation parameter) cycles, where the unfolded output of each step updates the prior for the next, progressively reversing the effects of detector resolution smearing and bin-to-bin migration while maintaining statistical stability. Here, $n_{\text{iter}} = 4$ is chosen from the systematics studies, presented in section 5.9.5.

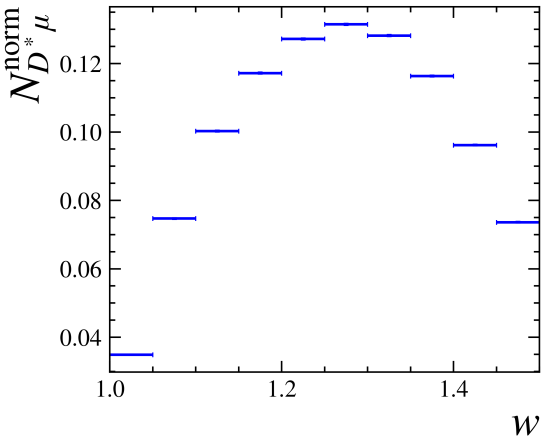


Figure 5.25: The normalised unfolded signal yield distribution in w bins.

The theoretical integrated decay rate in the j-th bin of w_{true} is defined as

$$\Delta\Gamma_j(\vec{p}) = \int_{w_{\text{true},j}} \frac{d\Gamma(B^0 \to D^*\mu\nu; \vec{p})}{dw_{\text{true}}} dw_{\text{true}} \tag{5.23}$$

where $\vec{p}$ represents the set of form factor parameters. These integrals are computed using the `SLOP` tool [157], which evaluates the decay rate by integrating the helicity amplitudes over the specified w ranges.
The expected number of events in the i-th bin of w_{rec} can then be expressed as

$$N_i^{\text{pred}} = \sum_{j=1}^{n_{\text{bins}}} m_{i,j} \cdot \Delta\Gamma_j(\vec{p}) \cdot \epsilon_j, \tag{5.24}$$

where ϵ_j is the efficiency of bin j. The unfolded and efficiency corrected signal yield in each w bin will be published after *unblinding*. The unblinding strategy is under discussion with the collaboration.

w range	$N^{\text{obs}}_{D^*\mu}$	$N^{\text{unf}}_{D^*\mu}$	$N^{\text{unf+corr}}_{D^*\mu}$
$1.00 < w \leq 1.05$	0.03964 ± 0.00029	0.03488 ± 0.00018	$XXX \pm 0.00039$
$1.05 < w \leq 1.10$	0.08317 ± 0.00182	0.07469 ± 0.00025	$XXX \pm 0.00046$
$1.10 < w \leq 1.15$	0.11480 ± 0.00257	0.10026 ± 0.00029	$XXX \pm 0.00050$
$1.15 < w \leq 1.20$	0.12842 ± 0.00275	0.11722 ± 0.00030	$XXX \pm 0.00052$
$1.20 < w \leq 1.25$	0.12937 ± 0.00220	0.12719 ± 0.00031	$XXX \pm 0.00055$
$1.25 < w \leq 1.30$	0.13099 ± 0.00184	0.13146 ± 0.00030	$XXX \pm 0.00055$
$1.30 < w \leq 1.35$	0.11463 ± 0.00155	0.12818 ± 0.00030	$XXX \pm 0.00055$
$1.35 < w \leq 1.40$	0.10430 ± 0.00120	0.11634 ± 0.00028	$XXX \pm 0.00053$
$1.40 < w \leq 1.45$	0.08725 ± 0.00107	0.09617 ± 0.00024	$XXX \pm 0.00049$
$1.45 \leq w \leq 1.52$	0.06742 ± 0.00085	0.07361 ± 0.00027	$XXX \pm 0.00047$

Table 5.14: Observed yields $N^{\text{obs}}_{D^*\mu}$, unfolded yields $N^{\text{unf}}_{D^*\mu}$ and unfolded yields corrected with the global efficiencies $N^{\text{unf+corr}}_{D^*\mu}$ for each w bin, all the yields are normalized to the total numbers over the whole w range. Uncertainties are only statistical.

5.9 Systematic uncertainties

This section lists the expected sources of systematic uncertainties with an overview of the methods to estimate them. Results of systematic uncertainties are in progress and only partially reported in this thesis. There are several sources of systematics considered in this analysis listed as

- Simulation sample size
- Data/MC differences
- Higher charm states background modelling
- Choice of FF parametrisation
- Unfolding procedure
- electromagnetic interaction between D^* and μ

From the studies presented in this section, the simulation sample size and data/MC difference are expected to be dominant ones while the other will have negligible effects on the overall systematic uncertainty.

5.9.1 Simulation sample size

The finite size of the MC samples introduces bin-by-bin statistical fluctuations into the template distributions used to model the signal and background components. Because these templates are treated as fixed probability density functions during the nominal fit, their internal statistical uncertainties propagate into the final measurement as a systematic uncertainty.

To evaluate the impact of this limited simulation statistics, a bootstrapping technique is employed. Bootstrapping [122] is a statistical resampling method designed to estimate the variance of an estimator by drawing repeatedly from the empirical distribution. For each simulated sample, an ensemble of pseudo-datasets is generated by randomly drawing events from the original sample with replacement until the new sample reaches the exact size of the nominal MC samples.

These resampled simulation events are then used to populate an ensemble of alternative, statistically fluctuated fitting templates. The entire fit procedure is subsequently repeated hundreds of times, replacing the nominal templates with a newly generated bootstrap template in each iteration. By analysing the resulting distribution of the number of signal yields across the ensemble of fits, the statistical spread—typically quantified as the standard deviation of the fitted yields—is extracted and assigned as the systematic uncertainty due to the finite simulation sample size.

5.9.2 Data and simulation differences

The agreement between data and simulation is primarily assessed by comparing occupancy, track and kinematic distributions in the post-fit cocktail, as detailed in section 5.6.2. The remaining disagreements are taken into account as a systematic uncertainty by assigning the resulting final weight from sequential reweighting scheme described in Tab. 5.13 to the simulation samples to construct the new m^2_{miss} templates. The m^2_{miss} fit is performed using these updated templates (Fit projections are provided in Appendix J). The resulting deviation in the extracted signal yield relative to the nominal fit result are reported in Tab. 5.15 with the relative systematic uncertainty. The relative systematic uncertainty is defined as

$$\delta_i^{\text{sys}}[\%] = \left(\frac{\sigma_i^{\text{sys}}}{N_i^{\text{nom}}} \right) \times 100, \tag{5.25}$$

where $\sigma_i^{\text{sys}} = |N_i^{\text{nom}} - N_i^{\text{Data/MC corr.}}|$

w bin	N_i^{nom}	$N_i^{\text{Data/MC corr.}}$	Rel. Systematic (%)
1.025	46750 ± 340	45161 ± 1437	3.400 ± 3.152
1.075	98090 ± 2100	95495 ± 1966	2.646 ± 2.892
1.125	135400 ± 3000	123727 ± 2736	8.621 ± 2.861
1.175	151500 ± 3200	145807 ± 3131	3.758 ± 2.899
1.225	152600 ± 2600	146757 ± 2285	3.829 ± 2.220
1.275	154500 ± 2200	155053 ± 1562	0.358 ± 1.750
1.325	135200 ± 1800	136346 ± 1906	0.848 ± 1.947
1.375	123000 ± 1400	126800 ± 1484	3.090 ± 1.683
1.425	103000 ± 1200	108296 ± 1322	5.142 ± 1.774
1.475	79500 ± 1000	86880 ± 482	9.283 ± 1.503

Table 5.15: The signal yields extracted with final data/MC weights and nominal procedure along with the relative systematic uncertainty.

While the analysis employs a specific data-driven reweighting scheme to correct for residual data/MC differences, the choices within this procedure—namely the selection of kinematic variables and their specific binning granularities—introduce a source of systematic uncertainty. To evaluate this effect completely, a second iteration of the reweighting procedure should be performed using the alternative sets of data/MC corrections by modifying the baseline binning schemes outlined in Tab. 5.13. These alternative weights should then be applied to the simulation to construct a new set of m^2_{miss} fit templates, then, the resulting difference in the fitted signal yields should also be reported.

5.9.3 Higher charm states background modelling

To maintain fit stability in the nominal fit, the broad and overlapping D^{**} background contributions are merged into three primary groups: $B \to D^{**}\mu\nu$, $B_s \to D_s^{**}\mu\nu$, $B \to D^{**}(\text{Higher})\mu\nu$. As indicated in Tab. 5.10, the total template for each group is constructed by combining the individual templates of the relevant submodes. These grouped templates are combined according to the expected branching fractions and relative selection efficiencies of each specific mode to accurately reflect the true physical composition. Consequently, a systematic uncertainty arises from the limited experimental precision of these input branching ratios and the resulting kinematic shape of the merged templates. To evaluate this systematic effect, the internal composition of each grouped D^{**} template is varied by fluctuating

the assumed relative branching fractions and efficiency profiles within their current experimental uncertainties. The fit is then repeated using these compositionally altered templates to determine the corresponding shift in the extracted signal yield. The selected sample in this analysis is signal-dominated, the various background components, particularly the D^{**} states, are measured to be near-zero yields in the fit for the several bins of w. Consequently, systematic uncertainties arising from this are expected to be heavily suppressed.

The contamination from double-charm backgrounds—where a second charm hadron undergoes a semileptonic decay, and the muon in the decay is reconstructed as signal, is heavily suppressed by the selection criteria. Given the purity of the signal region, the specific modelling and precise branching fractions of these decays are expected to have a negligible impact on the final extracted yields. Nevertheless, conservative variations of their expected overall yields will be tested during the fit procedure to confirm their minimal influence and assign any residual uncertainty.

5.9.4 Choice of form factor parametrisation

To account for the uncertainty in the baseline form factor model – BGL – used to reweight the generated signal MC, variations of the BGL parameters must be evaluated. This will be achieved by reweighting the simulated events, where the form factor parameter space will be re-sampled by utilizing the full covariance matrix provided by the Run 1 angular analysis presented in Ch. 4 [27]. The resulting deviations in the signal templates and the fit results will be assigned as the systematic uncertainty associated with the signal modelling.

The calculation of the selection efficiencies mentioned in section 5.7 relies on generator-level distributions, which inherently depend on the assumed form factor model. Similarly, to decouple the efficiency maps from the specific parameters chosen during the initial MC production –CLN–, the generator-level samples will also be reweighted for BGL model using HAMMER. By varying the underlying form factor configurations within their current experimental bounds, the shift in the bin-by-bin selection efficiencies can be evaluated and propagated as a dedicated systematic uncertainty.

Since m^2_{miss} template shapes are not so much dependent on the form factor parametrisation, this systematics will likely have a negligible effect on the total uncertainty. As an example, Fig. 5.26 shows the m^2_{miss} shape comparison with two

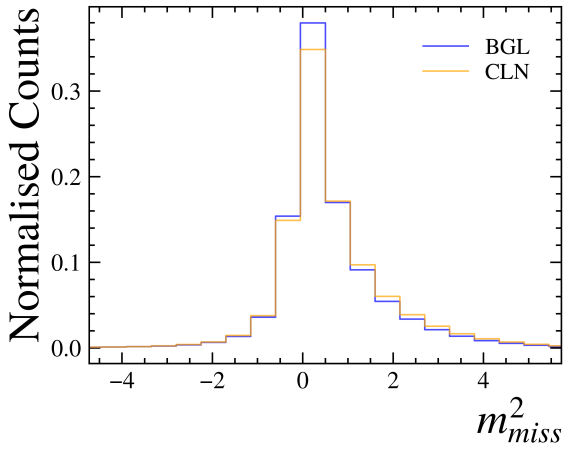


Figure 5.26: Normalised signal distribution in m^2_{miss} with two different form factor parametrisations.

different FF parametrisation, where we do not see a drastic change even with two different parametrisations.

5.9.5 Unfolding

To account for the regularization bias inherent in the unfolding procedure, a systematic uncertainty is assigned to the choice of the iteration parameter in `RooUnfold` algorithm. The nominal number of iterations ($n = 4$) was varied by ± 1, and the resulting shifts in the unfolded bin yields were evaluated. The systematic uncertainty for each bin is defined as the maximum absolute deviation between the nominal yield and the yields obtained from these variations, expressed as

$$\sigma_i^{\text{sys}} = \max(|N_i^{\text{nom}} - N_i^{n+1}|, |N_i^{\text{nom}} - N_i^{n-1}|) \tag{5.26}$$

The relative systematic uncertainty is defined as

$$\delta_i^{\text{sys}}[\%] = \left(\frac{\sigma_i^{\text{sys}}}{N_i^{\text{nom}}}\right) \times 100, \tag{5.27}$$

providing a measure of the sensitivity of the unfolded yields to the choice of the regularisation parameter. The results, summarised in Tab. 5.16, demonstrate that the unfolding procedure is highly stable under variations of the iteration parameter n.

w bin	N_i^{nom} $(n=4)$	N_i^{n-1} $(n=3)$	N_i^{n+1} $(n=5)$	σ_i^{sys}	Rel. Sys (%)
1.025	61949	61890	62059	85	0.14%
1.075	132672	133177	132427	375	0.28%
1.125	178078	178520	177922	299	0.17%
1.175	208202	208611	207977	317	0.15%
1.225	225928	225980	225845	68	0.03%
1.275	233510	233066	233680	307	0.13%
1.325	227679	226695	228261	783	0.34%
1.375	206652	205713	207312	799	0.39%
1.425	170818	171078	170583	247	0.14%
1.475	130750	131641	130070	786	0.60%

Table 5.16: Unfolded signal yield using different iterations and the relative systematic uncertainty from unfolding regularization.

5.9.6 Electromagnetic interactions

Standard MC generators often omit the electromagnetic interactions between the charged D^* meson and the muon. This Coulomb interaction can induce minor distortions in the decay kinematics, slightly altering the measured decay rate spectrum compared to the theoretically predicted pure weak decay. The systematic impact of neglecting this effect will be estimated analytically by following the framework outlined in Ref. [158]. However, the impact is expected to have a negligible impact on the total uncertainty as it is also the case for the Run 1 angular analysis presented in Ch. 4 [27].

5.10 Conclusion

The differential decay rate shape of $B^0 \to D^{*-}\mu^+\nu_\mu$ is measured in bins of the hadronic recoil parameter, w with 5.4 fb^{-1} integrated luminosity collected by LHCb experiment in p–p collisions at a centre of mass energy of 13 TeV (Run 2). The reconstructed spectrum is unfolded and efficiency-corrected to retrieve the physical distribution to be able to compare with theoretical predictions and other experimental results. Notably, the novel reconstruction techniques using Gaussian regression in this analysis yield a ∼20% improvement in w resolution compared to traditional approaches used in semileptonic decays. Statistical uncertainties on the measured signal yield in each w bin indicate the improved sensitivity compared to Belle II measurement in the same decay channel [5], which can be seen from Tab. 5.17.

w Range	This Work	Belle II [5]
1.00 – 1.05	0.00039	0.0014
1.05 – 1.10	0.00046	0.0019
1.10 – 1.15	0.00050	0.0020
1.15 – 1.20	0.00052	0.0021
1.20 – 1.25	0.00055	0.0020
1.25 – 1.30	0.00055	0.0020
1.30 – 1.35	0.00055	0.0019
1.35 – 1.40	0.00053	0.0018
1.40 – 1.45	0.00049	0.0018
1.45 – 1.52	0.00047	0.0018

Table 5.17: Statistical uncertainties on the unfolded and efficiency corrected signal yields binned in w from different measurements, normalized to the total yield.

This precision is particularly crucial in the low-w (high-q^2) kinematic region, where theoretical predictions i.e. LQCD calculations are most precise. A high-precision determination of this spectrum is currently of paramount importance to the flavour physics community. As detailed in section 2.5.2, recent full-kinematic-range LQCD calculations exhibit notable tensions with the existing differential measurements reported by the Belle and Belle II collaborations. By providing a highly precise, independent evaluation of the $d\Gamma/dw$ shape, this measurement will serve as a critical diagnostic tool to investigate the source of these discrepancies.

To prevent experimenter bias, efficiency corrected yields are not shown through out the thesis. When the measurement is finalised, the efficiency corrected and unfolded spectrum—alongside its detailed quantitative comparisons to state-of-the-art LQCD predictions and B-factory results—will be published and is not reported in this thesis. This distribution will also be fitted with BGL form factor parametrisation to extract the parameters of interest.

The Fig. 5.27 can be seen as the early demonstration of expected precision of this analysis, where the Run 1 angular analysis results for central values are in place of the still blinded results, but the statistical uncertainties are provided from the Run 2 shape measurement. The systematic uncertainties are expected to be below or equal to the statistical uncertainties, therefore, this measurement is expected to deliver competitive results. Fig. 5.27 shows the comparison of decay rate density in w from different LQCD predictions and experimental results from LHCb [27] and Belle-Belle II HFLAV average results [52], where systematics uncertainties included.

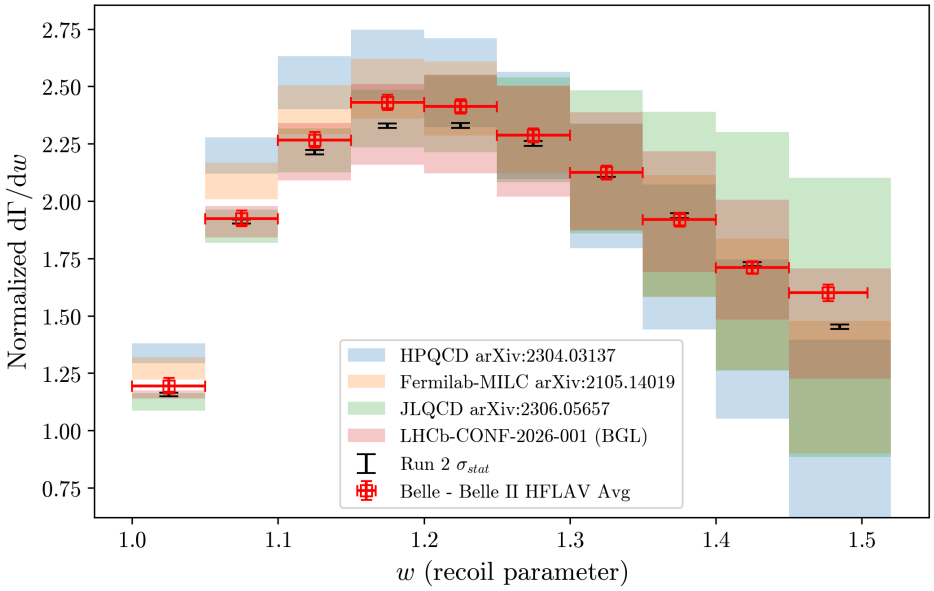


Figure 5.27: Normalised decay rate of $B^0 \to D^{*-}\mu^+\nu_\mu$ in w compared, with the total uncertainties (except the Run 2 measurement).

Furthermore, the robust framework established here is explicitly designed to extract the full suite of angular coefficients in near-future iterations of the analysis. By extracting the angular coefficients—which encode both the non-perturbative QCD information (form factors) and the electroweak couplings (Wilson coefficients)—this approach successfully isolates the model-dependent components of the decay rate from its underlying kinematic geometry. Consequently, it enables a rigorous reinterpretation of the experimental results without tying them to a specific New Physics model or rigid form-factor parametrisation.

Building on this model-independent foundation, future iterations of this analysis are uniquely positioned to perform a competitive measurement of the CKM matrix element $|V_{cb}|$. This will be achieved by utilizing $B \to D^*\pi$ decays as a normalization mode. By exploiting trigger selections on the charm hadron, numerous correlated systematic uncertainties can be cleanly cancelled in the ratio.

Chapter 6

Conclusion

This chapter summarises the key findings of this thesis, their impact in the research areas explored and outlines the outlook for future experimental efforts.

New Physics couplings and hadronic form-factor parameters are measured using 3fb^{-1} collected by LHCb experiment in p–p collisions at the centre of mass energies of 7 TeV and 8 TeV (Run 1) by exploiting the full angular structure of the decay through a five-dimensional fit, which maximizes sensitivity. The hadronic form-factor results have been presented at Moriond 2026 [27] (See section 4.8). This work provides substantial information on different form-factor parametrisations (CLN, BGL, BLPR) and the angular observables, while also offering direct comparisons with experimental results from Belle and LQCD predictions. These results are compatible with LQCD and theoretical predictions, while achieving improved precision.

Furthermore, an extensive study of NP parameter phase space was conducted using pseudo-data without imposing a single, rigid NP structure (See section 4.6.1.5). This exploration provides crucial input regarding different NP fit configurations and the correlations between their parameters. Notably, this analysis presents the first direct measurement of NP Wilson Coefficients in $B^0 \to D^{*-}\mu^+\nu_\mu$ decays, alongside with the first measurement of hadronic form-factor parameters in the same decay channel at the LHCb experiment. The NP results were presented in ICHEP 2026 [159]. The results (See section 4.8) are consistent with zero, in agreement with the SM predictions and compatible with recent global fits of Belle II and LQCD data while achieving improved precision.

Ultimately, these results improve constraints on both hadronic form factors and potential NP contributions, offering valuable input for future theoretical and experimental developments in semileptonic b-decays.

This work has established an advanced analytical framework for the study of

semileptonic $B^0 \to D^{*-}\mu^+\nu_\mu$ decays, utilising $5.4\,\text{fb}^{-1}$ of Run 2 data collected by the LHCb experiment at a centre-of-mass energy of 13 TeV. By integrating Gaussian process regression into the kinematic reconstruction pipeline, the analysis achieves a $\sim 20\%$ improvement in the hadronic recoil parameter (w) resolution compared to standard techniques. This technical advancement directly targets the low-w (high-q^2) kinematic domain, where LQCD calculations offer their highest theoretical precision. The resulting high-precision measurement of the differential decay rate, $\mathrm{d}\Gamma/\mathrm{d}w$, provides a crucial diagnostic tool for the flavour physics community. Specifically, it offers an independent evaluation to help clarify existing discrepancies between full-kinematic-range LQCD predictions and measurements from the Belle and Belle II collaborations. While the measurement is still being finalised to publish the unfolded and efficiency-corrected yields, the uncertainties demonstrate that the analysis is positioned to match or exceed the precision of existing results (See section 5.10), with systematic uncertainties anticipated to remain controlled at or below statistical limits.

In this thesis, we investigated two distinct yet complementary approaches for the differential decay rate measurements of semileptonic B decays. The first approach—the multi-dimensional fit—prioritises the new physics sensitivity, simultaneously extracting hadronic form-factor parameters and Wilson coefficients by exploiting the full kinematic and angular variables phase space. While this provides the most stringent constraints on New Physics, it remains inherently tethered to the validity of the underlying physics models and the chosen form-factor parametrisations. Conversely, the second approach of differential decay rate in hadronic recoil parameter — followed by the extraction of model-independent angular coefficients—serves as a precise, diagnostic probe for hadronic structure (and angular observables with angular coefficients). These approaches function as a mutually reinforcing system, where their respective strengths can serve to specific purposes.

In the context of detector design for the LHCb Upgrade II, this thesis drafted the baseline digitisation event model classes for the MightyPix sensors alongside a computationally efficient polynomial fast-track reconstruction algorithm for preliminary studies of track parameters in Mighty Tracker. Looking forward, as the Mighty Tracker transitions from the preliminary design to a finalised, full detector geometry, these stand-alone frameworks will serve as a foundation. The immediate next step requires integrating this digitisation into the full LHCb simulation chain. Ultimately, this work opens the door for scaling up robust, high-performance tracking

algorithms capable of operating in the extreme occupancy and data-rate conditions of the High-Luminosity LHC.

Appendices

A Single Wilson coefficient toys

A.1 S_{qLlL} toys

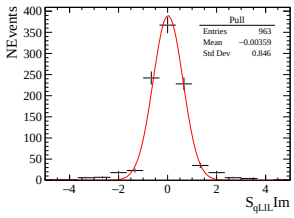


Figure A.1: Pull distributions of the Wilson coefficient.

A.1.1 Generation fixed to 0.0

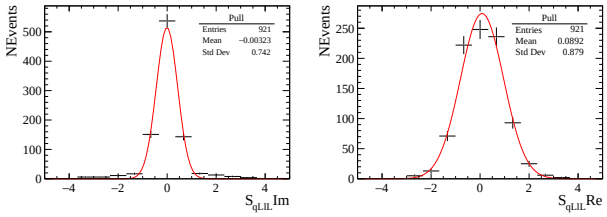


Figure A.2: Pull distributions of the Wilson coefficient.

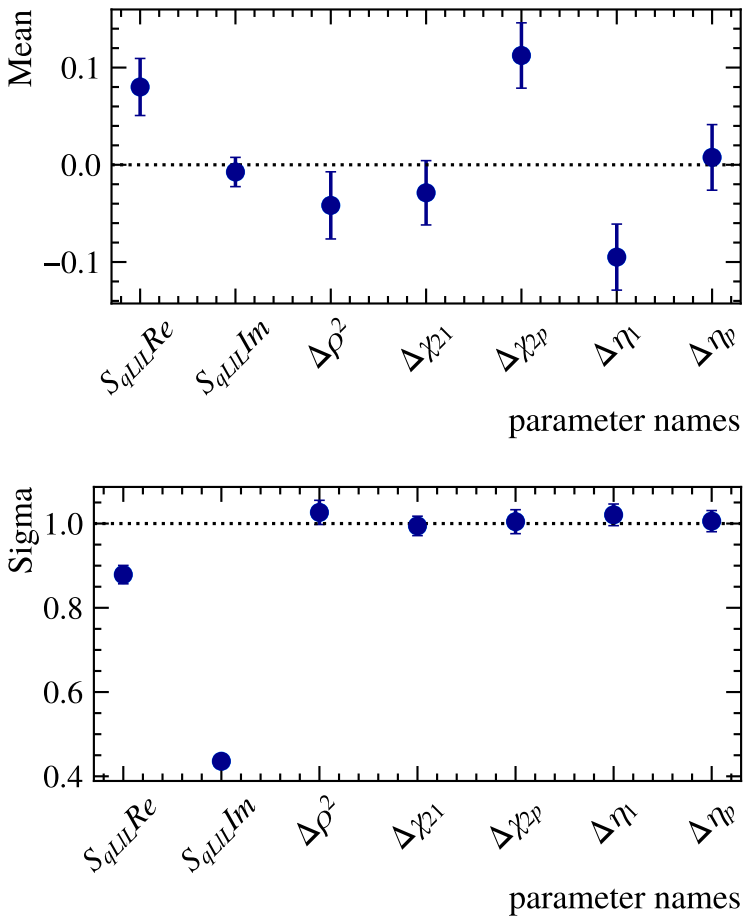


Figure A.3: Summary plot of the mean and sigma values of the pull distributions. The uncertainty on the data points is the error from the fit.

B Toy studies with multiple Wilson coefficients

B.1 Generation fixed to 0.0

Plots for toys when the Wilson coefficients generation is fixed to 0.0.

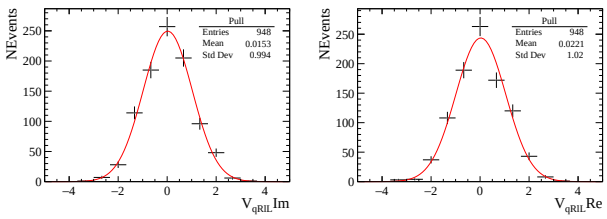


Figure B.1: Pull distributions of the Wilson coefficient.

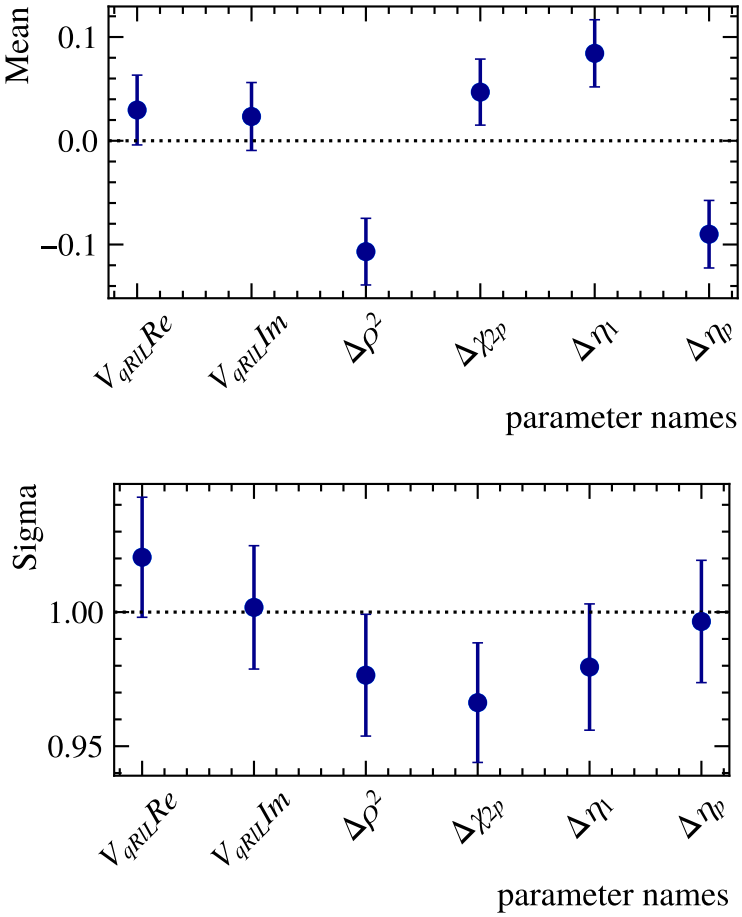


Figure B.2: Summary plot of the mean and sigma values of the pull distributions. The uncertainty on the data points is the error from the fit.

B.2 Generation fixed to 0.0

Imaginary part of the WC has highly overestimated uncertainty.

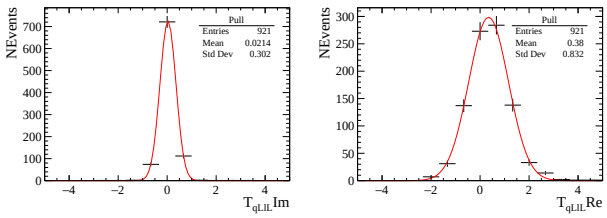


Figure B.3: Pull distributions of the Wilson coefficient.

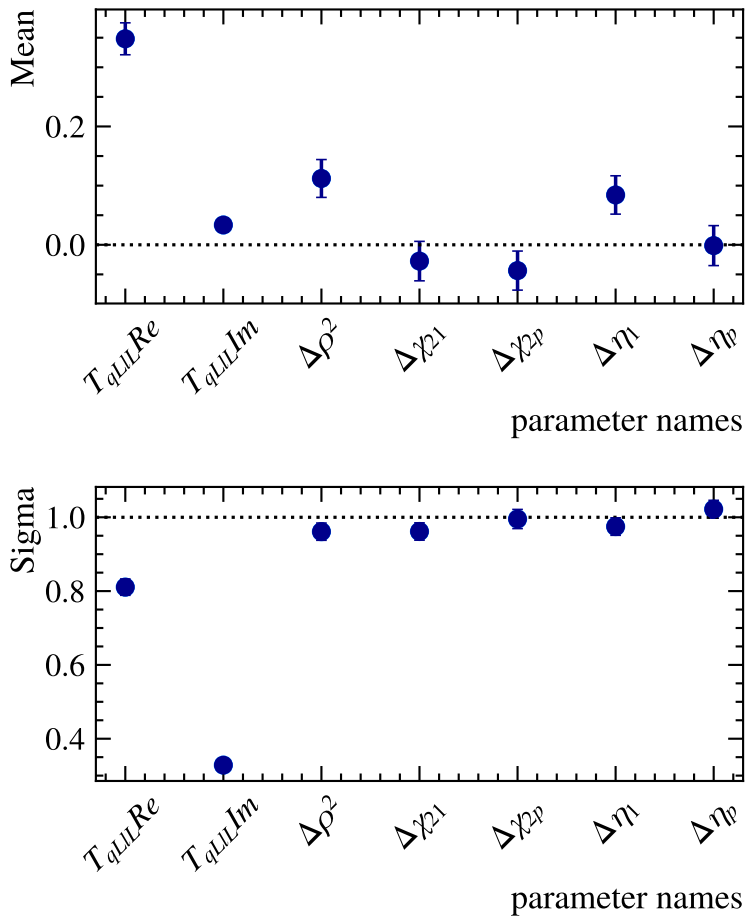


Figure B.4: Summary plot of the mean and sigma values of the pull distributions. The uncertainty on the data points is the error from the fit.

B.3 Scanning different WC values

In this section the results from the configurations namely; A, B, C, D in Tab. 6.1 when the WCs have a fixed generation value in the toys are presented. All the configurations from

Configuration	V_{qRlL}Re	V_{qRlL}Im	S_{qLlL}Re	S_{qLlL}Im	T_{qLlL}Re	T_{qLlL}Im
A	0.0	0.0	0.0	0.0	0.0	0.0
B	0.0	0.0	0.1	0.1	0.1	0.1
C	0.1	0.1	0.1	0.1	0.1	0.1
D	0.5	0.5	0.5	0.5	0.5	0.5

Table 6.1: Different WC generation values considered in the toys. Each row (labelled with different letter) represents the fixed generation value for the Wilson coefficient in the toys.

A: VRL=0.0, SLL=0.0, TLL=0.0

In this set of toys the generation values of WCs are fixed to 0.0 and they float starting from 0.0 in the range of [-1,1]. 1000 toys were fitted with a convergence rate of 98% where the converged fits are displayed in Fig. B.5. Correlations from one toy are given in Fig. B.7. Example likelihood scans are given in Fig. B.6.

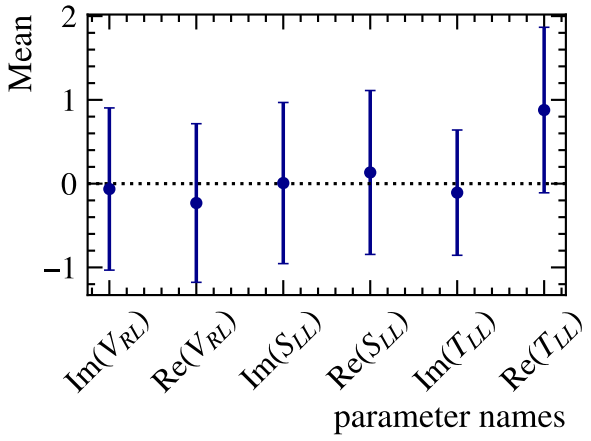


Figure B.5: Summary plot of the mean values of the pull distributions when the Wilson coefficients are generated at a fixed point of 0.0 and fitted starting from 0.0 in the range [-1,1]. The uncertainty of the data points are the standard deviation of the pulls

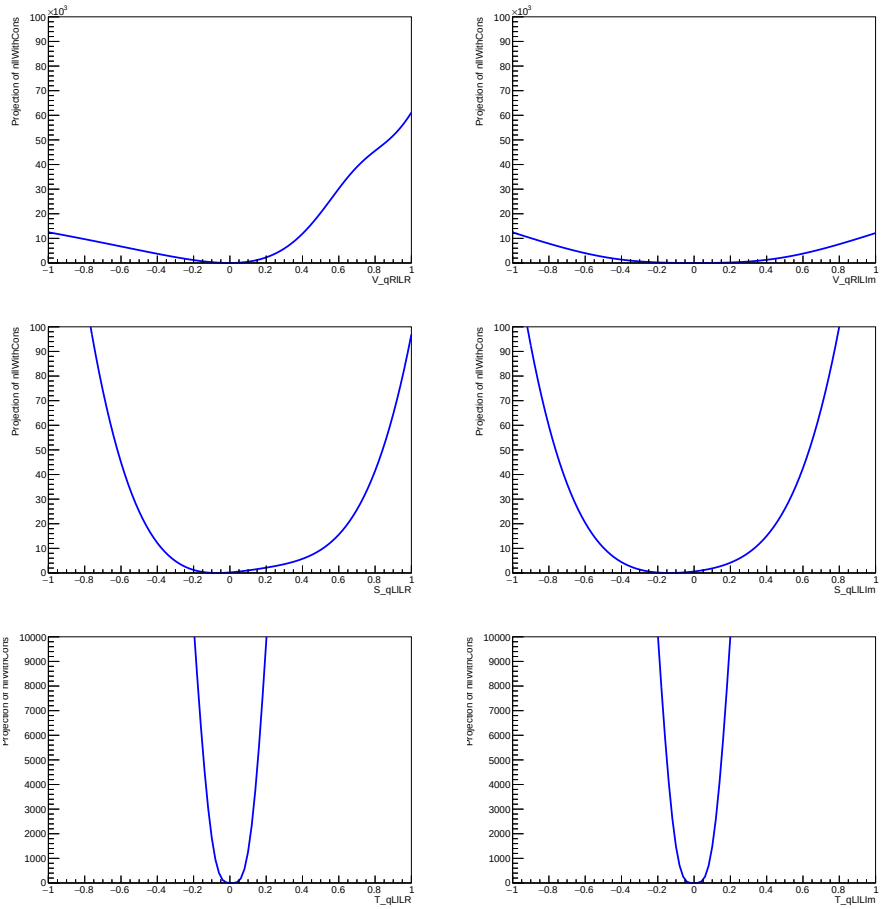


Figure B.6: Likelihood scans of WCs generated at 0.0 and float starting from 0.0 in the range of [-1,1].

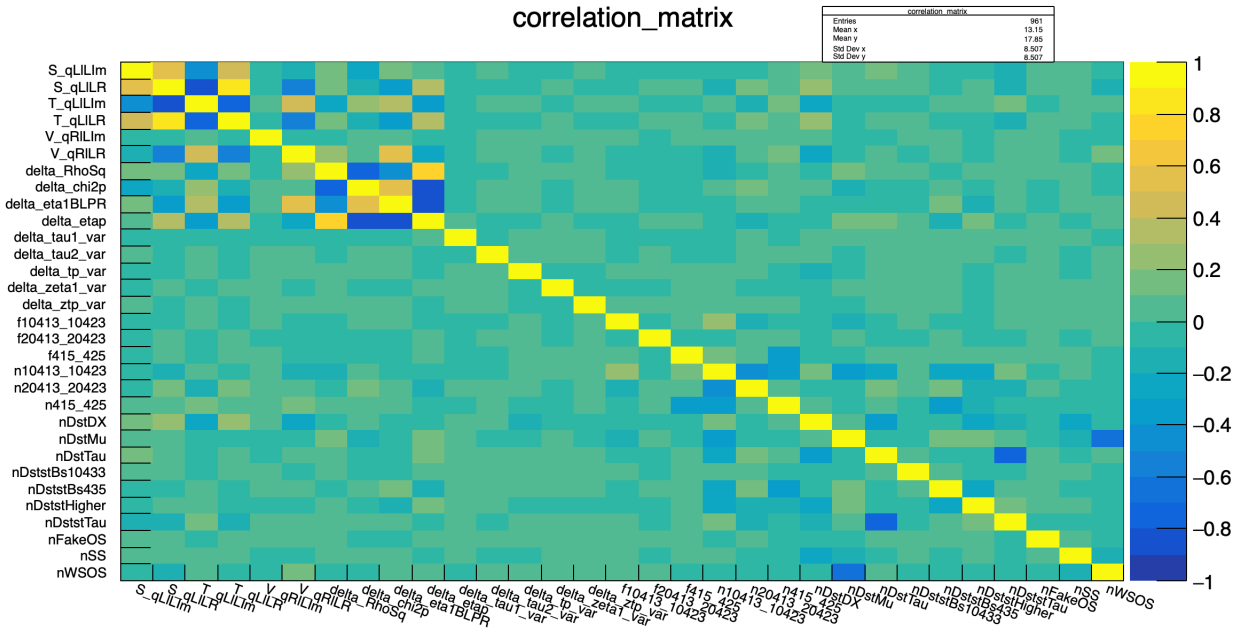


Figure B.7: Correlation matrix for the toy with WCs generated at 0.0 and float around 0.0 in the range of [-1,1].

B: VRL=0.0, SLL=0.1, TLL=0.1

Generation values of V_{qRlL}, S_{qLlL} and T_{qLlL} are fixed to 0.0, 0.1, 0.1 respectively and they float starting from 0.0, 0.1, 0.1 respectively in the range of [-1,1]. 1000 toys were fitted with a convergence rate of 85% and here only the converged fits are displayed. This configuration shows that the pulls of V_{qRlL}Re and T_{qLlL}Re (see Fig. B.8) become less biased ($\sim$ 10% and $\sim$ 90% decrease respectively) but with larger standard deviation ($\sim$ 20% increase) on scalar real and tensor comparing to the configuration A.

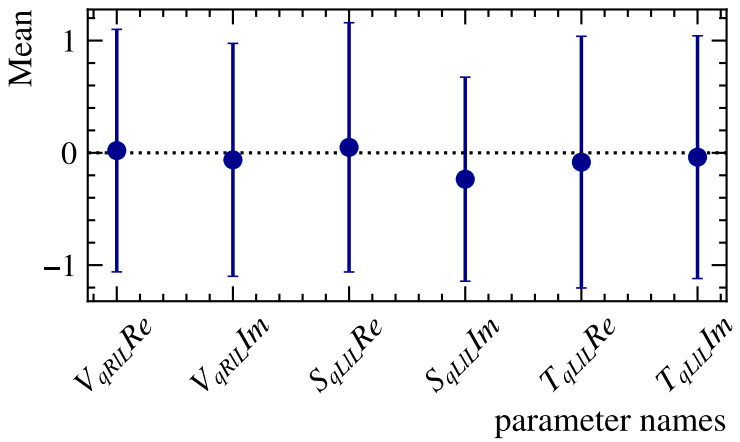


Figure B.8: Summary plot of the mean values of the pull distributions when vector part generated at 0.0 while other WCs generated at 0.1 and vector float around 0.0 while other Wilson coefficients at 0.1 in the range of [-1,1]. The uncertainty on the data points is the standard deviation of the pull distribution.

C: VRL=0.1, SLL=0.1, TLL=0.1

Generation values of WCs are fixed to 0.1 and they float starting from 0.1 in the range of [-1,1]. 1000 toys were fitted reporting a convergence rate of 84% and here only the converged fits are displayed. The results are shown in Fig. B.9 and example likelihood scan in Fig. B.10. Here we observe that double solution in the tensor Wilson coefficient appears.

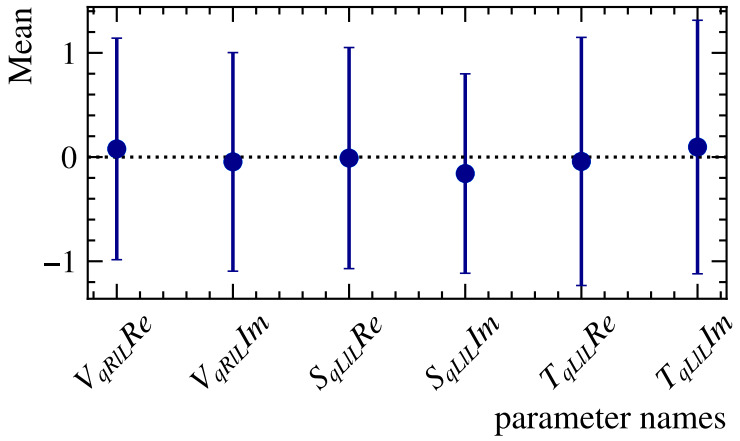


Figure B.9: Summary plot of the mean values of the pull distributions. The uncertainty on the data points is the standard deviation of the pull distribution.

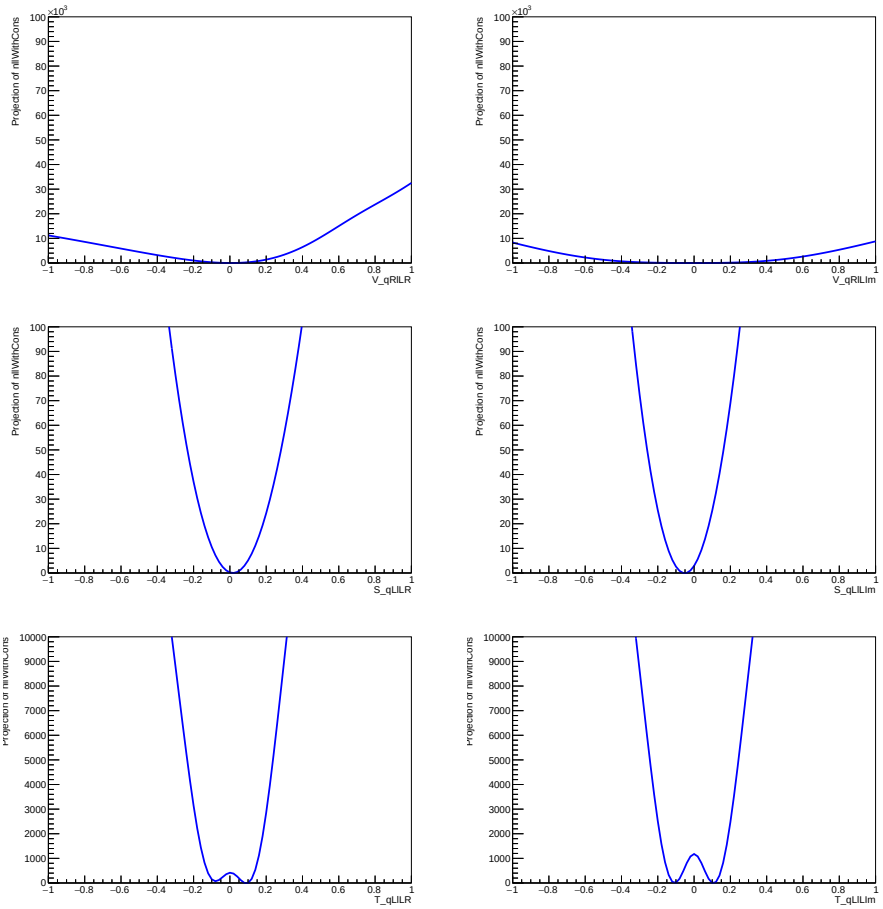


Figure B.10: Likelihood scans of WCs generated at 0.1 and float around 0.1 in the range of [-1,1].

D: VRL=0.5, SLL=0.5, TLL=0.5

Generation values of WCs fixed to 0.5 and they float around 0.5 in the range of [-1,1]. 1000 toys were fitted reporting a convergence rate of 89% with here only the converged fits displayed. We observe large biases of the WC as it can be seen in Fig. B.11, therefore, generating at 0.5 does not give well behaved pulls. Likelihood scans are also given in Fig. B.12 that confirm the tensor double solution.

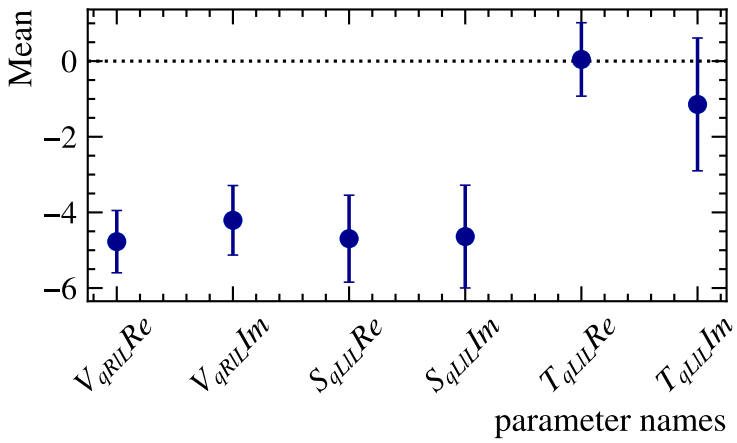


Figure B.11: Summary plot of the mean values of the pull distributions when WCs generated at 0.5 and float around 0.5 in the range of [-1,1]. The uncertainty on the data points is the standard deviation of the pull distribution.

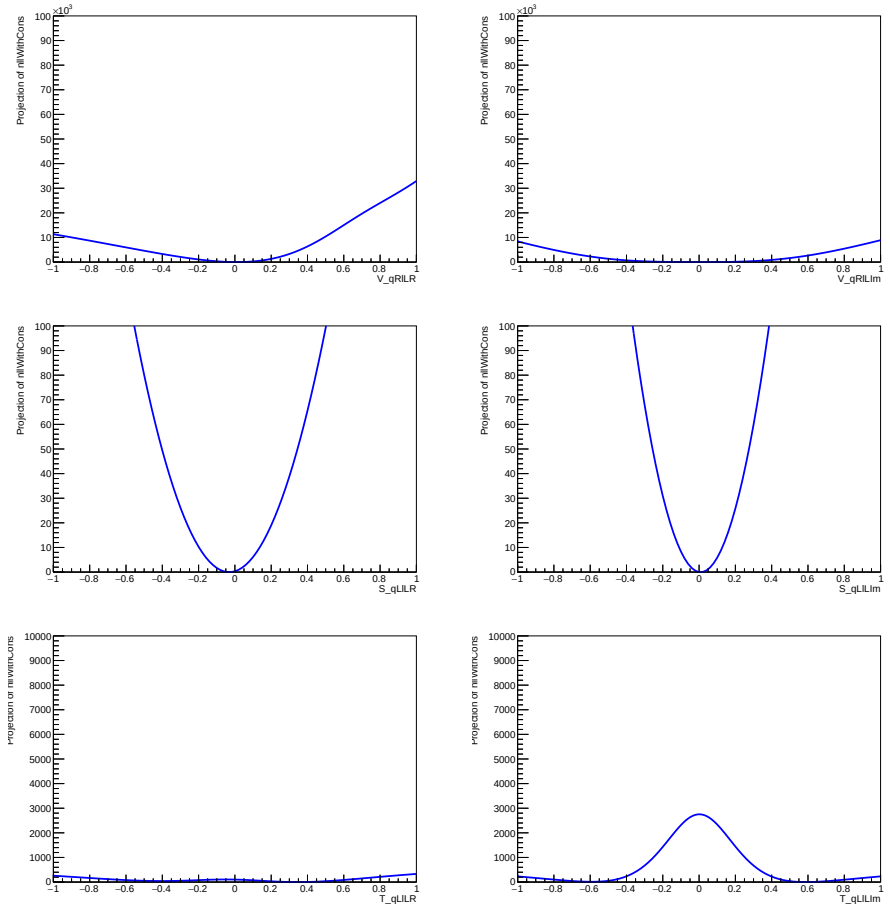


Figure B.12: Likelihood scans of WCs generated at 0.5 and float with starting value of 0.5 in the range of [-1,1].

Real WCs: VRL=0.1, SLL=0.1, TLL=0.1

In this part the generation values of WCs is fixed to a specific NP value of 0.1 (0.1 is arbitrarily chosen) for each toy. We fix the imaginary parts of the WCs to 0.0 as well. 1000 toys were fitted reporting a convergence rate of 99% with the pull distributions shown in Fig. B.13. This configuration shows well behaved pulls with well estimated uncertainties and no significant biases. From this it can be concluded that instabilities in the fit arise when we include the imaginary parts of the WCs in the multi-parameter scenario.

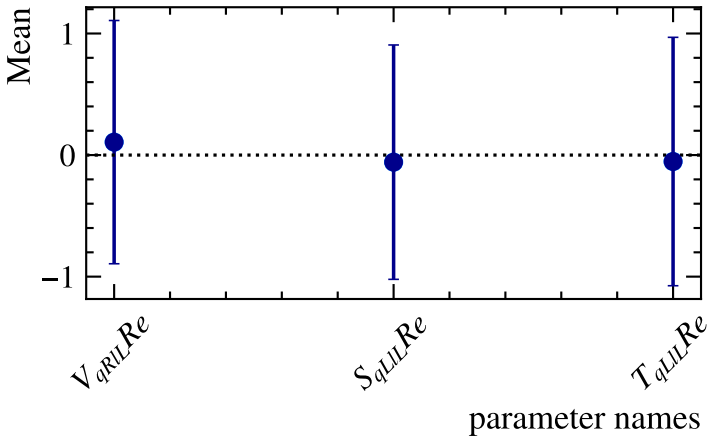


Figure B.13: Summary plot of the mean values of the pull distributions when WCs generated at 0.1 and only real parts are floated in the fit. The uncertainty on the data points is the standard deviation of the pull distribution.

B.4 Using asymmetric uncertainties in RooFit minimization

Some of the likelihood scans of the WCs are non parabolic, depending on the generated value they have different shape, therefore a check was made to include the asymmetric uncertainty in the minimization (by enabling MINOS) and further using it in calculating the pulls. By default in all the previous sections the symmetric HESSE uncertainties were used in all configurations. The following shows the converged fit results from 1000 fits where the generated value for the WCs is fixed to 0.0 with the asymmetric MINOS uncertainties. For the calculation of the pull of a

parameter x, Equation 6.1 is used:

$$\text{pull}(x) = \begin{cases} \frac{x_{\text{measured}} - x_{\text{generated}}}{\sigma_+}, & \text{if } x_{\text{measured}} > x_{\text{generated}} \\ \frac{x_{\text{measured}} - x_{\text{generated}}}{\sigma_-}, & \text{if } x_{\text{measured}} < x_{\text{generated}} \end{cases}, \tag{6.1}$$

where σ_+ and σ_- are the upper and lower MINOS uncertainty respectively. We observe that the uncertainties of the scalar and tensor WCs are overestimated. The results are shown in Fig. B.14.

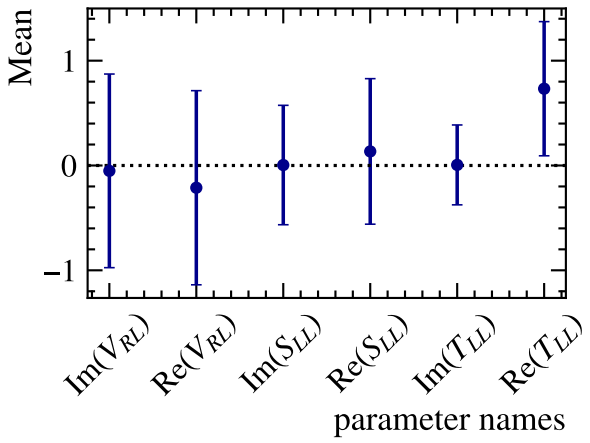


Figure B.14: Summary plot of the mean values of the pull distributions for the generation value of the WCs fixed at 0.0 and floated around 0.0 in the range of [-1,1]. The uncertainties used in the pull calculation is the MINOS uncertainty.

B.5 Fit behaviour for starting values of 0.0 for the Wilson coefficients

The results in the previous sections were produced in the setup when the starting value in the fitter for the WCs is the generated value. Here we investigate the result when the starting value is always 0.0, independent of the generated value.

It was noticed that the likelihood scan shows double solutions when the starting value in the fit is set to a different value than the generation. For example, two solutions appear for S_{qLlL}Im and T_{qLlL}Im shown in Fig. B.34 while this structure is not present in Fig. B.16 and this structure reflects on the pulls as it can be seen from Fig. B.17. To test if the two solutions add an additional instability in the fit a reparametrisation of the WCs with two solutions was considered, covered in section B.5.1.

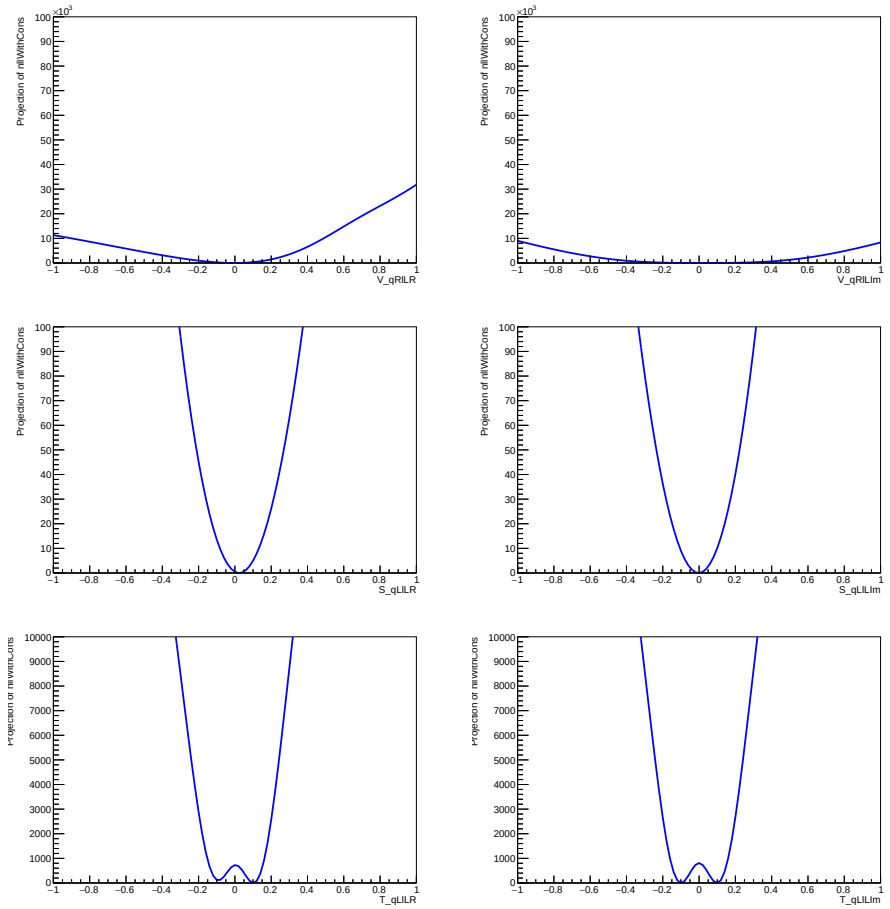


Figure B.15: Likelihood scans of WCs generated at 0.1 with starting value 0.0 in the range of [-1,1].

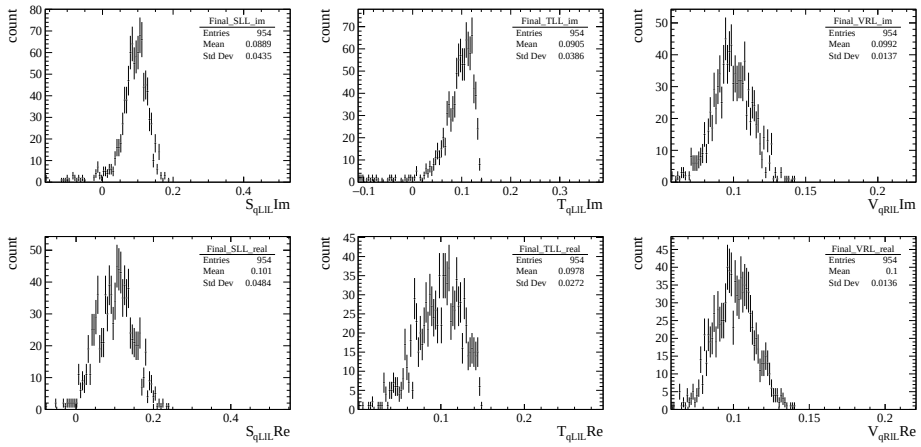


Figure B.16: Final value distributions of WCs generated at 0.1 and float around 0.1 in the range of [-1,1].

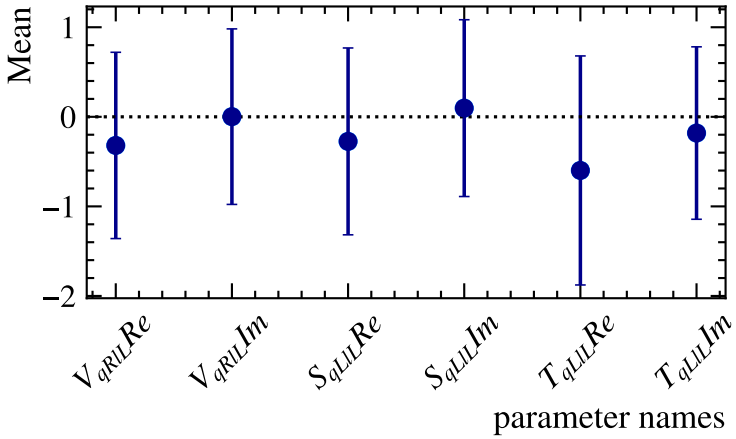


Figure B.17: Summary plot of the mean values of the pull distributions when WCs generated at 0.1 and float only real parts around 0.0 in the range of [-1,1]. The uncertainty on the data points is the standard deviation of the pull distribution.

B.5.1 Reparameterization of S_{qLlL}Im

We reparameterize S_{qLlL}Im as $|S_{qLlL}Im|$ such as positive S_{qLlL}Im are accepted in order to avoid the two-solution case shown in Fig. B.34.

1000 toys were fitted having a convergence rate of 78%. While removing the double structure for S_{qLlL}Im, the additional double structure for S_{qRlL}Re and T_{qLlL}Re appears as it can be seen from the Fig. B.18.

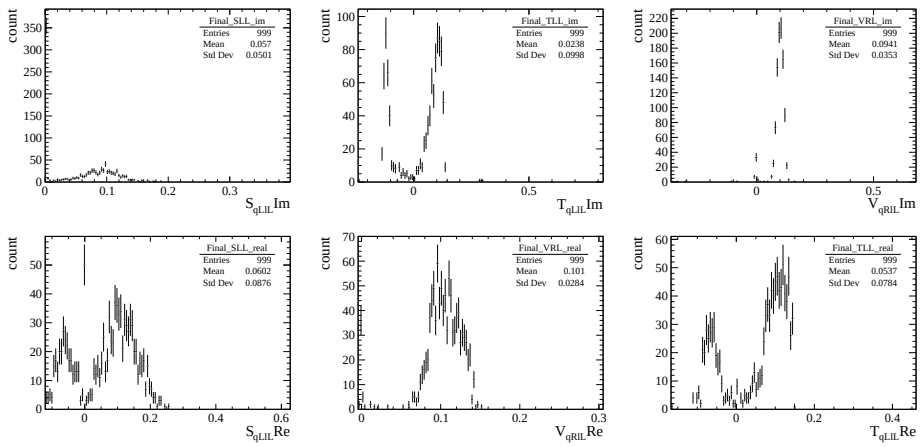


Figure B.18: Final value distributions of WCs when S_{qLlL}Im is reparameterised.

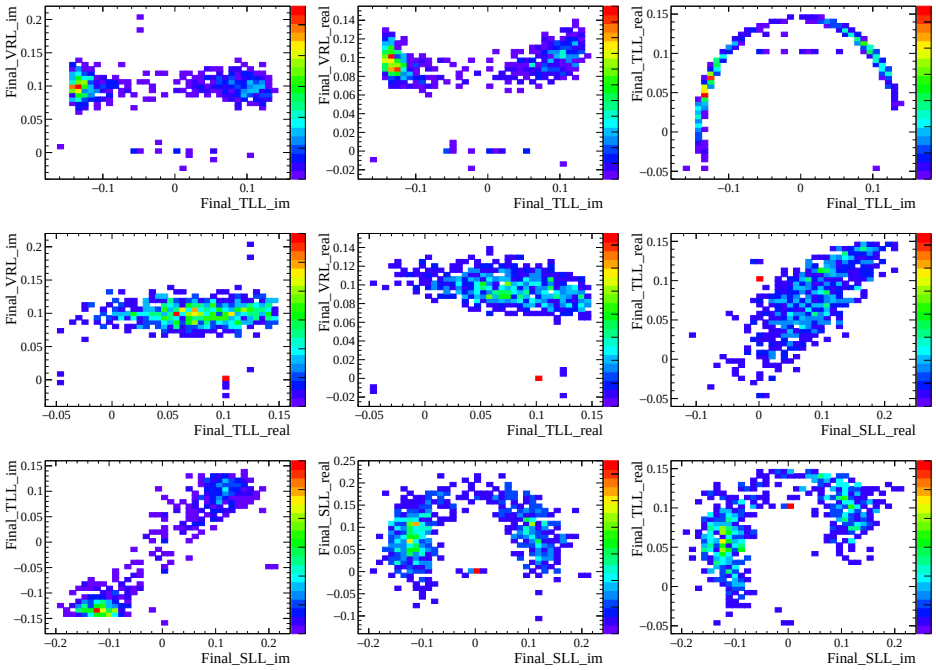


Figure B.19: Correlation plots of final values of WCs without reparametrisation of S_{qLlL}Im.

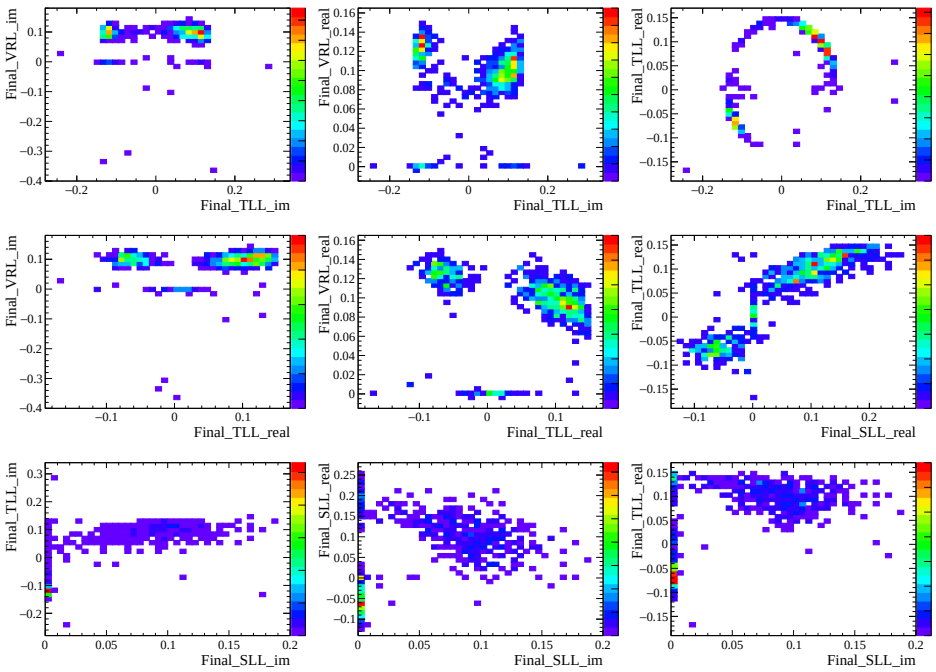


Figure B.20: Correlation plots of final values of WCs when S_{qLlL}Im is reparameterised.

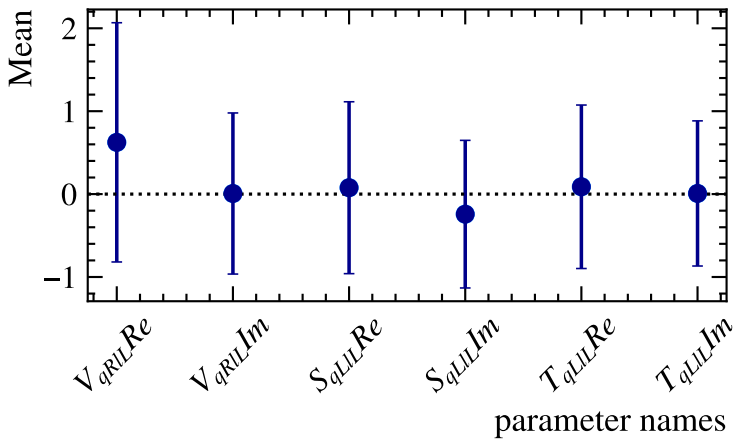


Figure B.21: Summary plot of the mean values of the pull distributions when S_{qLlL}Im is reparameterised to take positive values. The uncertainty on the data points is the standard deviation of the pull distribution.

B.5.2 Constraining S_{qLlL}Im, T_{qLlL}Re and T_{qLlL}Im

We constrain these 3 parameters to the positive values only because of the additional double solutions seen in Fig. B.18. 1000 toys were fitted having a convergence rate of 73%. The plots in Fig. B.22 and Fig. B.23 show that the while some biases are resolved other appear and we are not able to fully constrain the double solution in this way.

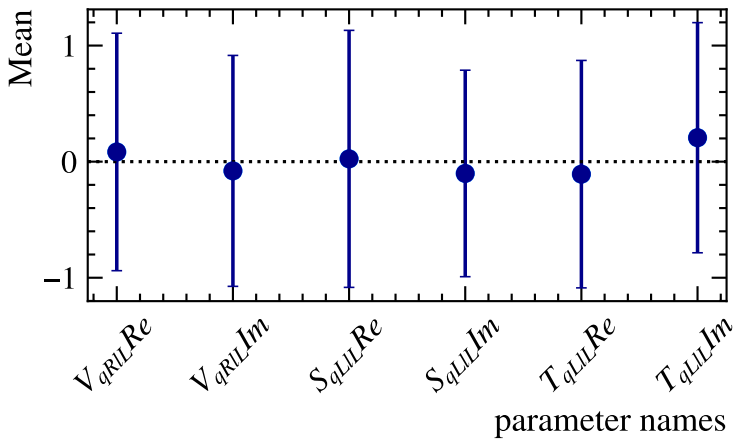


Figure B.22: Summary plot of the mean values of the pull distributions when the S_{qLlL}Im, T_{qLlL}Re and T_{qLlL}Im are floating around 0.0 in the range of [0,1].

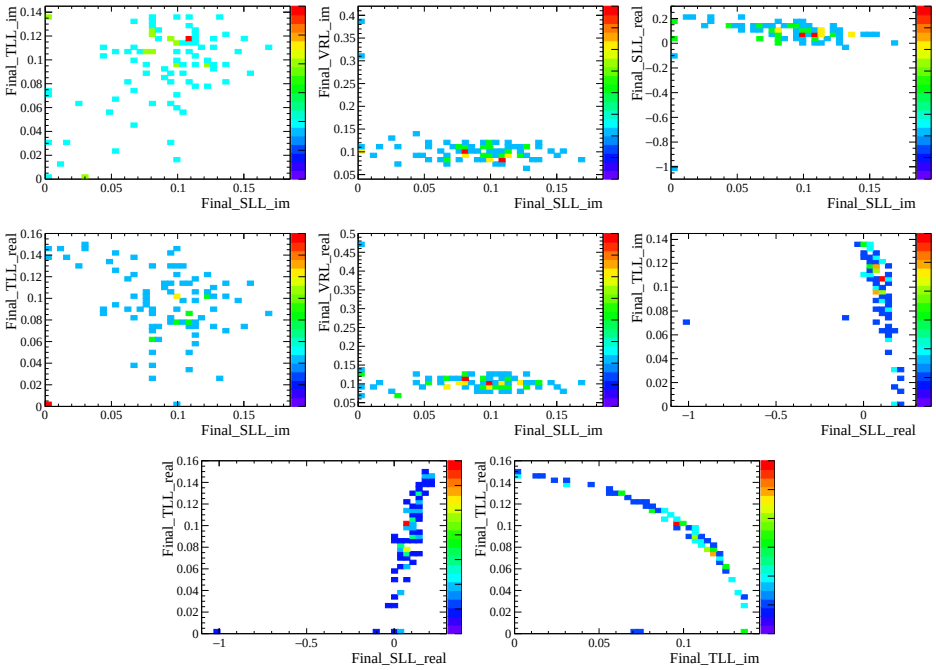


Figure B.23: Correlation plots of final distributions of the WCs when the S_{qLlL}Im, T_{qLlL}Re and T_{qLlL}Im are floating around 0.0 in the range of [0,1].

B.6 Further correlations between Wilson coefficients

There is a linear dependence between S_{qLlL} and T_{qLlL} and as well as a circular structure between the real and imaginary components of T_{qLlL}. These structures can be seen in the plots of Fig. B.24. The next fit setup is using principal component analysis in trial to check if the correlation affects the double solutions.

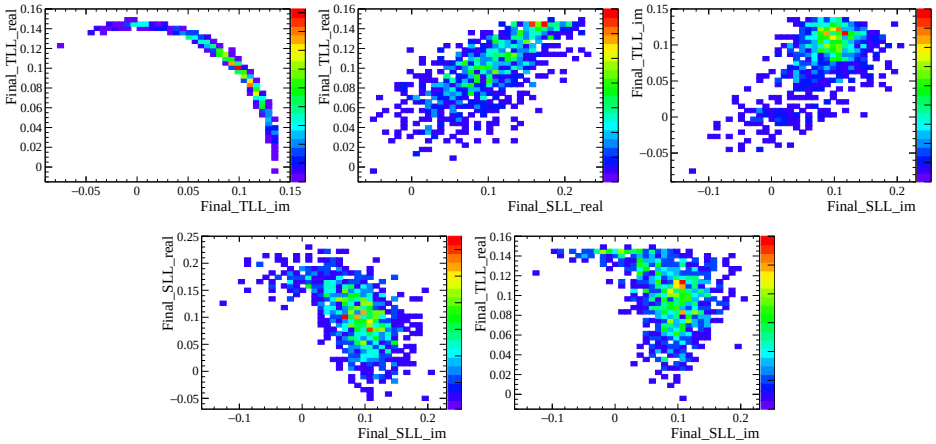


Figure B.24: Correlation plots of final values (Config A) of S_{qLlL} and T_{qLlL}.

B.6.1 Linear reparametrisation using Principal Component Analysis

In this linear reparametrisation of WCs the S_{qLlL} and T_{qLlL} coefficients are extracted using Principal Component Analysis (PCA) [160, 161] such that the new covariance matrix between these parameters after linear transformation is be diagonal. With this approach we arrive to the following expressions for S_{qLlL} and T_{qLlL} that are used when fitting the toys:

$$S_{qLlL}Re = 0.92S'_{qLlL}Re + 0.40T'_{qLlL}Re; \qquad T_{qLlL}Re = -0.40S'_{qLlL}Re + 0.92T'_{qLlL}Re$$
$$S_{qLlL}Im = 0.76S'_{qLlL}Im + 0.65T'_{qLlL}Im; \qquad T_{qLlL}Im = -0.65S'_{qLlL}Im + 0.76T'_{qLlL}Im$$

1000 toys were fitted reporting a convergence rate of 70% and here only the converged fits are displayed. This reparametrisation does not resolve any existing biases, correlations are shown in Fig. B.25 and results in Fig. B.26.

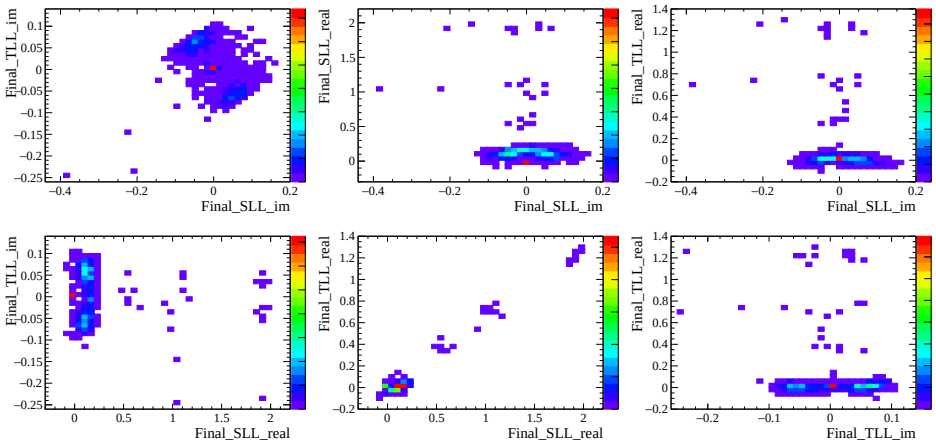


Figure B.25: Correlation plots of the final distributions of the WCs when they are reparameterised using PCA.

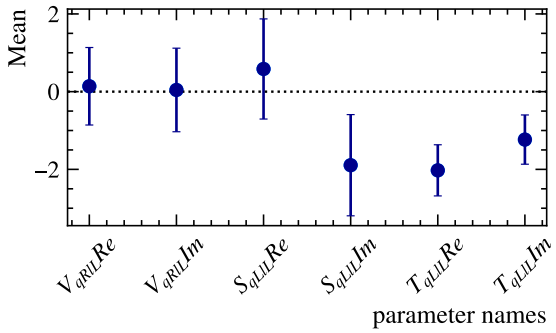


Figure B.26: Summary plot of the mean values of the pull distributions when the WCs are reparameterised using PCA.

B.7 Choice of positive real on different WCs in nominal configuration

Here, we present the results regarding the studies mentioned in Section 4.6.1.6 separating the results according the the choice of the WC to be positive and real.

B.7.1 Choosing vector to be real and positive

1000 toys were fitted reporting a convergence rate of 93% with the pull distributions shown in Fig. B.27. However, this configuration gives us biased pulls for every WC and around 40% underestimated uncertainties on the tensor WC.

	Central Generation Value	Starting value	Fitting Range
$V_{qRlL}Im$	0.1	0.1	fixed
$V_{qRlL}Re$	0.1	0.1	[0, 1]
C_pIm	0.0	0.0	[-2.2, 1.8]
C_pRe	0.0	0.0	[-2.2, 1.8]
C_sIm	0.2	0.2	fixed
C_sRe	0.2	0.2	fixed
$T_{qLlL}Im$	0.0	0.0	[-1, 1]
$T_{qLlL}Re$	0.1	0.1	[-1, 1]

Table 6.2: Wilson coefficients used in this parametrization shown here along with their generation and starting values and fitting intervals.

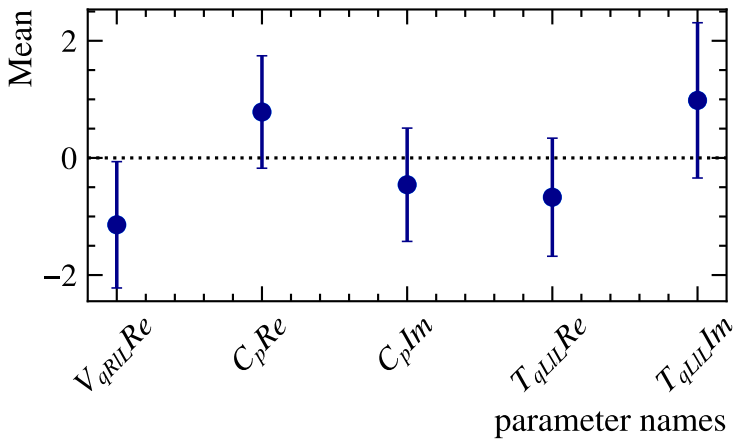


Figure B.27: Summary plot of the mean values of the pull distributions for the WCs generated and fitted as in Tab. 6.2. The uncertainty on the data points is the standard deviation of the pull distribution.

B.7.2 Choosing right handed scalar to be real and positive

1000 toys were fitted reporting a convergence rate of 99% with the pull distributions shown in Fig. B.28. However, this configuration gives us biased pulls for every WC and very much overestimated uncertainties for C_p and tensor WCs, respectively 70% and 40%. On the side of FFs, we have 30% more biased pulls comparing to the tensor fixed case.

	Central Generation Value	Starting value	Fitting Range
$V_{qRlL}Im$	0.1	0.1	[-1, 1]
$V_{qRlL}Re$	0.1	0.1	[-1, 1]
C_pIm	-0.2	-0.2	fixed
C_pRe	0.0	0.0	[-0.2, 1.8]
C_sIm	0.2	0.2	fixed
C_sRe	0.2	0.2	fixed
$T_{qLlL}Im$	0.0	0.0	[-1, 1]
$T_{qLlL}Re$	0.1	0.1	[-1, 1]

Table 6.3: Wilson coefficients used in this parametrization shown here along with their generation and starting values and fitting intervals.

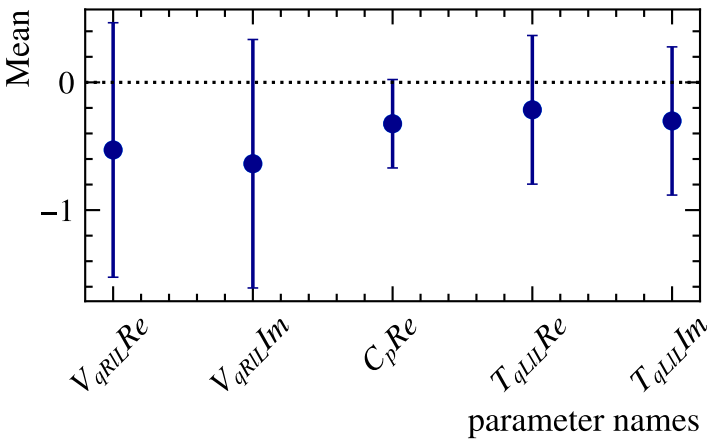


Figure B.28: Summary plot of the mean values of the pull distributions for the WCs generated and fitted as in Tab. 6.3. The uncertainty on the data points is the standard deviation of the pull distribution.

B.8 Toys with true distributions

To check if there is any effect by using the reconstructed variables a few sets of toys were run using true fitting variables for the three angles and the q^2 in a scenario where only the signal template ($B^0 \to D^*\mu\nu$) is present. 1000 toys were fitted with a convergence rate of 82% where only the converged fits are displayed. The distributions in Fig. B.29 do not show improvement over the toys when reconstructed variables are used. This eliminates that the fit biases and double solutions might be caused by the neutrino reconstruction procedure.

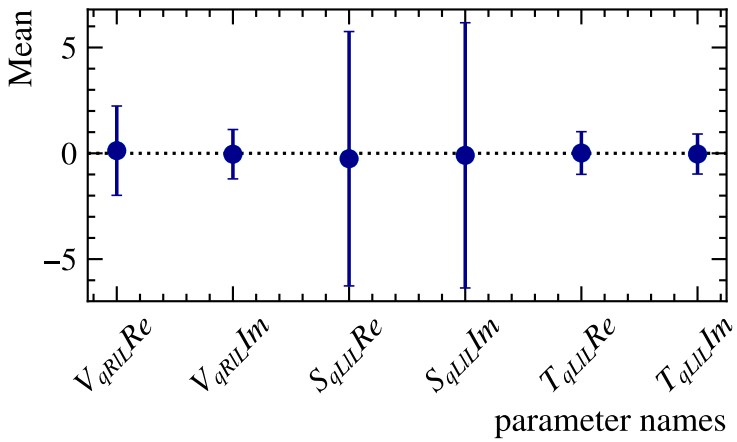


Figure B.29: Summary plot of the mean values of the pull distributions for the WCs generated and fitted as in Tab. 4.31 in true distributions. The uncertainty on the data points is the standard deviation of the pull distribution.

B.8.1 Generation values of WCs fixed to 0.0:

Generation values of WCs fixed to 0.0 and they float around 0.0 in the range of [-1,1] . 1000 toys were fitted reporting a convergence rate of 99%.

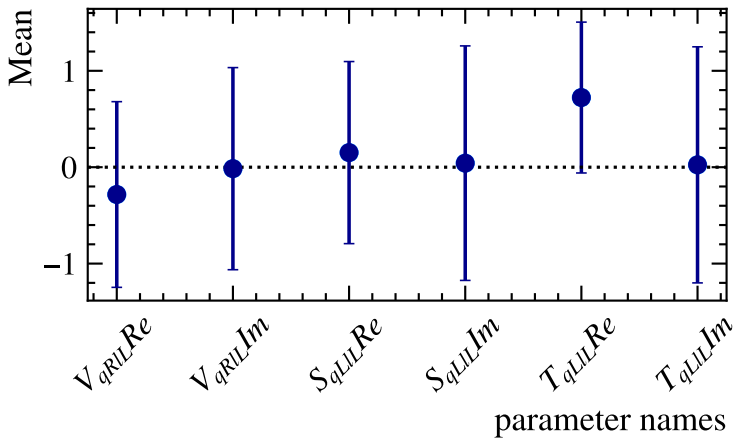


Figure B.30: Summary plot of the mean values of the pull distributions in true distributions WCs generated at 0.0 and float around 0.0 in the range of [-1,1]. The uncertainty on the data points is the standard deviation of the pull distribution.

B.8.2 Finer binning in toys with true distributions

Instead of usual binning of the three angles (See Fig. 2.6) and the q^2 as 5,5,5,4 respectively, in this section we use binning of 10,10,10,20. Toys were produced for

both when varying the generated value of the WC in the toys and as well at a fixed point of 0.0. For both cases there is no significant improvement as compared with the toys generated with the reconstructed variables from the increased number of bins.

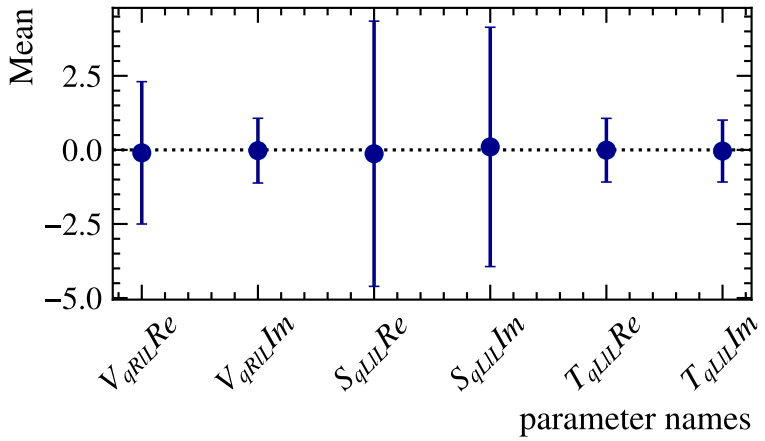


Figure B.31: Summary plot of the mean values of the pull distributions in true distributions with more binning for the WCs generated and fitted as in Tab. 4.31 in true distributions. The uncertainty on the data points is the standard deviation of the pull distribution.

Generation values fixed to 0.0: Generation values of WCs fixed to 0.0 and they float around 0.0 in the range of [-1,1] . 1000 toys were fitted reporting a convergence rate of %.

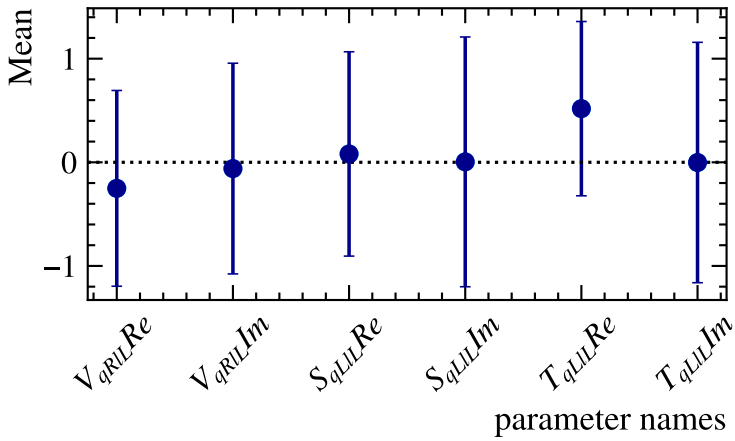


Figure B.32: Summary plot of the mean values of the pull distributions in true distributions with finer binning when WCs generated at 0.0 and float around 0.0 in the range of [-1,1]. The uncertainty on the data points is the standard deviation of the pull distribution.

In general further checks with various other toy configuration were made in Appendix B, however they all point that the biases and instabilities appear due to the double solutions in the likelihood. Below we summarize the different toy configurations checked in this analysis, after the summary the individual results are also given. The checks here are made with all real and imaginary parts floating. The checks in Appendix B can be summarized as following:

1. MINOS was activated in the fitter to make use of the asymmetric uncertainties during the pull calculation. The results of the toys are given in Appendix B.4 where we do not see any improvements in terms of the behaviour of the pulls as compared with the case when the symmetric uncertainties are used.

2. A range of toys were produced with fixed generation values of 0.0, 0.1 and 0.5 with the results shown in Appendix B.3. A summary of the pulls of the WCs is given in Fig. B.33. It can be seen that the biases appear in different WCs by changing the point in WC space.

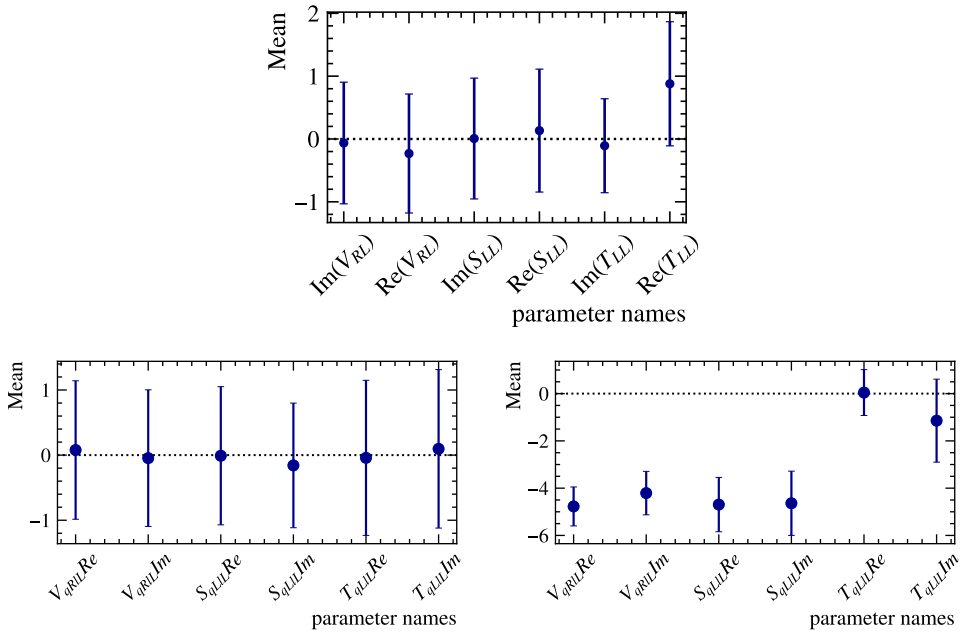


Figure B.33: Summary plot of the mean values of the pull distributions when the Wilson coefficients are generated at a fixed point of 0.0 (first row), 0.1 (second row - left), 0.5 (second row - right) and fitted in the range [-1,1].

3. A dependence of the fit with the starting values of the WCs was noticed and further investigated in the toys given in Appendix. B.5. Namely, when the starting value of the WCs is close to the generated value (different than 0.0) we see single solution in some of the WC final fit results. However when the starting value is 0.0 a double structure is observed for example in the S_{qLl}Im and T_{qLl}Im (as given in Fig. B.34) which is affecting the pull result.

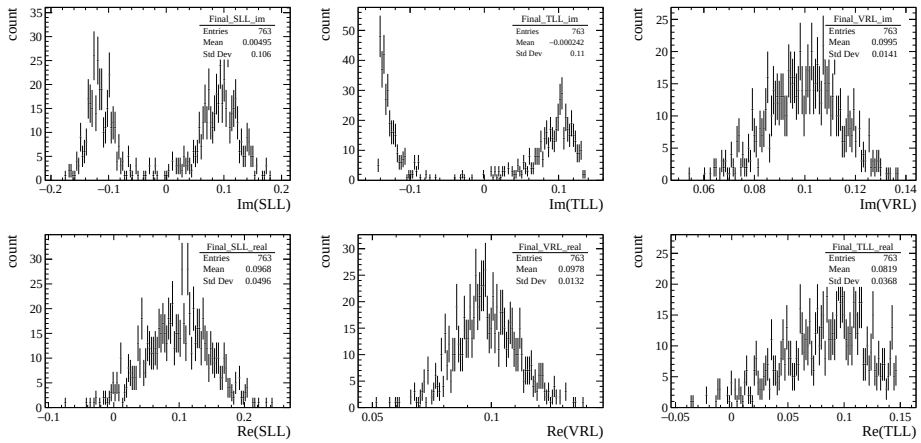


Figure B.34: Final value distributions of WCs generated at 0.1 but float around 0.0 in the range of [-1,1].

4. Reparametrisation was done in the toys to overcome the effect of WCs with double structure by accepting only positive values (given in Appendix B.5.1 and B.5.2). This brings the pull results to the same level as in discussed in point 2.

5. Furthermore some additional correlations were observed between the WCs as shown in Fig. B.35 with several other configurations also given in addition in Appendix B.6. The linear correlation seen between the scalar and the tensor WC can be resolved by using the Principal Component Analysis (PCA). However the results, given in Appendix B.6 do not resolve the above mentioned biases.

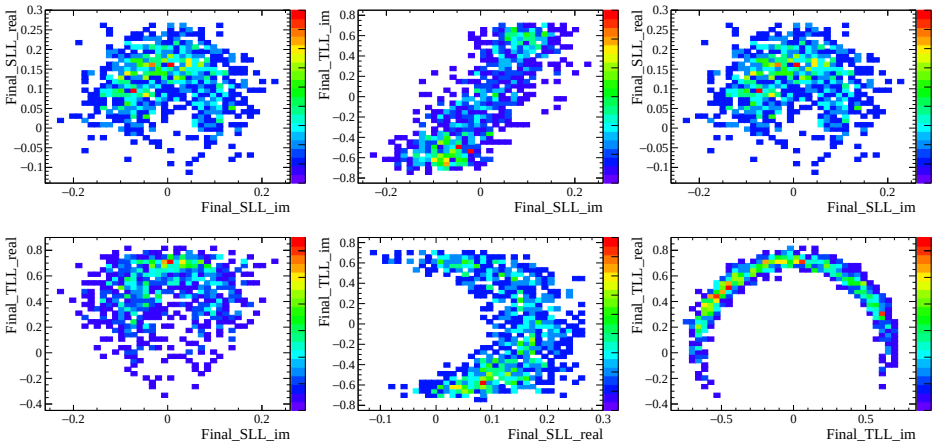


Figure B.35: Correlation plots of final values (Config D) of S_{qLlL} and T_{qLlL}.

6. Additionally toy studies were made using the true variables for constructing the fitting template. Using this setup we see similar behaviour as in point 1 from this list. The results are given in Appendix B.8.

7. A reparametrisation was done for the multi-parameter scenario using a sum and difference of the scalar Wilson coefficients together with requiring one Wilson coefficient to be real and positive. This results in a well behaved fit and is considered as the nominal fit configuration presented in this section.

C Toy study with different binning for the fit variables

In this section we study how the choice of bin numbers for the fit variables affects the pull distributions. In this study, m^2_{miss} variable was used representing the crucial variable to distinguish the background components. Toys were performed using the nominal fit setup (using 3 bins in the m^2_{miss}) and in addition using a binning of 8, 10 and 20 for the m^2_{miss}. Similarly, the effect of changing the binning in $cos\theta_l$ variable affect has been checked with the additional sets of toys in by using 10 and 20 bins. The toy fits are done in a yields only scenario (without including the WCs and the form factor parameters). The mean and the sigma values of the parameters' pull have been compared in Fig. C.1 and Fig. C.2. The results were compatible between different binnings.

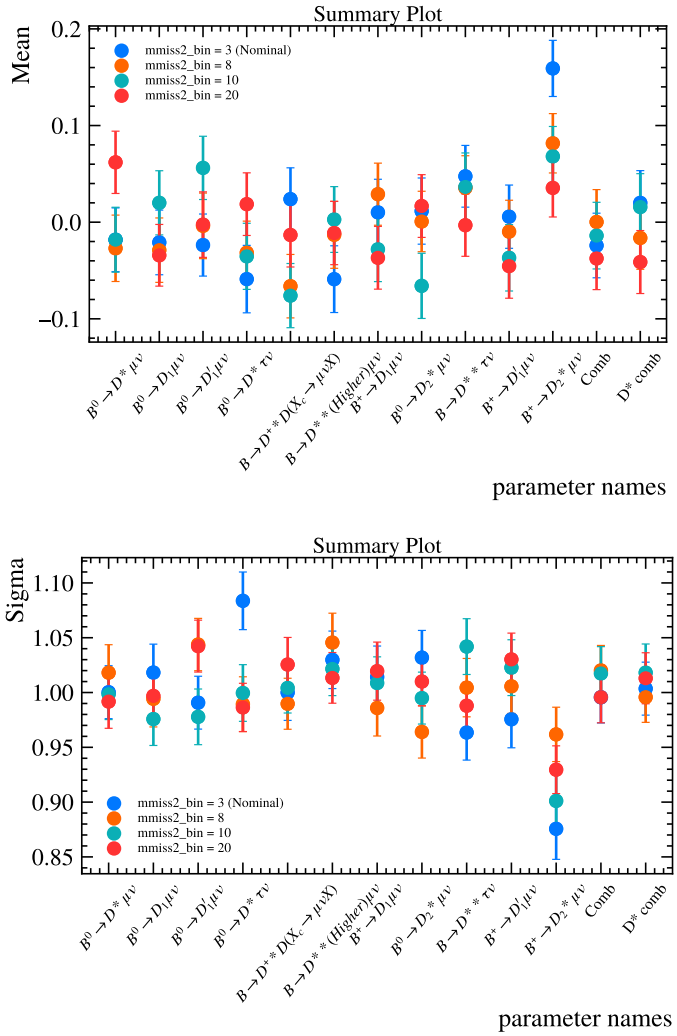


Figure C.1: Summary plot of mean and sigma values of the pull distributions on the components. The uncertainty on the data points is the uncertainty on the mean and the sigma parameters respectively of the Gaussian fit to the pull distributions. The colours of blue, orange, green and red respectively correspond to the 3 (nominal), 8, 10 and 20 binning.

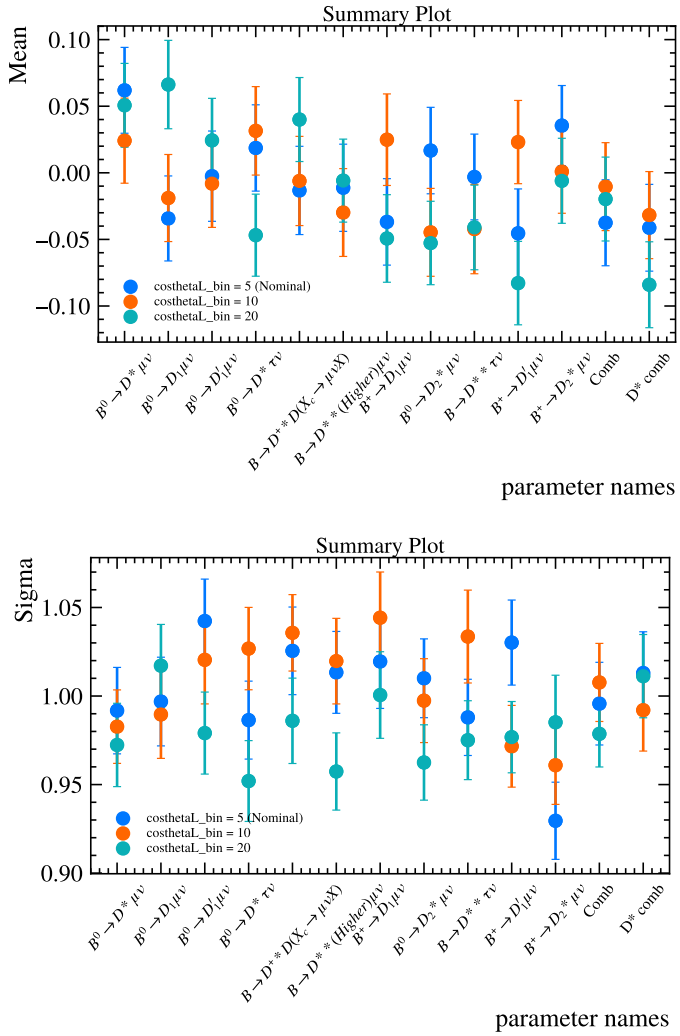


Figure C.2: Summary plot of mean and sigma values of the pull distributions on the components. The uncertainty on the data points is the uncertainty on the mean and the sigma parameters respectively of the Gaussian fit to the pull distributions. The blue, orange and green markers correspond to the 5 (nominal), 10 and 20 binning, respectively.

D Hadronic form factors measured in Run 1 analysis and theory predictions

Figures D.1 and D.2 compare the results obtained using the CLN and BLPR parametrisations to the recent lattice QCD calculation by the HPQCD collaboration, in the full q^2 range [7], the form-factor calculation at nonzero recoil by the Fermilab-MILC collaboration [127] as well as the result by the JLQCD collabora-

tion [128]. These comparisons are made in the BGL form-factor basis. Improved precision is achieved in the determination of the CLN form factors and a tension in the $\mathcal{F}_1$ value is observed with respect to the HPQCD result. The BLPR results are consistent with current lattice determinations with the tension in $\mathcal{F}_1$ being less pronounced.

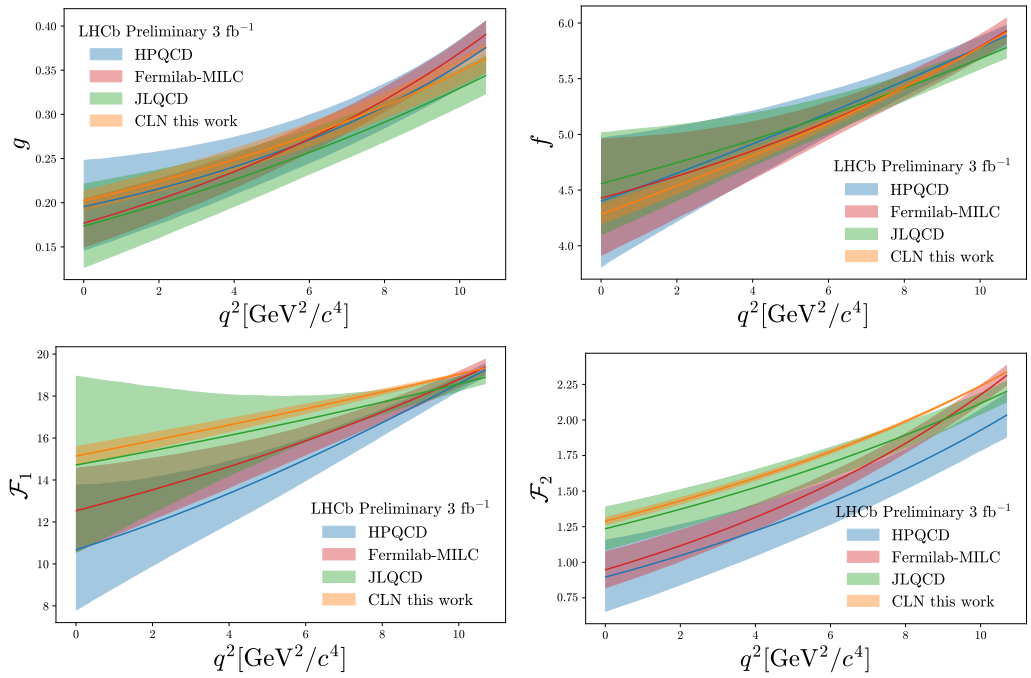


Figure D.1: Comparison of the results obtained in this form-factor measurement using the CLN parametrisation (orange) to lattice QCD calculations from HPQCD (blue), Fermilab-MILC (red) and JLQCD (green). The uncertainty bands for this work are derived assuming that systematic uncertainties are uncorrelated. The results are compared in the BGL form-factor basis.

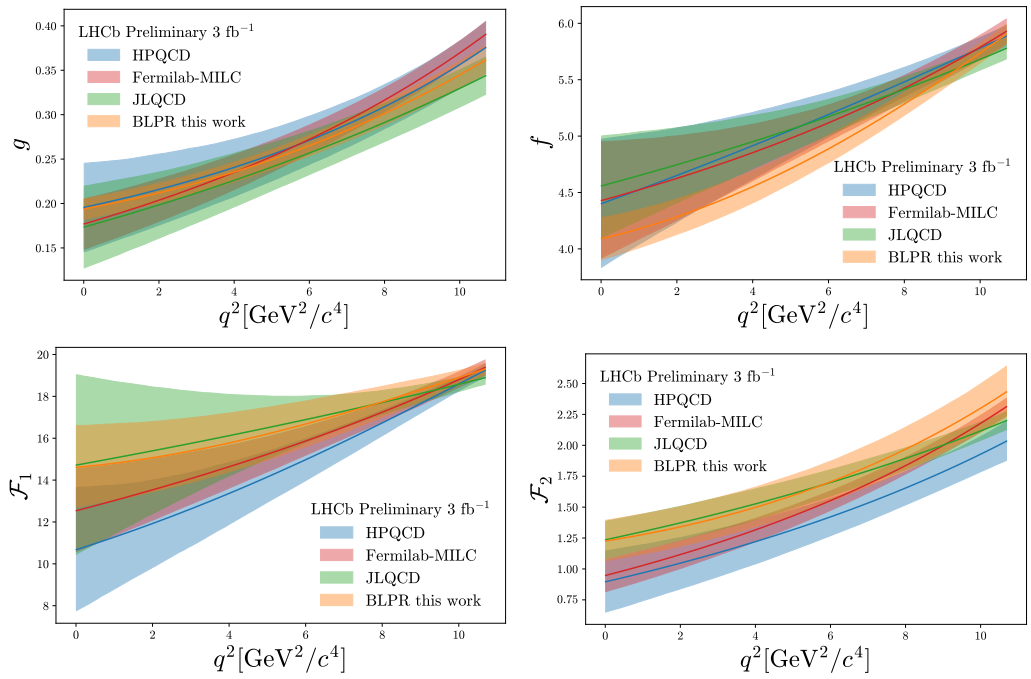


Figure D.2: Comparison of the results obtained in this form-factor measurement using the BLPR parametrisation (orange) to lattice QCD calculations from HPQCD (blue), Fermilab-MILC (red) and JLQCD (green). The uncertainty bands for this work are derived assuming that systematic uncertainties are uncorrelated. The results are compared in the BGL form-factor basis.

E GPFlow studies

Here, we provide the plots for each data taking years with magnet polarity. The improvements are similar across the different data year samples and different magnet polarities as well.

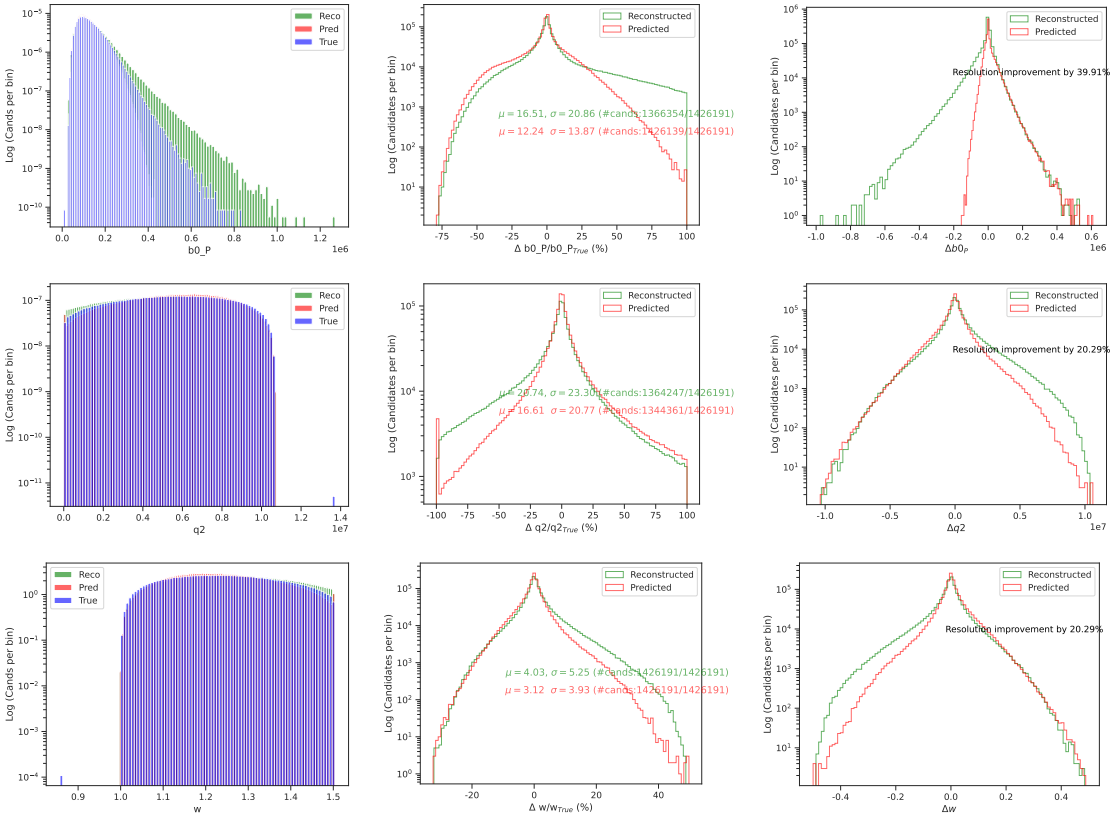


Figure E.1: Resolution improvements using GPR along with the distributions are shown here for the variables of interest in the signal simulation sample from 2016 with one magnet polarity.

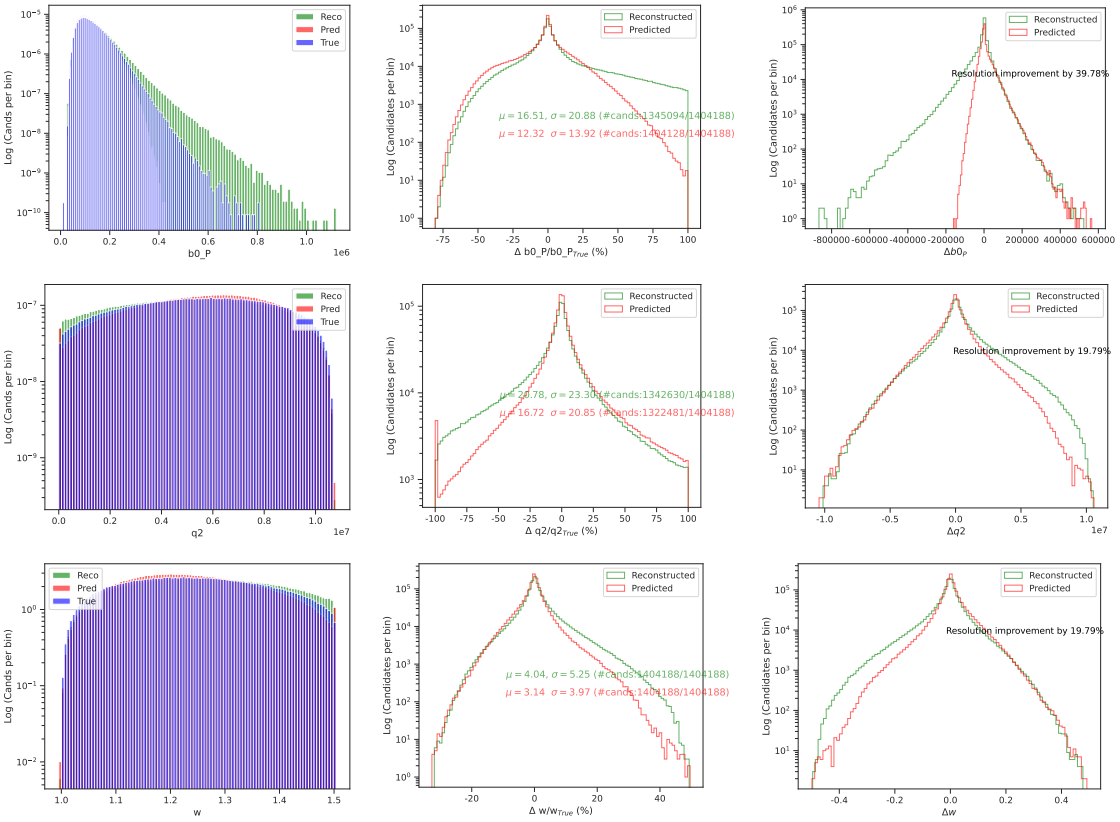


Figure E.2: Resolution improvements using GPR along with the distributions are shown here for the variables of interest in the signal simulation sample from 2017 with one magnet polarity.

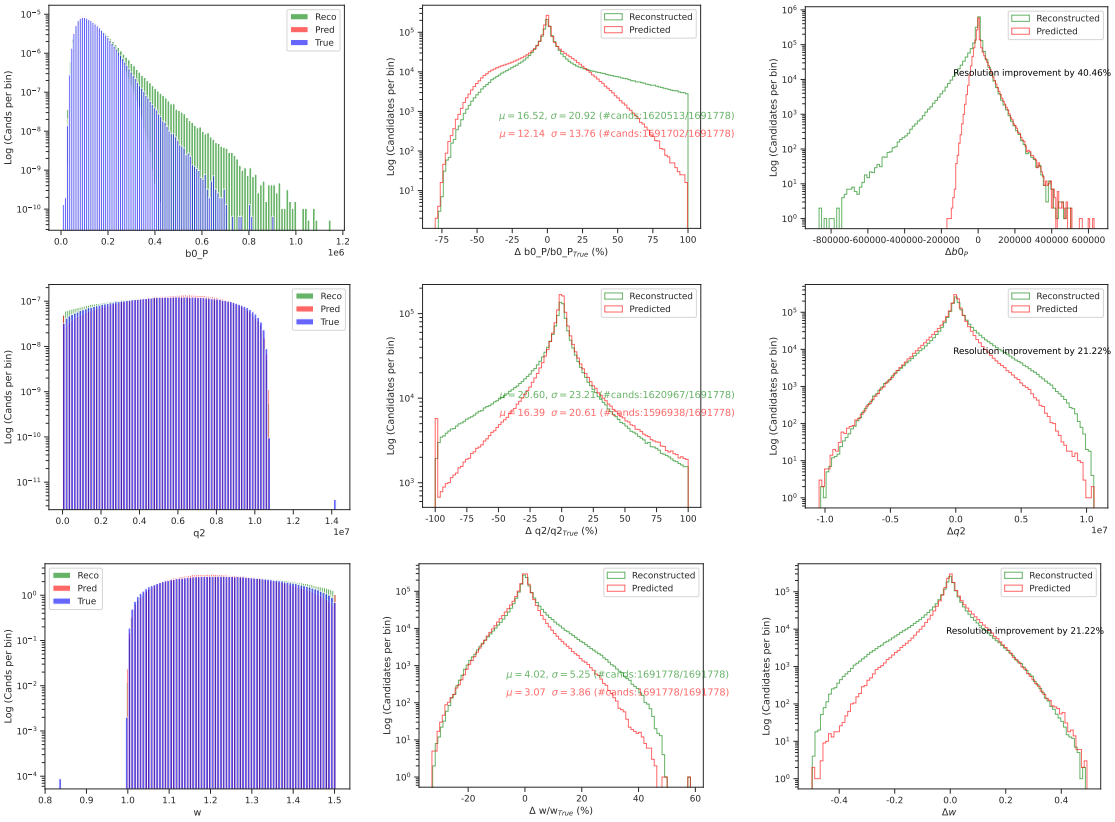
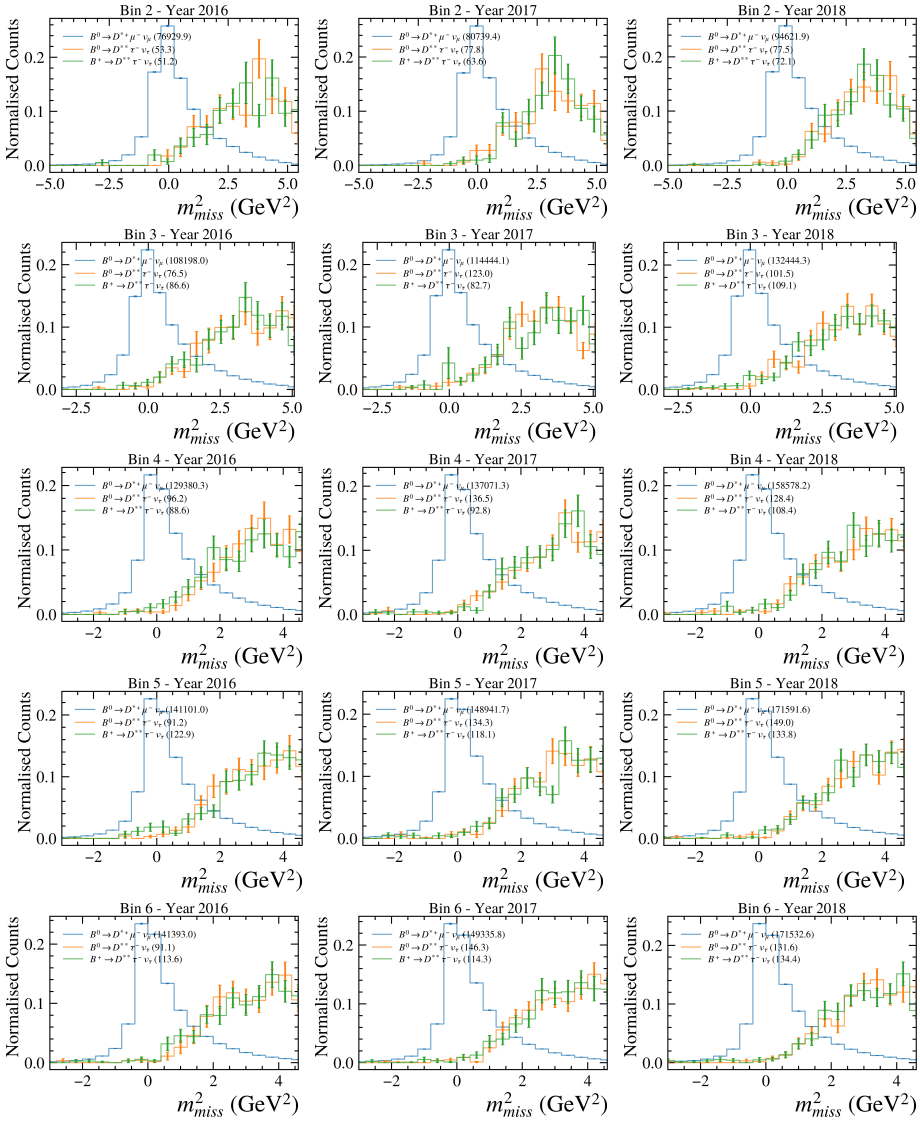


Figure E.3: Resolution improvements using GPR along with the distributions are shown here for the variables of interest in the signal simulation sample from 2018 with one magnet polarity.

F m^2_{miss} fit templates in Run 2

F.1 $B \to D^{**}\tau\nu$



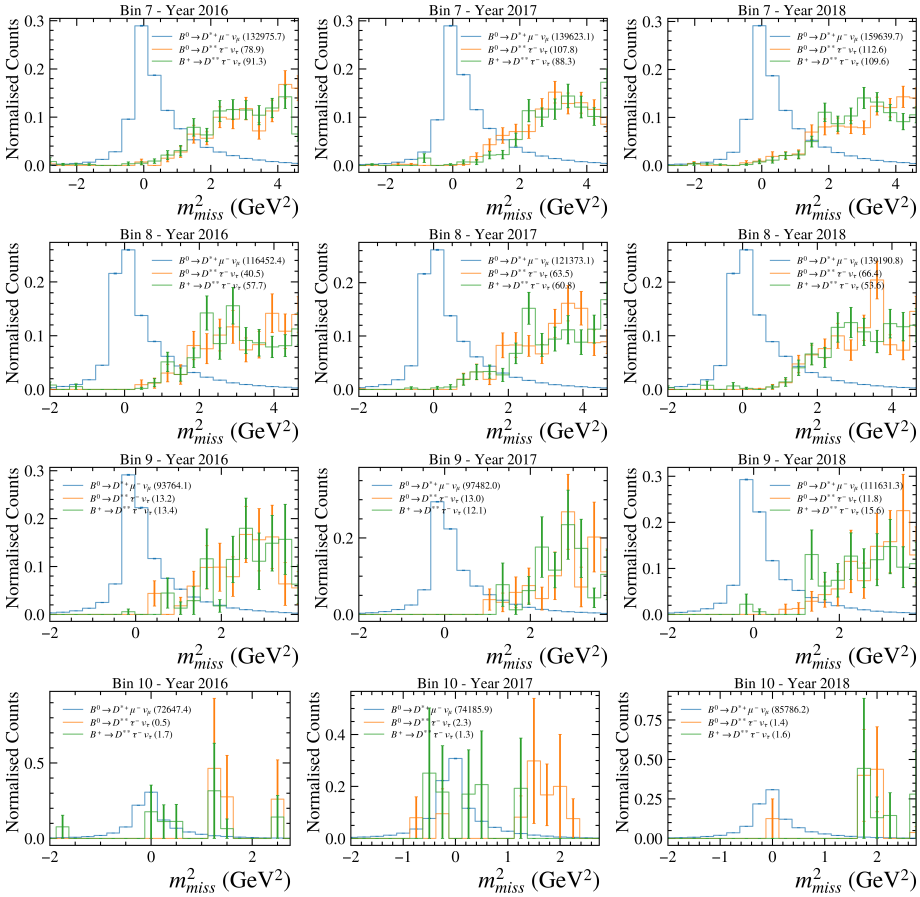
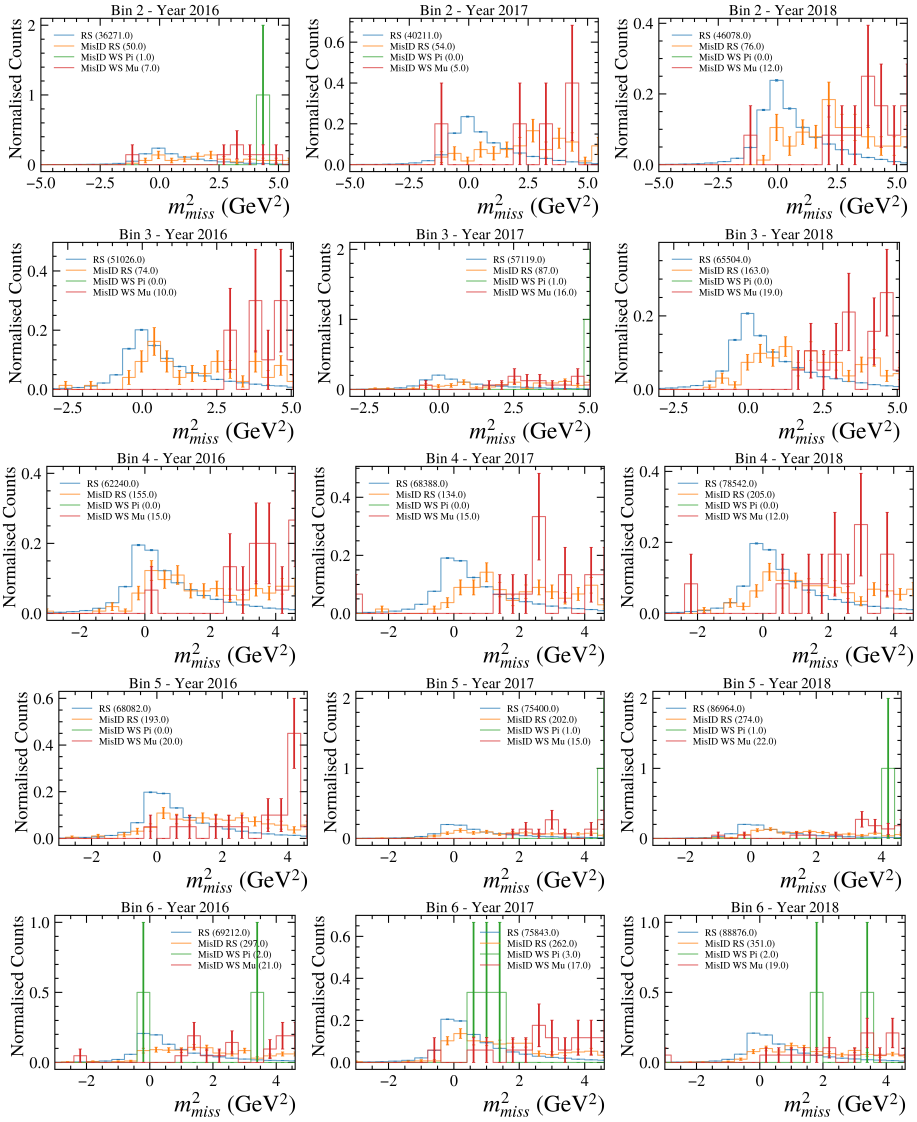


Figure F.1: The $B \to D^{**}\tau\nu$ template shapes shown for the w bins laid over signal template shape. Legend shows the number of events for both B meson charges from data taking years 2016/2017/2018 (left to right)

F.2 MisID


Bin 2 - Year 2016
RS (36271.0)
MisID RS (50.0)
MisID WS Pi (1.0)
MisID WS Mu (7.0)
Bin 2 - Year 2017
RS (40211.0)
MisID RS (54.0)
MisID WS Pi (0.0)
MisID WS Mu (5.0)
Bin 2 - Year 2018
RS (46078.0)
MisID RS (76.0)
MisID WS Pi (0.0)
MisID WS Mu (12.0)
Bin 3 - Year 2016
RS (51026.0)
MisID RS (74.0)
MisID WS Pi (0.0)
MisID WS Mu (10.0)
Bin 3 - Year 2017
RS (57119.0)
MisID RS (87.0)
MisID WS Pi (1.0)
MisID WS Mu (16.0)
Bin 3 - Year 2018
RS (65504.0)
MisID RS (163.0)
MisID WS Pi (0.0)
MisID WS Mu (19.0)
Bin 4 - Year 2016
RS (62240.0)
MisID RS (155.0)
MisID WS Pi (0.0)
MisID WS Mu (15.0)
Bin 4 - Year 2017
RS (68388.0)
MisID RS (134.0)
MisID WS Pi (0.0)
MisID WS Mu (15.0)
Bin 4 - Year 2018
RS (78542.0)
MisID RS (205.0)
MisID WS Pi (0.0)
MisID WS Mu (12.0)
Bin 5 - Year 2016
RS (68082.0)
MisID RS (193.0)
MisID WS Pi (0.0)
MisID WS Mu (20.0)
Bin 5 - Year 2017
RS (75400.0)
MisID RS (202.0)
MisID WS Pi (1.0)
MisID WS Mu (15.0)
Bin 5 - Year 2018
RS (86964.0)
MisID RS (274.0)
MisID WS Pi (1.0)
MisID WS Mu (22.0)
Bin 6 - Year 2016
RS (69212.0)
MisID RS (297.0)
MisID WS Pi (2.0)
MisID WS Mu (21.0)
Bin 6 - Year 2017
RS (75843.0)
MisID RS (262.0)
MisID WS Pi (3.0)
MisID WS Mu (17.0)
Bin 6 - Year 2018
RS (88876.0)
MisID RS (351.0)
MisID WS Pi (2.0)
MisID WS Mu (19.0)
Normalised Counts
m^2_{miss} (GeV^2)

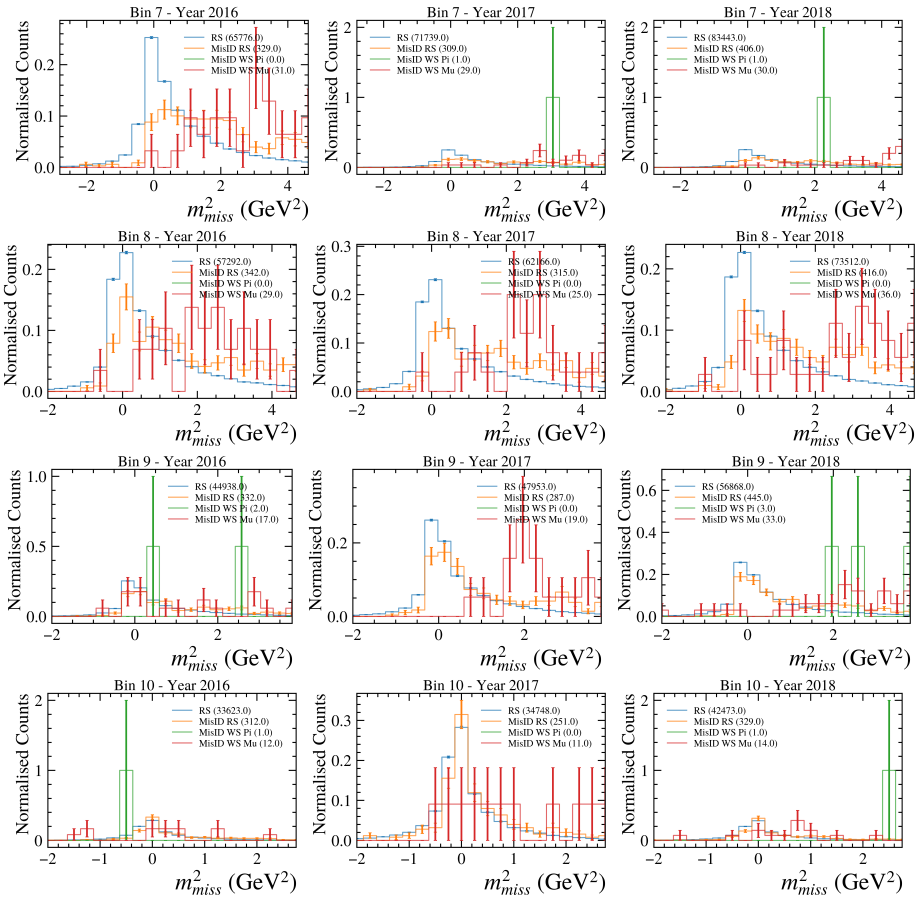
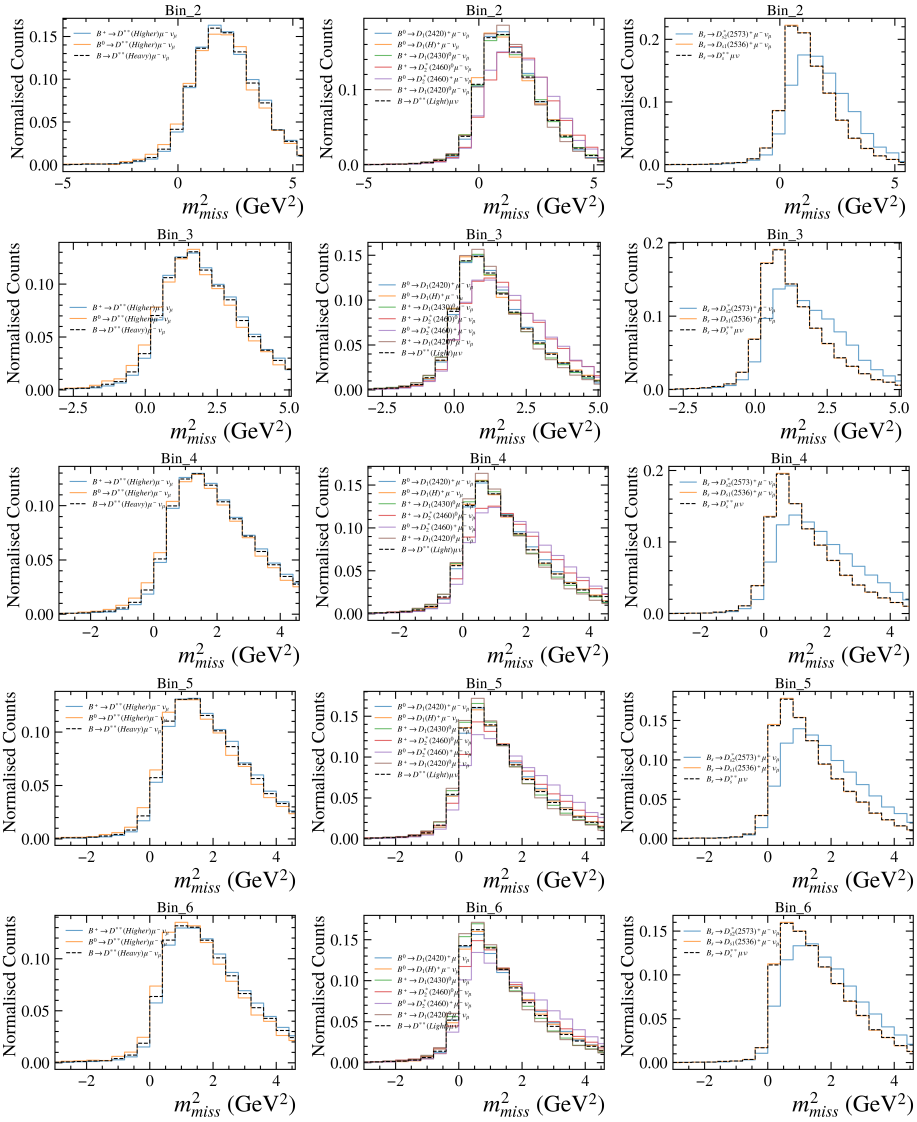


Figure F.2: The MisID template shapes shown different w bins along with nominal data templates. Legend shows the number of events for the different types of MisID components from data taking years 2016/2017/2018 (left to right)

F.3 D^{**} grouped templates



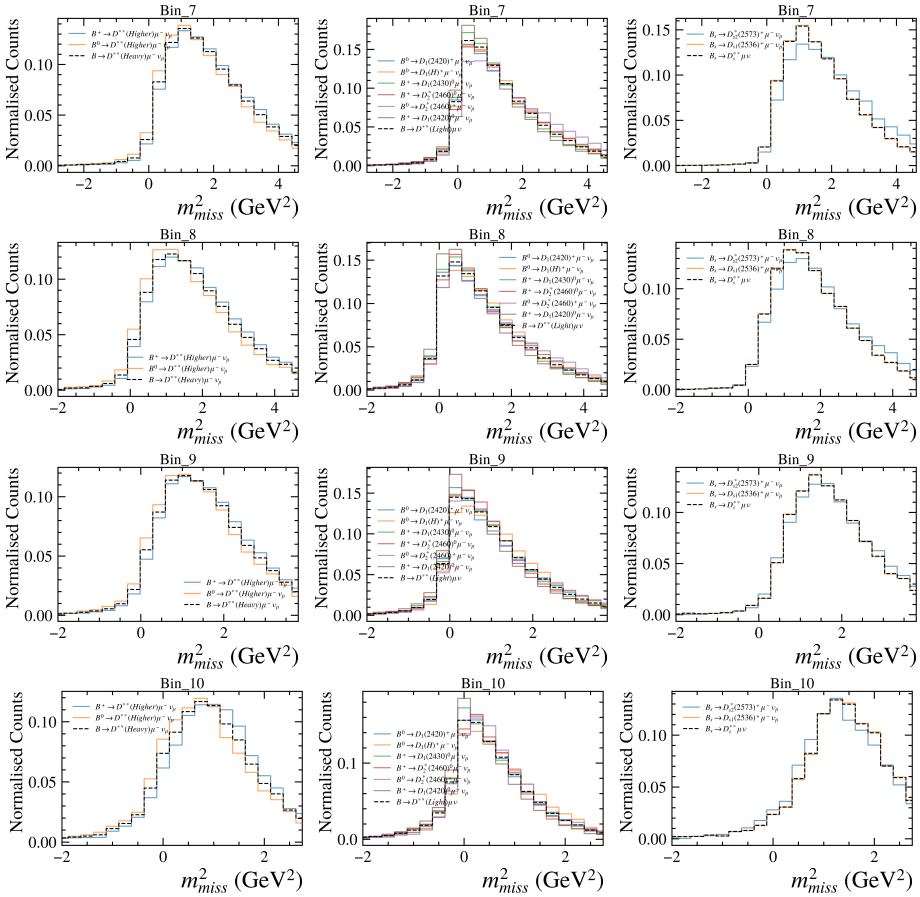


Figure F.3: Combined D^{**} template shapes (black dashed-line) are shown together with its sub-components described as in Tab. 5.10 for the first w bin.

G m^2_{miss}fit results

The stability of m^2_{miss}fits (see section 5.5.4) used to extract sample composition can be seen from the fit projections with the well-behaved *pulls* (pull = $(N^i_{\text{data}} - N^i_{\text{model}})/\sqrt{N^i_{\text{data}}}$) in Fig. J.1.

Bin 1: $1.0 < w \leq 1.05$	
Component	Fit Value ± Uncertainty
$N_{D^*\mu}$	46750 ± 340
$N_{D^*\tau}$	580 ± 140
N_{D^*DX}	850 ± 150
$N_{D^{**}\text{(Higher)}}$	0 ± 210
$N_{D^{**}}$	3540 ± 320
N_{D_s}	57 ± 15
N_{Comb}	320 ± 130
$N_{\text{D*Comb}}$	0 ± 5300
f_{B_s}	0.0161 ± 0.0040
f_τ	0.0125 ± 0.0031

Table 6.4: Fit results for Bin 1

Parameter	$N_{D^*\mu}$	N_{D^*DX}	$N_{D^{**}\text{(Higher)}}$	$N_{D^{**}}$	$N_{\text{D*Comb}}$	N_{Comb}	f_{B_s}	f_τ
$N_{D^*\mu}$	1.000	0.206	0.000	-0.690	0.013	-0.258	0.003	0.046
N_{D^*DX}	0.206	1.000	-0.000	-0.373	0.000	-0.428	0.020	-0.382
$N_{D^{**}\text{(Higher)}}$	0.000	-0.000	1.000	-0.001	-0.000	-0.000	-0.000	-0.000
$N_{D^{**}}$	-0.690	-0.373	-0.001	1.000	0.001	0.090	-0.094	-0.220
$N_{\text{D*Comb}}$	0.013	0.000	-0.000	0.001	1.000	0.001	0.000	-0.000
N_{Comb}	-0.258	-0.428	-0.000	0.090	0.001	1.000	-0.003	0.016
f_{B_s}	0.003	0.020	-0.000	-0.094	0.000	-0.003	1.000	0.001
f_τ	0.046	-0.382	-0.000	-0.220	-0.000	0.016	0.001	1.000

Table 6.5: Correlation matrix for the first w bin.

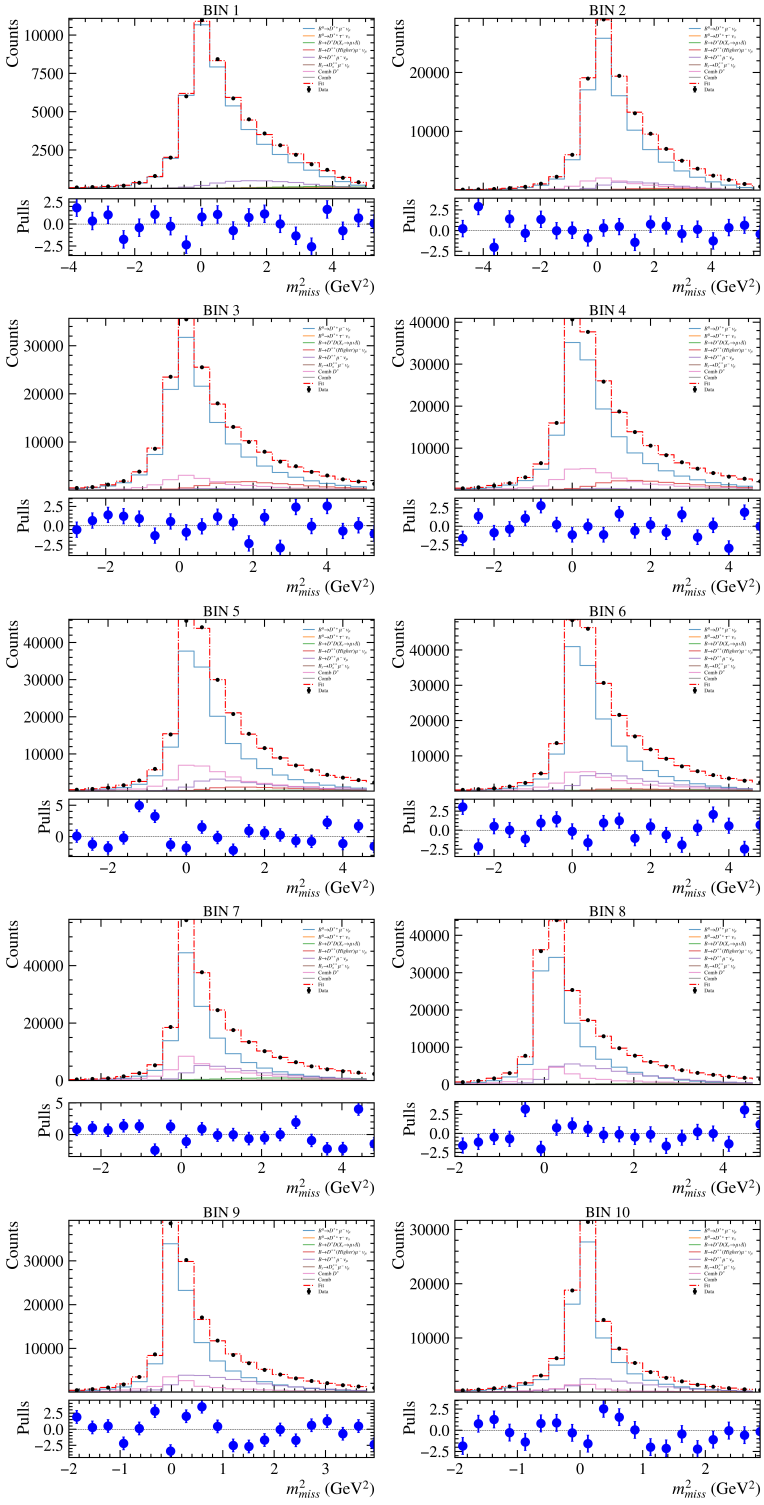


Figure G.1: Fit projections in each w bin.

H Initial reweighting

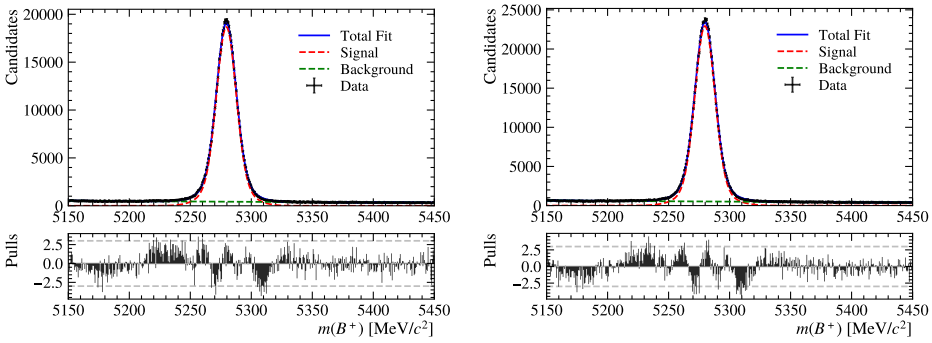


Figure H.1: Mass plot for 2017-2018 (left-right) $B \to J/\psi K$ decays.

I Final reweighting

J Alternative m^2_{miss} fit for systematics studies

This fit is performed with the updated templates which are reweighted with corrections presented in section 5.6.2.

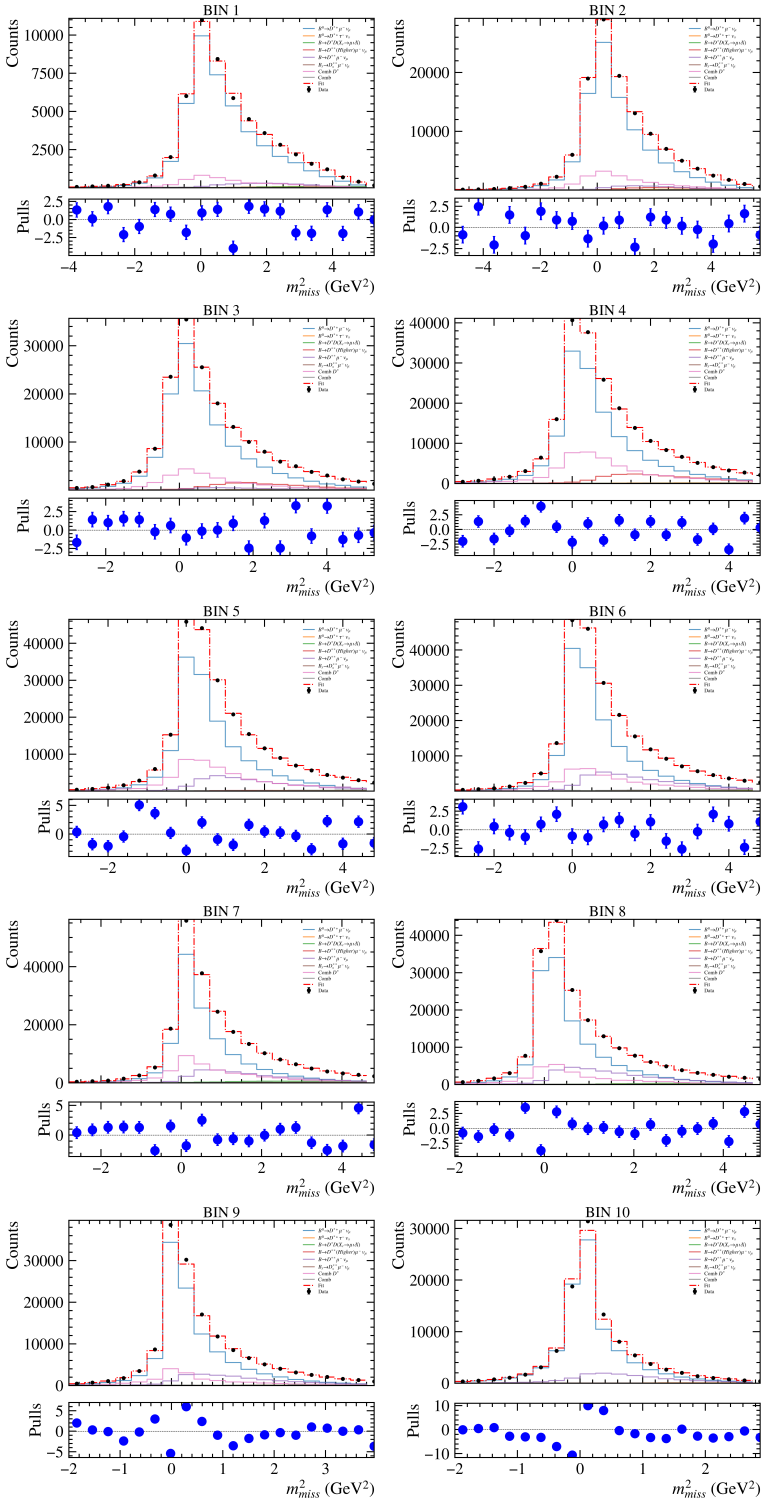


Figure J.1: Fit projections in each w bin after final reweighting.

Bibliography

[1] S. Iguro, T. Kitahara, and R. Watanabe, *Global fit to $b \to c\tau\nu$ anomalies as of Spring 2024*, Phys. Rev. D **110** (2024) 075005, arXiv:2405.06062. (Pages xi, 40, 41, and 43)

[2] F. U. Bernlochner, Z. Ligeti, M. Papucci, and D. J. Robinson, *Combined analysis of semileptonic b decays to d and D^*: $r(D^{(*)})$, $|V_{cb}|$, and new physics*, Phys. Rev. D **95** (2017) 115008, arXiv:1703.05330. (Pages xii, 27, 117, and 128)

[3] HFLAV collaboration, Y. Amhis *et al.*, *Averages of b-hadron, c-hadron, and τ-lepton properties as of summer 2016*, Eur. Phys. J. C **77** (2017) 895, arXiv:1612.07233. (Pages xii, xvi, 38, and 117)

[4] LHCb collaboration, R. Aaij *et al.*, *Measurement of the shape of the $B_s^0 \to D_s^{*-}\mu^+\nu_\mu$ differential decay rate*, JHEP **12** (2020) 144, arXiv:2003.08453. (Pages xvi, 45, 46, and 49)

[5] Belle-II collaboration, I. Adachi *et al.*, *Determination of $|Vcb|$ using $\bar{B}^0 \to D^{*-}\ell^+\nu$ decays with Belle II*, Phys. Rev. **D108** (2023) 092013, arXiv:2310.01170. (Pages xvii, 1, 45, 46, 49, 169, 170, 225, and 226)

[6] Belle collaboration, M. T. Prim *et al.*, *Measurement of differential distributions of $B \to D^*\ell\nu_\ell$ and implications on $|V_{cb}|$*, Phys. Rev. **D108** (2023) 012002, arXiv:2301.07529. (Pages xvii, 1, 38, 45, and 47)

[7] HPQCD, (HPQCD Collaboration)‡, J. Harrison and C. T. H. Davies, *$B \to D^*$ and $Bs \to Ds^*$ vector, axial-vector and tensor form factors for the full q2 range from lattice QCD*, Phys. Rev. D **109** (2024) 094515, arXiv:2304.03137. (Pages xvii, xviii, 47, 48, 49, 50, 161, 169, and 258)

[8] J. Haffner, *The CERN accelerator complex*, , General Photo. (Pages xviii and 53)

[9] LHCb collaboration, A. A. Alves, Jr. *et al.*, *The LHCb Detector at the LHC*, JINST **3** (2008) S08005. (Pages xviii, xix, 55, 56, 59, 62, 63, 64, and 65)

[10] LHCb collaboration, *Performance of the LHCb Vertex Locator*, JINST **9** (2014) . (Pages xviii, 57, and 58)

[11] LHCb collaboration, R. Aaij *et al.*, *Design and performance of the LHCb trigger and full real-time reconstruction in Run 2 of the LHC*, JINST **14** (2019) P04013, arXiv:1812.10790. (Pages xviii, xix, 59, 66, 67, 68, 69, and 71)

[12] J. Luisier, *Performance of lhcb silicon tracker detector in the lhc*, Physics Procedia **37** (2012) 851, Proceedings of the 2nd International Conference on Technology and Instrumentation in Particle Physics (TIPP 2011). (Pages xviii, 59, and 60)

[13] LHCb Outer Tracker Group, R. Arink *et al.*, *Performance of the LHCb Outer Tracker*, JINST **9** (2014) P01002, arXiv:1311.3893. (Pages xviii, 60, and 61)

[14] R. Calabrese *et al.*, *Performance of the LHCb RICH detectors during LHC Run 2*, JINST **17** (2022) P07013, arXiv:2205.13400. (Pages xviii and 62)

[15] Derkach, Denis, Hushchyn, Mikhail, and Kazeev, Nikita, *Machine learning based global particle identification algorithms at the lhcb experiment*, EPJ Web Conf. **214** (2019) 06011. (Pages xix and 65)

[16] LHCb collaboration, *Framework TDR for the LHCb Upgrade II* , CERN, Geneva, 2021. doi: 10.17181/CERN.NTVH.Q21W. (Pages xix, 72, 74, 76, 77, and 78)

[17] F. U. Bernlochner, Z. Ligeti, M. Papucci, and D. J. Robinson, *Combined analysis of semileptonic B decays to D and D^*: $R(D^{(*)})$, $|V_{cb}|$, and new physics*, Phys. Rev. **D95** (2017) 115008, Erratum ibid. **97** (2018) 059902, arXiv:1703.05330. (Pages xxiii, 2, 159, 160, 162, and 163)

[18] Belle collaboration, M. T. Prim *et al.*, *Measurement of angular coefficients of $B \to D^* \ell \nu$: Implications for $|V_{cb}|$ and tests of lepton flavor universality*,

Phys. Rev. Lett. **133** (2024) 131801, arXiv:2310.20286. (Pages xxiii, 1, 163, and 167)

[19] M. Bordone, O. Heald, and A. Jüttner, *Angular Analysis of $\bar{B} \to D^* \ell \bar{\nu}_\ell$ from Lattice and Experiment: $|V_{cb}|$ and New Physics Constraints*, arXiv:2606.23410. (Pages xxiii, 166, 167, and 168)

[20] A. Vaquero Avilés-Casco, *B meson semileptonic decays from lattice QCD*, PoS **DISCRETE2024** (2025) 081, arXiv:2504.07857. (Pages xxiv, 169, and 170)

[21] Belle collaboration, W. Dungel *et al.*, *Measurement of the form factors of the decay $B^0 \to D^{*-} \ell^+ \nu$ and determination of the CKM matrix element $|V_{cb}|$*, Phys. Rev. **D82** (2010) 112007, arXiv:1010.5620. (Page 1)

[22] Belle collaboration, E. Waheed *et al.*, *Measurement of the CKM matrix element $|V_{cb}|$ from $B^0 \to D^{*-} \ell^+ \nu_\ell$ at Belle*, Phys. Rev. D **100** (2019) 052007, arXiv:1809.03290, [Erratum: Phys.Rev.D 103, 079901 (2021)]. (Pages 1, 49, and 193)

[23] BaBar collaboration, B. Aubert *et al.*, *Determination of the form-factors for the decay $B^0 \to D^{*-} \ell^+ \nu_l$ and of the CKM matrix element $|V_{cb}|$*, Phys. Rev. **D77** (2008) 032002, arXiv:0705.4008. (Page 1)

[24] BaBar collaboration, J. P. Lees *et al.*, *Extraction of form Factors from a Four-Dimensional Angular Analysis of $\overline{B} \to D^* \ell^- \overline{\nu}_\ell$*, Phys. Rev. Lett. **123** (2019) 091801, arXiv:1903.10002. (Page 1)

[25] I. Caprini, L. Lellouch, and M. Neubert, *Dispersive bounds on the shape of $b \to d^* l \nu$ form factors*, Nucl. Phys. B **530** (1998) 153, arXiv:hep-ph/9712417v1. (Pages 1, 27, 33, 34, and 35)

[26] C. G. Boyd, B. Grinstein, and R. F. Lebed, *Precision corrections to dispersive bounds on form-factors*, Phys. Rev. **D56** (1997) 6895, arXiv:hep-ph/9705252. (Page 1)

[27] LHCb collaboration, *Measurement of hadronic form-factor parameters with an angular analysis of $B^0 \to D^{*-} \mu^+ \nu_\mu$ decays* , CERN, Geneva, 2026. (Pages 2, 223, 225, 226, and 228)

[28] K. G. Wilson, *Confinement of quarks*, Phys. Rev. D **10** (1974) 2445. (Page 7)

[29] Particle Data Group, S. Navas *et al.*, *Review of particle physics*, Phys. Rev. D **110** (2024) 030001. (Pages 13, 173, and 201)

[30] CKMfitter group, J. Charles *et al.*, *Current status of the standard model CKM fit and constraints on $\Delta F = 2$ new physics*, Phys. Rev. **D91** (2015) 073007, arXiv:1501.05013, updated results and plots available at http://ckmfitter.in2p3.fr/. (Page 14)

[31] Y. Sakaki, M. Tanaka, A. Tayduganov, and R. Watanabe, *Testing leptoquark models in $\bar{B} \to D^{(*)}\tau\bar{\nu}$*, Phys. Rev. D **88** (2013) 094012, arXiv:1309.0301. (Pages 18 and 42)

[32] M. Tanaka and R. Watanabe, *New physics in the weak interaction of $\bar{B} \to D^{(*)}\tau\bar{\nu}$*, Phys. Rev. D **87** (2013) 034028, arXiv:1212.1878. (Pages 20 and 21)

[33] D. Becirevic, S. Fajfer, I. Nisandzic, and A. Tayduganov, *Angular distributions of $B^0 \to D^* l\nu$ decays and search of New Physics*, Nucl. Phys. B **946** (2019) 114707, arXiv:1602.03030. (Pages 20, 23, 34, 40, and 107)

[34] J. C. Ward, *An identity in quantum electrodynamics*, Physical Review **78** (1950) 182. (Page 22)

[35] D. Becirevic, M. Fedele, I. Nisandzic, and A. Tayduganov, *Lepton flavor universality tests through angular observables of $\overline{B} \to d^{(*)}\ell\overline{\nu}$ decay modes*, 2019. (Pages 24 and 107)

[36] M. Duraisamy, P. Sharma, and A. Datta, *Azimuthal $b \to d^(*)\tau\nu$ angular distribution with tensor operators*, Physical Review D **90** (2014) , arXiv:1405.3719v. (Pages 24 and 42)

[37] C. G. Boyd, B. Grinstein, and R. F. Lebed, *Constraints on form factors for exclusive semileptonic heavy to light meson decays*, Phys. Rev. Lett. **74** (1995) 4603, arXiv:hep-ph/9412324v3. (Pages 26 and 27)

[38] M. Neubert, *Heavy-quark symmetry*, Physics Reports **245** (1994) 259, arXiv:hep-ph/9306320v1. (Pages 27, 30, and 34)

[39] C. G. Boyd, B. Grinstein, and R. F. Lebed, *Precision corrections to dispersive bounds on form factors*, Phys. Rev. D **56** (1997) 6895, arXiv:hep-ph/9705252v2. (Page 27)

[40] C. G. Boyd, B. Grinstein, and R. F. Lebed, *Model-independent determinations of $b \to dl\nu, d^*l\nu$ form factors*, Nucl. Phys. B **461** (1996) 493, arXiv:hep-ph/9508211. (Pages 27 and 29)

[41] D. Bigi, P. Gambino, and S. Schacht, *$R(D^*)$, $|V_{cb}|$, and the Heavy Quark Symmetry relations between form factors*, JHEP **11** (2017) 061, arXiv:1707.09509. (Pages 27, 29, and 159)

[42] R. F. L. C. Glenn Boyd, Benjamin Grinstein, *Model-independent determinations of $b \to d\ell\nu$, $d^*\ell\nu$ form factors*, Nucl. Phys. B (1996) **461** (1996) 493, arXiv:9508211v1. (Page 29)

[43] M. E. Luke, *Effects of subleading operators in the heavy quark effective theory*, Phys. Lett. B **252** (1990) 447, arXiv:1506.08896. (Page 30)

[44] M. Neubert, Z. Ligeti, and Y. Nir, *Qcd sum rule analysis of the subleading isgur-wise form factor*, Physics Letters B **301** (1993) 101. (Pages 31 and 34)

[45] F. U. Bernlochner and Z. Ligeti, *Semileptonic $B_{(s)}$ decays to excited charmed mesons with e, μ, τ and searching for new physics with $r(d^{**})$*, Phys. Rev. D **95** (2017) 014022, arXiv:1606.09300. (Pages 31, 33, 34, and 36)

[46] S. Fajfer, J. F. Kamenik, and I. Nišandžić, *$b \to D^*\tau\overline{\nu}_\tau$ sensitivity to new physics*, Phys. Rev. D **85** (2012) 094025, arXiv:1203.2654v. (Pages 34, 35, and 40)

[47] Y. Amhis *et al.*, *Averages of b-hadron, c-hadron, and τ - lepton properties as of 2018*, Eur. Phys. J. C **81** (2021) 226, arXiv:1909.12524. (Page 35)

[48] A. K. Leibovich, Z. Ligeti, I. W. Stewart, and M. B. Wise, *Semileptonic b decays to excited charmed mesons*, Phys. Rev. D **57** (1998) 308, arXiv:hep-ph/9705467v2. (Page 36)

[49] LHCb collaboration, R. Aaij *et al.*, *Measurement of the ratios of branching fractions $\mathcal{R}(D^*)$ and $\mathcal{R}(D^0)$*, Phys. Rev. Lett. **131** (2023) 111802, arXiv:2302.02886. (Page 37)

[50] LHCb collaboration, R. Aaij *et al.*, *Measurement of the Branching Fraction Ratios R(D+) and R(D*+) Using Muonic τ Decays*, Phys. Rev. Lett. **134** (2025) 061801, arXiv:2406.03387. (Pages 37, 188, 189, and 190)

[51] LHCb collaboration, R. Aaij *et al.*, *Test of lepton flavor universality using B0→D*-τ+ντ decays with hadronic τ channels*, Phys. Rev. D **108** (2023) 012018, arXiv:2305.01463, [Erratum: Phys.Rev.D 109, 119902 (2024)]. (Page 37)

[52] Heavy Flavor Averaging Group (HFLAV), S. Banerjee *et al.*, *Averages of b-hadron, c-hadron, and τ-lepton properties as of 2023*, Phys. Rev. D **113** (2026) 012008, arXiv:2411.18639. (Pages 38, 158, 162, and 226)

[53] Babar collaboration, B. Kowalewski *et al.*, *Evidence for an excess of $B \to D^*\tau\nu$decays*, Phys. Conf. Ser. **455** (2013) 012039, arXiv:1205.5442v. (Page 38)

[54] Belle collaboration, M. Huschle *et al.*, *Measurement of the branching ratio of $\bar{B} \to D^*\tau^-\bar{\nu_\tau}$ relative to $\bar{B} \to D^*l\bar{\nu_l}$ decays with hadronic tagging at Belle*, Phys. Rev. **D92** (2015) 072014, arXiv:1507.03233. (Page 38)

[55] Belle-II collaboration, I. Adachi *et al.*, *Test of lepton flavor universality with measurements of R(D+) and R(D*+) using semileptonic B tagging at the Belle II experiment*, Phys. Rev. D **112** (2025) 032010, arXiv:2504.11220. (Page 38)

[56] T. Kapoor, Z.-R. Huang, and E. Kou, *New physics search via angular distribution of $B \to D\ell\nu$ decay in the light of the new lattice data*, JHEP **02** (2025) 053, arXiv:2401.11636. (Page 38)

[57] BaBar collaboration, J. P. Lees *et al.*, *Evidence for an excess of $\bar{B} \to D^{(*)}\tau^-\bar{\nu}_\tau$ decays*, Phys. Rev. Lett. **109** (2012) 101802, arXiv:1205.5442. (Page 39)

[58] BaBar collaboration, J. P. Lees *et al.*, *Measurement of an Excess of $\bar{B} \to D^{(*)}\tau^-\bar{\nu}_\tau$ Decays and Implications for Charged Higgs Bosons*, Phys. Rev. D **88** (2013) 072012, arXiv:1303.0571. (Page 39)

[59] Belle collaboration, M. Huschle *et al.*, *Measurement of the branching ratio of $\bar{B} \to D^{(*)}\tau^-\bar{\nu}_\tau$ relative to $\bar{B} \to D^{(*)}\ell^-\bar{\nu}_\ell$ decays with hadronic tagging at Belle*, Phys. Rev. D **92** (2015) 072014, arXiv:1507.03233. (Page 39)

[60] Belle collaboration, Y. Sato *et al.*, *Measurement of the branching ratio of* $\bar{B}^0 \to D^{*+}\tau^-\bar{\nu}_\tau$ *relative to* $\bar{B}^0 \to D^{*+}\ell^-\bar{\nu}_\ell$ *decays with a semileptonic tagging method*, Phys. Rev. D **94** (2016) 072007, arXiv:1607.07923. (Page 39)

[61] Belle collaboration, S. Hirose *et al.*, *Measurement of the* τ *lepton polarization and* $R(D^*)$ *in the decay* $\bar{B} \to D^*\tau^-\bar{\nu}_\tau$, Phys. Rev. Lett. **118** (2017) 211801, arXiv:1612.00529. (Page 39)

[62] LHCb collaboration, R. Aaij *et al.*, *Measurement of the ratio of the* $B^0 \to D^{*-}\tau^+\nu_\tau$ *and* $B^0 \to D^{*-}\mu^+\nu_\mu$ *branching fractions using three-prong* τ*-lepton decays*, Phys. Rev. Lett. **120** (2018) 171802, arXiv:1708.08856. (Pages 39 and 42)

[63] LHCb collaboration, R. Aaij *et al.*, *Test of Lepton Flavor Universality by the measurement of the* $B^0 \to D^{*-}\tau^+\nu_\tau$ *branching fraction using three-prong* τ *decays*, Phys. Rev. D **97** (2018) 072013, arXiv:1711.02505. (Pages 39 and 42)

[64] LHCb collaboration, R. Aaij *et al.*, *Test of lepton flavor universality using* $B0 \to D^*\text{-}\tau + \nu\tau$ *decays with hadronic* τ *channels*, Phys. Rev. D **108** (2023) 012018, arXiv:2305.01463, [Erratum: Phys.Rev.D 109, 119902 (2024)]. (Pages 39 and 42)

[65] Belle collaboration, A. Abdesselam *et al.*, *Measurement of* $\mathcal{R}(D)$ *and* $\mathcal{R}(D^*)$ *with a semileptonic tagging method*, arXiv:1904.08794. (Page 39)

[66] LHCb collaboration, R. Aaij *et al.*, *Measurement of the ratio of branching fractions* $\mathcal{B}(\bar{B}^0 \to D^{*+}\tau^-\bar{\nu}_\tau)/\mathcal{B}(\bar{B}^0 \to D^{*+}\mu^-\bar{\nu}_\mu)$, Phys. Rev. Lett. **115** (2015) 111803, arXiv:1506.08614, [Erratum: Phys.Rev.Lett. 115, 159901 (2015)]. (Page 39)

[67] LHCb collaboration, *Measurement of the ratios of branching fractions* $\mathcal{R}(D^*)$ *and* $\mathcal{R}(D^0)$, Phys. Rev. Lett. **131** (2023) 111802, arXiv:2302.02886. (Page 39)

[68] Belle-II collaboration, I. Adachi *et al.*, *Test of lepton flavor universality with a measurement of R(D*) using hadronic B tagging at the Belle II experiment*, Phys. Rev. D **110** (2024) 072020, arXiv:2401.02840. (Page 39)

[69] LHCb collaboration, C. Chen, *$b \to cl\bar{\nu}$ decays at LHCb*, in *58th Rencontres de Moriond on QCD and High Energy Interactions*, 2024, arXiv:2405.08953. (Page 39)

[70] LHCb collaboration, R. Aaij *et al.*, *Measurement of the ratio of branching fractions $\mathcal{B}(B_c^+ \to J/\psi\tau^+\nu_\tau)/\mathcal{B}(B_c^+ \to J/\psi\mu^+\nu_\mu)$*, Phys. Rev. Lett. **120** (2018) 121801, arXiv:1711.05623. (Page 39)

[71] LHCb collaboration, R. Aaij *et al.*, *Measurement of the ratio of branching fractions $\mathcal{B}(B_c^+ \to J/)^+_{)/\mathcal{B}(B_c^+ \to J/)^+}$*, arXiv:2606.10018. (Page 39)

[72] Belle, Belle-II collaboration, K. Adamczyk, *Semitauonic B decays at Belle/-Belle II*, in *10th International Workshop on the CKM Unitarity Triangle*, 2019, arXiv:1901.06380. (Page 39)

[73] Belle collaboration, A. Abdesselam *et al.*, *Measurement of the D^{*-} polarization in the decay $B^0 \to D^{*-}\tau^+\nu_\tau$*, in *10th International Workshop on the CKM Unitarity Triangle*, 2019, arXiv:1903.03102. (Pages 39 and 42)

[74] LHCb collaboration, R. Aaij *et al.*, *Observation of the decay $\Lambda_b^0 \to \Lambda_c^+\tau^-\overline{\nu}_\tau$*, arXiv:2201.03497. (Page 39)

[75] LHCb collaboration, R. Aaij *et al.*, *Measurement of the D* longitudinal polarization in B0→D*-τ+ντ decays*, Phys. Rev. D **110** (2024) 092007, arXiv:2311.05224. (Page 39)

[76] CMS collaboration, V. Chekhovsky *et al.*, *Measurement of the ratio of the Bc+→J/ψτ+ντ and Bc+→J/ψμ+νμ branching fractions using three-prong τ lepton decays*, Phys. Rev. D **113** (2026) L111101, arXiv:2510.21559. (Page 39)

[77] Z. Ligeti, M. Papucci, and R. D. J. *New physics in the visible final states of $B \to D^*\tau\nu$*, JHEP **83** (2017) , arXiv:1610.02045. (Page 40)

[78] R. Mandal, C. Murgui, A. Penuelas, and P. A. *The role of right-handed neutrinos in $b \to c\tau\overline{v}$ anomalies*, JHEP **22** (2020) , arXiv:2004.06726. (Page 40)

[79] R. Mandal, *Angular analysis of $\overline{B} \to D_2^*(\to d\pi)\ell\overline{\nu}$ decay and new physics*, Phys. Rev. D **101** (2020) 033007, arXiv:1912.03835. (Pages 40 and 107)

[80] X. He and G. Valencia, *B decays with τ leptons in nonuniversal left-right models*, Physical Review D **87** (2013) , arXiv:1211.0348v. (Page 40)

[81] J. Kumar, D. London, and R. Watanabe, *Combined explanations of the $b \to s\mu^+\mu^-$ and $b \to c\tau^-\overline{\nu}$ anomalies: A general model analysis*, Phys. Rev. D **99** (2019) 015007, arXiv:1806.07403. (Page 40)

[82] S. Fraser *et al.*, *Towards a viable scalar interpretation of $R_{D^{(*)}}$*, Phys. Rev. D **98** (2018) 035016, arXiv:1805.08189. (Page 40)

[83] R. Alonso, B. Grinstein, and J. Martin Camalich, *Lifetime of B_c^- mesons constrains explanations for anomalies in $b \to D^{(*)}\tau\nu$*, Phys. Rev. Lett. **118** (2017) 081802, arXiv:1611.06676. (Page 40)

[84] S. Iguro and R. Watanabe, *Bayesian fit analysis to full distribution data of $\overline{\mathrm{B}} \to \mathrm{D}^{(*)}\ell\overline{\nu}$: $|\mathrm{V_{cb}}|$ determination and new physics constraints*, JHEP **08** (2020) 006, arXiv:2004.10208. (Pages 40 and 41)

[85] S. Iguro and K. Tobe, *$R(D^{(*)})$ in a general two Higgs doublet model*, Nucl. Phys. B **925** (2017) 560, arXiv:1708.06176. (Page 42)

[86] D. A. Faroughy, A. Greljo, and J. F. Kamenik, *Confronting lepton flavor universality violation in B decays with high-p_T tau lepton searches at LHC*, Phys. Lett. B **764** (2017) 126, arXiv:1609.07138. (Page 42)

[87] S. Iguro *et al.*, *D^* polarization vs. $R_{D^{(*)}}$ anomalies in the leptoquark models*, JHEP **02** (2019) 194, arXiv:1811.08899. (Page 42)

[88] I. Doršner, S. Fajfer, N. Košnik, and I. Nišandžić, *Minimally flavored colored scalar in $\bar{b} \to d^{(*)}\tau\bar{\nu}$ and the mass matrices constraints*, Journal of High Energy Physics **2013** (2013) 84, arXiv:1306.6493. (Page 42)

[89] B. Dumont, K. Nishiwaki, and R. Watanabe, *Lhc constraints and prospects for s_1 scalar leptoquark explaining the $b \to d^(*)\tau\nu$ anomaly*, Physical Review D **94** (2016) , arXiv:1603.05248. (Page 42)

[90] Y. Sakaki, R. Watanabe, M. Tanaka, and A. Tayduganov, *Testing leptoquark models in $\overline{B} \to D^{(*)}\tau\overline{\nu}$*, Phys. Rev. D **88** (2013) 094012, arXiv:1309.0301v. (Page 42)

[91] CMS collaboration, A. M. Sirunyan *et al.*, *Search for heavy neutrinos and third-generation leptoquarks in hadronic states of two τ leptons and two jets in proton-proton collisions at $\sqrt{s}$ = 13 TeV*, JHEP **03** (2019) 170, arXiv:1811.00806. (Page 42)

[92] ATLAS collaboration, M. Aaboud *et al.*, *Searches for third-generation scalar leptoquarks in $\sqrt{s}$ = 13 TeV pp collisions with the ATLAS detector*, JHEP **06** (2019) 144, arXiv:1902.08103. (Page 42)

[93] ATLAS collaboration, G. Aad *et al.*, *Search for pair production of third-generation scalar leptoquarks decaying into a top quark and a τ-lepton in pp collisions at $\sqrt{s}$ = 13 TeV with the ATLAS detector*, JHEP **06** (2021) 179, arXiv:2101.11582. (Page 42)

[94] HPQCD, UKQCD collaboration, E. Follana *et al.*, *Highly improved staggered quarks on the lattice, with applications to charm physics*, Phys. Rev. D **75** (2007) 054502, arXiv:hep-lat/0610092. (Page 44)

[95] HPQCD collaboration, J. Harrison and C. T. H. Davies, *Bs→Ds* form factors for the full q2 range from lattice QCD*, Phys. Rev. D **105** (2022) 094506, arXiv:2105.11433. (Page 47)

[96] LATTICE-HPQCD collaboration, J. Harrison, C. T. H. Davies, and A. Lytle, *$R(J/\psi)$ and $B_c^- \to J/\psi \ell^- \bar{\nu}_\ell$ Lepton Flavor Universality Violating Observables from Lattice QCD*, Phys. Rev. Lett. **125** (2020) 222003, arXiv:2007.06956. (Page 47)

[97] L. Evans and P. Bryant, *Lhc machine*, JINST **3** (2008) S08001. (Page 53)

[98] CERN, *The CERN accelerator complex*, CERN-ACC-2014-0337, CERN, 2014. (Page 53)

[99] LHCb Collaboration, *The LHCb Upgrade I*, JINST **19** (2024) P05065. (Page 54)

[100] ATLAS Collaboration, *The ATLAS experiment at the CERN LHC*, JINST **3** (2008) S08003. (Page 55)

[101] CMS Collaboration, *The CMS experiment at the CERN LHC*, JINST **3** (2008) S08004. (Page 55)

[102] ALICE Collaboration, *The ALICE experiment at the CERN LHC*, JINST **3** (2008) S08002. (Page 55)

[103] CERN, *The LHC experiments*, CERN-Brochure-2017-002-Eng, CERN, 2017. (Page 55)

[104] B. Muratori and T. Pieloni, *Luminosity levelling techniques for the LHC*, in *ICFA Mini-Workshop on Beam-Beam Effects in Hadron Colliders*, 177–181, 2014, arXiv:1410.5646. (Page 55)

[105] A. A. Alves, Jr. *et al.*, *Performance of the LHCb muon system*, JINST **8** (2013) P02022, arXiv:1211.1346. (Page 64)

[106] LHCb collaboration, L. Paolucci, *The LHCb Muon Detector Upgrades*, PoS **ICHEP2022** (2022) 683. (Page 64)

[107] LHCb collaboration, M. Stahl, *Machine learning and parallelism in the reconstruction of LHCb and its upgrade*, J. Phys. Conf. Ser. **898** (2017) 042042, arXiv:1710.08947. (Page 69)

[108] M. De Cian, S. Farry, P. Seyfert, and S. Stahl, *Fast neural-net based fake track rejection in the LHCb reconstruction*, LHCb-PUB-2017-011, 2017. (Page 69)

[109] LHCb collaboration, *Physics case for an LHCb Upgrade II — Opportunities in flavour physics, and beyond, in the HL-LHC era*, arXiv:1808.08865. (Page 72)

[110] M. Clemencic *et al.*, *The LHCb simulation application, Gauss: Design, evolution and experience*, J. Phys. Conf. Ser. **331** (2011) 032023. (Page 78)

[111] T. Sjöstrand *et al.*, *An introduction to pythia 8.2*, Computer Physics Communications **191** (2015) 159–177, arXiv:1410.3012v. (Page 79)

[112] D. J. Lange, *The EvtGen particle decay simulation package*, Nucl. Instrum. Meth. **A462** (2001) 152. (Page 79)

[113] P. Golonka and Z. Was, *PHOTOS Monte Carlo: A precision tool for QED corrections in Z and W decays*, Eur. Phys. J. **C45** (2006) 97, arXiv:hep-ph/0506026. (Page 79)

[114] Geant4 collaboration, S. Agostinelli *et al.*, *Geant4: A simulation toolkit*, Nucl. Instrum. Meth. **A506** (2003) 250. (Page 79)

[115] LHCb collaboration, R. Aaij *et al.*, *Measurement of the ratio of branching fractions* $\mathcal{B}(\bar{B}^0 \to D^{*+}\tau^-\bar{\nu}_\tau)/\mathcal{B}(\bar{B}^0 \to D^{*+}\mu^-\bar{\nu}_\mu)$, Phys. Rev. Lett. **115** (2015) 111803, arXiv:1506.08614. (Pages 94, 117, 121, and 178)

[116] F. U. Bernlochner *et al.*, *Das ist der HAMMER: Consistent new physics interpretations of semileptonic decays*, Eur. Phys. J. C **80** (2020) 883, arXiv:2002.00020. (Pages 103 and 170)

[117] A. Celis, M. Jung, X.-Q. Li, and A. Pich, *Sensitivity to charged scalars in* $\boldsymbol{B \to D^{(*)}\tau\nu_\tau}$ *and* $\boldsymbol{B \to \tau\nu_\tau}$ *decays*, JHEP **01** (2013) 054, arXiv:1210.8443. (Page 113)

[118] W. Verkerke and D. P. Kirkby, *The RooFit toolkit for data modeling*, eConf **C0303241** (2003) MOLT007, arXiv:physics/0306116. (Page 115)

[119] J. García Pardiñas *et al.*, *RooHammerModel: interfacing the HAMMER software tool with HistFactory and RooFit*, JINST **17** (2022) T04006, arXiv:2007.12605. (Page 115)

[120] G. Schwarz, *Estimating the dimension of a model*, The Annals of Statistics **6** (1978) 461. (Pages 121 and 122)

[121] C. Bobeth *et al.*, *Lepton-flavour non-universality of* $\bar{b} \to d^*\ell\bar{\nu}$ *angular distributions in and beyond the standard model*, The European Physical Journal C **81** (2021) . (Page 142)

[122] B. Efron, *Bootstrap methods: Another look at the jackknife*, Ann. Statist. **7** (1979) 1. (Pages 157 and 221)

[123] F. U. Bernlochner, Z. Ligeti, and D. J. Robinson, *N = 5, 6, 7, 8: Nested hypothesis tests and truncation dependence of* $|V_{cb}|$, Phys. Rev. **D100** (2019) 013005, arXiv:1902.09553. (Page 159)

[124] LHCb collaboration, R. Aaij *et al.*, *Measurement of the ratio of branching fractions* $\mathcal{R}(D^*)$ *and* $\mathcal{R}(D^0)$, Phys. Rev. Lett. **131** (2023) 111802, arXiv:2302.02886. (Page 159)

[125] S. de Boer, T. Kitahara, and I. Nišandžić, *Soft-photon corrections to $\bar{B} \to D\tau^-\bar{\nu}_\tau$ relative to $\bar{B} \to D\mu^-\bar{\nu}_\mu$*, Phys. Rev. Lett. **120** (2018) 261804, arXiv:1803.05881. (Page 160)

[126] Fermilab Lattice, MILC collaborations, J. A. Bailey *et al.*, *Update of $|V_{cb}|$ from the $\bar{B} \to D^*\ell\bar{\nu}$ form factor at zero recoil with three-flavor lattice QCD*, Phys. Rev. **D89** (2014) 114504, arXiv:1403.0635. (Pages 160 and 162)

[127] Fermilab Lattice, MILC collaborations, A. Bazavov *et al.*, *Semileptonic form factors for $B \to D^*\ell\nu$ at nonzero recoil from $2+1$-flavor lattice QCD*, Eur. Phys. J. **C82** (2022) 1141, Erratum ibid. **83** (2023) 21, arXiv:2105.14019. (Pages 161 and 258)

[128] JLQCD collaboration, Y. Aoki *et al.*, *$B \to D^*\ell\nu_\ell$ semileptonic form factors from lattice QCD with Möbius domain-wall quarks*, Phys. Rev. **D109** (2024) 074503, arXiv:2306.05657. (Pages 161 and 259)

[129] Belle collaboration, A. Abdesselam *et al.*, *Precise determination of the CKM matrix element $|V_{cb}|$ with $\bar{B}^0 \to D^{*+}\ell^-\bar{\nu}_\ell$ decays with hadronic tagging at Belle*, Phys. Rev. **D96** (2017) 092006, arXiv:1702.01521. (Page 162)

[130] Belle collaboration, R. Glattauer *et al.*, *Measurement of the decay $B \to D\ell\nu_\ell$ in fully reconstructed events and determination of the Cabibbo-Kobayashi-Maskawa matrix element $|V_{cb}|$*, Phys. Rev. **D93** (2016) 032006, arXiv:1510.03657. (Page 162)

[131] Fermilab Lattice, MILC collaborations, J. A. Bailey *et al.*, *$B \to D\ell\nu$ form factors at nonzero recoil and $|V_{cb}|$ from 2+1-flavor lattice QCD*, Phys. Rev. **D92** (2015) 034506, arXiv:1503.07237. (Page 162)

[132] M. Neubert, Z. Ligeti, and Y. Nir, *QCD sum rule analysis of the subleading Isgur-Wise form factor $\chi_2(vv')$*, Phys. Lett. **B301** (1993) 101, arXiv:hep-ph/9209271. (Page 162)

[133] M. Neubert, Z. Ligeti, and Y. Nir, *The subleading Isgur-Wise form-factor $\chi(3)$ (ν, ν') to order α_s in QCD sum rules*, Phys. Rev. **D47** (1993) 5060, arXiv:hep-ph/9212266. (Page 162)

[134] Z. Ligeti, Y. Nir, and M. Neubert, *The subleading Isgur-Wise form-factor $\chi(3)$ (ν, ν') and its implications for the decays $\overline{B} \to D^* \ell \bar{\nu}$*, Phys. Rev. **D49** (1994) 1302, arXiv:hep-ph/9305304. (Page 162)

[135] M. Bordone and A. Juttner, *New strategies for probing $B \to D^* \ell \bar{\nu}_\ell$ lattice and experimental data*, Eur. Phys. J. C **85** (2025) 129, arXiv:2406.10074. (Page 169)

[136] ROOT collaboration, K. Cranmer *et al.*, *HistFactory: A tool for creating statistical models for use with RooFit and RooStats* , New York U., New York, 2012. doi: 10.17181/CERN-OPEN-2012-016. (Pages 170 and 193)

[137] L. Gärtner *et al.*, *Constructing model-agnostic likelihoods, a method for the reinterpretation of particle physics results*, The European Physical Journal C **84** (2024) . (Page 170)

[138] D. Hill, M. John, W. Ke, and A. Poluektov, *Model-independent method for measuring the angular coefficients of $B^0 \to D^{*-} \tau^+ \nu_\tau$ decays*, JHEP **11** (2019) 133, arXiv:1908.04643. (Page 171)

[139] G. Ciezarek, A. Lupato, M. Rotondo, and M. Vesterinen, *Reconstruction of semileptonically decaying beauty hadrons produced in high energy pp collisions*, Journal of High Energy Physics **2017** (2017) . (Pages 179 and 181)

[140] M. Ebden, *Gaussian processes: A quick introduction*, 2015. (Page 179)

[141] A. G. d. G. Matthews *et al.*, *GPflow: A Gaussian process library using TensorFlow*, Journal of Machine Learning Research **18** (2017) 1. (Page 181)

[142] M. Abadi *et al.*, *TensorFlow: Large-scale machine learning on heterogeneous systems*, 2015. Software available from tensorflow.org. (Page 181)

[143] M. Genton, *Classes of kernels for machine learning: A statistics perspective*, The Journal of Machine Learning Research **2** (2002) 299. (Page 182)

[144] T. Chen and C. Guestrin, *Xgboost: A scalable tree boosting system*, in *Proceedings of the 22nd ACM SIGKDD International Conference on Knowledge Discovery and Data Mining*, KDD '16, 785–794, ACM, 2016. (Page 188)

[145] S. Tolk, J. Albrecht, F. Dettori, and A. Pellegrino, *Data driven trigger efficiency determination at LHCb*, LHCb-PUB-2014-039, 2014. (Page 189)

[146] L. Anderlini *et al.*, *The PIDCalib package*, LHCb-PUB-2016-021, 2016. (Page 191)

[147] R. Aaij *et al.*, *Selection and processing of calibration samples to measure the particle identification performance of the LHCb experiment in Run 2*, Eur. Phys. J. Tech. Instr. **6** (2019) 1, arXiv:1803.00824. (Page 191)

[148] M. Colonna *et al.*, *Redist, a python tool for model-agnostics binned-likelihood fits in high energy physics*, Python in Science Conference, 2025 (2025) . (Page 193)

[149] F. Herren and R. van Tonder, *On the simulated kinematic distributions of heavy meson decays*, arXiv:2602.18378. (Page 195)

[150] LHCb collaboration, R. Aaij *et al.*, *Precise measurement of the f_s/f_d ratio of fragmentation fractions and of B^0_s decay branching fractions*, Phys. Rev. **D104** (2021) 032005, arXiv:2103.06810. (Page 201)

[151] LHCb collaboration, R. Aaij *et al.*, *Study of $D_{sJ}^{(*)+}$ mesons decaying to D^{*+} K^0_S and D^{*0} K^+ final states*, JHEP **02** (2016) 133, arXiv:1601.01495. (Page 202)

[152] Belle collaboration, B. S. Gao *et al.*, *Observation of charmed strange meson pair production in Υ(2S) decays and in e+e- annihilation at s=10.52 GeV*, Phys. Rev. D **108** (2023) 112015, arXiv:2308.08900. (Page 202)

[153] M. De Cian *et al.*, *Measurement of the track finding efficiency* , CERN, Geneva, 2012. (Page 209)

[154] M. Pivk and F. R. Le Diberder, *sPlot: A statistical tool to unfold data distributions*, Nucl. Instrum. Meth. **A555** (2005) 356, arXiv:physics/0402083. (Page 209)

[155] L. Brenner *et al.*, *Comparison of unfolding methods using RooFitUnfold*, Int. J. Mod. Phys. A **35** (2020) 2050145, arXiv:1910.14654. (Page 218)

[156] G. D'Agostini, *A Multidimensional unfolding method based on Bayes' theorem*, Nucl. Instrum. Meth. A **362** (1995) 487. (Page 218)

[157] D. Vico Benet, *SLOP: A package for semi-leptonic observable predictions*, 2026. doi: 10.5281/zenodo.18601506. (Page 219)

[158] S. Calí, S. Klaver, M. Rotondo, and B. Sciascia, *Impacts of radiative corrections on measurements of lepton flavour universality in $B \to D\ell\nu_\ell$ decays*, Eur. Phys. J. C **79** (2019) 744, arXiv:1905.02702. (Page 225)

[159] T. K. Knospe, *Angular analyses of charged current decays at lhcb*, Talk at the 43rd International Conference on High Energy Physics (ICHEP 2026), 2026. Natal, Brazil, 31 July 2026. (Page 228)

[160] A. Maćkiewicz and W. Ratajczak, *Principal components analysis (pca)*, Computers Geosciences **19** (1993) 303. (Page 248)

[161] K. P. F. R. S. *Liii. on lines and planes of closest fit to systems of points in space*, Philosophical Magazine Series 1 **2** (1901) 559. (Page 248)